

THE UNIVERSITY OF HULL

**DEVELOPMENT OF A PET PROBE FOR THE
IMAGING OF COX-2 EXPRESSION IN CANCERS**

being a Thesis submitted for the degree of
Doctor of Philosophy
in the University of Hull

by Anna Pacelli

MSc (Università degli Studi di Bari “Aldo Moro”)

May 2015

*Considerate la vostra semenza:
fatti non foste a viver come bruti,
ma per seguir virtute e canoscenza”*

Dante Alighieri, Inferno, Canto XXVI

List of contents

Abstract	1
List of Abbreviations	2
List of Figures	5
List of Schemes	8
List of Tables	10
Acknowledgements	11
1. Cyclooxygenase	13
1.1 Eicosanoids	15
1.1.1 Biosynthesis of eicosanoids	15
1.1.2 Eicosanoids and inflammation	17
1.1.3 Eicosanoids and cancer	19
1.2 Involvement of COX-2 in cancers	20
1.2.1 Colorectal cancer	21
1.2.2 Oesophageal cancer	22
1.2.3 Gastric cancer	23
1.2.4 Breast cancer	24
1.2.5 Brain cancer	24
1.2.6 Lung cancer	25
1.2.7 Chemoresistance	26
1.2.8 COX-2 as a biomarker for stratification of cancer patients	27
1.3 COX inhibitors: NSAIDs	27

1.3.1 Structure-Activity Relationship studies	27
1.3.2 Kinetics of COX inhibition	31
1.3.3 COX inhibition assays	33
2. Molecular imaging	36
2.1 Fluorescence imaging (FI)	37
2.2 Single Photon Emission Computed Tomography (SPECT)	38
3. Positron Emission Tomography	39
3.1 Principles of PET	39
3.2 Development of a PET probe	41
3.3 Oncological PET imaging	46
3.3.1 Applications of PET imaging	47
3.3.2 Imaging of COX-2 expression	50
3.3.2.1 Carbon-11 radiolabelling	41
3.3.2.2 Fluorine-18 radiolabelling	52
3.3.2.3 Iodine-123 and Iodine-125 radiolabelling	54
3.4 Fluorine-18 Radiochemistry	57
3.4.1 Fluorine-18 radiolabelling via nucleophilic substitution	58
3.4.2 Fluorine-18 radiolabelling via electrophilic substitution	59
3.4.3 Novel approaches to fluorine-18 radiolabelling	60
4. Conclusions and aim of this project	66
5. 5,5-diphenyl hydantoins	67
5.1 Introduction	67
5.2 Rationale	70

5.3 Synthesis	73
5.4 Biological evaluation	78
6. 1,5-diphenyl imidazoles	82
6.1 Introduction	82
6.2 Rationale	85
6.3 Synthesis	88
6.4 Biological evaluation	93
7. Radiochemistry of 1,5-diphenyl imidazoles	104
7.1 Introduction	104
7.2 Synthesis of the precursors and radiolabelling	105
7.3 Further work	113
7.4 Conclusions	114
8. Experimental	116
8.1 General notes	116
8.2 Chemistry	118
8.2.1 5,5-diphenyl hydantoins	118
8.2.2 Celecoxib	128
8.2.3 1,5-diphenyl imidazoles	129
8.3 Biology	149
8.3.1 Purified enzyme assays	149
8.3.2 Whole cell assays	149
8.4 Radiochemistry	150
8.4.1 [¹⁸ F]fluoride production	150

8.4.2 Radiolabelling	150
9. Appendix	151
9.1 ¹ H NMR spectra of novel compounds	151
9.2 Some HPLC data of the final compounds	160
9.3 Colourimetric assay data	163
9.4 ELISA data	166
9.4.1 Cayman Chemical ELISA assay	167
9.4.2 GE Healthcare ELISA assay	167
9.4.3 R&D Systems ELISA assay	169
10. Bibliography	171

Abstract

The COX-2 isozyme is overexpressed in several kinds of cancer, including colorectal, lung, breast, and oesophageal cancer. High levels of COX-2 are usually associated with poor prognosis and advanced disease. Furthermore, studies have suggested that co-administering COX-2 inhibitors along with classic chemotherapy can improve disease outcome. Therefore, COX-2 is an attractive PET imaging biomarker for patient stratification.

A first library of potential COX-2 inhibitors with a 5,5-diphenyl hydantoin core was synthesised and screened for its affinity for COX isozymes. This structure was chosen for its novelty, its potential to improve the biodistribution of the tracer, due its lipophilicity, and its possible *in vivo* metabolic stability.

However, these compounds showed no affinity for COX-2, therefore its further development into PET probes was no longer pursued.

A second library with a 1,5-diphenyl imidazole structure was designed and synthesised, based on previous literature data with optimistic IC₅₀ values for COX inhibition. A candidate for fluorine-18 radiolabelling was identified, therefore nitro and trimethyl ammonium triflate precursors were synthesised. A variety of conditions were tested for the fluorine-18 radiolabelling reactions, which identified the trimethyl ammonium precursor as a better choice. Further experiments, however, are needed in order to fully optimise the conditions of the reaction and to calculate the specific activity.

In conclusion, two libraries of potential COX-2 inhibitors were designed, synthesised and tested in order to develop a PET imaging probe. A possible compound was identified, precursors were synthesised and radiolabelled with fluorine-18 in a variety of conditions, though further tests are necessary.

List of Abbreviations

ACF	Aberrant Crypt Foci
ACN	Acetonitrile
COX	Cyclooxygenase
CT	Computed Tomography
DCM	Dichloromethane
DisIDA	N-(2,6-diisopropylacetanilide)iminodiacetic acid
DME	Dimethylether
DMF	<i>N,N</i> -dimethylformamide
dmpe	1,2-Bis(dimethylphosphino)ethane
DMSO	Dimethylsulfoxide
ER	Endoplasmic Reticulum
EtOAc	Ethyl Acetate
EtOH	Ethanol
FAP	Familial Adenomatous Polyposis
FI	Fluorescence imaging
FLAP	5-Lipoxygenase Activating Protein
FLT	Fluorothymidine
GSH	Glutathione
HER	Human Epidermal growth factor Receptor
HETE	Hydroxyeicosatetraenoic acid
HPETE	Hydroperoxyeicosatetraenoic acid

HPLC	High Performance Liquid Chromatography
ICMT-11	Isatin-5-sulfonamide
IFN- γ	Interferon- γ
LOX	Lipoxygenase
LPS	Lipopolysaccharide
LT	Leukotriene
MAP	Mitogen Activated Protein
MDR	Multidrug Resistance
MRI	Magnetic Resonance Imaging
MRP-4	Multidrug Resistance Protein
NCS	N-chlorosuccinimide
NMF	<i>N</i> -Methylformamide
NSAIDs	Non Steroidal Anti-Inflammatory Drugs
(N)SCLC	(Non) Small Cell Lung Cancer
pAkt	Phosphorylated protein kinase B
PERCIST	PET Response Criteria In Solid Tumours
PET	Positron Emission Tomography
PG	Prostaglandin
PPAR	Peroxisome Proliferator Activated Receptor
RECIST	Response Evaluation Criteria In Solid Tumours
SPECT	Single Photon Emission Computed Tomography
THF	Tetrahydrofuran

TMPD	<i>N,N,N',N'</i> -tetramethyl- <i>p</i> -phenylenediamine
TPA	Terephthalic Acid
TX	Thromboxane
US	Ultrasound
VEGF	Vascular Endothelial Growth Factor

List of Figures

Figure 1: structure of selective COX-2 substrates

Figure 2: 5-LOX pathway leading to the biosynthesis of LTs

Figure 3: PGs biosynthesis from arachidonic acid *via* COX catalysis

Figure 4: binding of a COX-2 inhibitor to COX-2

Figure 5: chemical structure of COX-2 selective inhibitor DuP697

Figure 6: schematic drawing of the interactions between celecoxib and carbonic anhydrase II (A) and between SC-558 and COX-2 (B)

Figure 7: the annihilation process

Figure 8: compartmental model scheme of PET tracer uptake

Figure 9: [¹¹C]radiolabelled COX-2 inhibitors

Figure 10: [¹⁸F]radiolabelled COX-2 inhibitors

Figure 11: radioiodinated COX-2 inhibitors

Figure 12: structures of diarylheterocycles with COX-2 inhibitory activity

Figure 13: docking studies of the unsubstituted hydantoin within COX-2

Figure 14: SAR studies planned for the 5,5-diphenyl hydantoin core

Figure 15: applications of Oxone® to organic synthesis

Figure 16: docking of cimicoxib to COX-2

Figure 17: comparison of intensity between the aldehyde proton peak and the imine peak of compound **[30]**

Figure 18: structure and ¹H NMR spectrum of the oxazole impurity in the synthesis of **[45]**

Figure 19: general structures of the 4,5-diaryl imidazoles (A) and 1,2-diaryl imidazoles (B) in literature

Figure 20: schematic representation of the ELISA

Figure 21: binding saturation curve of COX-2 inhibition by celecoxib as assessed *via* Cayman Chemical ELISA assay

Figure 22: literature data of binding saturation curve of COX-2 inhibition by celecoxib

Figure 23: binding saturation curve of COX-2 inhibition by celecoxib as assessed *via* GE Healthcare ELISA assay

Figure 24: example of radioTLC of fluorine-18 radiolabelling of **[52]**

Figure 25: radioTLC of fluorine-18

Figure 26: ¹H NMR spectra of product and byproduct from the synthesis of **[55]**

Figure 27: radioTLC of radiolabelling of **[55]** after 5 minutes

Figure 28: radioTLC of radiolabelling of **[55]** after 10 minutes

Figure 29: ¹H NMR spectrum of **[2]**

Figure 30: ¹H NMR spectrum of **[3]**

Figure 31: ¹H NMR spectrum of **[4]**

Figure 32: ¹H NMR spectrum of **[6]**

Figure 33: ¹H NMR spectrum of **[7]**

Figure 34: ¹H NMR spectrum of **[8]**

Figure 35: ¹H NMR spectrum of **[9]**

Figure 36: ¹H NMR spectrum of **[10]**

Figure 37: ¹H NMR spectrum of **[11]**

Figure 38: ¹H NMR spectrum of **[12]**

Figure 39: ¹H NMR spectrum of **[22]**

Figure 40: ¹H NMR spectrum of **[23]**

Figure 41: ¹H NMR spectrum of **[24]**

Figure 42: ¹H NMR spectrum of **[25]**

Figure 43: ¹H NMR spectrum of **[26]**

Figure 44: ¹H NMR spectrum of **[27]**

Figure 45: ¹H NMR spectrum of **[28]**

Figure 46: HPLC chromatogram of celecoxib

Figure 47: HPLC chromatogram of **[5]**

Figure 48: HPLC chromatogram of **[11]**

Figure 49: HPLC chromatogram of **[19]**

Figure 50: HPLC chromatogram of **[27]**

Figure 51: IC₅₀ curve of celecoxib

Figure 52: IC₅₀ curve of **[19]**

Figure 53: IC₅₀ curve of **[20]**

Figure 54: IC₅₀ curve of **[21]**

Figure 55: IC₅₀ curve of **[22]**

Figure 56: IC₅₀ curve of **[24]**

Figure 57: IC₅₀ curve of **[25]**

Figure 58: IC₅₀ curve of **[26]**

Figure 59: IC₅₀ curve of **[27]**

Figure 60: IC₅₀ curve of **[28]**

Figure 61: binding saturation curve of COX-2 inhibition by **[19]**, as assessed via Cayman Chemical ELISA assay

Figure 62: binding saturation curve of COX-2 inhibition by **[19]**, as assessed via GE Healthcare ELISA assay

Figure 63: binding saturation curve of COX-2 inhibition by **[20]**, as assessed via GE Healthcare ELISA assay

Figure 64: binding saturation curve of COX-2 inhibition by **[21]**, as assessed via GE Healthcare ELISA assay

List of Schemes

Scheme 1: radiofluorination of aryl iodium salts

Scheme 2: radiofluorination of spirocyclic iodonium ylides

Scheme 3: Pd- catalysed radiofluorination of electron-rich arenes

Scheme 4: Ni- catalysed radiofluorination of electron-rich arenes

Scheme 5: Cu-catalysed radiofluorination of diaryliodonium salts

Scheme 6: Pd-catalysed radiofluorination of cinnamyl carbonates and halides

Scheme 7: enantioselective radiofluorination of racemic epoxides

Scheme 8: strain-promoted Cu-free alkyne-azide cycloaddition using [¹⁸F]FB-DBCO

Scheme 9: example of tetrazine-trans-cyclooctene ligation proposed by Li and colleagues

Scheme 10: synthesis of 5,5-diphenyl hydantoins

Scheme 11: mechanism of step a, a Friedel-Crafts acylation

Scheme 12: mechanism of step b, a Riley oxidation

Scheme 13: mechanism of step c, the synthesis of the hydantoin core

Scheme 14: mechanism of reaction for step d, the oxidation of sulfide to sulfone

Scheme 15: synthesis of mesylates

Scheme 16: oxidation of TMPD

Scheme 17: keto-enol tautomerism of the unsubstituted hydantoin

Scheme 18: proposed mechanism of radiodefluorination *in vivo*

Scheme 19: synthesis of 1,5-diaryl imidazoles

Scheme 20: mechanism of the oxidation of sulfide to sulfone

Scheme 21: mechanism of aldimine synthesis

Scheme 22: mechanism of Van Leusen imidazole synthesis

Scheme 23: mechanism of radical chlorination by NCS

Scheme 24: the acetylcholinesterase reaction on Ellman's reagent

Scheme 25: fluorine-18 radiolabelling of flumazenil

Scheme 26: synthesis of **[52]**

Scheme 27: radiolabelling of **[52]**

Scheme 28: synthesis of **[55]**

Scheme 29: radiolabelling of **[55]**

List of Tables

Table 1: prostanoid receptors, their biodistribution and their biological effect

Table 2: comparison of selectivity profile between a methylsulfone and its methylthioether analogue

Table 3: IC₅₀ values of JTE-522

Table 4: IC₅₀ of some coxibs for different isoforms of carbonic anhydrases

Table 5: comparison of imaging modalities

Table 6: COX-2 IC₅₀ values of the radiolabelled compounds

Table 7: IC₅₀ values of several COX-2 inhibitors

Table 8: IC₅₀ values of Zarghi's library of hydantoins

Table 9: library of hydantoins synthesised and cLogP values

Table 10: IC₅₀ data (μM) of the hydantoins library

Table 11: IC₅₀ values of Almansa's library of imidazoles

Table 12: structure and IC₅₀ values of cimicoxib

Table 13: library of imidazoles synthesised and their cLogP values

Table 14: IC₅₀ values of the imidazoles library

Table 15: comparison of absorbance at 450 nm in two R&D Systems ELISA assays performed

Table 16: R&D Systems ELISA assays performed with three standards

Table 17: list of conditions tested for the radiolabelling of **[52]**

Table 18: comparison of absorbance at 450 nm in all the R&D Systems ELISA assays performed

Acknowledgments

I would like to thank my supervisors, Dr Smith, Dr Cawthorne and Professor Greenman for guiding me throughout my PhD.

My sincere gratitude goes to Dr Allam for funding my research project.

I would also like to thank my friends and colleagues inside and outside the chemistry department, especially Alberto, Julia, Dario, Ippolita and Kayleigh, for their continued support.

A huge thank you to my parents as well, who don't speak English, so *grazie per il vostro supporto morale e ogni tanto anche economico*. And thanks to my eldest sister, Dr Consiglia Pacelli, for bearing with my numerous requests of sending me papers I did not have access to.

And finally, my biggest thank you goes to my partner, Enrico, for never doubting we could make this really long distance relationship work for three years. You are the biggest reason why I never gave up on this PhD.

1. CYCLOOXYGENASE

Cyclooxygenase (COX) is the membrane-bound enzyme that catalyses the conversion of arachidonic acid to PGH_2 in the biosynthesis of prostaglandins (PGs). COX has three isoforms:

- COX-1, referred to as a “constitutive isoform”, and is considered to be expressed in most tissues under basal conditions; [1]
- COX-2, mostly known as an inducible isoform and involved in inflammatory and carcinogenic processes;
- COX-3, mainly present in the brain, and sensitive to inhibition by paracetamol. [2]

Further studies have actually shown that constitutive COX-2 expression is well recognised in brain, kidney, and the female reproductive tract, and evidence for induction of COX-1 during the lipopolysaccharide (LPS)-mediated inflammatory response and cellular differentiation has been reported. [3]

These findings show that the role of COX-2 in the human body is not only pathological and confined to the inflammatory process, but it also has a homeostatic role; genetic deletion of COX-2 produces a severe disruption of postnatal kidney development, and female knockout mice are infertile due to failure of ovulation and embryo implantation. [4]

Both COX-1 and COX-2 have a molecular weight of 71 kDa and both have just over 600 amino acids; furthermore, their sequence homology reaches the 63%. However, the human COX-2 gene is a small immediate early gene (8.3 kb), while human COX-1 originates from a much larger gene (22 kb). The mRNA they produce are also different: the mRNA for COX-2 is approximately 4.5 kb, while that of COX-1 is 2.8 kb. [5]

Both isoforms contain three high mannose oligosaccharides, one of which facilitates protein folding. A fourth oligosaccharide, present only in COX-2, regulates its degradation. [6]

They are both homodimers, and each subunit contains three domains:

- the epidermal growth factor domain
- the membrane binding domain

- the catalytic domain, which contains the cyclooxygenase and peroxidase active sites on either side of the heme prosthetic group. [7]

The X-ray crystal structure of human or murine COX-2 can be superimposed on that of COX-1; the amino acids of the substrate binding channel and the catalytic sites are the same except for two small variations. In these two positions, the same substitutions occur; Ile in COX-1 is exchanged for Val in COX-2 at positions 434 and 523. The smaller size of Val523 creates a side pocket off the main substrate binding channel in COX-2. [8] [9]

Another structural difference between the isoforms, whose effect is still unknown, is the absence of the COX-1 N-terminal sequence of 17 amino acids and the presence of a sequence of a C-terminal 18 amino acid sequence in COX-2, which is absent in COX-1. The C-terminal sequence in COX-2 does not alter the last four amino acid residues, which in both enzymes form the signal for attachment to the membrane of the endoplasmic reticulum (ER). However, while COX-1 is attached only to the membranes of ER, COX-2 is located also on the nuclear membrane. The different sequence of the C-terminus might be the reason for the selective localization. [6] [10]

COX-2 accepts a wider range of fatty acids as substrates than COX-1. Both enzymes can oxygenate arachidonic acid, but COX-2 oxygenates other fatty acid substrates, such as eicosapentaenoic acid, α -linolenic acid, γ -linolenic acid and linoleic acid more efficiently than COX-1 does (Figure 1). [11]

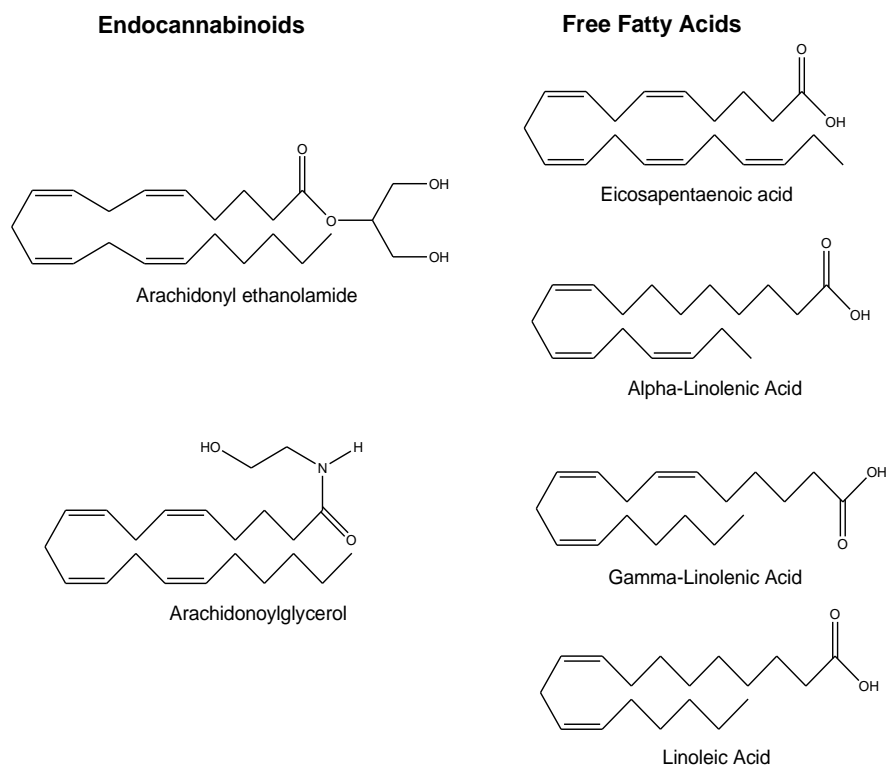


Figure 1: structure of selective COX-2 substrates. Unlike arachidonic acid, which is oxygenated by both COX-1 and 2, these molecules are oxygenated by COX-2 only.

1.1 EICOSANOIDS

The metabolism of arachidonic acid by COX and 5-lipoxygenase (5-LOX) generates eicosanoids, signalling molecules which include prostanoids (PGs and thromboxanes, TXs) and leukotrienes (LTs).

Eicosanoids act as autacoids, taking parts in several biological functions (smooth muscle tone, haemostasis, gastric acid secretion) and pathological processes (inflammation, carcinogenesis).

1.1.1 Biosynthesis of eicosanoids

Arachidonic acid is the precursor for eicosanoids synthesis. In response to several stimuli, arachidonic acid is released from cell membranes by phospholipase PLA₂ and in this free form it acts as a substrate for COX, 5-LOX and cytochrome P450. [7]

In the 5-LOX pathway, this enzyme translocates to the nuclear membrane, where it associates with 5-Lipoxygenase Activating Protein (FLAP) to convert arachidonic acid in 5-Hydroperoxyeicosatetraenoic acid (5-HPETE), which spontaneously reduces to 5-Hydroxyeicosatetraenoic acid (HETE). 5-LOX converts 5-HETE to LTA₄, an unstable

epoxide. This may be converted to LTB_4 in cells equipped with LTA_4 hydrolase or it might be conjugated to glutathione (GSH) to form cysteinyl LTs (LTC_4 , LTD_4 , LTE_4) in cells equipped with LTC_4 synthase (Figure 2). [12]

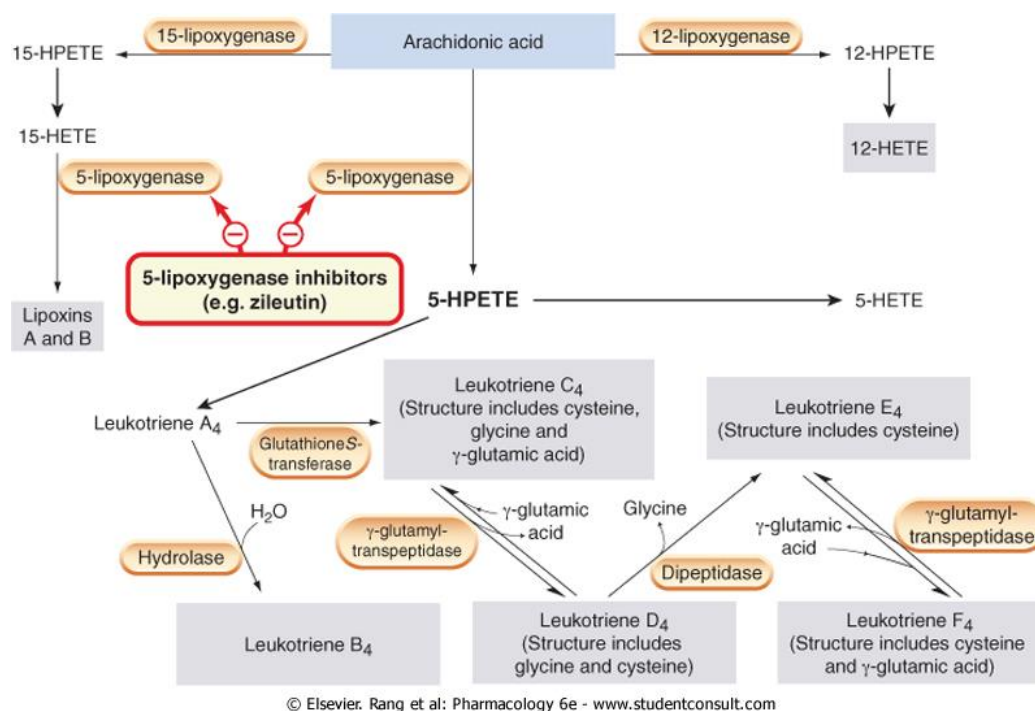


Figure 2: 5-LOX pathway leading to the biosynthesis of LTs. 12-, 15-, and 5-LOX produce the respective HETEs through HPETE. 15-HETE generates lipoxines A and B, while $LT A_4$, precursor of several other LTs, is produced from 5-HPETE. Biologically active molecules are shown in grey boxes. [12]

In the COX pathway, COX catalyses the first step in the biosynthesis of PGs, thromboxanes and other eicosanoids, consisting of two sequential reactions. The initial reaction converts arachidonic acid to PGG_2 , which is then reduced to PGH_2 . The latter is then converted to several biologically active PGs, such as PGE_2 , $PGF_{2\alpha}$, PGI_2 by cell specific isomerases and synthases (Figure 3). These products act as secondary messengers of the signal transduction by interacting with prostanoid G-protein coupled receptors mostly. [7]

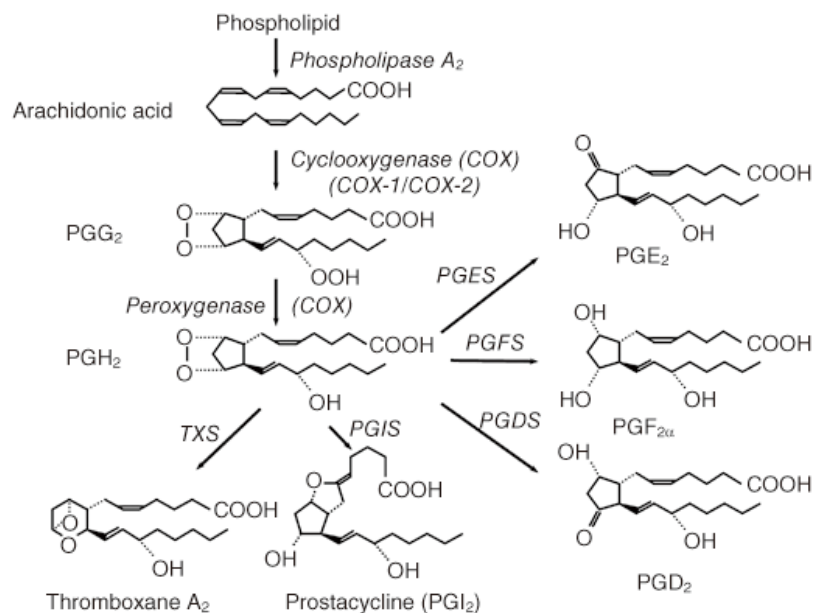


Figure 3: PGs biosynthesis from arachidonic acid via COX catalysis. When arachidonic acid is released from the membrane by PLA₂, COX metabolises it into the PGG₂ intermediate and then into PGH₂, which is further transformed into several PGs by cell specific isomerases and synthases. [13]

1.1.2 Eicosanoids and inflammation

LTs are produced in white cells, as their name suggests. The effects of LTs and cysteinyl LTs are mediated respectively by BLT receptors and CysLT receptors. These receptors are all coupled with G_q proteins.

LTB₄ is a potent chemotactic agent for neutrophils and macrophages. On neutrophils, it up-regulates membrane adhesion molecule expression, and increases the production of toxic oxygen products and the release of granule enzymes. On macrophages and lymphocytes, it stimulates proliferation and cytokine release.

Cysteinyl-LTs cause contraction of the bronchiolar smooth muscle and increased mucus secretion; the CysLT antagonists zafirlukast and montelukast are used in the treatment of asthma. [12]

The table below lists the subtypes of prostanoid receptors, their location and the biological effects activated when PGs and TXs bind to them.

Table 1: prostanoid receptors, their biodistribution and their biological effect [12]

PG/TX	Receptor	Tissue	Biological effect
PGE ₂	EP ₁ (G _q)	Monocytes	Regulation of the tone of smooth muscle
	EP ₂ (G _s)	Kidneys	Reduction of acid secretion
	EP ₃ (G _q /G _i /G _s)	Stomach	Lowering of pain threshold
	EP ₄ (G _s)	Uterus	Increased diuresis and natriuresis
		Hypothalamus	Hypertermia
PGF _{2α}	FP (G _q)	Uterus	Increased tone of smooth muscle
		Blood vessels	Luteolysis
		Bronchus	
PGI ₂	IP (G _s)	Blood vessels	Inhibition of platelet aggregation
		Stomach	Vasodilation
		Renal cortex	Gastric mucus secretion
			Increased renal blood flow
PGD ₂	DP (G _s)	Blood vessels	Bronchoconstriction
		Platelets	Vasodilation
		Brain	Inhibition of platelet aggregation
		Bronchus	Regulation of sleep cycle
TXA ₂	TP (G _q)	Platelet	Platelet aggregation
		Blood vessels	Vasoconstriction
		Lungs	Bronchoconstriction
		Renal cortex	Reduced renal blood flow

During the acute inflammatory response prostanoids are released, especially PGE₂ and PGI₂, generated by the local tissue and the blood vessels, and PGD₂, released by mast cells. During the chronic inflammation, monocytes and macrophages also release TXA₂ and PGE₂.

PGE₂, PGI₂ and PGD₂ are powerful vasodilators and synergise with other inflammatory vasodilators such as histamine and bradykinin. This combined dilator action on precapillary arterioles contributes to the redness and increased blood flow in areas of acute inflammation. Prostanoids do not directly increase the permeability of the postcapillary venules, but potentiate this effect of histamine and bradykinin. Similarly, they do not induce pain, but increase the effect of bradykinin by sensitising afferent C fibres to the effects of other noxious stimuli. PGs of the E series are also pyrogenic.

However, under some circumstances some prostaglandins have anti-inflammatory effects. An example is PGE₂, which causes a reduction of lysosomal enzyme release and of the generation of toxic oxygen metabolites from neutrophils. It also induces the release of histamine from mast cells. [12]

1.1.3 Eicosanoids and cancer

Animal and epidemiological studies prove that a high fat diet can increase the risk of cancer, especially colorectal breast, pancreatic and prostate. The biologically active lipids derived from arachidonic acid, which is one of the major ingredients of animal fats, play key roles in chronic inflammation and carcinogenesis. The activation of COX and LOX during chronic inflammation results in aberrant metabolism of arachidonic acid, which might be one of the mechanisms contributing to the carcinogenic effect of dietary fats. [14]

Emerging evidence suggests that LOX is also involved in carcinogenesis. 5-LOX is generally absent in normal epithelia, but is induced by pro-inflammatory stimuli and is constitutively expressed in several epithelial cancers including colon, oesophagus, lung, prostate and breast. [14]

The correlation between high levels of PGE₂ and cancer is well established and is discussed later on (“Involvement of COX-2 in cancers”)

On the other hand, the role of PGD₂ is still debated. An anti-tumour role has been suggested based on the observation that overexpression of PGD₂ synthase in *Apc^{Min/+}*

mice reduces intestinal tumour growth; however, genetic disruption of DP receptor has no effect on colon tumour formation on the azoxymethane mouse model. [15] [16]

A possible explanation for this discrepancy is that the PGD₂ derived product 15dPGJ₂ inhibits tumour growth by activation of PPAR γ ; another possibility is that the overexpression of PGD₂ synthase might reduce the conversion of PGH₂ to PGE₂. [14]

As for the role of LTs in cancer, LTB₄ levels are increased in human colon and prostate cancer and the expression of LTB₄ receptors is increased in human pancreatic cancer. [17] [18]

The CysLT1 receptor is highly expressed in human colon and prostate cancers and it negatively correlates with patient survival, while reduced expression of CysLT2 receptor is associated with poor prognosis in patients with colorectal cancer. [19] [20]

1.2 INVOLVEMENT OF COX-2 IN CANCERS

The strongest evidence for COX-2 involvement in cancers arises from the beneficial outcome of NSAIDs administration to cancer patients, such as repression of intestinal polyps. [21] [22] [23]

The mechanism by which COX-2 is upregulated in human cancers is largely unknown. One hypothesis suggests that cancer cells become intrinsically more active in expressing COX-2 because COX-2 gene expression is induced by activation of oncogenes, which in turn activate signal transducers such as MAP kinases and pAkt that can stimulate COX-2 transcription and increase the stability of the transcript. [24] [25]

COX-2 is expressed in several types of adenocarcinomas. In every organ, the frequency of COX-2 expression depends on the histological subtypes; for example, in breast tissue a ductal cancer is more likely to overexpress COX-2 than a lobular breast cancer. [26, 27]

As discussed in further details later on, studies have shown that COX-2 expression is correlated with the depth of invasion and advanced tumour stage, as positive expression of COX-2 is more common among advanced stage tumours than in early stage tumours. [28] [29]

1.2.1 Colorectal cancer

Colorectal cancer is the second most common cause of cancer death among over 40 year old men. [30]

Several studies show that non-steroidal anti-inflammatory drugs (NSAIDs) reduce the risk of developing colon cancer. Early studies carried by Kudo and co-workers using animal models of colon cancer indicated that NSAIDs were chemopreventive. [21]

Furthermore, Waddell and Loughry observed that sulindac decreased intestinal polyp burden in patients with familial adenomatous polyposis (FAP). [31] Further studies carried by different research group confirmed the repression of polyps by NSAIDs, which lead to the FDA approval of celecoxib for the treatment of FAP. [22] [23]

If NSAIDs reduce the risk of developing colon cancer, then high levels of PGs might be present in tumour sites. Indeed, it has been reported that PGE₂ and 6-keto PGF_{1α} levels were elevated in colorectal cancers. [32] These higher PG levels may be explained by either an increased COX expression or an increased COX catalytic activity: 85% of adenocarcinomas had increased expression of COX-2, which suggests that COX-2 could be involved in colorectal carcinogenesis. [33]

Further evidence implicating COX-2 in colorectal carcinogenesis can be found in studies of animal models of colorectal cancer. The azoxymethane treated rat is one of the most common animal model used. The progression of the lesions advances from ACF, to polyp, and finally to carcinoma. This animal model shows increased level of COX-2 and sulindac seems to reduce aberrant crypt foci (ACF) formation, polyp number and carcinogenesis. [34] [35]

Oshima and co-workers used a genetic model to test the role of COX-2 in tumourigenesis. They provided genetic evidence that COX-2 is important for polyp promotion by breeding ApcD716 mutant mice, which are heterozygous for an adenomatous polyposis coli mutant allele and develop hundreds of intestinal polyps, with *cox-2* null mice; their offspring showed a decreased tumour burden in a gene dose-dependent way. [36]

However, Grösch *et al.* monitored the inhibition of the growth of colon cancer xenografts in nude mice caused by celecoxib and showed that it was significant in HCT-15 colon cancer xenografts, which are COX-2 deficient, while celecoxib had no relevant effect on HT-29 tumours that express COX-2. This study supports the hypothesis that the anti-tumoural effects of celecoxib is not a consequence of COX-2 inhibition only. This hypothesis is further supported by comparison of the concentration of celecoxib required to inhibit COX-2 and tumour cell proliferations; the latter is four times higher. [37]

Studies suggest that these COX-2 independent anti-tumoural effects are not a prerogative of celecoxib, but are common among coxibs. This suggests a chemotherapeutic role for this class of compounds. [38]

Since COX-2 overexpression promotes formation of polyps, which progress to carcinoma, imaging of COX-2 would be a useful tool for detection of predisposition to malignancy, at a stage where it can be treated more efficiently. [39]

1.2.2 Oesophageal cancer

There are two main types of oesophageal cancer, squamous cell carcinoma and adenocarcinoma.

Oesophageal adenocarcinoma usually develops from Barrett's oesophagus, a metaplastic change of the normal squamous epithelium of the oesophagus to a columnar epithelium caused by gastro-oesophageal reflux. [40]

Five studies compared the expression of COX-2 in normal squamous cells and in metaplastic epithelium, finding COX-2 to be overexpressed in Barrett's metaplasia-dysplasia-adenocarcinoma sequence; while the normal squamous epithelium was negative or weakly positive for COX-2, 78 to 100% of the adenocarcinomas showed COX-2 expression. [41] [42] [43] [44] [45]

It has been reported a chemopreventive effect of aspirine in both adenocarcinoma and squamous cell carcinoma. These findings are further supported by nine studies containing 1813 cancer cases who were independently reviewed; these studies show a protective effect of NSAIDs in both hystologic types of oesophageal cancer. [46]

Elevated COX-2 levels seem to be associated with reduced survival in Barrett's carcinoma patients who underwent oesophageal resection, as they were more likely to develop regional recurrences and distant metastases. [45] This evidence supports the use of COX-2 as a prognostic biomarker.

1.2.3 Gastric cancer

Several factors play a role in gastric carcinogenesis, including diet, *H. pylori* infection, and genetic factors.

Lauren classification of gastric carcinoma recognises two different types, intestinal type and diffuse type. Intestinal type adenocarcinoma tumour cells show irregular tubular

structures, harboring pluristratification, multiple lumens, and reduced stroma. This variant also has certain precursor lesions that lead to invasive carcinoma. Diffuse type adenocarcinoma tumour cells are poorly differentiated, discohesive and secrete mucus which is delivered in the interstitium. [47]

The association between NSAIDs use and gastric cancer was analysed in four studies, three of which showed a protective effect of NSAIDs against gastric cancer. In these studies, COX-2 expression in normal tissue was low or below the detection limit, while the neoplastic mucosa showed elevated COX-2 levels, suggesting that COX-2 may play a role in gastric carcinogenesis. [48] [49] [50] [51]

The correlation between gastric cancer and overexpression of COX-2 seems to be related to the intestinal type. [26] [52]

However, unlike the latter, expression of COX-2 was not found to correlate with prognosis in gastric cancer patients, suggesting that the prognostic value of COX-2 is limited to a subgroup of gastric cancer patients. [53] [54] Nonetheless, it is crucial to consider that non-imaging measurements of COX-2 might not be entirely accurate, due to tumour heterogeneity and variability of immunohistochemistry.

Elevated levels of COX-2 are associated with invasive disease and metastasis, similarly to oesophageal adenocarcinoma. [55] [53] [56] Therefore, COX-2 has a potential use as a prognostic biomarker for gastric cancer patients.

1.2.4 Breast cancer

A recent meta-analysis suggested that the incidence of breast cancer might be reduced among NSAIDs users. Furthermore, in a transgenic mouse model expression of COX-2 was enough for formation of invasive breast tumours. [57] [58]

Elevated COX-2 levels have been reported to be more frequent in ductal type than in lobular type carcinomas. A recent study also suggested that COX-2 expression is elevated in breast cancer samples that also overexpress HER-2. [27] [59]

As prostanoids synthesised by COX-2 seem to enhance stromal cell aromatase expression, it is possible that COX-2 overexpression in oestrogen receptor positive cancers might induce oestrogen production via the aromatase pathway, promoting tumour cells growth. [60] [61]

Studies have suggested also a correlation between COX-2 activation and invasiveness of chemotherapy-resistant breast cancer cells. [62]

COX-2 overexpression seems to be associated with an unfavourable outcome, leading from ductal carcinoma *in situ* to invasive breast cancer. These studies support the prognostic value of COX-2 expression; this prognostic role seems to be more relevant in cancers with oestrogens receptor positivity, low level of p53 expression and no amplification of the HER-2 oncogene. [27]

1.2.5 Brain cancer

Malignant gliomas are the most common tumours of the central nervous system, especially astrocytic gliomas, which account for more than 25% of all central neoplasms. [63]

The role of COX-2 in human glioma formation and progression has not been completely elucidated, as different studies show opposite results; Deininger and co-workers initially reported that COX-2 expression occurred in only 20% of glioma cells, while Joki *et al.* demonstrated that high-grade glioma tissues expresses elevated levels of COX-2 and that NS-398, a selective COX-2 inhibitor, increases apoptosis, reduces proliferation and invasion of cultured human glioma cells. [64] [65] This discrepancy between studies may be due to the variability of COX-2 measurements with a more traditional technique than imaging.

Further research conducted by Shono *et al.* showed that COX-2 was localised predominantly in necrosis areas, which suggests induction of COX-2 by hypoxia or hypoglycosemia. Furthermore, increasing tumour grade seems to correlate with a high percentage of COX-2 expressing tumour cells and with poor prognosis in patients with astrocytic brain tumours. [66] These findings suggest a prognostic role for COX-2 as a biomarker for brain cancer.

1.2.6 Lung cancer

Most primary lung cancers are carcinomas, which are divided into small cell lung carcinoma and non-small cell lung carcinoma. The first type is usually more aggressive, but it responds initially well to treatment with chemotherapy and/or radiotherapy.

Small cell lung carcinomas (SCLCs) have been reported to express only low or undetectable levels of COX-2. [67]

As reviewed by Mascaux and co-workers, the analysis of the literature data about the impact of COX-2 overexpression on survival of non-small cell lung cancer (NSCLC) did not reach statistical significance; however, when the analysis was restricted to stage I

NSCLC, a statistically relevant detrimental effect of COX-2 on survival was observed, suggesting that COX-2 could be a prognostic marker for early stage NSCLC, being also a sign of more aggressive disease and of worse prognosis. Therefore, high levels of COX-2 would be useful to determine among stage I patients those who would benefit from a more aggressive treatment. [68]

Furthermore, in clinical studies on NSCLC patients who were given carboplatin with or without celecoxib, patients with COX-2 overexpression who did not receive celecoxib showed an inferior outcome, suggesting also a predictive role for COX-2 as a biomarker. [69]

In a phase II clinical study the efficacy and toxicity of coxibs in combination with chemoradiotherapy for patients with inoperable stage III lung cancer was examined. An improved response rate or survival was not observed. However, a urinary assay based on PGE-M (the major urinary metabolite of PGE₂) levels was developed to predict response to COX-2 inhibition with celecoxib in association with chemoradiotherapy; celecoxib decreased PGE-M production in patients with NSCLC, which suggests that COX-2 overexpression is responsible for the excess of PGE₂ production, which is known to be involved in tumour growth. Notably, the best response was not from patients with upregulation of COX-2, which is consistent with COX-2 overexpression being correlated with more aggressive disease and worse prognosis. [70]

1.2.7 Chemoresistance

Studies have suggested a correlation between COX-2 overexpression and resistance to chemoradiotherapy, which renders COX-2 a valuable marker for the prediction of chemoradiotherapy efficacy. [71]

Celecoxib has been shown to suppress COX-2 expression in cancer and to induce tumour suppression. [7] [72] Chemotherapy based on coxibs alone is not efficient, however it does enhance the anti-tumoural activity of other chemotherapeutic agents; the reason might lie in the inhibition of IFN- γ and VEGF angiogenesis activity by coxibs. [73] [74] [75]

Furthermore, coxibs also enhance radiotherapy efficacy through cell cycle arrest, inhibition of DNA repair processes and activation of caspases 8 and 3. [76] [77] [78] [79]

However, *in vitro* and clinical trials showed antitubulin agents such as taxanes induce COX-2 expression. [80] [81] This suggests that administration of celecoxib as a chemotherapy drug along with taxanes might not be a favourable approach. This was also suggested by further studies investigating the efficacy of celecoxib in increasing the

effect of carboplatin and taxanes on early stage lung carcinoma; this study describes a reduced survival time in patients treated with a combination of celecoxib and irinotecan-docetaxel compared to those who were administered chemotherapy only. [82] A further explanation of these findings was proposed by Gradilone and co-workers, who found that celecoxib induced MRP-4, an ATP binding cassette transporter involved in the resistance to anticancer drugs such as topotecan and cyclophosphamide, in lung cancer cells. By inducing MRP-4 expression and localisation on the plasma membrane, celecoxib could increase the efflux of irinotecan from tumour cells, reducing its efficacy and worsening the patients' prognosis. [83]

On the other hand, several studies have shown that coxibs might be useful in prevention or reduction of multidrug resistance (MDR) in colon cancer cell lines or patients with cancer, for example ovarian cancer. [84] [85] A recent study carried on MCF-7, MCF7-MX and MDA-MB-231 cells showed that celecoxib reverses the enhancing effect of TPA, a COX-2 inducer, on the activity of the ATP binding cassette ABCG2, which is responsible for MDR in breast cancer. [86] Furthermore, studies suggest that COX-2 inhibition may be beneficial in 35% cases of advanced NSCLC whose cells have moderate to high COX-2 expression. [87]

These studies suggest not only the use of COX-2 as a biomarker for prediction of chemotherapy efficacy, but also as a biomarker for stratification of patients which might benefit from the administration of coxibs.

1.2.8 COX-2 as a biomarker for stratification of cancer patients

Stratification is the identification of a group of patients who share the same biological trait via molecular, biochemical or imaging diagnostic techniques in order to select the optimal management for the patients and achieve the best possible outcome in terms of prevention, risk assessment and treatment. [88]

The correlation of high levels of COX-2 with premalignancy and cancer progression suggests that COX-2 is a useful target for imaging early lesions. As several kinds of cancer show an association between COX-2 levels and chronic inflammation in premalignant conditions, the assessment of COX-2 expression may be useful to determine predisposition to malignancy and for the early detection of cancer. [68]

Since chronic inflammation can predispose tissues to develop malignancy, imaging probes that can highlight regions of inflammation, such as COX-2 inhibitors, may be able to monitor high-risk premalignant lesions and guide preventive measures. [89]

1.3 COX INHIBITORS: NSAIDS

COX-2 is a cytoplasmic enzyme located on both immune and tumour cells; therefore, in order to reach this target, COX-2 probes need to be able to cross both the endothelial barrier and the plasma membrane of the targeted cell. Furthermore, in order to achieve selectivity for COX-2, the probe must enter the active site of COX-2 only, which is embedded beyond a small constriction; therefore, COX-2 probes need to be small enough to be able to cross this port. Established structures for such probes are derivatives of celecoxib and indomethacin, which are NSAIDs. [89]

NSAIDs are chemically heterogeneous compounds capable of inhibiting COX-1 and/or COX-2, showing antipyretic, anti-inflammatory and analgesic properties.

The use of anti-inflammatory analgesic drugs traces back to the early Chinese, Indian, African and American eras and were initially described in some detail by Roman and Greek medical authorities; extracts of *Salix alba* and other salicylate-containing plants were used in the treatment of fever, pain and inflammatory conditions.

The active ingredient was isolated in the early 19th century, followed by the synthesis of salicylic and acetylsalicylic acids, the latter being commercialised by Bayer AG as Aspirin™ over 100 years ago. [90]

The first NSAID developed was phenylbutazone in 1946 and later indomethacin in the 1960's. Phenylbutazone was for almost 30 years used for the treatment of arthritic and other painful inflammatory conditions until it was associated with agranulocytosis and bone marrow suppression, upper gastrointestinal ulcers and bleeding. [91]

Ibuprofen was developed in the 1950–1960's and it was the first NSAID (other than aspirin) to be approved for non-prescription use in the UK.

The target of these drugs was cloned in 1988 and only in 1991 another isoform of COX was found, starting the research that developed selective COX inhibitors.

1.3.1 Structure-activity relationship (SAR) studies

NDSAIDs containing a carboxylic acid group ion pair with the guanidinium group of Arg120, which also ion pairs with the carboxylate of arachidonate. [10] When the arginine residue in COX-1 is substituted with glutamine or glutamate, the protein becomes resistant to inhibition by carboxylic acid-containing NSAIDs. Arg120 interacts with Glu524 and Tyr355 through hydrogen bonds, which stabilize the interactions between

the substrate and the inhibitor. If this hydrogen-bonding network is disrupted, the substrate/inhibitor complex released. Opening and closing of the Arg120–Glu524–Tyr355 network may contribute to the time dependence of all COX inhibitors. [8]

Selective COX-2 inhibition requires:

- two lipophilic substituents (one of which must be a phenyl ring) on adjacent positions within the central unsaturated ring system;
- a methylsulfone/sulfonamide moiety on the necessary phenyl ring.

COX-2-selective inhibitors bind to regions accessible in COX-2 but not COX-1. Figure 4 shows how the sulfonamide or the methylsulfone moiety in selective COX-2 inhibitors interacts with a lipophilic side pocket of COX-2 bordered by Val523 and forms hydrogen bonds with Arg513 and a peptide bond with Phe518.

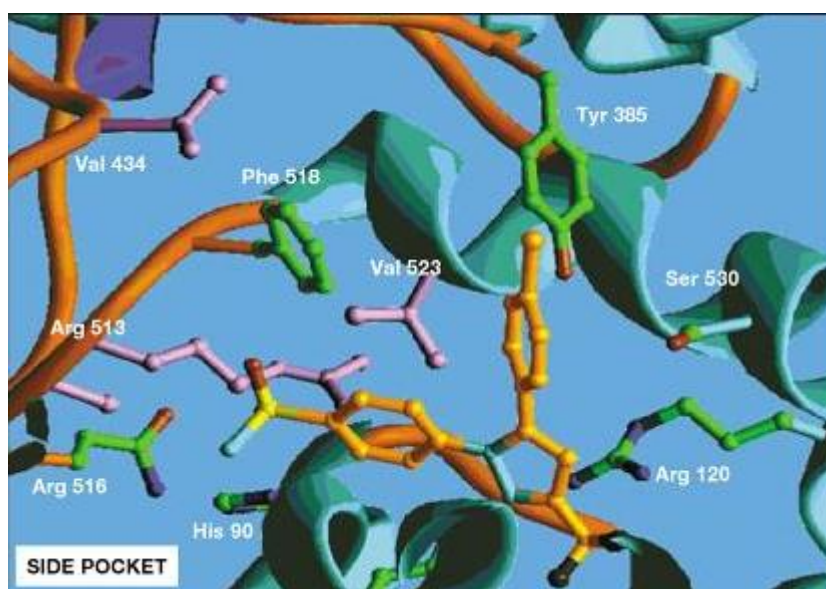


Figure 4: binding of a COX-2 inhibitor (yellow) to COX-2. Arg513, Phe518 and His90 interact with the sulphonamide group of the coxib. When a coxib binds to COX-2, it prevents the access of arachidonic acid to the catalytic substrate at Tyr385. [92]

The 4-methylsulfonyl diarylheterocycle combination was first observed in DuP697 (Figure 5). [93]

SAR studies on potential methylsulfone bioisosters resulted in the discovery of the 4-sulfonamido group which retained the COX-2 inhibitory potency, with a loss of COX-2 selectivity. [94]

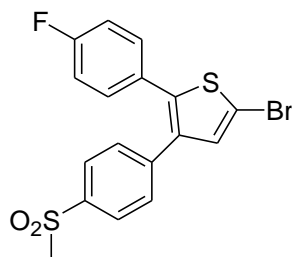
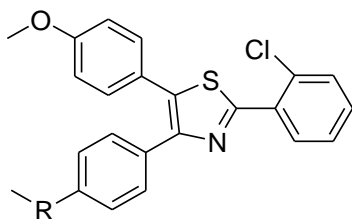


Figure 5: chemical structure of COX-2 selective inhibitor DuP697

The oxidation state of the sulfur atom in the pharmacophore is pivotal for selective COX-2 inhibition, as its reduction to sulfoxide or sulfide reverses isozyme selectivity. As an example, table 2 shows the IC_{50} values of methylsulfone SC-8092 and the methylthioether analogue SC-8076. [95]

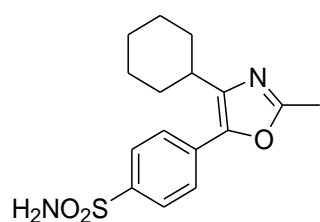
Table 2: comparison of selectivity profile between a methylsulfone and its methylthioether analogue.

Compound	R	IC_{50} (μM)	
		COX-1	COX-2
SC 8092	SO ₂	>100	0.06
SC 8076	S	0.1	>100



The phenyl ring that does not contain the sulfonamide/methylsulfone pharmacophore can be substituted with a cyclohexyl ring, as seen in JTE-522 (Table 3). [96] [97]

Table 3: IC_{50} values of JTE-522

	IC_{50} (μM)	
	COX-1	COX-2
	>100	0.3

It is worth mentioning that coxibs with a sulfonamide moiety have been shown to inhibit carbonic anhydrases, similarly to commercially available carbonic anhydrases inhibitors, which are sulfonamides as well. As shown in figure 6A, the sulfonamide moiety forms ion bonds with the Zn^{2+} in the active site of carbonic anhydrase. [98]

Sulfonamide binding to carbonic anhydrase in erythrocytes slows down the blood clearance of this class of COX-2 inhibitors. [99]

This feature is ideal for a compound with therapeutic purposes, as administration of drugs with a short plasma half-life requires frequent dosing and often results in poor patient compliance; however, it is not favourable for a compound designed for imaging purposes, as it causes high blood pool background in the imaging target tissue.

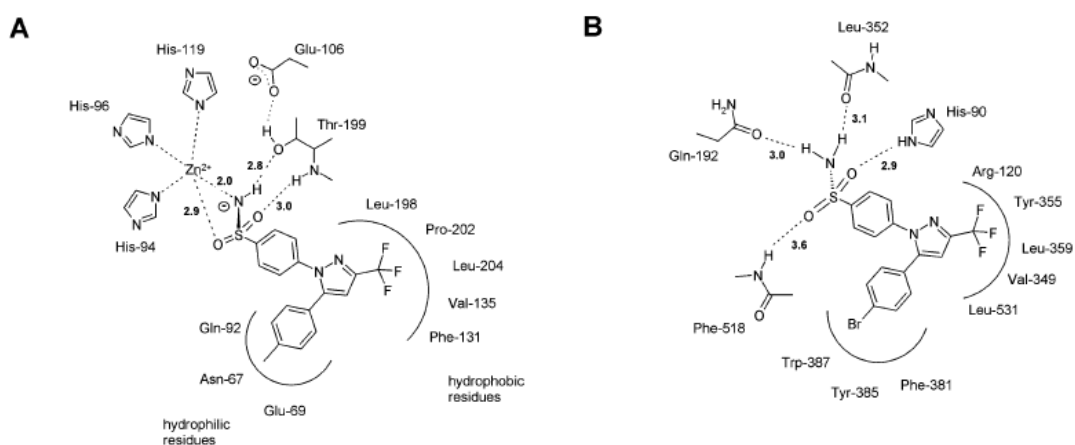


Figure 6: schematic drawing of the interactions between celecoxib and carbonic anhydrase II (A) and between SC-558 and COX-2 (B). Bond lengths are given in Å. The interactions that the sulfonamide establishes with the Zn^{2+} of carbonic anhydrase and the active site of COX-2 are shown. [98]

Table 4 shows the affinity data of some coxibs and some commercially available carbonic anhydrase inhibitors, all bearing a sulfonamide moiety, as measured by Weber and co-workers. Acetazolamide and methazolamide are diuretics, dorzolamide is an

antiglaucoma agent. As shown by the IC_{50} values, the sulfonamide moiety is pivotal for carbonic anhydrase inhibition; rofecoxib, being a methylsulfone, does not inhibit such enzyme. [98]

Table 4: IC_{50} (nM) of some coxibs for for different isoforms of carbonic anhydrases (CA). [98]

Inhibitor	IC_{50} (nM)			
	hCA I	hCA II	bCA IV	hCA IX
acetazolamide	250	12	70	25
methazolamide	50	14	36	27
dorzolamide	50000	9	43	52
celecoxib	50000	21	290	16
rofecoxib	>100 μ M	>100 μ M	>100 μ M	>100 μ M

In conclusion, in order to hit as few biological targets as possible and therefore generate a reliable COX-2 image, a COX-2 inhibitor used as a probe for COX-2 imaging should have:

- a diaryl heterocycle core structure;
- a methyl sulfone moiety instead of a sulfonamide group to assure COX-2 affinity and avoid binding to carbonic anhydrase.

1.3.2 Kinetics of COX inhibition

Traditional NSAIDs show one of three different modes of binding:

- reversible binding, such as ibuprofen,
- rapid, low affinity reversible binding followed by a time-dependent, higher affinity, slowly reversible binding (flurbiprofen),
- rapid, reversible binding followed by a covalent modification of the enzyme (aspirin).

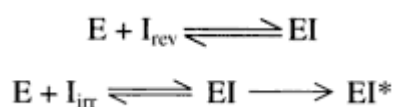
Aspirin is unique in its mechanism, since it causes irreversible inhibition of the enzyme by acetylating a serine residue (530 of COX-1 and 516 of COX-2), thus preventing the access of arachidonic acid in the active site. While acetylation of COX-1 blocks the

metabolism of arachidonic acid completely, inhibition of COX-2 by aspirin still allows the biological substrate to reach the peroxidase site and be metabolised to 15-HPETE. [11]

The most potent COX inhibitors are slow, tight binding inhibitors that form very stable complexes. Many selective COX-2 inhibitors appear to be competitive inhibitors of COX-1, but show time-dependent inhibition of COX-2 which is responsible for their selectivity. [100] [101] [102] [103]

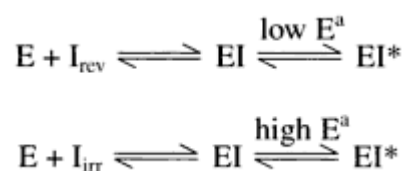
Fluorescence quenching analysis shows that diarylheterocycles bind to both enzymes and the kinetics of fluorescence decay reveals that sequential bimolecular and unimolecular steps occur at comparable rates. A third unimolecular step is only observed with COX-2; the first two steps are reversible, while the third step is pseudo irreversible. Recovery of fluorescence in the presence of excess flurbiprofen takes 3 hours with COX-2 and 40 seconds with COX-1. [104] [105]

It was originally believed that competitive inhibitors formed only a reversible complex (EI) and that time-dependent inhibitors could additionally form tightly bound irreversible complexes (EI*):



Therefore, it was believed that the selectivity of COX-2 inhibitors may be due to the formation of EI* with COX-2 and reversible EI with COX-1. [101] [106]

However, it was later proposed that both reversible time-dependent inhibitors and irreversible time-independent inhibitors bind by the same mechanism and differ by the activation energy (E^a) of the transition from EI to EI*, which will be faster with a low E^a : [107]



More recently, it was proposed that COX-2 inhibitors with a diaryl heterocycle structure could generate a three-step time-dependent irreversible COX-2 inhibition: [100]



The fact that potent COX-2 inhibitors are slow and tight binding compounds which form a stable complex with the enzyme has some repercussion on the imaging of this biomarker; for instance a radiolabelled probe that binds tightly to its biological target might show negligible washout from the tissue during the course of a typical study, which would make it impossible to measure the washout rate and to calculate the levels of said biological target. [108]

1.3.3 COX inhibition assays

The assessment of the inhibition kinetics of COX, as well as the affinity for the isozymes, is a complex matter that has been attempted in several ways, with both *in vitro* and *ex vivo* methods, with a high inter-assay variability degree of the results.

The methods for the determination of COX activity are based on the two enzymatic activities exhibited by the enzyme: cyclooxygenation and peroxidation.

In the biosynthesis of PGs, the insertion of two oxygen atoms in arachidonic acid catalysed by COX consumes O₂ from the reaction environment; therefore, COX activity can be measured by monitoring the initial rate of O₂ consumption using an oxygraph equipped with an oxygen electrode. This assay has the advantage of reflecting directly COX activity, but it is not suitable for the screening of numerous compounds, as it uses relatively high amounts of enzyme (100-200 µg) because of the poor sensitivity of the oxygen sensor. [109] [110]

Most of the currently used methods for the screening of COX inhibitors detect the enzyme peroxidase activity. The peroxidase co-substrate oxidation assay is based on the sequential reactions catalysed by the cyclooxygenase activity (generating PGG₂ from arachidonic acid) and the peroxidase activity (converting PGG₂ to PGH₂). In this assay, a peroxidase co-substrate is oxidised to a stable chromophore in a known stoichiometric relationship with PGG₂ reduction. A common co-substrate is *N,N,N',N'*-tetramethyl-*p*-phenylenediamine (TMPD), which can undergo one-electron oxidation by the peroxidase with two moles of TMPD oxidised per mole of hydroperoxide reduced by the peroxidase. The reaction forms a blue product whose absorbance maximum is at 590 nm.

The rate of TMPD oxidation is measured by the change of absorbance at 590 nm; the initial rate of this change caused by the test compound is compared to the one caused by the reference in order to obtain the inhibitory activity of the compound.

This assay can be used for high throughput screening of compounds by performing it in a 96 well plate and is considered a fast, reliable and relatively inexpensive method. [109] [110]

However, inhibition values can greatly be influenced by several factors, such as the volumes of arachidonic acid that are added; a COX inhibitor might function by competing with arachidonic acid, thus making the concentration of the latter decisive for the calculation of the IC_{50} value. Furthermore, as coxibs are time-dependent inhibitors, incubation time of these compounds with COX-2 is an important variable; optimisation of the protocol is therefore needed, even when instructions are provided by the manufacturer.

Another approach is the assessment of PG production from arachidonic acid in whole cells; one of the methods for this quantification is ELISA, which is usually based on the competition between unlabelled PGE_2 in the samples and a fixed quantity of peroxidase labelled PGE_2 for a limited amount of binding sites on a PGE_2 specific antibody. The amount of peroxidase labelled ligand bound to the antibody is inversely proportional to the concentration of free PGE_2 in the sample.

Several ELISA kits are commercially available for the quantification of both supernatant and intracellular PGE_2 levels, the latter providing more accurate readings than the first.

Whole cell methods avoid the complicated process of COX purification; furthermore, since COX-2 is an intracellular enzyme, this system is also used to check whether potential coxibs are able to cross the cell membrane. These methods, however, have similar disadvantages to the TMPD based assays.

Variations in the biosynthesis of PGs can be analysed also by assessing $[1-^{14}C]$ PG production from $[1-^{14}C]$ arachidonic acid. An efficient method was developed by Uddin and co-workers and can be applied to both purified enzymes and whole cells.

The protocol is similar whether it is performed with purified enzymes or whole cells. The enzyme or the cells are incubated with the inhibitor, then radiolabelled arachidonic acid is added; the reaction is terminated by solvent extraction and, after centrifugation of the phases, the organic layer is spotted on a TLC, which is then developed and read with an appropriate radioactivity scanner. [111]

This method allows precise measurements which are not perturbed by variations of the volume of arachidonic acid added in the assays, which is one of the main limiting factors of “cold” assays. On the other hand, it requires expensive equipment and substrates.

Another commonly used method is the human blood assay, which usually requires addition *ex vivo* of the inhibitors to whole blood. COX-1 activity is assessed by production of TXA₂ generated via platelet COX-1, while COX-2 activity is assayed by measuring the levels of PGE₂ produced by LPS activated monocytes.

This assay has the advantage of performing the assessment in relevant cell populations in physiological conditions, which account for plasma protein binding. Furthermore, prostanoids are synthesised from endogenous arachidonic acid, thus removing the variations that might be caused by the addition of exogenous substrate. However, studies from different laboratories cannot be compared, as suggested by the different results. Furthermore, due to the high cost, it is not suitable for high throughput screening. [92]

A large degree of intervariability in the IC₅₀ values can be observed using different systems. This inter-assay variability is the effect of many factors, including variety of species, tissue types, purity of the enzymes, whether endogenous or exogenous arachidonic acid is used, and incubation time. [109]

For some mechanisms, the results of *in vitro* assays depend on variables such as enzyme and substrate concentration, presence or absence of membranes, and time and order of addition of substrate and inhibitor; furthermore, lowering the concentration of substrate in an assay will favour the competitive versus the time-dependent component of COX-2 inhibition, reducing the apparent selectivity of these compounds. Therefore, the same compound could show different IC₅₀ values when tested with a different assay and/or according to a different protocol.

Another factor which complicates COX screening is the allosteric inhibition of COX-1 by arachidonic acid when used at concentrations of 50 nM-1µM, which decreases the affinity of COX-1 inhibitors, but not COX-2 inhibitors. This allosterism is not observed in the presence of hydroperoxide, suggesting a role of this oxidant in regulating COX-1 catalysis *in vitro* and *in vivo*. [112]

2. MOLECULAR IMAGING

Molecular imaging is defined as the non-invasive visualization, characterisation, and measurement of biological processes at the molecular and cellular level.

Molecular imaging technology has seen progresses in early diagnosis, therapeutic monitoring of several pathologies, including cancer, neurodegenerative disorders and cardiovascular conditions. It is also useful for drug discovery and development and understanding nanoscale reactions such as protein-protein interactions and enzymatic conversions. [113]

In oncology, modern clinical treatments require precise information such as the localisation of the tumour, its size, the possible involvement of lymph nodes; these pieces of information are provided by both anatomical imaging methods such as computed tomography (CT) and ultrasound (US), and molecular imaging methods such as (single photon emission computed tomography (SPECT), positron emission tomography (PET) and fluorescence imaging (FI).

Table 5 compares CT, US, MRI, PET, SPECT, and FI in terms of costs, means of detection, resolution, depth, and target. [114]

Table 5: comparison of imaging modalities. Resolution and depth are indicated for small animal systems. [114]

Imaging	Means of detection	Resolution and depth	Target	Costs
CT	Ionising radiation (X-rays)	50 μ m, no limit	Anatomical, physiological	Intermediate
US	Acoustic waves	50 μ m, up to 3 cm	Anatomical	Low
MRI	Electromagnetism	10-100 μ m, no limit	Anatomical, physiological	High
FI	Fluorescent light	1-2 mm, up to <5 cm	Physiological, molecular	Low

SPECT	Ionising radiation (γ -rays)	0.3-1 mm, no limit	Physiological, molecular	High
PET	Ionising radiation (γ -rays)	1-2 mm, no limit	Physiological, molecular	High

Being based on specific molecules, molecular imaging methods are more flexible than anatomical imaging techniques, which rely on the physical properties of a tissue or a pathological change in a tissue. The small molecule COX-2 probes subject of this thesis have applications in fluorescence, PET and SPECT imaging, depending on the label added to the compound.

2.1 FLUORESCENCE IMAGING (FI)

FI is a popular imaging modality for the observation of cells and tissues *in vitro* and *in vivo*. This technique provides several advantages, including high signal to noise ratio, high sensitivity, and the low cost of the instruments required. [115]

In oncology, FI has a significant relevance when applied to surgery. The first line of treatment for many cancers is surgical resection, and complete removal of malignant cells is essential to the patients' survival. Surgeons rely on white light reflectance, which has very low sensitivity for identifying malignant cells, and on anatomical distortion or discoloration when performing surgical resection; the presence or absence of remaining tumour cells in the surgical margin is a strong predictor of tumour recurrence and survival.

Furthermore, in order to achieve optimal patient outcome, it is equally important to preserve structures such as nerves, blood vessels, ureters and bile ducts.

Enhancing the visual differences between tissues by using a targeted fluorescent probe would remove potential ambiguity during surgery, leading to decreased morbidity and surgical duration. [116]

In case of metastatic disease, FI could be useful also for sentinel lymph node mapping. A sentinel lymph node is the first draining lymph node for a given anatomical site, and is usually removed and examined for evidence of cancer invasion; if there is no sign of it in the sentinel lymph node, the patient is spared from having the other lymph nodes in that region removed. This technique is widely used only for breast cancer and melanoma, mostly because of the more complex lymphatic anatomy of other anatomical sites such

as the pelvis. Currently, lymphatic imaging is performed using dye-injection, nuclear imaging, CT, and MRI, each with their specific limitations regarding sensitivity, resolution, and exposure to radioactivity, or practical use. [116] [117]

2.2 SINGLE PHOTON EMISSION COMPUTED TOMOGRAPHY (SPECT)

SPECT is a tomographic technique which uses γ camera data from many projections to obtain multiple 2D images called projections, which can be manipulated in order to obtain a 3D image.

This imaging technique is similar to PET, but the isotopes used in SPECT emit a single γ -ray instead of a double, therefore SPECT images have less sensitivity and can only image larger structures. [118]

The technique requires the administration of a γ emitting radiopharmaceutical to the patient, and the γ camera is rotated around the patient every 3-6 degrees. Since position detection of the photons does not convey adequate information about the origin of the photon, it is not possible to define a line of response; therefore, a lead or tungsten collimator is added in order to exclude any diagonally incident photons. The limitation of this collimator is that it rejects most of the photons that are not travelling at right angles to the crystal in the camera, so the sensitivity is much lower than PET.

Unlike MRI, SPECT requires only a small amount of imaging agent, therefore it is usually nontoxic and unlikely to exert pharmacological effects. [119]

The isotope most commonly used in SPECT is ^{99}Tc ; its half-life is six hours and its γ energy is 140 KeV. [118]

^{123}I is also used; its half-life is 13.2 hours and the predominant γ energy is 159 KeV. [118]

3. POSITRON EMISSION TOMOGRAPHY

Positron emission tomography (PET) is a non-invasive nuclear medicine technique used for *in vivo* visualisation of physiological and pathological processes at the molecular and cellular levels by following the path of a radiolabelled ligand, capable of emitting positrons, which was previously administered in the body.

The tracer is administered at much lower concentrations than those used to obtain pharmacological effects, which makes PET tracers safe to use. [120]

However, they also have some limitations:

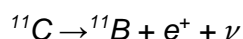
- suitable precursors for radiolabelling a number of compounds may not be available;
- in some cases, the multistep chemistry required for labelling precludes radiolabelling and purification of molecules rapidly enough to avoid substantial decay of radioactivity;
- the position of the label may not be robust to metabolic degradation. [121]

3.1 PRINCIPLES OF PET

Decay by positron emission is the basis for PET imaging.

The positron emitting isotopes are prepared in a cyclotron (a particle accelerator), which propels protons to high speeds; these protons are used to bombard stable nuclei of nitrogen, oxygen, and carbon. The incorporation of another proton in the nuclei produces an unstable isotope; in order to regain its stability, the nucleus must decay through positron emission (also called β^+ decay): a proton in the nucleus is converted into a neutron and a positron. Positrons are the antiparticles to the electrons, having the same mass and opposite charge. The positron is ejected from the nucleus, along with a neutrino (ν) that is not detected. [122]

An example of radionuclide that decays by β^+ decay is ^{11}C :



The positron that is ejected after the decay has a very short lifetime in electron rich materials such as tissue. As positrons travel through human tissue, they give up their kinetic energy principally by Coulomb interactions with electrons. As the rest mass of the positron is the same as that of the electron, the positrons may undergo large deviations in direction with each Coulomb interaction, and they follow a random path through the tissue as they give up their kinetic energy. When the positrons reach thermal energies, they start to interact with electrons either by annihilation or by the formation of a hydrogen-like orbiting couple called positronium. The positronium state lasts for about 10^{-10} seconds before the annihilation occurs, converting the mass of the electron and the positron into electromagnetic energy. As the positron and the electron of the positronium are almost at rest when the annihilation occurs, the net momentum is close to zero. Since momentum and energy must be conserved, it is generally not possible for annihilation to result in the emission of a single photon; otherwise, a net momentum would occur in the direction of that photon. Instead, two photons are emitted simultaneously in opposite directions, carrying an energy of 511 keV (Figure 7). [122]

The annihilation photons are very energetic, therefore they have a good chance of escaping the body for external detection; furthermore two photons are emitted with a precise geometry, so if they can be detected externally, the line joining the detected locations passes directly through the point of annihilation, and since this point is close to the point of positron emission, this gives a good indication of where the tracer was.

All positron emitting radionuclides lead to the emission of two 511 keV photons, therefore PET scanners can be designed and optimised from imaging all of them at this single energy. One drawback of this property is that it is not possible to perform dual radionuclide studies with PET and distinguish between two radionuclides based on the emission energy. [122]

The following image reconstruction provides quantitatively accurate cross-sectional images of the distribution of the radiotracer injected in the object that is scanned. [122]

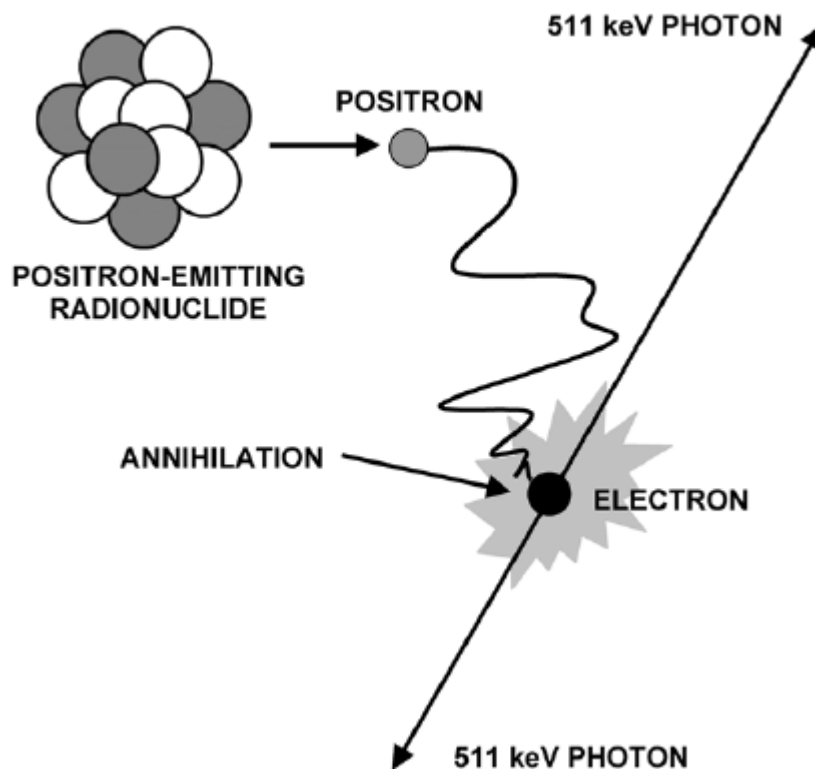


Figure 7: the annihilation process; an electron collides with a positron, emitting two 511 keV gamma rays at 180° to each other. [122]

3.2 DEVELOPMENT OF A PET PROBE

When developing a PET imaging agent, the first criterion to consider is the identification of an unmet clinical need and the potential to significantly improve patients' care. In order to determine the need for and the likely impact of a new tracer, we might consider the following cases:

- agents that target processes found in a large number of disease, i.e. aberrant glycolysis;
- specific targets in common diseases, such as radioiodine for thyroid disorders;
- specific targets in uncommon diseases, where there are no suitable alternatives, such as somatostatin receptor imaging for neuroendocrine tumours;
- situations where the use of a radioactive agent offers several advantages over other methods, such as the use of trapped nuclear perfusion agents in the imaging of myocardial perfusion. [123]

As for the chemical and biological properties, a potential PET probe has to satisfy the following criteria.

High affinity

The lower the density of the target, the higher must be the affinity of the ligand to the molecule to be able to image it. Normally, the K_d constant (the dissociation constant of the ligand-target complex, which is the inverse of the binding affinity) is in the nM range. [124]

As COX-2 is present at low levels even when it is overexpressed, this feature is particularly important.

However, in some cases the affinity is too high, so that the delivery of the tracer is the limiting factor for binding, and in this case tracer retention would reflect perfusion. A lower affinity might be desirable also in order to ease the dissociation between tracer and target and the displacement by and endogenous or exogenous ligand to achieve a pseudo-equilibrium in shorter time. [125]

High selectivity

An ideal radiotracer should bind to one type (or subtype) of receptor, enzyme or transporter. As a general rule, the binding of the tracer to the target is considered acceptable if it is 100 times stronger than the binding to non-target molecules. [124]

As for cancer imaging of COX expression, putative PET tracers should be selective for COX-2, since COX-1 is mostly expressed in physiological conditions, and therefore a tracer that binds to COX-1 would have no diagnostic value.

High contrast ratio

As conclusions drawn from low quality images can be misleading, high contrast images with high signal-to-noise ratio are necessary in order to ensure appropriate interpretation of the condition of the disease. A tracer with high uptake and slow wash-out in target tissue and low uptake and fast clearance from normal organs is desirable. [126]

The optimal target to non-target ratio is the maximum target density (B_{max}) divided by the highest affinity (K_d). The B_{max} / K_d ratio is used to eliminate potential labelled antagonists and inhibitors before starting *in vivo* preclinical studies, since it is taken from *in vitro* studies to predict the maximum bound to free ratio. As *in vitro* measurements involve

very low non-specific binding and are conducted in the absence of complicating factors such as blood flow, metabolism and permeability, these ratios provide best-condition values. A maximal ratio of >25 would warrant further investigation of the probe. [123]

Adequate lipophilicity

Tissue uptake of a drug is analysed using the compartmental model; a compartment is defined as a space in which the concentration of a drug is uniform.

In most PET models of receptor-ligand interactions, we hypothesise three kinetically distinct compartments and an arterial plasma pool of tracer, all of which contribute to the measured PET radioactivity. The arterial pool must exist to drive the model: if no activity is introduced into the plasma, none is ever taken up into the tissue of interest. A version of the compartmental model corresponding to free (F), specifically bound (B), and non-specifically bound (NS) tracer is shown below (Figure 8). K_1 and k_2 are first-order constants that are related to blood flow; k_{on} is a second-order rate constant which describes the association of tracer and receptor; k_{off} is the dissociation rate constant. B'_{max} represents the concentration of receptors available for binding, k_5 and k_6 are first-order constants that measure the rates of forward and reverse non-specific binding. [127]

Free and non-specifically bound ligand cannot be washed away as they are during *in vitro* studies, therefore a high ratio of specific to non-displaceable uptake is required in order to obtain reliable data. While increasing lipophilicity enhances the permeability of a compound, on the other hand it also tends to increase non-specific binding to plasma protein, therefore an ideal PET tracer should have an intermediate lipophilicity value; for example, it has been reported for many drug classes that the optimum logP value for targeting the central nervous system lies between 2.0 and 3.5. [128]

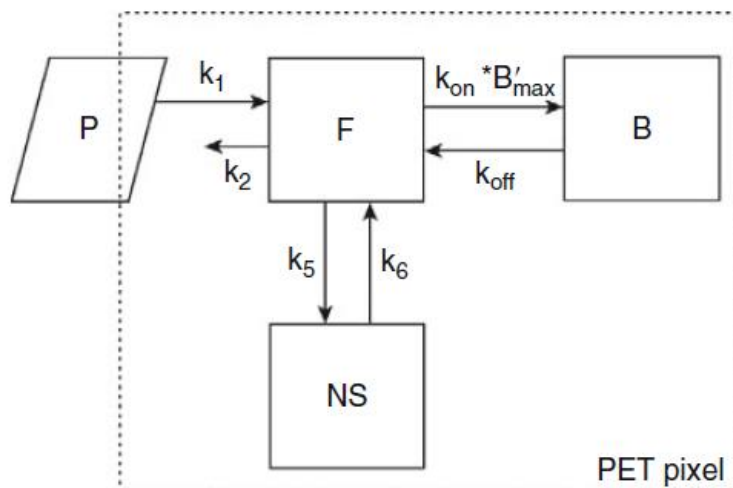


Figure 8: compartmental model scheme of PET tracer uptake showing free (F), specifically bound (B), and non-specifically bound (NS) tracer. The PET pixel indicates that the measured quantity is the sum of radioactivity in F, B, NS and some in the blood. P indicates that the metabolite corrected plasma concentration is not a compartment, as it is measured separately from the PET images and is assumed to be known. [127]

Adequate effective half-life

The effective half-life of a PET tracer (T_{eff}) is the period of time required to reduce the radioactivity level of an organ or of the whole body to one half its original value due to both elimination and decay, therefore it is a function of both its physical half-life (T_p) and its biological half-life (T_b). The correlation is described by the following equation:

$$\frac{1}{T_{eff}} = \frac{1}{T_b} + \frac{1}{T_p}$$

Therefore, if $T_p \gg T_b$, $T_{eff} \simeq T_b$, and if $T_b \gg T_p$, then $T_{eff} \simeq T_p$.

The biological half-life increases with reduced excretion and metabolism. Pathological conditions can alter this component; for example, renal or hepatic failure slows down excretion.

The chemical properties of the tracer also determine the biological half-life; high lipophilicity, and high plasma protein binding, for example, extend the biological half-life.

The effective half-life should match the time window required to image the desired process, such as the uptake of the tracer in the desired target structure; it should be short enough to minimise radiation exposure and long enough to allow patient's scanning. [129]

High stability in vivo and adequate metabolism

The quality of the image as well as the validity of the quantitative analysis of the images heavily depend on the *in vivo* stability of the imaging probe. [126]

The slower equilibrium due to the slower irreversible kinetics of high affinity tracers such as COX-2 inhibitors, imposes longer PET acquisition times to quantify potential changes in binding density as accurately as possible. However, radio-metabolites entering the site can complicate this quantification. In cases where uptake and washout of the parent drug are faster than production and accumulation of radio-metabolites in plasma, their contribution to the total measured activity might be negligible during the PET study; for longer acquisition times, however, this is seldom the case, as radio-metabolites can reach sufficient concentrations to confound the PET signal. [108]

The candidate tracer should therefore not generate troublesome radiometabolites; for example, if the target is in the brain the radiometabolites should not be able to cross the blood-brain barrier, especially if they bind to the target molecule too. [124]

In this case, when carbon-11 labelled PET radiotracers produced by carbon-11 methylation at hetero atoms are used, they offer the advantage of being metabolised by demethylation, leading to small polar radiometabolites, which are excluded by the blood-brain barrier and therefore have little interference with brain measurements. [130]

As for fluorine-18 labelled PET probes, their defluorination produces [^{18}F]fluoride ion, which binds to the bone. Since the spatial resolution of PET is limited to 1-4 mm, there will be a “spill-over” of radioactivity from the bone to the nearby tissue (and vice versa) through a partial volume effect, rendering quantitation of radiotracer binding inaccurate. This problem can be avoided by labelling to an aromatic carbon atom within a phenyl or pyridinyl ring. [130]

Accordingly, as discussed later on (“Imaging of COX-2 expression”), rapid *in vivo* defluorination is a recurring issue for COX-2 imaging probes when fluorine-18 radiolabelling occurs on an aliphatic position.

Ease of radiolabelling of precursor

Due to the relatively short half-lives of the isotopes, the radionuclide must be incorporated quickly into appropriate precursors in no more than two synthetic steps just before the imaging study is performed. [128]

Furthermore, in order to allow routine clinical use of the tracer, its production should be automatable and economically feasible. [126]

Low immunogenicity and toxicity

Although tracers are administered in low concentration, the biological effects caused by an imaging probe still require close monitoring. A molecular imaging probe should have minimal or acceptable level of immunogenicity and toxicity before it can be safely employed in humans. [126]

3.2 ONCOLOGICAL PET IMAGING

As medical experts agree that most cancers can be treated effectively when detected early, the ability of medical imaging in recognising early manifestations of cancer and small otherwise undetectable tumours holds a key role in the diagnosis and treatment of cancers. [131]

The actual diagnosis of cancer generally requires laboratory tests of tissue sample collected through biopsy or surgery, the need of which is usually determined by blood tests and/or imaging.

Once a histologic diagnosis is made, imaging is the key diagnostic tool for the staging of cancer, i.e. to determine where the primary tumour is located, how far the cancer has spread and whether metastases are present. Staging is pivotal for the selection of the appropriate treatment; once a course of treatment has been chosen, the patient's response to the therapy is monitored *via* imaging. [131]

The patient's response to the administered drugs is evaluated through a series of criteria called RECIST (Response Evaluation Criteria in Solid Tumours), which were published in 2000 and are based on the anatomic tumour response metrics.

According to RECIST, the number of lesions to evaluate should be up to 10 and not be more than 5 per organ. Considering that transaxial imaging like CT would be performed, RECIST specifies that only the single longest dimension of the tumour should be mentioned and it should be used as the metric for determining response. [132]

The RECIST categories for response include complete response (disappearance of all tumour foci for at least 4 weeks), partial response (decrease of at least 30% in tumour diameters for at least 4 weeks), stable disease (neither decrease nor increase in tumour size) and progressive disease (at least 20% increase in the sum of all tumour diameters). [132]

Wahl *et al.* have raised some concerns regarding RECIST. For example, limiting the continuous data in tumour size and response to four classes of response might lead to important information loss, especially with newer cancer treatment which are mostly cytostatic; in this case, stable disease is a beneficial outcome. [132]

These authors propose using PERCIST criteria (PET Evaluation Response Criteria In Solid Tumours) on the premise that cancer response evaluated by PET is a time-dependent variable and that metabolic response criteria could have a greater predictive value than that of anatomic studies. [132]

It is important to keep in mind that extensive heterogeneity between individual tumours exists. A single tumour biopsy specimen reveals a minority of genetic aberrations that are present in an entire tumour. This heterogeneity highlights the limitation of biopsy versus PET, which may provide a more comprehensive diagnosis. [133]

Recent studies have shown that tumours with more genomic heterogeneity are more likely to develop a resistance to treatment and to metastasise. Lambin *et al.* proposed a “Radiomics hypothesis”, according to which advanced image analysis on conventional and novel medical imaging could capture additional information not currently used, and more specifically, that genomic and proteomics patterns can be expressed in terms of macroscopic image-based features; the Radiomics hypothesis suggest that genomic heterogeneity could translate to an expression in intra-tumoural heterogeneity that could be assessed through imaging. [134]

The first step in the workflow of Radiomics involves the acquisition of high quality and standardised imaging, either via CT, MRI or PET-CT. From this image, the macroscopic tumour is defined. Quantitative imaging features, such as intensity distribution, texture heterogeneity patterns and descriptors of shape and of the relations of the tumour with the surrounding tissues, are subsequently extracted from the tumour region. The most informative features are identified based in their independence from other traits, reproducibility and prominence on the data. The selected features are then analysed for their relationship with the treatment outcomes or gene expression. The ultimate goal is to provide accurate risk stratification by incorporating the imaging traits into predictive models for treatment outcome and to evaluate their added value to commonly used predictors. [134]

3.2.1 Applications of PET imaging

The key processes involved in the evaluation of cancer patients are diagnosis, staging, treatment planning, therapeutic monitoring and post-treatment surveillance. Imaging, because of its non-invasive nature, plays a crucial role in all these phases and is currently highly dependent upon anatomical imaging techniques such as CT and MRI. However, size criteria might lead to important data loss; similarly, benign processes may form lesions that may be mistaken for tumours.

In the past few years, however, the clinical applications of PET have increased significantly, especially [¹⁸F]FDG-PET, for which there is now plenty of evidence about

its superior accuracy than conventional imaging techniques for the diagnosis of cancer. [135]

The use of [^{18}F]FDG for oncological imaging is based on the Warburg effect; while normal cells use oxidative phosphorylation performed by mitochondria to generate ATP, cancer cells consume glucose to generate ATP via glycolysis. Like glucose, [^{18}F]FDG is phosphorylated by hexokinase on position 6, which prevents it from exiting the cell; unlike glucose, though, it cannot enter glycolysis, and becomes trapped in the cells as [^{18}F]FDG-6-phosphate.

One of the applications of [^{18}F]FDG-PET, especially coupled with CT, is tumour staging, which is essential for an appropriate therapeutic strategy. For instance, [^{18}F]FDG-PET-CT is commonly used for the staging of NSCLC, and has shown to change the management of patients in 20 to 30% of cases, mostly by upstaging the disease and redefining unresectable a previously considered resectable disease by traditional radiological techniques. Several studies have also reported that tumour staging with [^{18}F]FDG-PET revealed more patients with mediastinal and distant metastases than conventional imaging. [136]

PET imaging is particularly useful in radiotherapy planning, especially when the patient has poorly defined target volumes, or when the intent of radiotherapy is to deliver higher than standard doses. This approach needs accurate definition of the metabolically active tumour volume and its differentiation from the surrounding tissue. PET-CT can be more accurate than standard CT, as it might be able to detect unsuspected lymph nodes or distant metastases and it might be able to prevent the irradiation of tissues that don't contain tumour cells. For instance, inclusion of [^{18}F]FDG-PET in the care of NSCLC patients alters the planned treatment in up to 30% of cases by making them ineligible for radical radiotherapy, because of distant metastases or extensive intrathoracic disease. [137]

Assessment of tumour response to treatment is equally as important. In patients with locally advanced oesophageal cancer, preoperative chemotherapy or chemoradiotherapy has been shown to improve outcome; in this case, [^{18}F]FDG-PET could be a useful tool for the assessment of chemosensitivity early during treatment. In a clinical study with 37 patients presenting locally advanced adenocarcinoma of the oesophago-gastric junction, [^{18}F]FDG-PET-CT was carried out at the baseline and after 14 days of cisplatin-based polychemotherapy, demonstrating that this imaging technique

allowed prediction of pathological response by metabolic response assessment as early as two weeks after initiation of chemotherapy. [138]

However, [^{18}F]FDG has been shown to be an inferior tracer than [^{18}F]FLT for the assessment of early response to chemotherapy, where DNA synthesis decrease is to be expected after cytostatic or cytotoxic therapies. This compound is a fluorine-18 labelled analogue of thymidine, and is used for the imaging of proliferation in cancer, as thymidine phosphate is only incorporated in DNA and not RNA. [139]

Another probe that could be used for the determination of the patients' response to treatment is [^{18}F]ICMT-11, the first caspase-3/7 specific PET tracer, which has the potential of early assessment of apoptosis induced by both cytotoxic and mechanism-based drugs. [140]

Another possible approach accounts for the disruption mitochondrial membrane potential ($\Delta\Psi_m$) that occurs in the early stages of apoptosis.

Phosphonium cations can pass through the lipid bilayer because their charge is delocalised and they are sufficiently lipophilic; furthermore, since the membrane potential of mitochondria is the highest in cells, phosphonium cations might accumulate selectively in the mitochondria and therefore, loss of $\Delta\Psi_m$ during apoptosis would decrease the concentration of phosphonium cations in cells. [141]

In vivo studies of [^{18}F]fluorobenzyl triphenylphosphonium cation ([^{18}F]-FBnTP) were performed in orthotopic prostate tumour-bearing mice. [^{18}F]-FBnTP and [^{18}F]FDG were administered 48 hours after treatment with docetaxel; 60 minutes after the injection, the uptake of [^{18}F]-FBnTP was higher in the prostate tumour of untreated mice, while levels of [^{18}F]FDG in both cases were very similar. Treatment with docetaxel resulted in a significant decline in tumour uptake of the first tracer, while the latter showed no significant change, meaning that measurement of $\Delta\Psi_m$ could be an effective strategy for early detection of apoptosis. [142]

Another possible tracer for the assessment of treatment success is [^{89}Zr]bevacizumab, a clinically used monoclonal antibody for VEGF-A. [^{89}Zr]bevacizumab was evaluated in 22 patients with metastatic renal cell carcinoma to assess the possibility of using VEGF-A as a predictive biomarker for anti-angiogenic treatment of this tumour. Tumour uptake of the tracer was high in cancer cells, with remarkable interpatient and inpatient heterogeneity. Treatment with bevacizumab and IFN- α strongly decreased tumour uptake, while sunitinib results in a modest reduction with an overshoot after 2 drug-free weeks. These results suggest that [^{89}Zr]bevacizumab could be a reliable tool for

assessing tumour uptake rate in metastatic renal cell carcinoma, and therefore predicting the treatment success. [143]

While [¹⁸F]FDG-PET holds great promise in the diagnosis of certain cancers, images must be carefully evaluated in order not to avoid false positives. Besides tumour cells, brain and heart cells show high glucose consumption due to their high metabolic demand. Glucose is also used for healing and detoxification, therefore kidneys and bladder both contain byproducts of this process; during intense stress, large muscle groups also increase the metabolism of glucose. Inflammation and infection can also lead to false positives.

It is therefore crucial to develop PET tracers that are based on more specific cancer features, rather than increased glucose metabolism. [144]

[¹⁸F]FDG-PET has some limitations and areas of uncertainty, regarding its lack of specificity, which narrows its use for patients' management. On the other hand, while COX-2 cannot be used as a biomarker for angiogenesis, apoptosis or cell proliferations like other markers discussed before, it directly effects tumourigenesis, for instance, by promoting formation of intestinal polyps, which eventually progress to carcinoma, or by inducing the aromatase production of oestrogen, which promotes breast tumour growth; therefore, COX-2 is a more representative biomarker in a clinical setting.

3.3.2 Imaging of COX-2 expression

As previously discussed, COX-2 is overexpressed in several cancers, therefore molecular imaging of this target has strong potential for the early detection of cancer. Furthermore, COX-2 levels might be associated with progression and invasive disease, which suggests imaging COX-2 may improve the staging of cancer and ultimately patient management. Stratification of patients may also be possible, as some studies showed that the addition of coxibs to standard chemotherapy regimens improves therapeutic outcomes. [145]

3.3.2.1 Carbon-11 radiolabelling

The first approach to a COX-2 PET probe was radiolabelling celecoxib with carbon-11; this was carried from a tributylstannyl precursor *via* Stille reaction using [¹¹C]methyl iodide by Prabhakaran and co-workers, while an alternative Pd catalysed [¹¹C]methylation of celecoxib was proposed by Hirano *et al.*, who also converted [¹¹C]celecoxib to the known metabolite [¹¹C]SC-62807 by oxidising the tolyl carbon using potassium permanganate. [146] [147]

[¹¹C]celecoxib was not tested as a COX-2 imaging agent, but for imaging hepatobiliary excretion via drug transporters; however, it proved to be a poor imaging agent, as it showed slow blood clearance. [147]

Gao *et al.* synthesised a library of celecoxib derivatives that were radiolabelled using [¹¹C]methyl triflate at either the phenolic methyl ether or at the methyl ester. The cold compounds were tested in an MTS assay using MDA-MB-435 cells, where they showed inhibitory properties similar to celecoxib. No further assessment, however, was performed. [148]

Rofecoxib was also radiolabelled with carbon-11. The approach used by de Vries and co-workers was an alkylation of the sulfinate precursor with [¹¹C]methyl iodide. The authors assessed the uptake of this tracer in the brain of healthy rats, demonstrating that it correlated with regions of high basal COX-2 mRNA expression. This accumulation was also displaceable by the COX-2 inhibitor NS398. However, [¹¹C]rofecoxib uptake could not be demonstrated in preclinical inflammation models. [149]

Tanaka and co-workers synthesised and evaluated indole and imidazole derivatives. These compounds showed higher COX-2 selectivity and acceptable metabolic stability. However, they resulted sub-optimal imaging agents because of the non-specific, non-displaceable binding. [150]

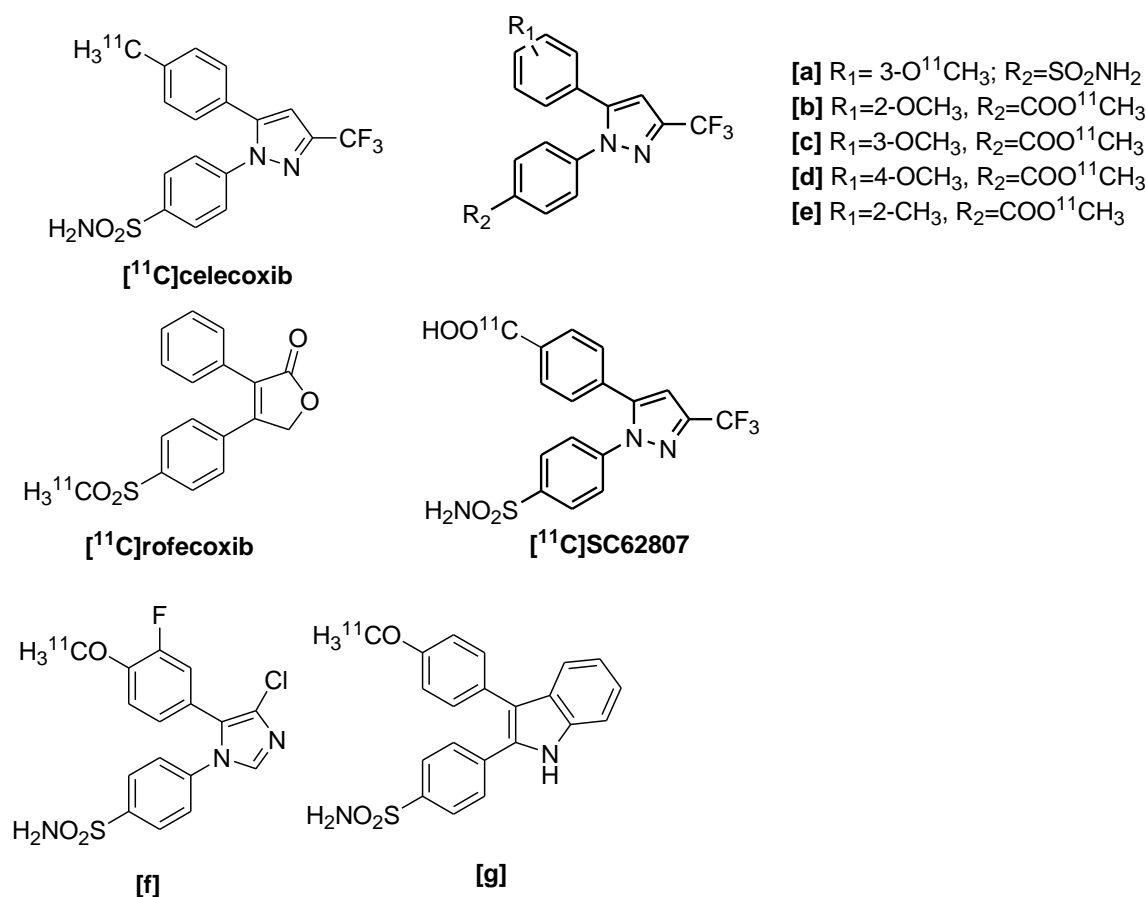


Figure 9: [¹¹C]radiolabelled COX-2 inhibitors. They all have a diphenyl heterocycle core, varying in the central cycle and the substitutions on the phenyl ring.

3.3.2.2 Fluorine-18 radiolabelling

Prabharakan and co-workers radiolabelled celecoxib at the trifluoromethyl position by S_N2 displacement of a bromo-difluoromethyl precursor. The radiotracer defluorinated *in vivo* during imaging of 2-h duration; the authors pointed out that the rate of defluorination was slower in baboons than in rats, therefore it could be slower in humans; however, it also was rapidly metabolised in baboons. [151]

A similar analogue of valdecoxib was also synthesised and radiolabelled with fluorine-18, showing rapid *in vivo* defluorination as well. [152]

SC58125 was radiolabelled by direct nucleophilic displacement of the trimethylammonium triflate precursor. Although *in vitro* cell studies showed selective uptake that was reversed by pre-incubation with cold compound, blocking studies *in vivo* were unsuccessful in rats. As the tracer showed high retention in rat brain, baboon studies were carried out, however the cerebral uptake could not be correlated with the known expression of COX-2 in the brain. This suggested non-specific binding. [153] [154]

Desbromo-DuP-697 was radiolabelled *via* nucleophilic substitution on the corresponding nitro precursor. Biodistribution studies in rats showed displaceable uptake in sites where COX-2 is known to be expressed (heart, kidney, lung), but also non-displaceable uptake in intestines and fat, probably due to the high lipophilicity of the tracer ($\log P=3.72 \pm 0.16$) and its biliary excretion. This suggests that the tracer is not suitable for abdomen imaging, but it might be able to cross the blood brain barrier, therefore it might be useful for neuroimaging. [155]

Uddin *et al.* reported an extensive library of fluorinated celecoxib and indomethacin derivatives. Their lead candidate, a fluoromethyl analogue of celecoxib, was radiolabelled by nucleophilic substitution of a tosylate precursor and then evaluated *in vivo* using a carrageenan-induced inflammation model in male rats, demonstrating higher uptake in the inflamed versus control paw. Biological evaluation in tumour models showed displaceable uptake in HSNCC1483 xenografts with high COX-2 expression and negligible uptake in HCT116 xenografts with low COX-2 expression. However, the radiotracer showed defluorination in line with previously discussed tracers. [111]

An indole-based radiotracer was radiolabelled by Kniess and co-workers *via* substitution of a trimethylammonium salt precursor followed by McMurry cyclisation. *In vitro* evaluation of the tracer showed uptake in COX-2 expressing cell lines that was blocked by pre-incubation with cold compound. *In vivo* evaluation showed good metabolic stability; however, evaluation in a mouse HT-29 xenograft model showed no significant tumour uptake, probably due to the lower affinity of the probe. [156]

The synthesis of 1,2,3-triazole ring *via* Huisgen 1,3-dipolar cycloaddition is a common strategy in fluorine-18 radiolabelling. Wuest and co-workers have studied COX-2 inhibitors incorporating a triazole ring; a copper catalyst yielded 1,4-disubstituted triazoles, while a ruthenium catalyst afforded the 1,5-disubstituted triazole structure, which is more conventional for COX-2 inhibition. The 1,4-disubstituted triazoles showed a surprisingly high affinity for COX-2; however, the 1,5-disubstituted triazoles showed greater COX-2 affinity. [157]

The same group evaluated the use of a tetrazole as core heterocyclic structure, but the compounds showed reduced COX-2 affinity. So far, no biological evaluation of this class of compounds was reported. [158]

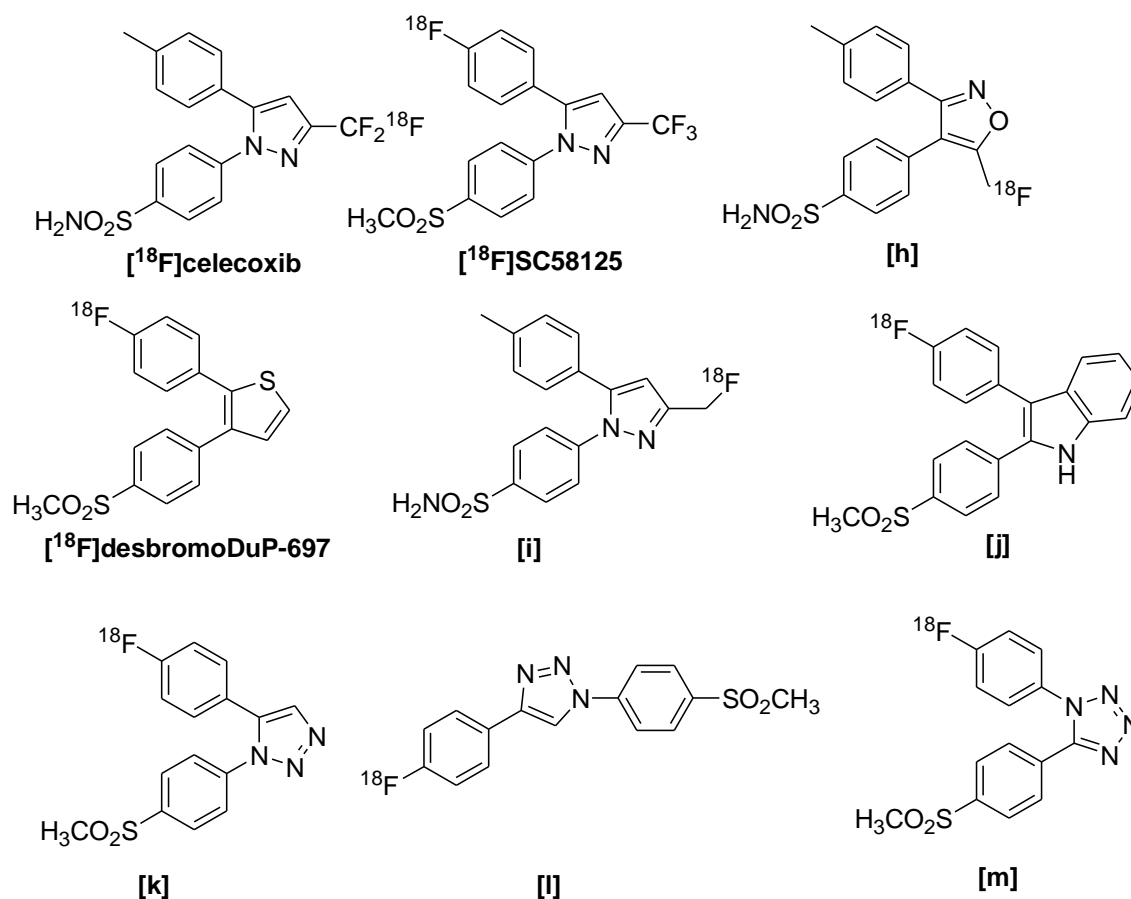


Figure 10: ^{18}F radiolabelled COX-2 inhibitors. The substitution with fluorine-18 has been explored in both aromatic and aliphatic positions. The latter appeared less stable due to *in vivo* defluorination.

3.3.2.3 Iodine-123 and iodine-125 radiolabelling

Kuge and co-workers synthesised two iodocelecoxib derivatives, with either a methylsulfone or a sulfonamide moiety, by halogenation exchange from a bromine precursor with iodine-125. The rationale for this study was to investigate the possibility that sulfonamide binding to carbonic anhydrases in erythrocytes slowed blood clearance. *In vivo* evaluation of the two tracers showed that the sulfonamide derivative cleared indeed more slowly from blood than the sulfone analogue. Uptake of the sulfonamide was blocked with incubation of carbonic anhydrase with inhibitors such as acetazolamide, while blood uptake of the methylsulfone was unaffected under the same conditions. [159]

The same group also investigated a radioiodinated derivative of lumiracoxib, which was radiolabelled by iodo-destannylation followed by base-induced hydrolysis of an amide precursor to give the final benzoic acid. This tracer showed uptake in an *in vitro* inflammation induced macrophage model that was blocked by incubation with cold

analogue. Biodistribution in normal rats showed rapid clearance from blood, but time-dependent accumulation in intestines. [99]

Uddin and co-workers synthesised a library of sulfonamide and methylsulfone celecoxib derivatives with *meta* or *para* iodo substitution on the vicinal aryl ring and various substituents at the 3-pyrazole position. A lead compound was chosen based on COX-2 inhibitory profile and radiolabelled with iodine-123 by iodo-destannylation to give an alternative radiolabelled version of the radiotracer evaluated by Kuge *et al.* and discussed previously. The radiotracer showed selective and displaceable uptake in a carrageenan-induced model of inflammation in the rat paw. [160]

The same research group also explored the synthesis of indomethacin derivatives in order to radiolabel them with iodine-123. From a COX-2 enzyme assay and a COX-2 inhibition assay in intact cell compounds, two, a carboxylic acid and an amide, were selected for further investigation. Radiolabelling via iododestannylation gave the desired radiotracers. The carboxylic acid was metabolically stable *in vivo* and was able to accumulate in a COX-2 expressing tumour *in vivo* at 3 h post-injection, although full biodistribution findings were not reported in this non-radiolabelled study. [161]

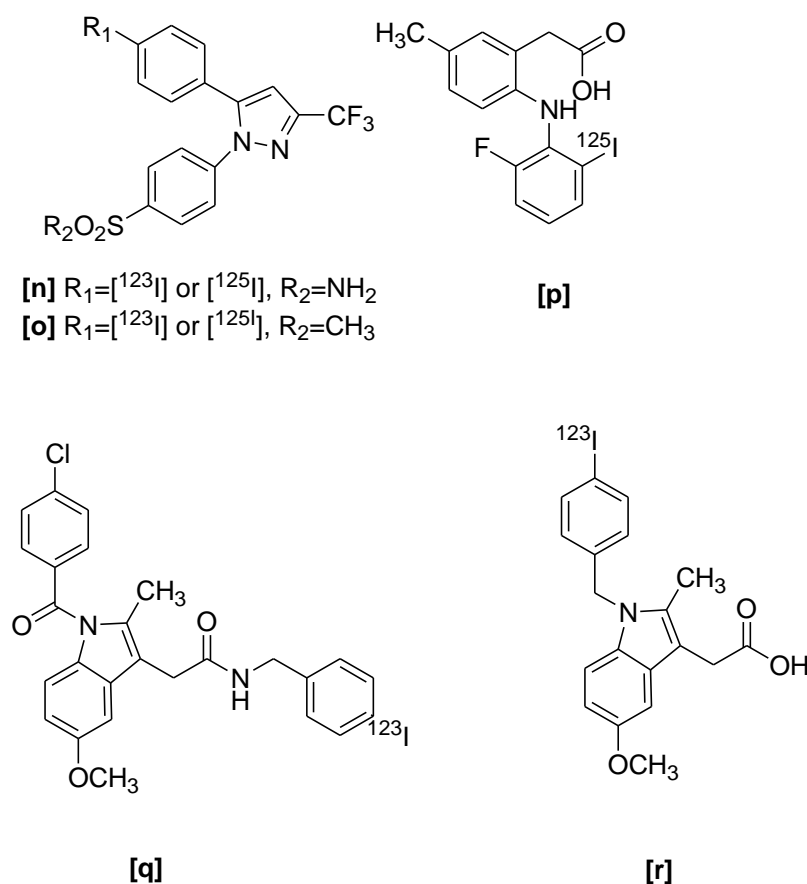


Figure 11: radiolabeled COX-2 inhibitors. Both iodine-123 and iodine-125 have been explored.

Table 6: COX-2 IC₅₀ (nM) values of the radiolabelled compounds.

Compound	IC₅₀
Celecoxib	870
Rofecoxib	530
[f]	4
[g]	0.006
SC58125	<86
[h]	8
[i]	160 (purified enzyme) 80 (whole cell)
[j]	20
[k]	30
[l]	21
[m]	0.0027
[n]	0.0082
[o]	0.00516
[p]	0.00246
[q]	120 (purified enzyme) 1000 (whole cell)
[r]	1710 (purified enzyme) 1490 (whole cell)

To summarise, several attempts of developing a feasible COX-2 PET tracer have been made, but many have shown limitations.

The approach of translating a coxib used in therapy into an imaging probe has displayed some flaws regarding the pharmacokinetics of the molecule. Slow blood clearance is desirable for therapeutic agents, while it is not the case for tracers; therefore, a successful COX-2 probe should have a methylsulfone moiety, rather than a sulfonamide.

Furthermore, non-specific binding due to fat and intestine uptake was an issue; in order to avoid this problem, the logP of a potential COX-2 imaging agent should be lower than desbromo-DuP-697 (3.72 ± 0.16).

Finally, *in vivo* defluorination was quite common when the fluorine-18 radiolabelling point was on an aliphatic position; thus, improved metabolic stability should be achieved by radiolabelling with fluorine-18 on an aromatic position.

3.4 FLUORINE-18 RADIOCHEMISTRY

Fluorine-18 is commonly used for the preparation of radiopharmaceuticals, as it is an ideal radionuclide for several reasons:

- low positron energy (0.64 MeV) with a short range in tissue (max 2.4 mm), which helps provide high resolution images;
- can be produced in high specific activity;
- can be produced in large amounts in a cyclotron (> 10 Ci);
- has relatively high labelling yields (20-40%) in the synthesis of ^{18}F -PET tracers;
- has acceptable radiation dosimetry for multiple studies in a patient;
- its half-life ($t_{1/2} = 110$ min) allows for transport from the production site to the PET centres. [162]

Therefore, fluorine-18 was the isotope of choice for this project.

The most common method to produce fluorine-18 is to start from oxygen-18 enriched water through the $^{18}\text{O}(p,n)^{18}\text{F}$ reaction, which is the most effective and delivers [^{18}F]fluoride of high molar radioactivity. [163]

The low concentrations of fluorine-18 even when GBq of radioactive source is used restricts the available chemistry; as macroscopic and small amounts of fluorine react differently, in most cases existing “cold” fluorine chemistry cannot be converted to “hot” reactions. [164]

There are two basic way to introduce fluorine-18 into organic molecules, a nucleophilic attack by [^{18}F]fluoride and an electrophilic attack by either [^{18}F]fluorine gas or less reactive reagents derived from [^{18}F]fluorine gas.

3.4.1 Fluorine-18 radiolabelling via nucleophilic substitution

All nucleophilic substitutions start with a drying step, as [^{18}F]fluoride in aqueous solution is a very weak nucleophile due to the hydrogen bonds with water molecules. Therefore, [^{18}F]fluoride must first be passed through an activated ion exchange cartridge to remove the bulk of the H_2^{18}O from the target. The trapped [^{18}F]fluoride is then eluted with a mixture of ACN, K_2CO_3 solution and Kryptofix 2.2.2[®], a crown ether that complexes potassium ions, so that after the drying step [^{18}F]fluoride is present as unsolvated and highly reactive anion whose counterion is the complexed potassium. ACN is used in this step because it forms an azeotrope with water, lowering its boiling point and easing its removal. The vial containing [^{18}F]fluoride is then heated and a low N_2 flow is maintained to ease the drying step, as it prevents the condensation of the evaporated solvents. Further ACN is added twice to the vial to complete the removal of water. [164]

Nucleophilic substitutions with [^{18}F]fluoride are usually carried in polar aprotic solvents such as ACN, DMSO and DMF because they ease the ionic dissociation of Kryptofix 2.2.2[®].

The reactivity of the leaving group depends on its ability to stabilise the negative charge due to the [^{18}F]fluoride attack, therefore in aliphatic substitutions, triflate is the most reactive leaving group. However, triflate precursors have a short shelf life and are hygroscopic; furthermore, they can be hard to purify due to their reactivity, as they usually are not stable in columns. This happens less frequently with mesylates and tosylates, therefore they are more commonly used. [164]

Nucleophilic aromatic substitutions work best in activates systems, with a negative inductive and/or a negative mesomeric effect substituents in ortho or para positions to the leaving group. The leaving groups commonly used in aliphatic substitutions are not applicable to nucleophilic aromatic substitutions; fluorine itself is the best leaving group in such reactions, however only low specific activity [^{18}F]compounds are usually produced due to the high excess of the precursor when compared to fluorine-18. Commonly used leaving groups are nitro and trimethyl ammonium. [164]

3.4.2 Fluorine-18 radiolabelling via electrophilic substitution

Electrophilic attacks are carried by either [^{18}F]fluorine gas or less reactive reagents derived from [^{18}F]fluorine gas such as acetylhypofluorite and xenon difluoride. Due to the necessary carrier addition in the [^{18}F]F₂ production in order to allow the recovery of the radioisotope and due the fact that each [^{18}F]F₂ carries only one fluorine-18 atom, the maximum theoretical achievable radiochemical yield is 50%; thus, this reaction is used only for radiopharmaceuticals where a high specific activity is not required. Furthermore, due to the high reactivity of electrophilic labelling, side reactions occur, therefore this method requires extensive purification. [163]

As xenon difluoride has a rich chemistry for fluorination organic molecules under relatively mild conditions, fluorine-18 labelled XeF₂ has been recognised as a potentially useful electrophilic radiofluorination agent. [165]

[^{18}F]XeF₂ has been prepared by fluorine exchange of XeF₂ with [^{18}F]fluoride, which is particularly interesting because of the direct use of readily available cyclotron-produced [^{18}F]fluoride. However, literature shows conflicting results. [166] [167]

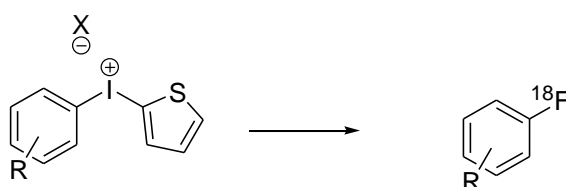
Therefore, Lu and Pike further investigated this reaction, studying the effect of several reaction parameters, such as the reaction vessel material and the solvent use. The synthesis of [^{18}F]XeF₂ gave higher yields when DCM was used instead of ACN and when reactions were conducted in glass vials instead of polypropylene vessels. These trends seem to confirm the hypothesis according to which hydrogen fluoride has a major role in promoting the synthesis of [^{18}F]XeF₂. HF might be produced through the reaction of XeF₂ with the glass, trace water, solvent or K 2.2.2, therefore XeF₂ is less stable in Pyrex glass than Teflon vessels. The instability in glass is due to the acidity of the borosilicate surface, which may generate some HF from fluoride. Furthermore, XeF₂ is known to react with DCM at RT, but more with ACN, generating in both cases HF₂⁻ anion via the formation of HF; this might explain why the radiochemical yield was generally lower in ACN than DCM. Finally, XeF₂ has been shown to react slowly with K 2.2.2, likely producing HF as well.

Further investigation to explore the utility of this labelling agent is currently in progress. [165]

3.4.3 Novel approaches to fluorine-18 radiochemistry

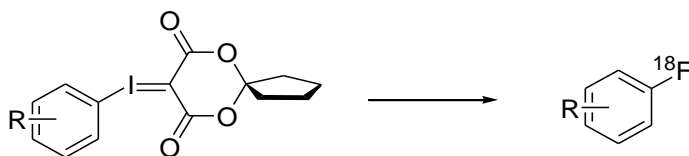
As traditional nucleophilic aromatic substitutions of non-activated systems usually affords low yields, an alternative has been introduced with diaryliodonium salts. The nucleophilic attack usually happens at the more electron-deficient ring; furthermore, an “ortho effect” is observed, meaning that the substitution occurs more favourably at this position, probably due to the iodine-centred trigonal bipyramidal intermediate with the sterically more demanding ortho-substituted ring in the equatorial position upon attack of the nucleophile (Scheme 1). [168]

However, the starting compounds can be challenging to prepare and they usually have short shelf lives. Moreover, radiolabelling of electron-neutral or rich substrates often require extreme temperatures and show low regioselectivity, providing modest radiochemical yields. [169]



Scheme 1: radiofluorination of aryl iodide salts. [168]

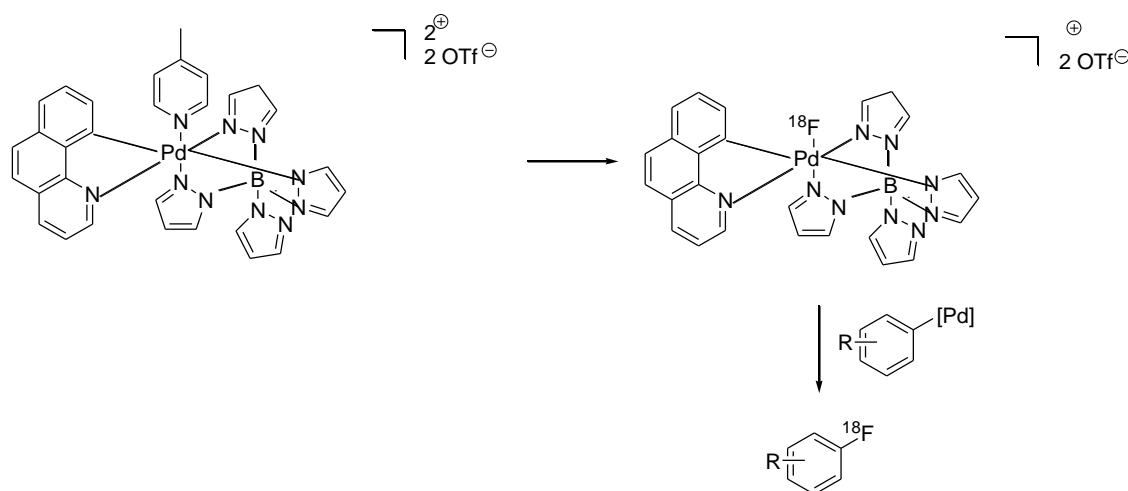
An approach to improving this reaction was introduced by Coenen and co-workers, who used iodonium ylides, which enable fluorination of electron rich arenes. This concept was further explored by Rotstein and colleagues, who used spirocyclic iodonium ylides to address the stability issue of the previous ylides, as these spiro compounds are stable crystals. They proved these compounds enable direct and regioselective fluorine-18 labelling of non-activated and sterically hindered arenes with broad functional group compatibility (Scheme 2); furthermore, they used this methodology to synthesise several PET tracers, which were easily isolated in high radiochemical yields and specific activities. [170]



Scheme 2: radiofluorination of spirocyclic iodonium ylides. [170]

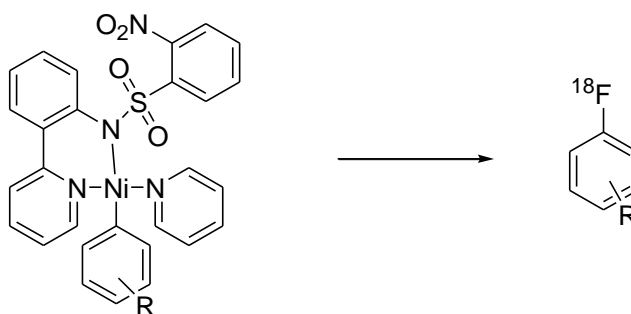
Another recently developed strategy for nucleophilic radiofluorination of electron-rich arenes requires transition metal catalysts, which could enhance reactivity and selectivity, as well as accelerate the rate of reactions.

Hooker and Ritter have generated *in situ* a fluorophilic Pd(IV) species with [^{18}F]KF which forms an intermediate that is able to react with Pd(II) arenes to form Pd(IV) aryl fluoride complexes; these complexes can undergo C-F coupling to yield the radiotracer (Scheme 3). This radiolabelling route gives reasonable yields; however, the need for a two-step procedure and the sensitivity of the first intermediate to air and moisture, complicates the automation of this synthetic route.



Scheme 3: Pd-catalysed radiofluorination of electron-rich arenes. [171]

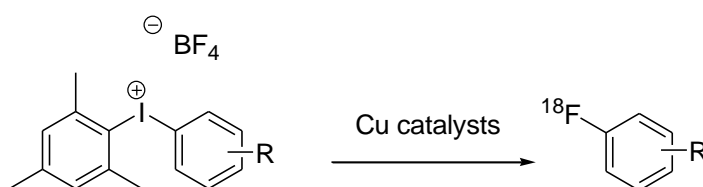
In order to overcome these limitations, the Ritter group followed up this work with a method for radiofluorination of arylnickel complexes which offers a one-step oxidative fluorination of arenes using aqueous [^{18}F]fluoride (Scheme 4). However, increasing the volume of aqueous [^{18}F]fluoride degraded the Ni complex and the oxidant, and classical azeotropic drying of [^{18}F]fluoride resulted in solutions that were too basic, affording low radiochemical yield. Efforts to improve the chemistry included elution of the [^{18}F]fluoride from the ion exchange cartridge with tetrabutylammonium bicarbonate to produce [^{18}F]TBAF and the addition of pyridinium *p*-toluenesulfonate to produce a bicarbonate buffer that was compatible with the oxidant.



Scheme 4: Ni-catalysed radiofluorination of electron-rich arenes. [172]

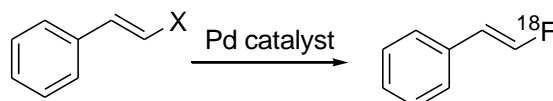
As Sanford's group showed that copper salts catalyse the fluorination of stable and synthetically accessible mesityl-substituted diaryliodonium salts, Cu-catalysed radiofluorination of arenes was also studied (Scheme 5). While in cold chemistry Cu(II) catalysts provided the highest yields, Cu(I) catalysts provided higher yields of hot fluorination in the 20 minutes time constraint of the radiochemical reaction; this is attributed to the rate of the reaction being higher for Cu(I) catalysis, which makes them more suitable for radiochemistry. On the other hand, Cu(II) catalysts are more suitable for cold chemistry, as they afford higher yields over longer reaction times, due to less side reactions. [173] [174]

Current limitations of this strategy are the multi-step synthesis of the diaryliodonium precursors and the automation of the process, which requires further optimisation, as the isolated radiochemical yield was low. [174]



Scheme 5: Cu-catalysed radiofluorination of diaryliodonium salts. [174]

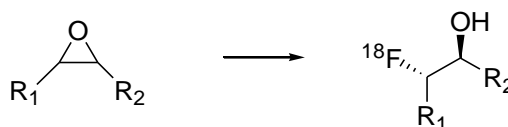
Metal-catalysed radiofluorination is also being investigated for aliphatic systems. One approach focuses on Pd-catalysed allylic fluorination, such as the conversion of cinnamyl carbonates and cinnamyl halides to their corresponding allylic fluorides, which was investigated by Gouverneur's group. (Scheme 6). [175]



Scheme 6: Pd-catalysed radiofluorination of cinnamyl carbonates and halides. [175]

Iridium-catalysed allylic radiofluorination was also investigated. These allylic reactions, however, haven't been used yet to synthesise radiopharmaceuticals, as the allylic fluoride moiety is uncommon. [176]

The first example of enantioselective radiosynthesis was reported by Doyle and co-workers, whose research focused on the synthesis of radiotracers containing the [^{18}F]fluorohydrin moiety (Scheme 7). These radiopharmaceuticals were usually prepared from the corresponding cyclic sulfonates or by selective displacement of protected diols. These routes are both effective, but require separation of regioisomers and stereochemistry had to be set prior to radiolabelling if the radiolabelled product was required as a single enantiomer. The approach suggested by Doyle overcomes these issues by treating racemic epoxides with [^{18}F](salen)CoF, a chiral transition metal [^{18}F]fluoride catalyst, to generate radiotracers as single enantiomers. Doyle's group showed that [^{18}F](*R,R*)-(salen)CoF could be generated from a quaternary ammonium ion-exchange cartridge using (*R,R*)-(salen)CoOTs, with a process analogous to the preparation of [^{18}F]KF, which can be carried out under air and without the use of dried solvents. The subsequent radiofluorination proceeds under mild conditions. [177]

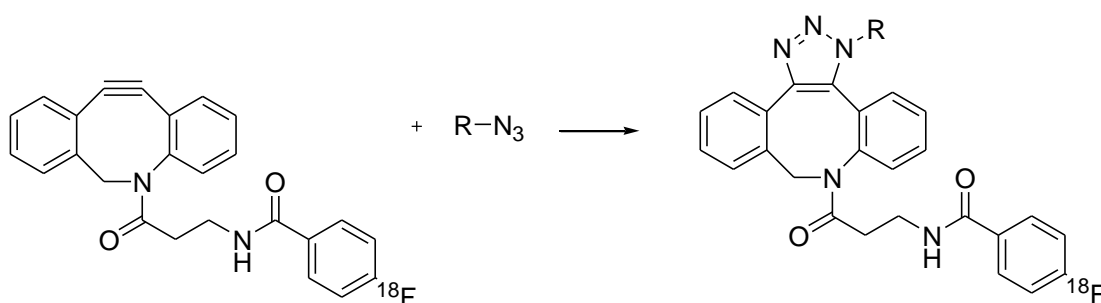


Scheme 7: enantioselective radiofluorination of racemic epoxides. [177]

Due to their mild reaction conditions, short reaction times, high yield and regioselectivity, azide-alkyne 1,3-dipolar Huisgen cycloadditions, more commonly known as “click reactions”, have become more prevalent in radiochemistry. These reactions are usually catalysed by Cu, which is potentially cytotoxic, therefore metal-free methods are under investigation.

The first attempt dealt with strain-promoted Cu-free alkyne-azide cycloaddition, focusing on cyclooctynes and dibenzocyclooctynes; such molecules required complex and low yielding synthesis, therefore only few papers were published regarding this subject. However, nowadays plenty of cyclooctynes are commercially available, which encourages this approach. [178]

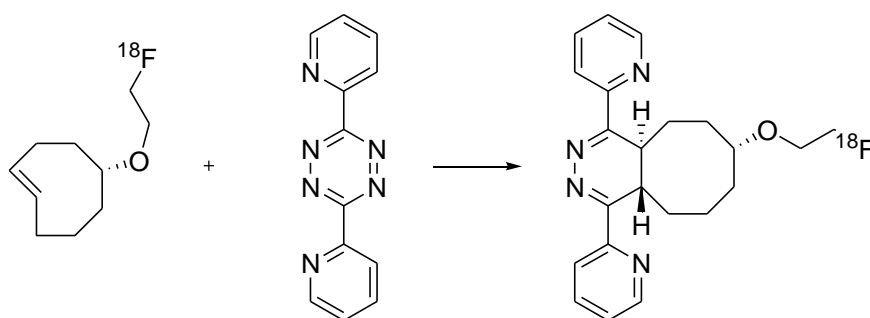
The first example was published by Bouvet and colleagues, who used fluorine-18 labelled aza-dibenzocyclooctyne [^{18}F]FB-DBCO with a series of azides; all tracers were produced with good to excellent radiochemical yield, however the formation of two regioisomers (1,4- and 1,5-triazole) was observed, and separation via HPLC was not always possible (Scheme 8). [179]



Scheme 8: strain-promoted Cu-free alkyne-azide cycloaddition using [^{18}F]FB-DBCO. [179]

Another approach for Cu-free click reactions was first explored by Li and co-workers, who proposed a tetrazine-*trans*-cyclooctene ligation, which is an inverse electron demand of Diels Alder cycloaddition between a cyclooctene and a tetrazine. Considering the instability of tetrazines, cyclooctenes are much more suitable for direct fluorination than tetrazines, therefore they functionalised the biomolecule with a tetrazine, followed by the reaction with a fluorine-18 labelled cyclooctene (Scheme 9). [180]

Both Cu-free methods show promising results; however, only the tetrazine-*trans*-cyclooctene ligation has a potential for *in vivo* application, given the short reaction time and radiochemical yield (respectively, <10 seconds and 98% in the example shown below).



Scheme 9: example of tetrazine-*trans*-cyclooctene ligation proposed by Li and colleagues. [180]

Despite the development of several modern fluorination methods to fluorine-18 radiolabelling, the projected significant increase in the number of available PET tracers has not occurred yet. Short reaction time and high functional group tolerability are only two of the desirable features for a radiochemical reaction to show promise in practical

PET tracer synthesis. It is also crucial to focus on easily automatable procedures and efficient purification protocols. [181]

4. CONCLUSIONS AND AIM OF THIS PROJECT

Elevated expression of COX-2 correlates with premalignancy and cancer progression, which suggests a potential use of COX-2 as a target for imaging early lesions.

In many cases, cancers show an association between high COX-2 levels and chronic inflammation in premalignant conditions, therefore the assessment of COX-2 expression may be useful to determine predisposition to malignancy and for the early detection of cancer.

Most importantly, clinical studies have reported that NSCLC patients have benefited from the co-administration of celecoxib and carboplatin, therefore a COX-2 tracer could be a useful tool for stratification of patients.

The complete development of such a tracer, from the design of a novel library of COX-2 inhibitors to the radiolabelling of a lead compound, was the aim of this project.

This library would be based on the diarylheterocycle core with a methylsulfone pharmacophore, which is able to inhibit COX-2 selectively; the methylsulfone is preferable over the sulfonamide moiety to avoid binding to carbonic anhydrase in erythrocytes, which might be the reason for the slow blood clearance of this class of drugs. The lipophilicity of these compounds would have to be low enough to reduce plasma protein binding, but high enough to be able to cross cell membranes.

The synthesised compounds would be then screened in appropriate assays to determine their SAR and find a lead probe candidate. Colourimetric assays based on the peroxidase activity of COX would be ideal, as they are regarded as fast, reliable and relatively inexpensive; the protocol of this assay would need optimisation, especially the incubation time of these compounds with the enzyme, being coxibs time-dependent inhibitors.

Efforts would then be focused on synthesising an appropriate precursor for the lead probe candidate, considering also the accessibility of the synthetic route. Finally, fluorine-18 radiolabelling of this precursor would be attempted and carried out in a variety of conditions in order to optimise the radiochemical reaction.

5. 5,5-DIPHENYL HYDANTOINS

5.1 Introduction

The first selective COX-2 inhibitor, DuP697, was synthesized before the existence of COX-2 was confirmed. The development of DuP697 was later discontinued, but its structure served as a starting point for the synthesis of the most extensive chemical class of COX-2 selective inhibitors, which is diarylheterocycles. In DuP697 case, the central heterocycle is a thiophene and the two aryl groups are differently substituted phenyl rings. [93]

Extensive research has been carried out starting from this core, both for imaging and therapeutic purposes; libraries of compounds from this building block were originated by exploring substitutions either of the aryl groups or of the heterocycle.

Examples include:

- **celecoxib**, whose structure includes a pyrazole instead of a thiophene; [182]
- **rofecoxib**, which has a furan-2-one as central heterocycle; [183]
- **valdecoxib** and its prodrug **parecoxib**, which show an isoxazole; [184] [185]
- **etoricoxib**, which includes two pyridines, one as central ring; [186]
- **apricoxib**, whose central ring is a pyrrole; [187]
- **tilmacoxib**, with an oxazole as an heterocycle and a cyclohexane instead of a phenyl ring; [188]
- **firocoxib**, with a furan-2-one as central heterocycle and a cyclopropane instead of a phenyl ring. [189]

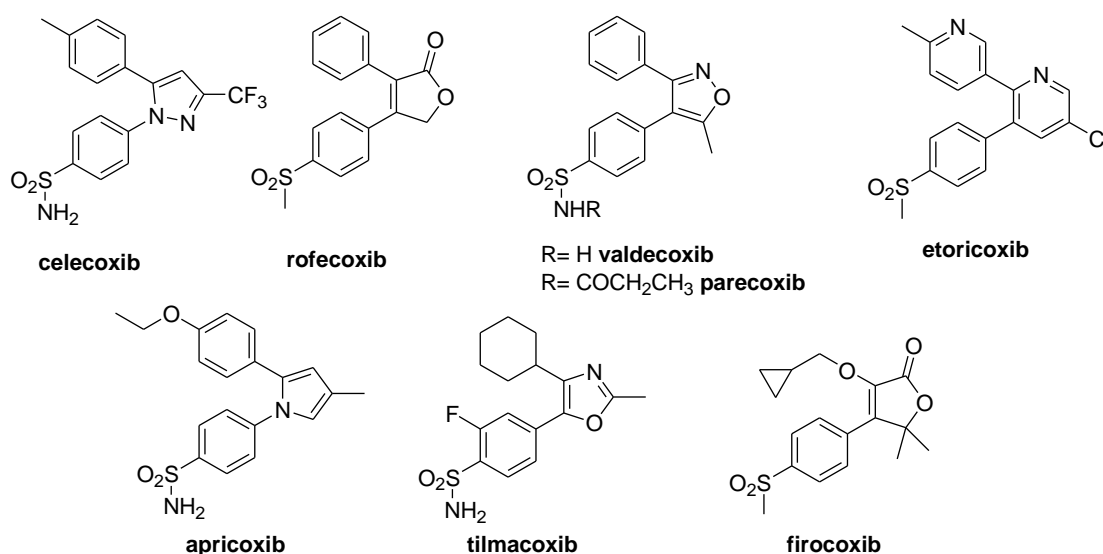


Figure 12: structures of diarylheterocycles with COX-2 inhibitory activity.

Mimicking DuP697 structure, these inhibitors show both aryl groups in adjacent positions of the central (usually) five membered heterocycle.

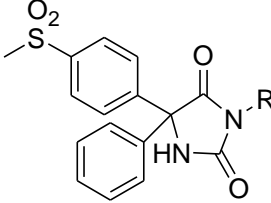
Table 7 shows IC₅₀ values of the compounds mentioned.

*Table 7: IC₅₀ values (μM) of several COX-2 inhibitors. *: as calculated by assessing PG synthetic capability in homogenates from COX expressing cells [190]; **: as calculated by whole blood assays [191] [192] [193]; *** as calculated with a [¹⁴C]arachidonic acid purified enzyme assay [194]*

Compound	IC ₅₀ (μM)	
	COX-1	COX-2
DuP697 *	0.8	0.01
Celecoxib **	6.7	0.87
Rofecoxib **	19	0.53
Valdecoxib **	26	0.87
Etoricoxib **	116	1.1
Apricoxib **	2.2	0.31
Tilmacoxib ***	6.2	0.01
Firocoxib **	105	0.3

However, recently Zarghi and co-workers proposed a novel structure of COX-2 inhibitors that stands out, as both rings are bound to the same carbon atom; despite this modification, this core seemed to be suitable, according to their COX-1 and COX-2 inhibition data (Table 8). [195]

Table 8: IC₅₀ values of Zarghi's library of hydantoin. [195]

	R	IC ₅₀ (μM)		SI
		COX-1	COX-2	
	H	>100	0.077	>1298
	Me	22.69	0.081	280.1
	Et	20.21	0.098	206.2
	Pr	12.01	0.171	70.2
	Allyl	14.96	0.099	151.1

Docking studies on the unsubstituted hydantoin show that the *p*-MeSO₂ moiety is oriented towards the secondary pocket of COX-2 (Arg513, Phe518, Val 523), with one of its O atom forming a hydrogen bond with the amino group of Arg513 at a distance of 4.6 Å, and the other O atom at 3.5 Å from NH of Arg513. An additional hydrogen bond forms between the NH in position 3 of the hydantoin ring and the N atoms of Arg120 at a distance of 4.8 Å (Figure 13). [195]

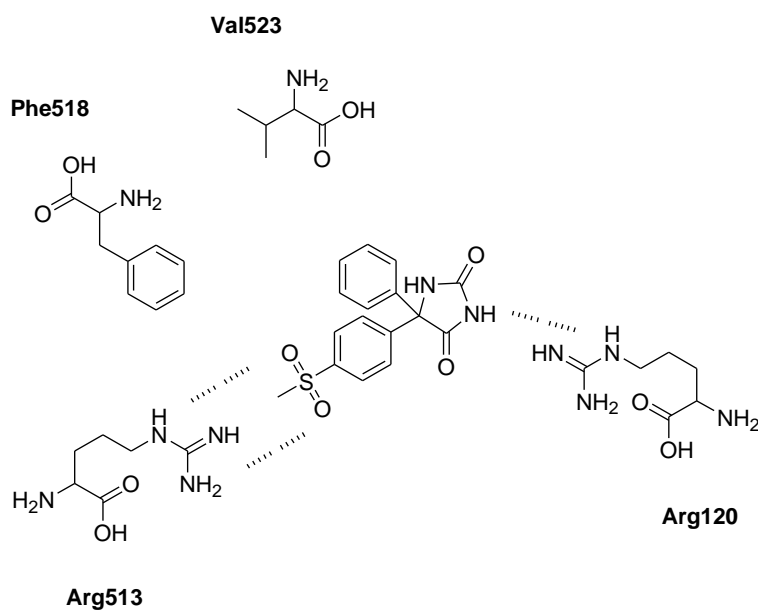


Figure 13: docking studies of the unsubstituted hydantoin within COX-2. Docking studies were performed using Autodock version 5.3; the coordinates of the X-ray crystal structure of the selective COX-2 inhibitor SC-558 bound to the murine COX-2 enzyme were obtained from the RCSB Protein Data Bank. [195]

Analysing this particular study in further details and expanding their library (Table 2) was the main focus of this research project.

5.2 Rationale

The novelty of the 5,5-diphenyl hydantoin core versus the traditional COX-2 inhibitor scaffolds was only one reason to choose this as a starting point for this research.

The strategy of labelling compounds used in therapy in order to use them for diagnostic purposes is not always beneficial, as their pharmacokinetic properties are optimised for therapeutic purposes. For instance, carbon-11 celecoxib has been found to have slow blood clearance, which causes high blood pool background in the imaging target tissue; fluorine-18 desbromo DuP-697 showed high non-specific intestine uptake, probably due to its high lipophilicity.

The 5,5-diphenyl hydantoin core has never been used for the development of coxibs. The central heterocycle is the main difference among this class of pharmaceuticals, while the two aryl rings are most commonly phenyl. By comparing the cLogP of hydantoin versus the pyrazole of celecoxib and the thiophene of desbromo DuP-697 (respectively, 1.69 \pm 0.24 versus -0.72 \pm 0.56 and 1.90 \pm 0.22), there is reason to believe that this 5,5-diphenyl hydantoins would have a more suitable lipophilicity.

Table 9 lists cLogP values of the designed hydantoins. While an aliphatic R group corresponds to lower than ideal lipophilicity, an aromatic R substitution on N3 results in logP values high enough for crossing the cell membrane, but low enough to avoid elevated plasma protein binding. This level of lipophilicity should reduce the biological half-life to a more suitable value for imaging. This is further achieved by limiting the possibility of plasma protein binding, by using the methylsulfone pharmacophore instead of the sulfonamide. The latter has been shown to inhibit carbonic anhydrases, and might be responsible for the slow blood clearance of this class of COX-2 inhibitors, due to the affinity of this moiety for this enzyme in erythrocytes. [99]

The fluoro-aromatic substitution is potentially superior to the fluoro-aliphatic group also in terms of metabolic stability. As reviewed in the introduction of this thesis, [^{18}F] celecoxib, [^{18}F]valdecoxib, the [^{18}F]fluoromethyl analogue of celecoxib synthesised by Uddin and co-workers all were subject to *in vivo* defluorination.

However, since SAR studies of the 5,5-disubstituted hydantoin core structure were scarce, the aliphatic substitutions were included as well in the library in order to get a

more comprehensive investigation on the COX-2 inhibitory activity of these compounds (Figure 14).

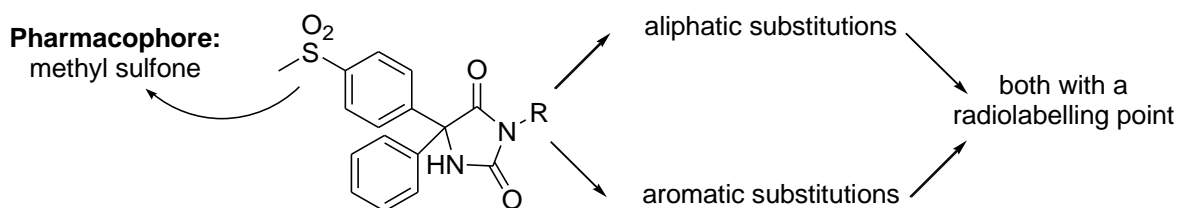


Figure 14: SAR studies planned for the 5,5-diphenyl hydantoin core.

A variety of alkyl groups were designed in order to analyse the affinity and selectivity trend while increasing the chain length from methyl to *n*-butyl; in order to explore the effect of aromatic substitution, several benzyl groups were also included (Table 9).

Since a phenyl ring containing the *p*-sulfonamide/methylsulfone and a further lipophilic group bound to the central heterocycle are necessary for COX-2 inhibition, the two phenyl groups were retained as well. These cycles were considered a reasonable starting point for the investigation of a new core structure, as they are the most established substitutions in commercially available COX-2 inhibitors.

Most compounds also contain a radiolabelling point, either with carbon-11 (**[6]**), fluorine-18 (such as **[2]**) and I isotopes (**[12]**), which make them suitable for PET/SPECT imaging purposes.

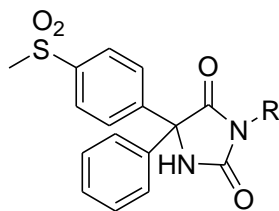
Focusing on fluorine-18 radiolabelling, **[2]** could be radiolabelled *via* aromatic nucleophilic substitution starting from the 4-nitro precursor; its synthesis is easily accessible by reacting the non-substituted hydantoin with 4-nitrobenzyl bromide, which is commercially available at an affordable price.

A valid alternative is reducing the nitro group of this precursor and methylate it to get the trimethylammonium precursor. This reduction would have to be either targeted to the nitro group alone, or carried out before the oxidation of the methylthio group to methylsulfone, in order not to lose the pharmacophore. Several methods for chemoselective nitroreduction of compounds with reduction-sensitive groups have been reported, including Fe powder or SnCl₂ under ultrasonic irradiation, Fe powder and CaCl₂, and a Pd catalysed method with aqueous KF and polymethylhydrosiloxane. [196] [197] [198]

As for the potential aliphatic fluorine-18 radiolabelling, [5] for instance could be radiolabelled starting from the mesylate or the tosylate precursor, which are produced from the corresponding alcohol. The synthesis of this intermediate would require 2-bromoethanol, which is commercially available and affordable.

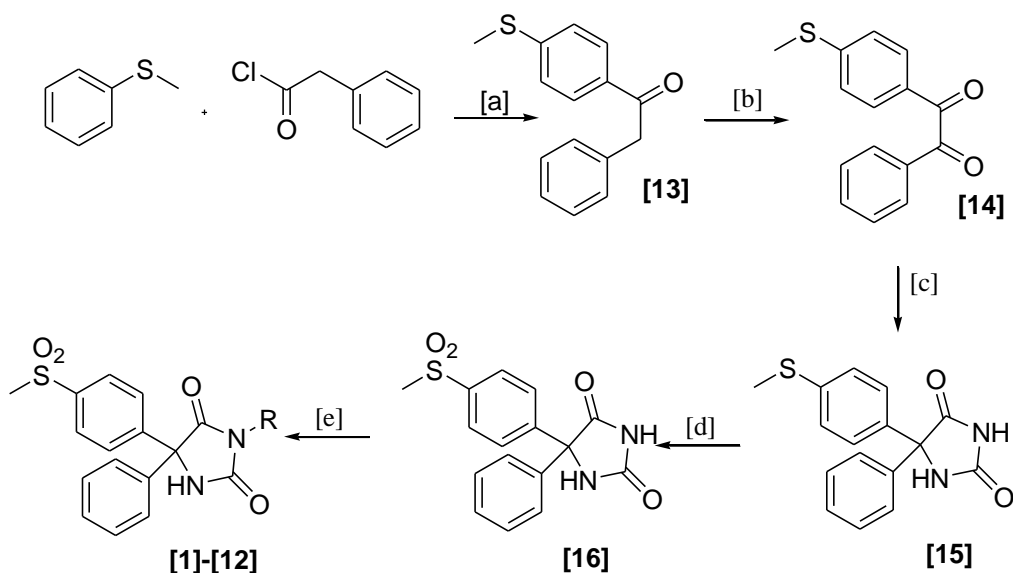
Table 9: library of hydantoins synthesised and cLogP values, calculated using ACD/Chemsketch, version 14.01.

Compound	R	cLogP
[1]	Allyl	0.91+/- 0.69
[2]	4-Fluorobenzyl	2.23+/- 0.71
[3]	Propargyl	0.85+/- 0.69
[4]	3-Fluoropropyl	0.96+/- 0.70
[5]	Fluoromethyl	0.56+/- 0.71
[6]	Methyl	0.31+/- 0.68
[7]	3-Iodobenzyl	3.21+/- 0.71
[8]	2-Fluoroethyl	0.65+/- 0.70
[9]	4-Fluorobutyl	0.96+/- 0.70
[10]	Benzyl	2.17+/- 0.68
[11]	3-Fluorobenzyl	2.23+/- 0.71
[12]	4-Iodobenzyl	3.21+/- 0.71



5. 3 Synthesis

The synthesis route followed was the same as Zarghi *et al.*. A Friedel-Crafts acylation yields an intermediate which undergoes Riley oxidation; the resulting dione reacts with urea to form the hydantoin core. Oxidation of the sulfide to sulfone yields the pharmacophore. The final products are synthesised via alkylation on the N3 of the heterocycle (Scheme 10).



Scheme 10: synthesis of 5,5-diphenyl hydantoin. [a]: AlCl₃, dry DCM, N₂ atmosphere, 0°C for 2.5 h, RT, overnight; [b]: SeO₂, refluxing glacial acetic acid, 3 h; [c] urea, refluxing EtOH and NaOH 30%, 3 h; [d]: Oxone®, THF/water, rt, 4 h; [e]: K₂CO₃, RX or ROMs, DMF, rt, 3 h

Step a

The first reaction is a Friedel-Crafts acylation between thioanisole and phenacetyl chloride catalysed by AlCl₃, which afforded [13] at high yields.

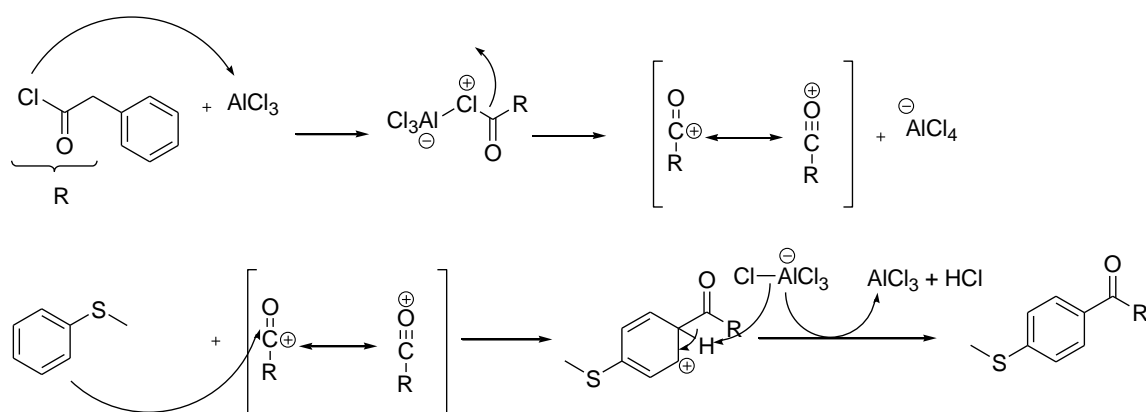
The reaction was performed in dry DCM under N₂ atmosphere, as anhydrous conditions are necessary whenever AlCl₃ is used, since it reacts with water yielding HCl and Al(OH)₃.

While in Friedel-Crafts alkylation the Lewis acid is used in catalytic quantities, in an acylation it can complex to any oxygen atoms present, therefore more acid is required, usually slightly over one equivalent.

A Friedel-Crafts acylation yields a monoacylated product starting from an arene and an acyl chloride; the product is deactivated and does not undergo a second substitution, as

due to the electron withdrawing effect of the carbonyl group, the product is always less reactive than the starting arene.

The mechanism of the reaction (Scheme 11) requires the formation of an electrophilic acylium ion from the Lewis acid (in this case, AlCl_3) and the acyl chloride (phenacetyl chloride). The aromatic ring of thioanisole performs a nucleophilic attack on the acylium ion, losing its aromaticity and forming a cyclohexadienyl cation intermediate. Removal of the proton on the sp^3 hybridised C atom bearing the acyl group regenerates the aromaticity of the system and the catalyst.



Scheme 11: mechanism of step a, a Friedel-Crafts acylation. An electrophilic acylium ion is formed, which is then attacked by the aromatic system; chloride ion deprotonates the ring, regenerating the aromaticity of the system and the catalyst.

Step b

The second step is the oxidation of the methylene in alpha to the carbonyl group to yield a 1,2-dione. This reaction is called Riley oxidation. [199]

This oxidation was carried differently than the reference paper, as a large excess of SeO_2 and acidic conditions afforded higher yields than refluxing 1,4-dioxane/water and a 2:1 ratio of SeO_2 :**[13]**.

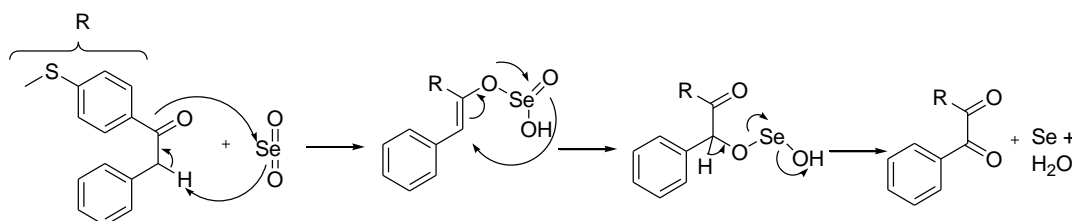
As shown on Scheme 12, this step requires an ene reaction, which produces a seleninic acid. Ene reactions, also called “Alder ene”, are pericyclic reactions between an ene (usually, an alkene with an allylic H atom) and an enophile (a compound containing a multiple bond), which form a new σ bond and causes the migration of the ene double bond and H transfer.

Considering the orbital orientation of this reaction, the C-H orbital is parallel with the p orbitals of the ene, so that the orbitals that overlap to form the σ bond are already parallel. The electrons involved in this reaction are both σ and π , with the ene having two

components, σ^2 and π^2 , and the enophile having one π^2 component. The three components are involved in a suprafacial reaction; since all three components are of the $(4n+2)_s$ type, the reaction is allowed, according to the Woodward-Hoffmann rules.

Considering the cyclic intermediate, this stage can be classified as a 6-endo-dig, which is allowed according to Baldwin's rules.

The ene reaction is followed by a [2,3] sigmatropic rearrangement to seleninic ester and by the elimination which yields the desired 1,2-diketone. This step is a 5-endo-dig reaction, which is allowed.



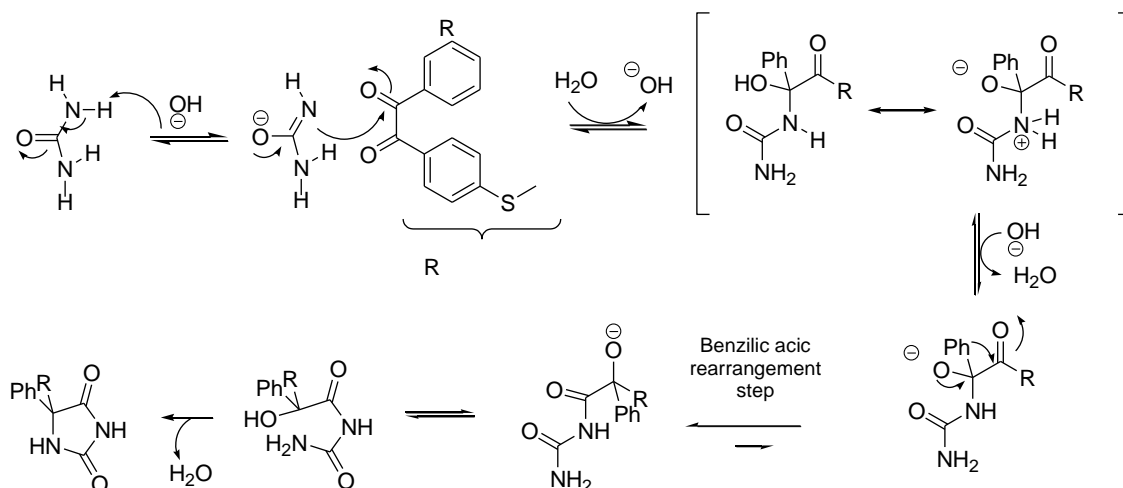
Scheme 12: mechanism of step b, a Riley oxidation. The dione is produced after the seleninic acid and the seleninic ester intermediates.

Step c

The hydantoin was synthesised via nucleophilic addition of urea. This reaction was first used for the synthesis of phenytoin, an anticonvulsant drug, achieved by Blitz.

Early literature described this reaction as the result of a pinacol rearrangement. However, the mechanism is actually based on a rearrangement that closely resembles the benzil-benzilic acid rearrangement. [200] [201]

Due to resonance, urea is a weak base ($pK_a = 26.8$), therefore needs the presence of a stronger base in order to increase its nucleophilicity to attack one of the carbonyl groups of the dione. The loss of a proton from the quaternary nitrogen atom yields an intermediate which undergoes the benzilic acid rearrangement. This rearrangement precedes through a 1,2-phenyl migration to produce an amide and a tertiary alkoxide in the resulting intermediate. Final dehydration produces the desired product.



Scheme 13: mechanism of step c, the synthesis of the hydantoin core.

Step d

The methylsulfone pharmacophore was achieved by oxidising the sulfide to sulfoxide with Oxone®. Oxone® is a triple salt with the formula $\text{KHSO}_5 \cdot 0.5 \text{KHSO}_4 \cdot 0.5 \text{K}_2\text{SO}_4$, and the active compound is KHSO_5 . Its use as an oxidant has grown rapidly due to its stability, its non-toxic nature, its low cost, and its versatility; as shown in Figure 15, it is well known for its oxidation of a variety of compounds containing N, S, B or P atoms and it is also frequently used to prepare dimethyldioxirane, which epoxidises olefins. [202]

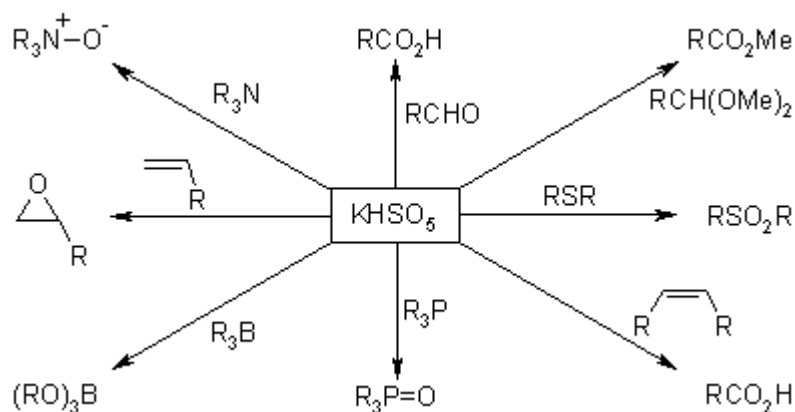
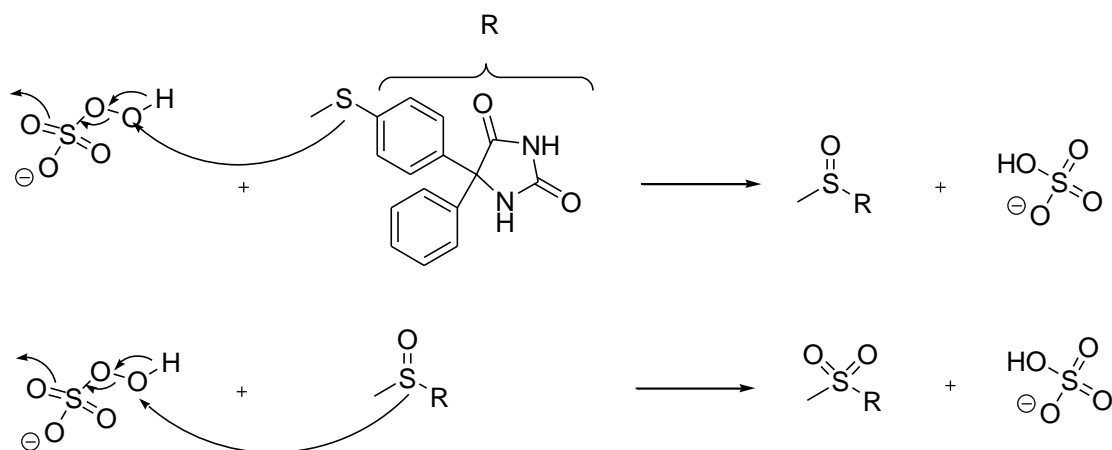


Figure 15: applications of Oxone® to organic synthesis. [202]

The mechanism of action is shown in Scheme 14. The S atom of the sulfide attacks the terminal O atom of the peroxide group; the peroxide bond breaks, forming HSO_4^- and a sulfoxide group. The oxidation of sulfoxide to sulfone follows the same mechanism.



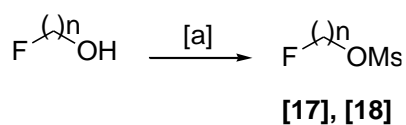
Scheme 14: mechanism of reaction for step d, the oxidation of sulfide to sulfone by Oxone®, which requires an intermediate sulfoxide step

Step e

The final compounds were synthesised via alkylation on the *N3* of the starting hydantoin. *N3* is alkylated over *N1*, as the imidic proton is more acidic ($pK_a \approx 9$) than the lactam proton ($pK_a \approx 12$).

A 1:1 ratio between substrate and halo-alkylating agent afforded the *N*-substituted product only, and no trace of *N,N'*-dialkylated product was isolated.

When the halo-alkylating agent was not available (compounds **[4]** and **[8]**), the final step was performed with the mesylate equivalent, which was synthesised from the corresponding alcohol (Scheme 15). Mesylates are good leaving group in nucleophilic substitutions, as the resulting negative charge is delocalised on the mesylate group.

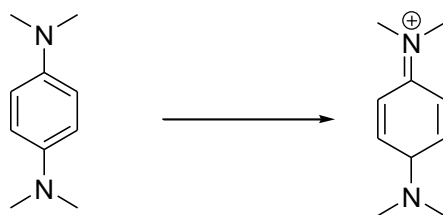


Scheme 15: synthesis of mesylates. [a]: MsCl, TEA, DCM, 0°C-5°C, 2 hours

5.4 Biological evaluation

The COX-1 and COX-2 inhibitory activity and COX-2 selectivity of these library was tested by performing colourimetric COX (ovine) inhibition kits (Cayman Chemical, MI, USA, Item number 760111).

This assay measures the peroxidase component of COX. The peroxidase activity is assayed colourimetrically by monitoring the absorbance of oxidised TMPD at 590 nm (Scheme 16).



Scheme 16: oxidation of TMPD to a blue-violet compound which absorbs at 590 nm.

The assays were performed on a 96 well plate, testing each concentration in triplicates, including background wells, containing only assay buffer and heme, and 100% activity wells, containing also enzyme. Compounds were dissolved in DMSO to reach a final concentration between 4 μ M and 20 nM. Colourimetric substrate and arachidonic acid were added after a period of incubation; the plate was then read kinetically, collecting as many time points as possible in the course of 2 minutes. Considering the acquisition times of the absorbance reader, in order to get more accurate results, only half a plate was used, so that the least amount of time would pass between the reading of the first line and the last. Initial rates were then analysed as described by the manufacturer in order to generate IC₅₀ curves.

This assay kit is widely used, as it is relatively inexpensive, fast and requires extensively available instrumentations.

However, despite the existence of a set of instructions provided by the manufacturer, the protocol needs to be optimised. Particular attention needs to be addressed to the incubation step; as most COX-2 inhibitors are time-dependent inhibitors, different incubation times could result in a different IC₅₀ values for the same compound. In case these compounds were time-dependent inhibitors as well, the incubation step was set at 30 minutes, which was previously assessed as suitable for celecoxib.

While celecoxib showed concentration-dependent inhibition of COX-2 and no inhibition of COX-1, the hydantoin core, the hydantoin core, the hydantoin core, the hydantoin core, the hydantoin core,

therefore, was acknowledged as unsuitable for COX inhibition, despite previously published data (Table 10).

Table 10: IC₅₀ data (μ M) of this library of compounds, as assessed by colourimetric pure enzyme assay.

Compound	IC ₅₀ (μ M)	
	COX-1	COX-2
[1]	>4	>4
[2]	>4	>4
[3]	>4	>4
[4]	>4	>4
[5]	>4	>4
[6]	>4	>4
[7]	>4	>4
[8]	>4	>4
[9]	>4	>4
[10]	>4	>4
[11]	>4	>4
[12]	>4	>4
Celecoxib	>4	0.1

Several considerations can be made when speculating why this core structure failed as a coxib.

For the screening of their compounds, Zarghi's co-workers used a similar kit, with a chemiluminescent method of detection instead of a colourimetric one; however, a precise comparison cannot be drawn because they did not report their protocol. As stated in the introduction, variations of the assay protocol (such as incubation times and volumes of

reagents added) can result in different data, which might explain this discrepancy, especially for [1] and [6], which are also part of Zarghi's library.

Other hypotheses could be formulated, such as poor solubility of the compounds in the assay buffer; however, no precipitation was observed when the compounds, dissolved in DMSO, were added to the wells.

Possibility of degradation of the compounds was also considered; however, some compounds were tested *via* HPLC after a year and were found unaltered.

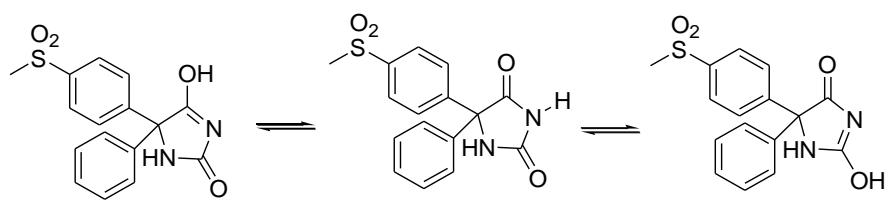
As for the docking studies performed by Zarghi and co-workers, the interactions between the non-substituted hydantoin and COX-2 are shown, one of which is an H bond between the NH in position 3 of the hydantoin ring and the N atoms of Arg120 at a distance of 4.8 Å. When *N*3 is derivatised, this interaction is suppressed if the group introduced does not bear H bond donors at the appropriate distance, which might have lowered the affinity of these compounds for COX-2.

This theory seems to collide with the observation that none of the structures of the COX-2 inhibitors mentioned in the introduction paragraph of this chapter bear such an H atom on their heterocycles. However, those compounds are all vicinal diaryl heterocycles; considering the wide variety of heterocycles that are regarded as suitable, it can be assumed that the position of the two aryl groups is more important for the affinity to COX-2 than the nature of the ring, as the former is responsible for the orientation of the aromatic rings in space. [203]

In the non-substituted hydantoin, the different spatial orientation of the two phenyl rings might be compensated by the extra H bond provided by the heterocycle; however, when this is removed, the compounds lose any affinity for COX-2.

A positive confirmation of this theory would come from a library of 1,5-diaryl hydantoins that act as COX-2 inhibitor. However, so far such a library has been only synthesised and not tested for its biological activity. [204]

Finally, a contribution might come from the keto-enol tautomerism of the non-substituted hydantoin (Scheme 17). It is possible that the enol forms of the molecule contribute to the affinity for COX-2 *via* additional H bonds; in this case, the loss of this contribution by derivatising the molecule on the *N*3 atom could explain the loss of COX-2 affinity.



Scheme 17: keto-enol tautomerism of the unsubstituted hydantoin.

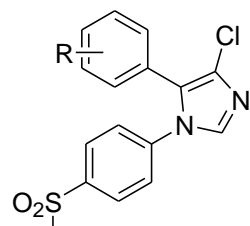
6. 1,5-DIPHENYL IMIDAZOLES

6.1 Introduction

As the hydantoin proved to be ineffective COX inhibitors, the attention was turned to 1,5-diaryl imidazoles, which proved to be potent and selective COX-2 inhibitors by Almansa and co-workers (Table 11). [205]

These compounds show the more traditional approach to COX-2 inhibitors scaffold design, as the two aromatic rings are in vicinal positions of the central heterocycle, which has been extensively used and documented in literature and therefore is more likely to successfully inhibit COX-2.

Table 11: IC_{50} values of Almansa's library of imidazoles. [205]

	R	IC_{50} (μ M)	
		COX-1	COX-2
	4-F	>10	0.014
	3-F	>10	0.065
	2-F	100	0.028
	H	>10	0.123
	4-Me	>10	0.016
	4-OMe	1.3	0.011
	4-OEt	>10	0.004
	4-OPr	>10	10
	4-OCF ₃	>10	10
	4-Pr	>10	0.100
	4-SMe	0.9	0.011

4-SEt	>10	0.053
4-SO ₂ Et	>10	>10
4-NH ₂	>10	0.187
4-AcNH	>10	>10
4-NEt ₂	>10	0.187
2,4-diF	23.8	0.007
4-OMe-2-F	0.11	0.015
4-OMe-3-F	>10	0.004
4-OMe-3-Me	>10	0.013
4-Me-3-OMe	>10	0.015
4-Cl-3-Me	4.0	0.011
4-NMe ₂ -3-Cl	1.9	0.027
4-OMe-3-Cl	>10	0.008
4-OEt-3-Cl	>10	0.007
4-OEt-3-F	>10	0.025
4-F-3-OMe	>10	0.016
4-OMe-3,5-diCl	>10	0.007
3,5-di-OEt	>10	>10
3,5-diF	>10	0.075

Their work lead to the discovery of cimicoxib, a COX-2 selective inhibitor used in veterinary medicine (Table 12).

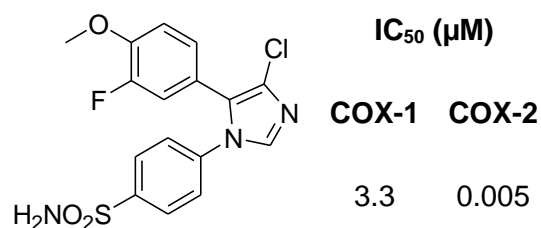


Table 12: structure and IC₅₀ values of cimicoxib. [205]

Docking studies on cimicoxib show that this inhibitor forms hydrogen bonds with COX-2 only through its sulfonamide group: the oxygen atoms bind to Phe518 and Arg513, while the NH₂ moiety interacts with Gln192 (Figure 16). [205]

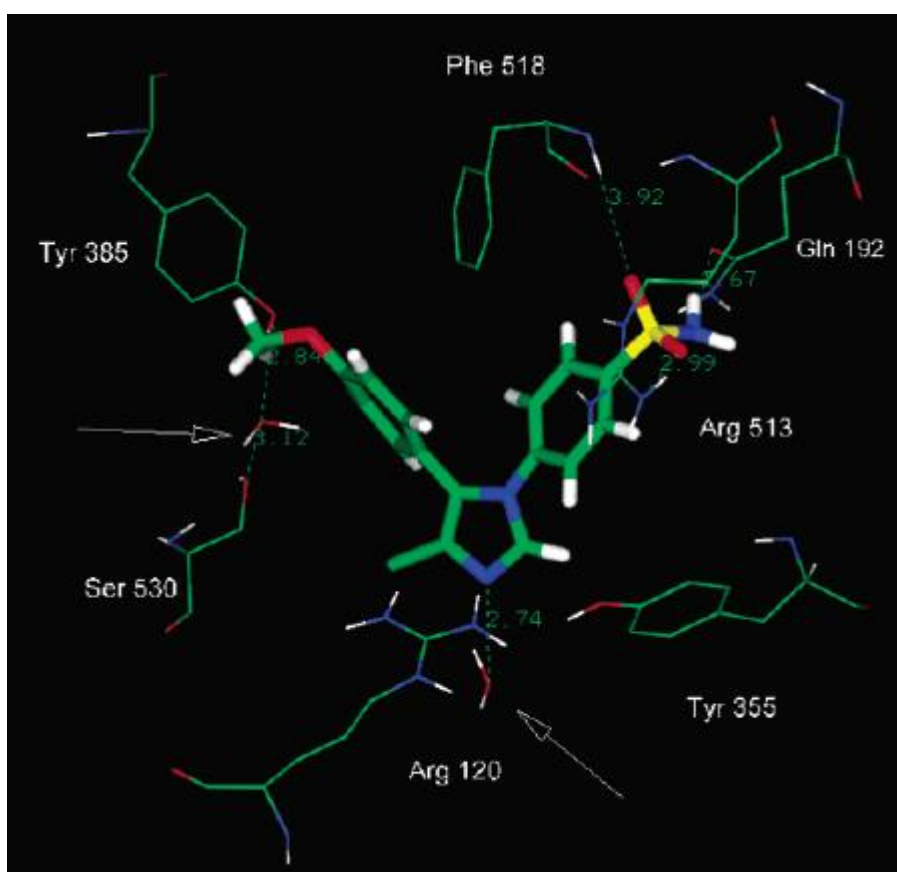


Figure 16: docking of cimicoxib to COX-2. The arrows indicate two structural water molecules hydrating the imidazole ring and bridging Tyr385 to Ser530. Cimicoxib was modeled in the active site of COX-2 from the crystal structure of murine COX-2 complex with SC558. [205]

6.2 Rationale

Based on the work published by Almansa and colleagues, which afforded high affinity and selectivity COX-2 inhibitors with intermediate lipophilicity values, a library of compounds was designed and synthesised for PET imaging rather than therapeutic purposes (Table 13).

The compounds all differ on the phenyl moiety bound to C5 of the heterocycle, as literature extensively reported how this position is the most accommodating in terms of substitutions.

Some fluorinated compounds that were part of Almansa's work were kept, such as **[19]**, in case none of the novel compounds would show biological effects.

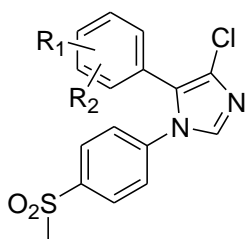
The possibility of a double fluorine substitution was also considered; as the 3,5 difluoro derivative already proved to be biologically active, a 3,4 difluoro isomer (**[22]**) was added, as the radiolabelling on C4 of the phenyl ring would be more accessible than C3.

[25] is the methylsulfone analogue of cimicoxib; as the latter has been radiolabelled with carbon-11 and has shown non-specific, non-displaceable binding, **[25]** was included; this compound has a potential of showing the same biological activity as cimicoxib, with an improvement on the pharmacokinetic properties due to the removal of the sulfonamide moiety, which is responsible for the binding to carbonic anhydrase in erythrocytes.

The tolyl moiety of celecoxib is oriented towards hydrophobic amino acids in the COX-2 active site, including Leu531, Ile345, Val349, and Met535. The same group was kept in **[27]** and **[28]**, adding though a F atom for radiolabelling purposes. On the other hand, the positions between the methyl and the F groups were inverted in **[23]** and **[24]** to explore variations in affinity and selectivity.

Table 13: library of imidazoles synthesised and their cLogP values, calculated using ACD/Chemsketch, version 14.01.

Compound	R ₁	R ₂	cLogP
[19]	4-F	H	2.43+/- 0.95
[20]	3-F	H	2.52+/- 0.92
[21]	2-F	H	3.00+/- 0.93
[22]	3-F	4-F	2.36+/- 1.00
[23]	2-Me	5-F	2.98+/- 0.92
[24]	2-Me	4-F	2.89+/- 0.95
[25]	3-F	4-OMe	2.77+/- 0.89
[26]	3-F	5-F	2.58+/- 0.97
[27]	3-F	4-Me	2.98+/- 0.92
[28]	2-F	4-Me	3.46+/- 0.93



5,5-diphenyl hydantoin resulted inactive probably due to the inadequate spatial orientation of the two aromatic rings; therefore for this library typical coxib structure was chosen, with a central heterocycle substituted with two aromatic rings in adjacent positions, as this is usually associated with high affinity and high selectivity for COX-2.

As for the hydantoin library, the methyl sulfone pharmacophore was favoured over the sulfonamide, since the latter has been shown to bind to carbonic anhydrases as well, therefore its use is not adequate for PET imaging and would increase the biological half-life to more acceptable levels for imaging purposes. [159]

Some predictions of the radiolabelled equivalents of some of these compounds can be made by drawing some comparisons with literature data of COX-2 probes with similar structures.

[¹⁸F]desbromo-DuP-697 is a diphenyl thiophene with high affinity for COX-2 (IC₅₀= 0.25 μM); due to the high lipophilicity of the tracer (logP=3.72 ± 0.16) and its biliary excretion, its biodistribution studies showed non-displaceable uptake in intestines and fat. On the

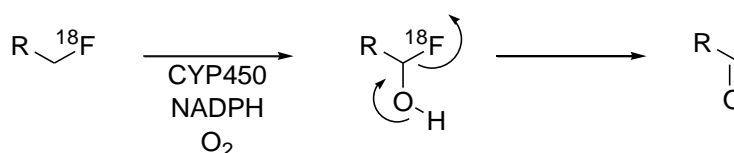
other hand, the clogP of most compounds of this library is much lower, with the exception of **[28]**, therefore they might be more appropriate for abdomen imaging than [¹⁸F]desbromo-DuP-697.

Potentially, they could be useful as brain imaging agents as well, since the optimum logP value for central nervous system targeted drugs lies between 2.0 and 3.5. This interval should assure that the imaging agent is lipophilic enough to cross the blood-brain barrier, but not too lipophilic to extensively bind to blood proteins, thereby reducing the fraction of radiotracer that is freely available in plasma to cross the barrier. [128]

The fluoromethyl analogue of celecoxib synthesised and radiolabelled by Uddin was subject to defluorination. This is often the case among tracers with a fluorine-18 isotope on an aliphatic position, such as [¹⁸F]fallypride, a D₂/D₃ antagonist, and [¹⁸F]FCWAY, a 5-HT_{1A} tracer whose *in vivo* defluorination was successfully inhibited with miconazole. [206] [207]

A proposed mechanism for the *in vivo* radiodefлуorination involves the cytochrome P450-catalysed oxygenation of the carbon atom in the α-position to the fluorine atom, as shown in Scheme 18. [208]

Since the compounds proposed all bear the fluorine atom on the aromatic position, *in vivo* defluorination should not occur, avoiding the issue of fluorine-18 accumulation in the bones.



Scheme 18: proposed mechanism of radiodefлуorination *in vivo*. [208]

While fluorine atoms in some positions were included for SAR purposes only, particularly to explore the positions on the C5 phenyl ring where the fluorine atom would be best accommodated, some of them make for a good labelling point. For instance, the labelled equivalents of **[19]** and **[21]** could be radiofluorinated starting from the nitro precursors; their synthesis would follow the same steps of the synthetic route of this library of compounds, therefore it would be fairly established and accessible. Furthermore, the starting compounds needed (4-nitrobenzaldehyde and 2-nitrobenzaldehyde, respectively) are commercially available at affordable prices.

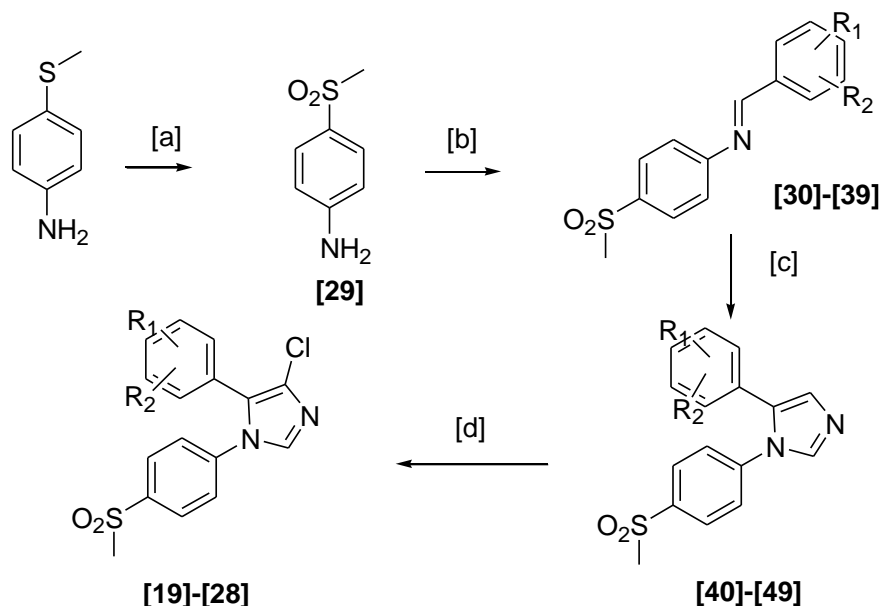
A trimethylammonium precursor could also be synthesised from these nitro-compounds, *via* reduction and complete methylation of the aniline. As stated for potential precursors of the hydantoin, the reduction reaction would have to be nitro-specific, in order to avoid reducing the methylsulfone pharmacophore.

[24] could be radiolabelled *via* the trimethylammonium precursor as well; the starting compound needed, 4-dimethylamino-2-methyl-benzaldehyde, is commercially available at a reasonable price.

[22], on the other hand, could be radiolabelled on the C4 *via* the iodonium salt, using the commercially available 3-fluoro-4-iodo-benzaldehyde as starting material; the potential of cold fluorine itself to act as a leaving group during the radiolabelling reaction should not be an issue, considering its position on the phenyl ring.

6.3 Synthesis

The synthesis was performed according to literature. The methylthio group of 4-methylthioaniline was oxidised to methylsulfone, and the product underwent condensation with the appropriate benzaldehyde to yield an aldimine. The cyclisation to imidazole followed, and the final chlorination on the C4 of the heterocycle yielded the final compounds (Scheme 19).

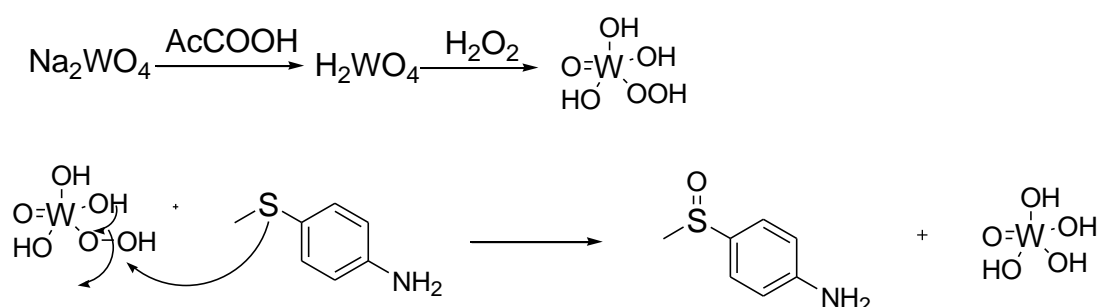


Scheme 19: synthesis of 1,5-diaryl imidazoles. [a]: Na₂WO₄, H₂O₂, acetic acid, H₂O, 65°C, 1.5 h; [b]: aldehyde, refluxing toluene, 2 days; [c]: TosMIC, K₂CO₃, refluxing MeOH and DME, 2 h; [d]: NCS, refluxing CHCl₃, 18 h

Step a

The synthesis starts with the oxidation of 4-methylthioaniline to yield the methylsulfone pharmacophore. Na_2WO_4 is the favourable oxidizing agent, as other oxidants afford higher quantities of amino-oxidation byproducts (mainly azoxy and nitroderivatives). [205]

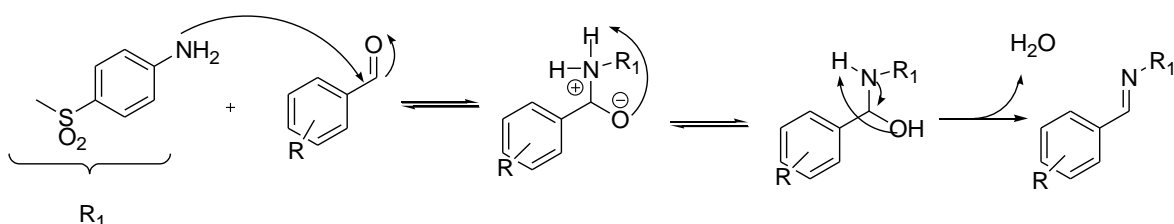
Na_2WO_4 catalyses the reaction of H_2O_2 through the formation of inorganic peracid, which undergoes heterolysis of the O-O bond with a nucleophile. Although H_2O_2 is a relatively weak electrophile, substitution of H atom by an electron withdrawing oxometal group renders the peroxidic oxygens more electrophilic. As shown in Scheme 20, this hydroxyl peracid is formed *via* a reaction involving the addition of H_2O_2 to the oxometal group. The conjugate base of the acid provides an excellent leaving group for nucleophilic displacement after the attack of the S atom of the sulfide to the terminal O atom of the peroxide group, forming a sulfoxide. In the presence of enough Na_2WO_4 , the oxidation continues to sulfone.



Scheme 20: mechanism of the oxidation of sulfide to sulfoxide by Na_2WO_4

Step b

In this step, aldimines are prepared by condensation of the primary amine to the aldehyde via nucleophilic addition, giving an hemiaminal intermediate; the elimination of water yields the final imine (Scheme 21).



Scheme 21: mechanism of aldimine synthesis via nucleophilic addition to the $\text{C}=\text{O}$ bond.

As the equilibrium of the reaction favours the starting compounds, the water produced has to be removed. The use of dried molecular sieves afforded good yields and only small traces of aldehydes remained, as seen in Figure 17.

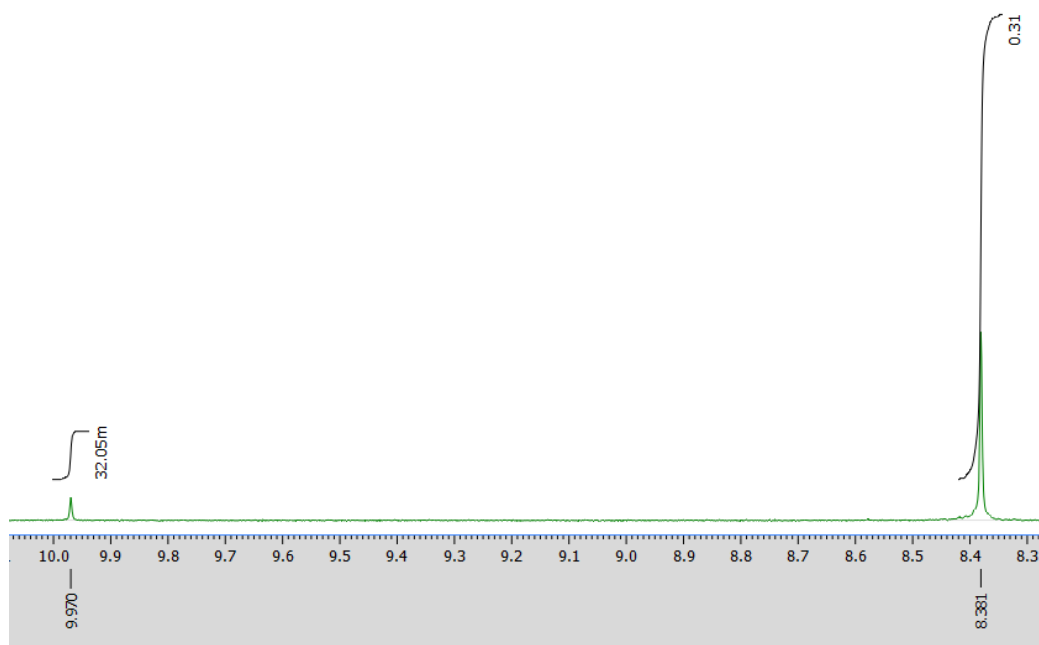


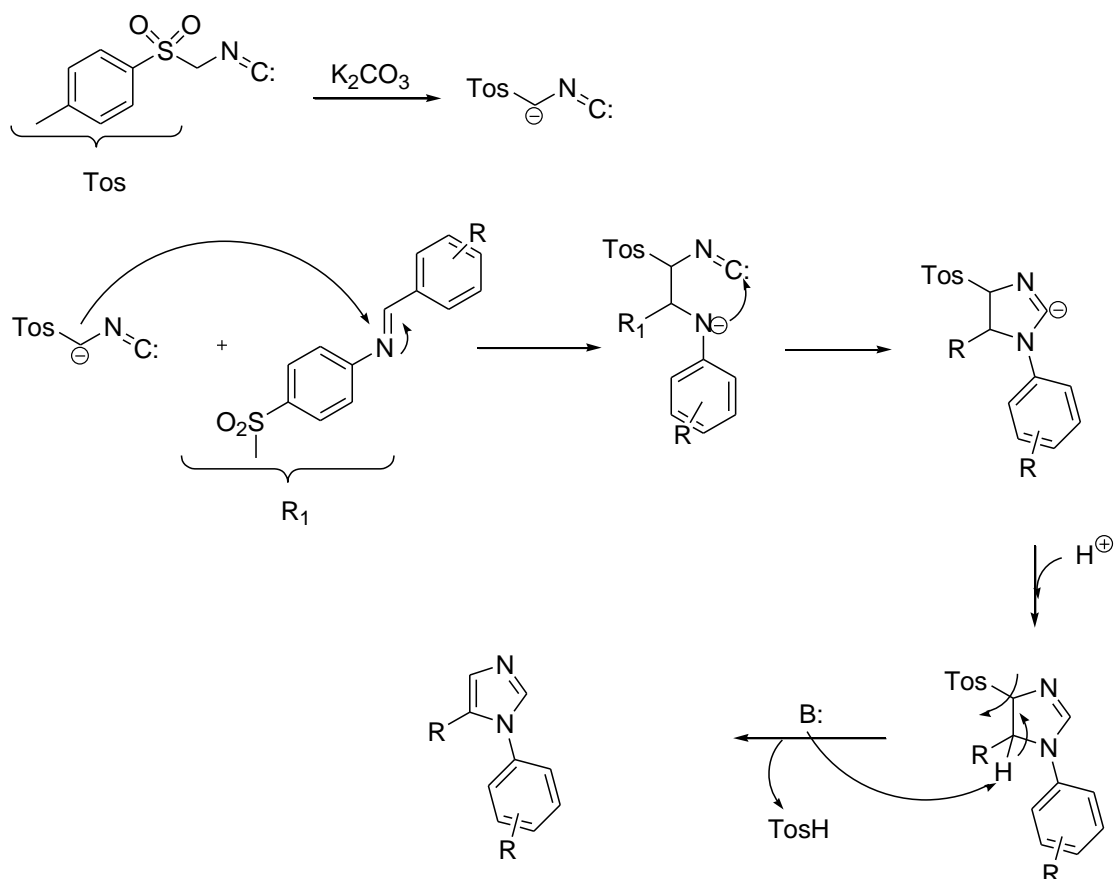
Figure 17: comparison of intensity between the aldehyde proton peak ($\delta=9.97$ ppm) and the imine peak ($\delta=8.38$ ppm) of compound [30]. The imine peak is approximately ten times more intense.

The aldimines resulted unstable in silica, as they most probably hydrolyse back to the starting materials; therefore they were used directly in the next reaction.

Step c

The following reaction was a Van Leusen cyclisation to imidazole with tosyl methyl isocyanide (TosMIC), which has a reactive isocyanide C atom, an active methylene and a good leaving group. [209]

The $\text{CH}_2\text{N}=\text{C}$ moiety can undergo a stepwise cycloaddition to a polarised double bond under basic conditions. Elimination of the *p*-toluene sulfinic acid from the imidazoline intermediate provides a 1,5-disubstituted imidazole (Scheme 22).



Scheme 22: mechanism of Van Leusen imidazole synthesis with TosMIC.

Small amounts of oxazoles produced by cyclisation of the aldehyde traces were also isolated (Figure 18).

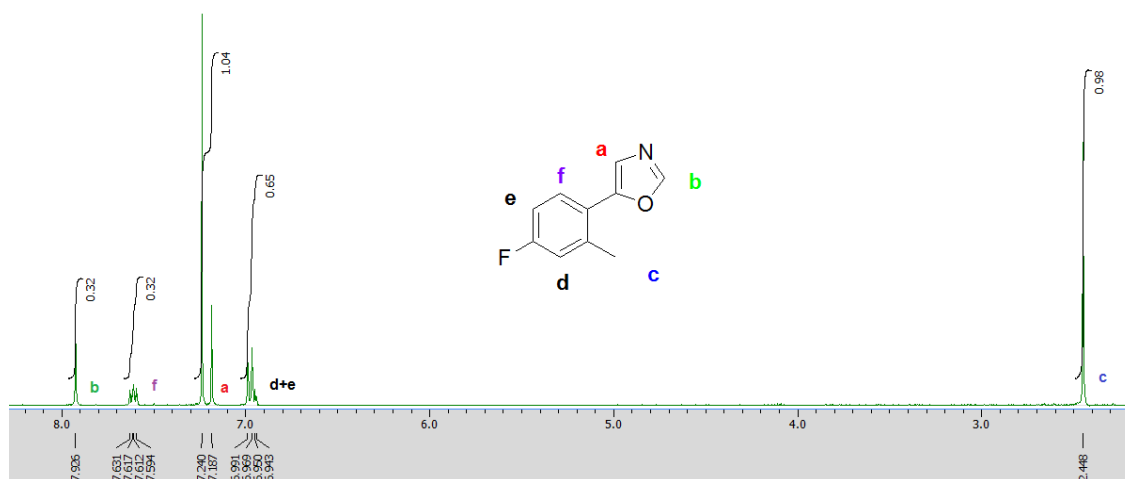
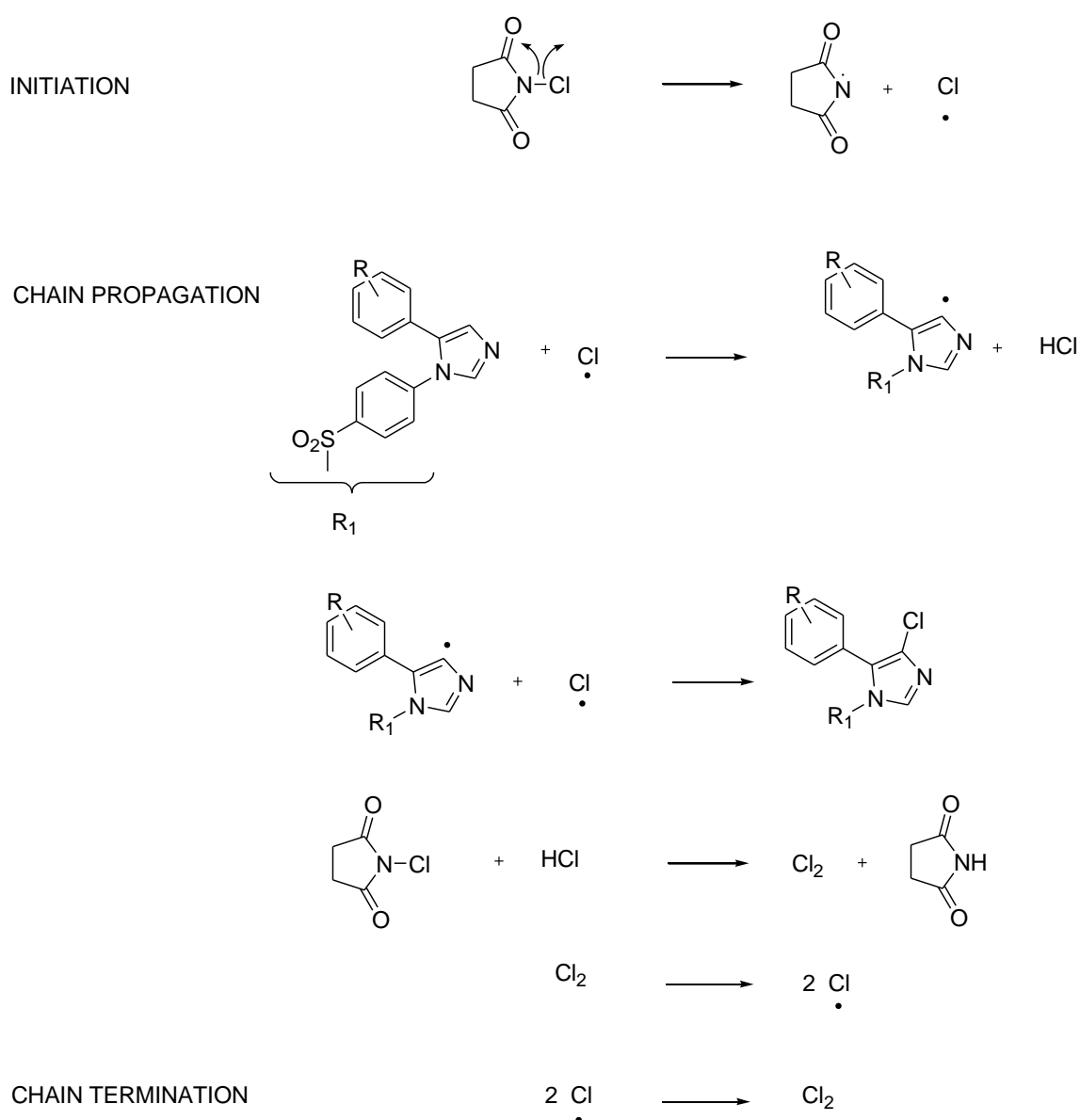


Figure 18: structure and ^1H NMR spectrum of the oxazole impurity in the synthesis of [45].

Step d

Chlorination of position 4 of the imidazole yielded the final compounds. As reported by literature, this reaction was regioselective; only small amounts of 2-chloro and dichloro derivatives were found in comparison to the main product, and identified *via* ^1H NMR spectra of the fractions of side products.

N-chlorosuccinimide (NCS) is commonly used as a source of chlorine in radical reactions, as it can undergo homolysis to yield a Cl radical which initiates the reaction. In the chain propagation step, an H atom is pulled off, leaving a radical and HCl; HCl reacts with the Cl radical to yield Cl_2 , which generates more Cl radicals. The chain reaction terminates by recombination of two free radicals (Scheme 23).



Scheme 23: mechanism of radical chlorination by NCS.

6.4 Biological evaluation

6.4.1 Colourimetric purified enzyme assays

As with the hydantoin library, these imidazoles were tested using purified COX colourimetric assays. Table 14 summarises the IC₅₀ values of this library.

Table 14: IC₅₀ values of this library of compounds (μM).

Compound	IC ₅₀	
	COX-1	COX-2
[19]	>3	1.9
[20]	>3	0.4
[21]	>3	0.5
[22]	>3	0.4
[23]	>3	>3
[24]	>3	3
[25]	>3	0.5
[26]	>3	0.7
[27]	>3	0.4
[28]	>3	1.2
Celecoxib	>3	0.1

Except for [23], all compounds showed reasonable affinity to COX-2 with no binding of COX-1, confirming the efficacy of the methyl sulfone moiety as a pharmacophore for COX-2 inhibition.

The monosubstituted derivatives were all active; surprisingly, however, the affinity trend was the opposite of the one described by Almansa's work, as these tests found the *m*-

fluoro isomer to be the most potent and the *p*-fluoro the least potent. Che and co-workers also synthesised these three molecules and tested them for PGE₂ production inhibition in LPS induced RAW 264.7 cells at a concentration of 10 μM, and found the *p*-fluoro and *o*-fluoro isomer to be to more potent, showing respectively 93% and 96% of inhibition versus 86% for the *m*-fluoro isomer. [210]

Interestingly, the double fluorine substitution was well tolerated by the COX-2 binding site, as both [22] and [26] inhibited the isozyme. The IC₅₀ value of the 3,5-difluoro derivative was in agreement with Almansa's findings; the 3,4-difluoro compound hadn't been reported, and showed higher affinity (0.4 μM versus 0.7 μM). These findings are in line with the data collected for the monosubstituted compounds, as the *m*-fluoro substitution seems to be linked to lower affinity than the *p*- and the *o*- positions.

The methyl-fluoro derivatives showed higher affinity when the methyl group was on the *p*- position, while the *o*-methyl isomers showed either lower affinity ([24]) or no affinity at all ([23]). Since, on the other hand, the *o*-fluoro substituted compounds ([21] and [28]) showed lower IC₅₀ values, it is reasonable to believe that the group on this position is close to hydrophilic amino acids in the binding pocket, which can interact through hydrogen bonds with fluorine atoms.

When the *p*-methyl group of [27] was changed with a methoxy group ([25]), the affinity remained high (IC₅₀= 0.4 versus 0.5 μM), showing that the interposed oxygen atom was well tolerated by the binding pocket. This high affinity suggests a potential use of this compound as a carbon-11 radiolabelled PET tracer, as [¹¹C]methoxy tracers are easily radiolabelled from the corresponding phenol precursors.

A comparison can be drawn with the indole-based radiotracer synthesised by Kniess and co-workers. The lower affinity of this probe (IC₅₀=1.2 μM) was considered the probable cause for its lack of uptake in a mouse HT-29 xenograft model showed no significant tumour uptake. Most 1,5-diphenyl imidazoles synthesised have higher affinities, which potentially suggest a more favourable *in vivo* profile for these compounds.

More COX-2 inhibitors with a diaryl imidazole structure can be found in literature, though with the two aromatic rings bound to two different vicinal positions.

4,5-diaryl imidazoles (Figure 19) have been explored by Salimi and co-workers; however, their sulfonamides, including the fluorinated ones, showed high affinity but low selectivity for COX-2. [211]

Considering the SAR for COX-1 selectivity reviewed by Perrone *et al.*, it is possible that the low selectivity of these compounds is due to a “hybrid” core structure containing elements for both COX-2 selectivity (the sulfonamide group) and COX-1 selectivity (the presence of a methylthio group that could be responsible for the same interactions as a thienyl moiety). [212]

The 1,2-diaryl imidazole core structure has been explored successfully by Khanna and co-workers (Figure 19). They noted that COX-2 inhibition was higher when the (methylsulfonyl) phenyl group was bound to N1 (such as the library subject of this thesis) and when their compounds included a CF₃ group on the central imidazole. This is further confirmation to Almansa’s comment regarding the need for this moiety in order to keep COX-2 affinity, as this group reduces the desolvation of the molecule upon binding; this can be accomplished as well with a Cl atom, as seen with these 1,5-diaryl imidazoles. [205] [213]

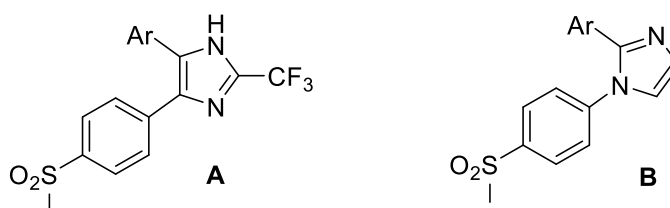


Figure 19: general structures of the 4,5-diaryl imidazoles (A) and 1,2-diaryl imidazoles (B) in literature.

6.4.2 Whole cell assays

Whole cell experiments were also planned in order to check whether these compounds would cross the membrane. RAW 264.7 are macrophages which have shown to express COX-2 when treated with stimuli such as LPS and IFN- γ , therefore this system was chosen for whole cell activity evaluation *via* the assessment of the levels of PGE₂ produced by LPS-induced COX-2. [214]

Three different ELISA kits were used for this evaluation, one purchased from Cayman Chemical (Item number 560131), one from R&D Systems (catalogue number KGE004B) and one from GE Healthcare (Bio-Sciences Corp., Piscataway, NJ, product code RPN222).

The first attempt was made with the Cayman Chemical kit. RAW 264.7 cells were grown to 40% confluence, then COX-2 expression was stimulated by adding LPS and IFN- γ ; then, cells were exposed to inhibitors at several concentrations and incubated for 30

minutes. Supernatants were collected and used to assay $\text{PGF}_{2\alpha}$ levels, generated by SnCl_2 oxidation of the COX-derived PGH_2 , according to the manufacturer's instructions.

As shown in Figure 20, this assay is based on the competition between PGs and a PG-acetylcholinesterase conjugate (PG tracer) for a limited amount of PG antiserum. Since the concentration of PG tracer is held constant, while the concentration of PG varies according to COX inhibition, the amount the PG tracer that is capable of binding to the PG antiserum is inversely proportional to the concentration of PG in the well. The rabbit antiserum-PG (either free PG or PG tracer) complex binds to a mouse monoclonal anti-rabbit antibody that has been previously attached to the plate. The plate is washed to remove unbound reagents, then Ellman's Reagent, containing acetylthiocholine and 5,5'-dithio-*bis*-(2-nitrobenzoic acid), is added; the product of this reaction, 5-thio-2-nitrobenzoic acid (Scheme 24), absorbs at 412 nm and appears yellow. The intensity of the colour is determined spectrophotometrically; the absorbance is inversely proportional to the amount of free PG in the well during incubation, and directly proportional to the concentration of the bound PG tracer.

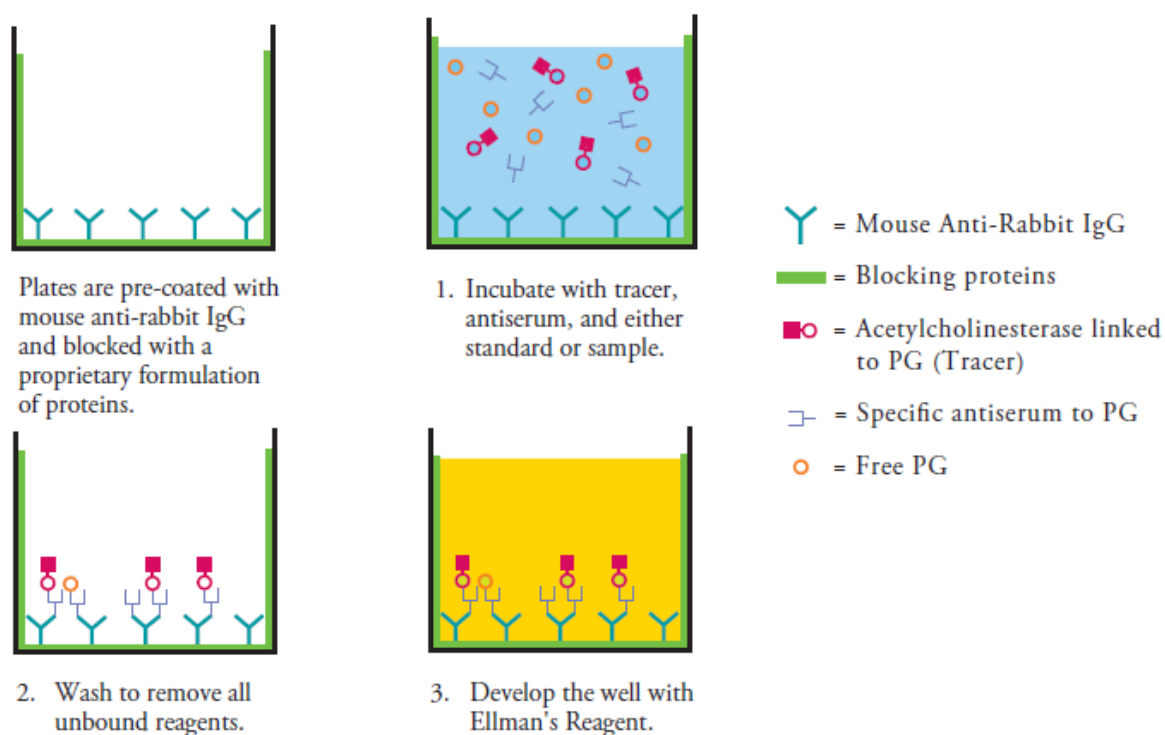
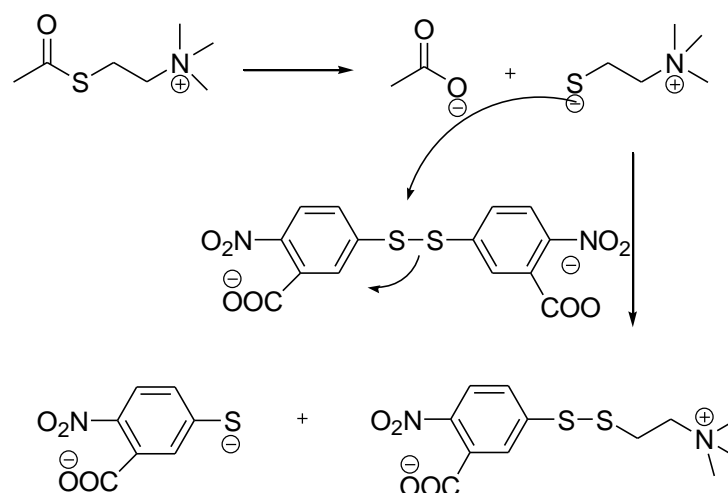


Figure 20: schematic representation of the ELISA. [215]



Scheme 24: the acetylcholinesterase reaction on Ellman's reagent.

This assay is also performed on 96 well plates, with data assayed in duplicates, including blank (absorbance caused by Ellman's reagent), background samples (containing inactivated COX), 100% initial activity samples (containing viable COX), non-specific binding (non-immunological binding of the tracer to the well), total activity (enzymatic activity of the acetylcholinesterase linker), maximum binding (maximum amount of the tracer that the antibody can bind in absence of free PG) and PG screening standards, necessary to generate the standard curve, a plot of the % bound/maximum bound values versus concentration of the wells containing various amounts of PG.

As with the colourimetric assay, this kit is widely used in literature, because of its relatively low cost and the use of standard equipment. The disadvantages of this kit are similar to the colourimetric assay: the incubation time after adding the inhibitors needs to be optimised, as it can cause variations of the results.

The assay was performed first with **[19]** and celecoxib; however, IC_{50} curves for both inhibitors could not be achieved, as data showed incongruous results; the percentile inhibition, calculated by subtracting the inhibitor sample from the 100% activity sample, dividing by the 100% activity and multiplying by 100, resulted in negative values. Figures 20 and 21 compare the binding saturation curve of celecoxib as calculated *via* this assay, versus literature data. [216]

The negative values of the percentile inhibition are usually a sign of interference by impurities in the sample; however, the purity of these compounds was assessed *via*

HPLC prior to performing this assay, and was over 95%. Therefore, attempts with this kit were not pursued any further (Figure 21 and Appendix).

The most probable cause of this unsuccessful attempt lies in the inter-variability of COX-2 inhibition assessments, which are strongly dependent on the assay condition and whose protocol needs to be optimised for each case, especially the incubation step with inhibitors.

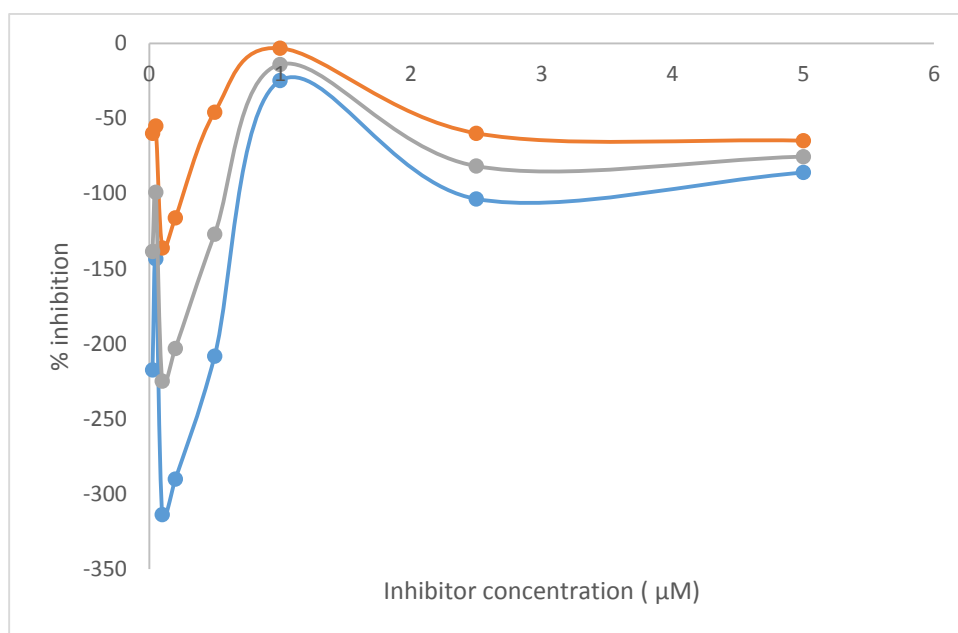


Figure 21: binding saturation curve of COX-2 inhibition by celecoxib as assessed via Cayman Chemical ELISA assay kit (% inhibition versus inhibitor concentration in μM). The grey plot is the average between the duplicates, shown in orange and blue.

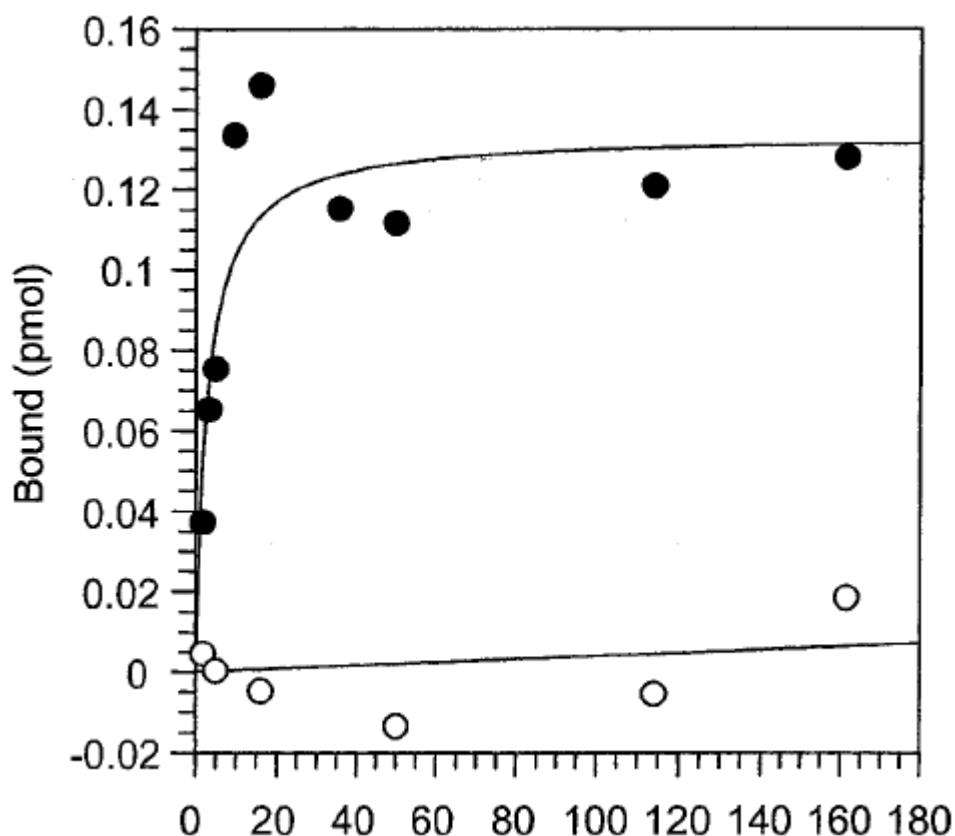


Figure 22: literature data of binding saturation curve of COX-2 inhibition by celecoxib. [216]

Given the unsuccessful results of this kit, more attempts were planned with GE Healthcare and R&D Systems ELISA kits; the principle of these ELISA kits is similar to the previous one, but COX derived PGE₂ levels are assessed instead of PGF_{2α}.

The GE Healthcare kit was chosen because of the possibility of assessing intracellular COX derived PG levels, which is able to get a tenfold increase in sensitivity over measurements on supernatant alone, as stated by the manufacturer. While levels of PGE₂ in supernatant will reflect production from before and after inhibition depending on timing, intracellular PGE₂ levels measure actual cell responsiveness and provides an accurate reflection of the action of the inhibitor on cellular processes. Measuring only secreted PGE₂ secreted in supernatants may underestimate the activities of these compounds.

RAW 264.7 cells were grown to 40% confluence, then COX-2 expression was induced by adding LPS and IFN-γ; cells were then exposed to celecoxib, [19], [20] or [21] and incubated for 30 minutes. Supernatants were then removed, cells were washed with DMEM and lysed in order to collect intracellular PGE₂.

However, the absorbance values read when this kit was performed did not correlate to PGE₂ concentrations, as they were mostly in the 0.5-0.6 range, which resulted in almost

homogeneous inhibition despite assaying concentrations between 25 nM and 5 μ M (Figure 23 and Appendix).

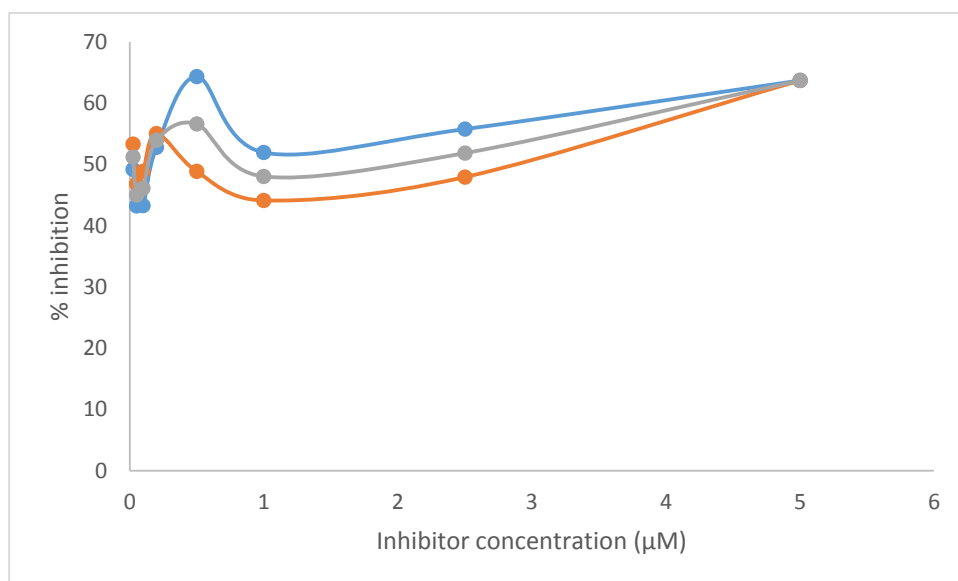


Figure 23: binding saturation curve of celecoxib as assessed via GE Healthcare ELISA assay kit. The grey plot is the average between the duplicates, shown in orange and blue.

Given the unsuccessful attempts with the previous ELISA assays, the R&D kit system was first tested using only few conditions, in order to optimise the protocol before attempting to screen the imidazoles. The conditions assayed were:

- cells whose expression of COX-2 was induced with LPS and IFN- γ . Then, activated cells were assayed in presence and absence of celecoxib;
- cells that were not treated to induce COX-2.

Each condition was assayed in duplicates. The absorbance read at the end of the assay is inversely proportional to the concentration of PGE₂ in the sample, therefore the “no induction” wells should have high absorbance, since the cells which weren’t treated with LPS and IFN- γ do not express COX-2, as well as the “celecoxib + LPS + IFN- γ ” wells, since celecoxib was added at high concentrations, therefore it would inhibit the production of PGE₂ induced by COX-2 completely; on the other hand, the “LPS + IFN- γ ” wells should show low absorbance.

Several attempts were performed. Table 15 compares the results of an assay in which these expectations were met (Assay 1), except for one “LPS + IFN- γ ” well, and one in which they were not (Assay 2). The optimistic results obtained in Assay 1 were not replicated in the following assays (Table 15 and Appendix).

Table 15: comparison of absorbance at 450 nm in two R&D Systems PGE₂ ELISA assays performed. The data below were recorded 10 minutes after adding the stop solution.

Wells	Absorbance at 450 nm	
	Assay 1	Assay 2
NSB	0.077	0.069
Well	1.4	1.207
No induction	1.54	0.18
No induction	1.273	0.123
LPS + IFN- γ	1.131	0.807
LPS + IFN- γ	0.541	0.615
celecoxib + LPS + IFN- γ	0.911	0.908
celecoxib + LPS + IFN- γ	0.921	0.957

In order to investigate these discrepancies, a further assay was run, in which three standards at known PGE₂ concentrations were tested (Table 16).

However, this attempt was inconclusive, since the lowest concentration standard (S₁) showed the lowest absorbance, while S₂ and S₃ showed similar absorbance levels, despite S₃ being almost 20 times higher than S₂.

Table 16: R&D Systems PGE₂ ELISA test performed with three standards; S₁= 39 pg/ml, S₂= 156 pg/ml, S₃= 2500 pg/ml.

Well	Absorbance at 450 nm
	Assay 4
NSB	0.077
Well	1.4
No induction	1.54
LPS + IFN-γ	1.273
celecoxib + LPS + IFN-γ	1.131
S₁	0.541
S₂	0.911
S₃	0.921

These inconsistent findings with all three ELISA kits highlight the complexity of the screening of potential COX-2 inhibitors and of the optimisation of the assays required. For whole cell experiments, along with the incubation time of the compounds, the amount of arachidonic acid added to the wells needs to be strictly controlled, as variations of this volume can greatly influence the results.

This variable could be resolved by running an assay based on the [1-¹⁴C]arachidonic acid conversion to [1-¹⁴C]PG products. This technique, used extensively by Uddin and co-workers, can be applied to both purified enzyme and whole cell assays and is a fast and more reliable way to screen COX inhibitors.

However, carbon-14 is a low-energy β emitter (average decay energy is around 50 keV and the maximum is 156 keV), and it is detected most efficiently using liquid scintillation counting.

The detectors available in the laboratories where this project was carried out are a PMT/NaI detector and a plastic scintillator-based PMT. The first one has an aluminium end window and therefore the carbon-14 β particles will be unable to penetrate through to the NaI scintillation crystal. On the other hand, the carbon-14 β particles can penetrate through the end window of the latter; however, due to the low energy, the efficiency is very low and further limited by the collimator.

Considering these limitations, these assays could not be performed and further development of a potential PET tracer was carried out based on the colourimetric assays results.

7. RADIOCHEMISTRY OF 1,5-DIPHENYL IMIDAZOLES

7.1 Introduction

All 1,5-diphenyl imidazoles synthesised have a fluorine atom bound to a phenyl ring, therefore the radiolabelling method would be an aromatic substitution.

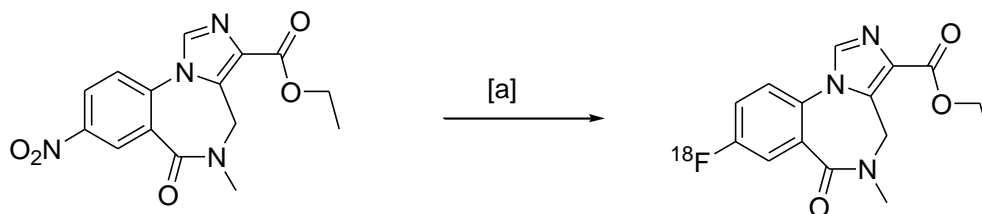
Radiolabelling via aromatic substitutions can be achieved via electrophilic and nucleophilic substitution.

As stated previously, with electrophilic substitutions high specific activities cannot be achieved; furthermore, due to high reactivity of electrophilic fluorine-18, the selectivity of electrophilic substitution is low, as radical side reactions occur.

Therefore, nucleophilic substitution is the preferred method, as it achieves the radiolabelling of fluorine-18 radiopharmaceuticals with highest specific activity.

From the SAR studies carried on the library of imidazoles synthesised, several candidates for fluorine-18 radiolabelling emerged. Excluding **[23]** and **[24]**, all of them were potent and selective COX-2 inhibitors. At first, an aromatic nucleophilic substitution of a precursor with a nitro as a leaving group was considered, as the synthesis of the nitroprecursor is accessible. In this case, the best candidates were the *o*-F and *p*-F substituted compounds (**[19]**, **[21]**, **[22]**, **[28]**); however, the starting benzaldehydes were commercially available for only two of these compounds (**[19]** and **[21]**). At the time the radiosynthesis was planned, biological evaluation was still undergoing, therefore **[19]** was eventually chosen on the basis of its higher affinity and selectivity for COX-2, as evaluated by Almansa and co-workers. Furthermore, its cLogP value (2.43+/- 0.95) and the fluorine atom in **[19]** is in an aromatic position, which makes it resistant to *in vivo* defluorination, make **[19]** a feasible choice for a potential PET tracer.

Although the imidazole in para position is slightly deactivating, previous research studies have shown that medium yields are still possible; flumazenil, for example, was radiolabelled with fluorine-18 starting from a nitro precursor, reaching a yield of 55-60% (Scheme 25).



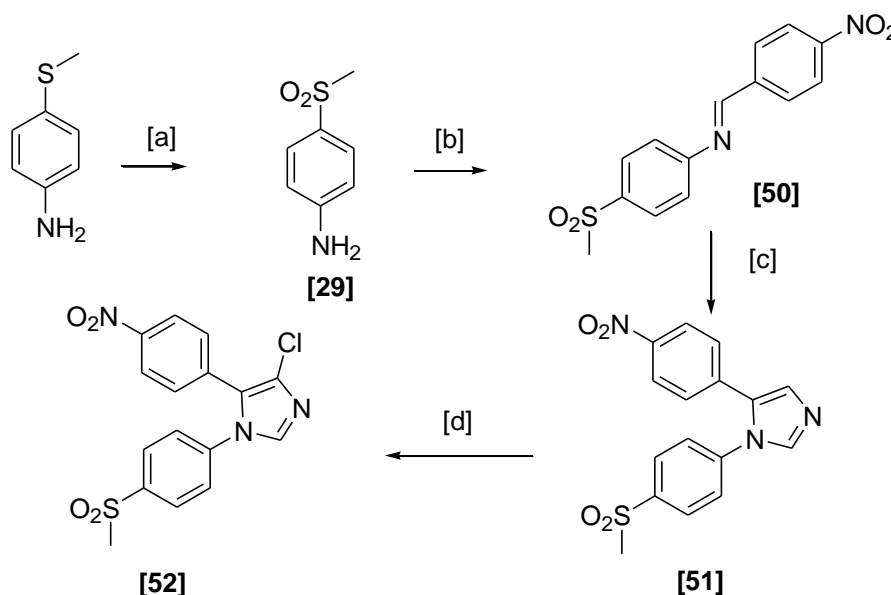
Scheme 25: fluorine-18 radiolabelling of flumazenil; [a]: $K^+K^{222}/[^{18}F]F^-$, 160°C, DMF, 30 m

7.2 Synthesis of the precursors and radiochemistry

The synthesis of a nitro precursor **[52]** for **[19]** was planned accordingly, as this route was well-established and used throughout the synthesis of the library of 1,5-diphenyl imidazoles.

The methylthio group of 4-methylthioaniline was oxidised to methylsulfoxide, and the product underwent condensation with 4-nitrobenzaldehyde to yield the corresponding aldimine. The cyclisation to imidazole followed, and the chlorination on the C4 of the heterocycle yielded the final compound (Scheme 26).

The protocol of these reactions was optimised during the development of the library of imidazoles, therefore the synthesis of **[52]** proceeded efficiently.



Scheme 26: synthesis of **[52]**. [a] Na_2WO_4 dihydrate, acetic acid, H_2O , H_2O_2 , 65°C, 1.5 h; [b]: refluxing toluene, 2 d; [c]: TosMIC, K_2CO_3 , refluxing MeOH+DME, 2 h; [d]: NCS, refluxing $CHCl_3$, 18 h

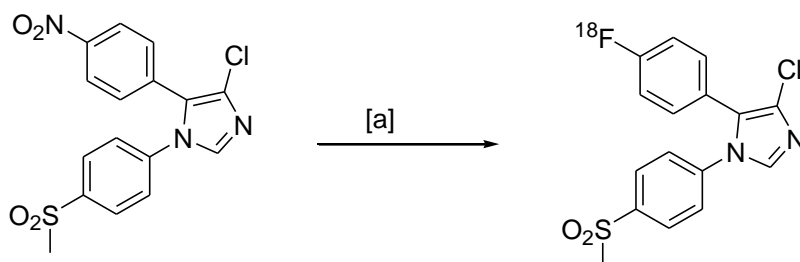
[19] and **[52]** were then analysed by HPLC to find an appropriate system that would separate them, in order to be able to monitor the radiochemical reaction. Several

conditions were attempted, but due to the similarities between the two compounds, such a system was not found. This is often the case with fluorine-18 radiolabelling of nitro precursors; notable examples are the [^{18}F]flumazenil and [^{18}F]PK14105 cases. [164] [217]

As a consequence, the possibility of monitoring *via* radioTLC was explored.

While radio-TLC does not usually have the high resolution of HPLC, it can detect all non-volatile radioactivity, and therefore it is useful in determining the spectrum of crude radioactive products from any radiosynthesis. [218] For instance, in HPLC studies of $^{99\text{m}}\text{Tc}(\text{dmpe})_2\text{Cl}_2^+$ and $^{99\text{m}}\text{Tc}$ -DisIDA, 5-10% of the sample activity was not recovered from the column due to trapping and adsorption of some radiolabelled species, with a radiocolloid being trapped at the head of the column; on the other hand, the same compound was detectable on radio-TLC with a retention factor of 0. [219]

The system eventually chosen was ACN: buffer (ammonium acetate 10 mM, pH= 4.5 corrected with acetic acid) 50:50 and normal silica plates.



Scheme 27: radiolabelling of [52]; [a]: several conditions

Table 17 lists the conditions that were tested for this radiochemical reaction in order to improve the yield of the radiochemical conversion. Each reaction was carried out by changing time, temperature and solvent, but keeping the amount of Kryptofix 2.2.2 (6 mg) and of base (2 mg) constant.

Table 17: list of conditions tested for the radiolabelling of [52]. The amount of the base and of Kryptofix 2.2.2 were kept constant (respectively, 2 mg and 6 mg).

Solvent	Volume (μl)	Time (m)	Temperature (°C)	Heating	Amount of precursor (mg)	Base	Incorporation
DMSO	250	10	130	Conventional	2 mg	K ₂ CO ₃	11.5%
DMSO	250	30	130	Conventional	2 mg	K ₂ CO ₃	5.2%
ACN	250	10	130	Conventional	2 mg	K ₂ CO ₃	3.1%

ACN	250	20	130	Conventional	2 mg	K ₂ CO ₃	3.6%
ACN	250	10	100	Conventional	2 mg	K ₂ CO ₃	None
ACN	250	20	100	Conventional	2 mg	K ₂ CO ₃	1.7%
ACN	250	10	160	Conventional	2 mg	K ₂ CO ₃	4.5%
ACN	250	30	160	Conventional	2 mg	K ₂ CO ₃	5%
DMF	250	10	160	Conventional	2 mg	K ₂ CO ₃	7%
DMF	250	30	160	Conventional	2 mg	K ₂ CO ₃	7.3%
DMF	250	5	160	Microwave	2 mg	K ₂ CO ₃	16.8%
DMF	250	10	160	Microwave	2 mg	K ₂ CO ₃	18.8%
DMF	250	15	160	Microwave	2 mg	K ₂ CO ₃	20.3%
DMF	250	10	180	Microwave	2 mg	K ₂ CO ₃	7.4%
DMF	250	20	180	Microwave	2 mg	K ₂ CO ₃	7.6%
DMF	250	5	160	Microwave	2 mg	KHCO ₃	9.3%
DMF	250	10	160	Microwave	2 mg	KHCO ₃	10.7%
DMF	250	15	160	Microwave	2 mg	KHCO ₃	12.2%
DMF	50	5	160	Microwave	2 mg	K ₂ CO ₃	10.9%
DMF	50	15	160	Microwave	2 mg	K ₂ CO ₃	10.7%
DMF	500	5	160	Microwave	2 mg	K ₂ CO ₃	5.1%
DMF	500	10	160	Microwave	2 mg	K ₂ CO ₃	6.2%
DMF	500	15	160	Microwave	2 mg	K ₂ CO ₃	5.2%
NMF	500	5	160	Microwave	2 mg	K ₂ CO ₃	2.1%
NMF	500	10	160	Microwave	2 mg	K ₂ CO ₃	2.1%
DMF	250	5	160	Microwave	6 mg	K ₂ CO ₃	15.7%
DMF	250	10	160	Microwave	6 mg	K ₂ CO ₃	19.3%
DMF	250	15	160	Microwave	6 mg	K ₂ CO ₃	18.5%

DMSO	250	5	160	Microwave	6 mg	K ₂ CO ₃	8%
DMSO	250	10	160	Microwave	6 mg	K ₂ CO ₃	11%
DMSO	250	15	160	Microwave	6 mg	K ₂ CO ₃	14.3%

Attempts have been made to optimise the temperature (from 120 °C to 180 °C), and 160 °C was found to be the most suitable.

Among the several dry solvents used (DMF, DMSO, ACN, NMF), DMF afforded the highest yield.

A substantial improvement was obtained when switching from conventional heating to microwave heating; while conventional heating of 2 mg of **[52]** in 250 µl of DMF at 160 °C gave a 7% yield in 30 minutes, performing the reaction in a microwave reactor afforded a 16.8% yield after 5 minutes, 18.8% yield after 10 minutes and 20.3% yield in 15 minutes, as shown in Figure 24.

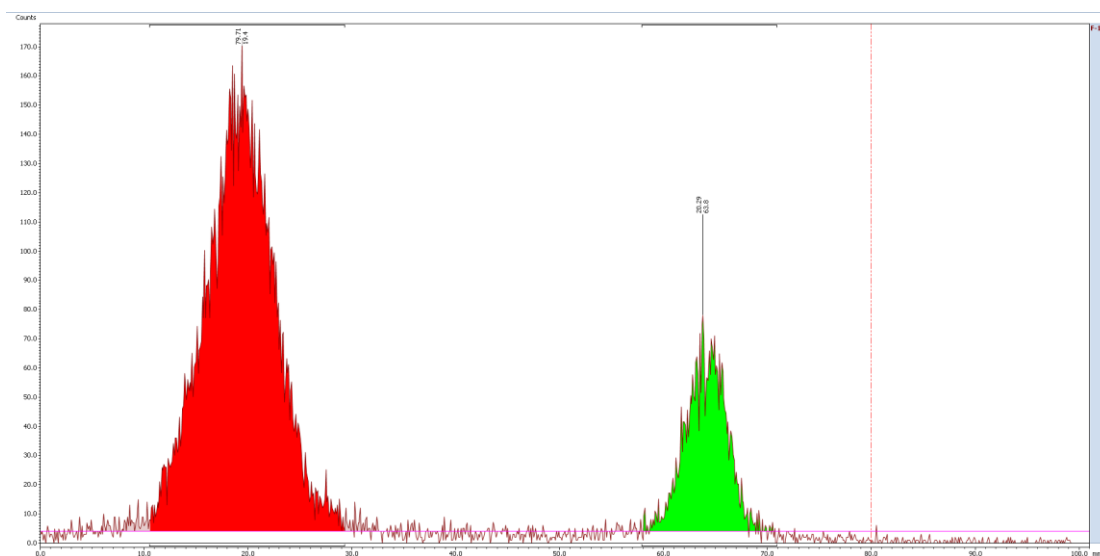


Figure 24: example of radioTLC of fluorine-18 radiolabelling of **[52]**.

The major peak was identified as fluoride-18 by spotting it on a separate TLC plate (Figure 25).

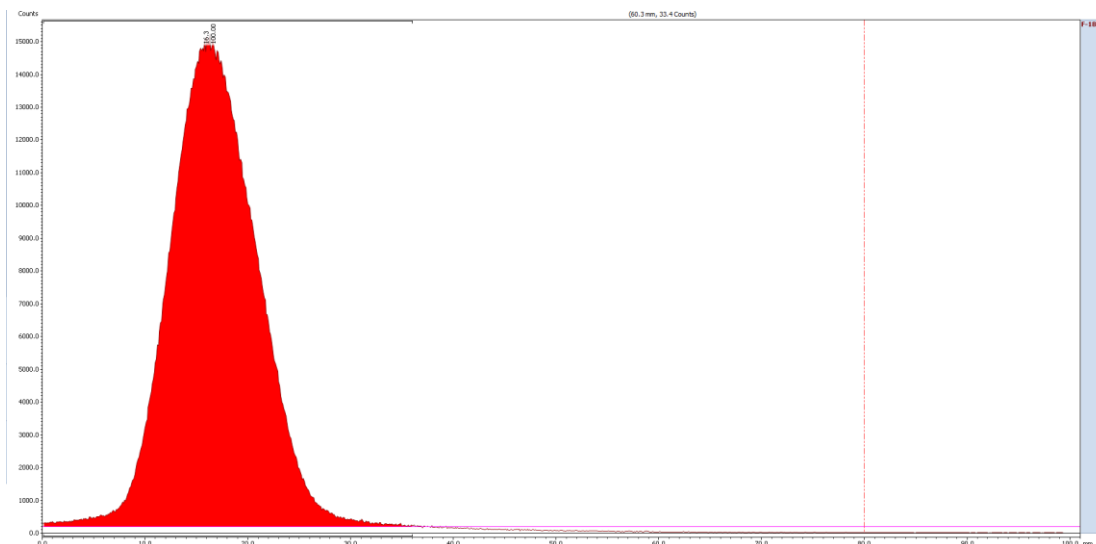


Figure 25: radioTLC of fluorine-18.

Other modifications were applied in order to further increase the radiochemical conversion.

A milder base (KHCO_3 in place of K_2CO_3) was used; however, the yields were almost halved.

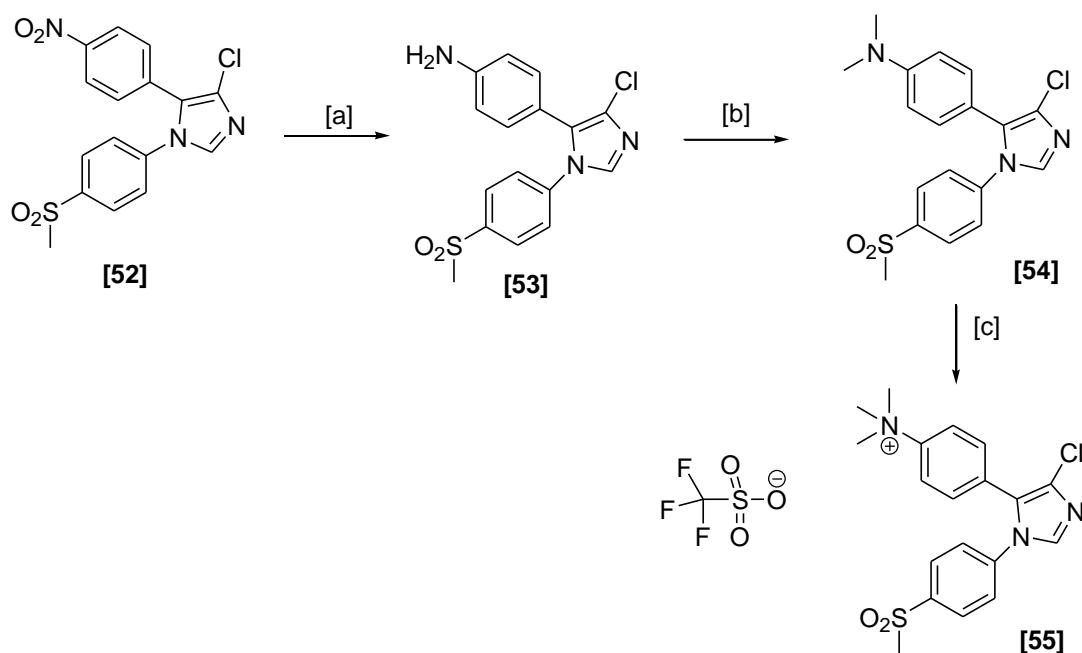
Similar results were obtained when a smaller amount of solvent was used (50 μl), keeping the amount of **[52]** constant in order to increase the concentration.

Despite the fact that a reduced volume usually seems to improve the radiochemical incorporation, the reaction was also run in a larger amount of solvent (500 μl), as an hypothesis was made that the microwaves might not be efficiently heating the solvent due to the larger size of the vessel compared with the volume of the reaction mixture. However, this attempt was unsuccessful, as the highest yield obtained was 6.2%.

Another attempt was made by triplicating the amount of precursor used, keeping the volume constant, in order to verify whether the yields were low because the amount of **[52]** was insufficient. However, the radiochemical conversion was unaffected by this modification.

As the yield was still unsatisfactory, an alternative precursor was planned, i.e. a trimethylammonium triflate derivative, as these salts have been shown to allow higher radiochemical yields at lower temperatures, which lowers the potential risk of non-radioactive byproducts formation. [220]

For this purpose, **[52]** was reduced to the aniline analogue, which was methylated with MeI first to yield the tertiary amine and with methyl triflate to yield the ammonium salt (Scheme 28).



Scheme 28: synthesis of trimethyl ammonium precursor **[55]**. [a]: iron, concd HCl, refluxing EtOH and water, 90 m; [b] MeI, refluxing EtOH, 24 h; [c] methyl triflate, DCM, RT, overnight

The first two steps of this synthesis proceeded fairly smoothly, the reduction yielding only the desired compound and the alkylation yielding only the dimethyl derivative when an excess of MeI was used. However, the last step was not always efficient, as during some attempts a byproduct was also synthesised. This impurity was not clearly identified, but it appeared to include an extra methyl group on the imidazole, as shown by proton NMR (Figure 26).

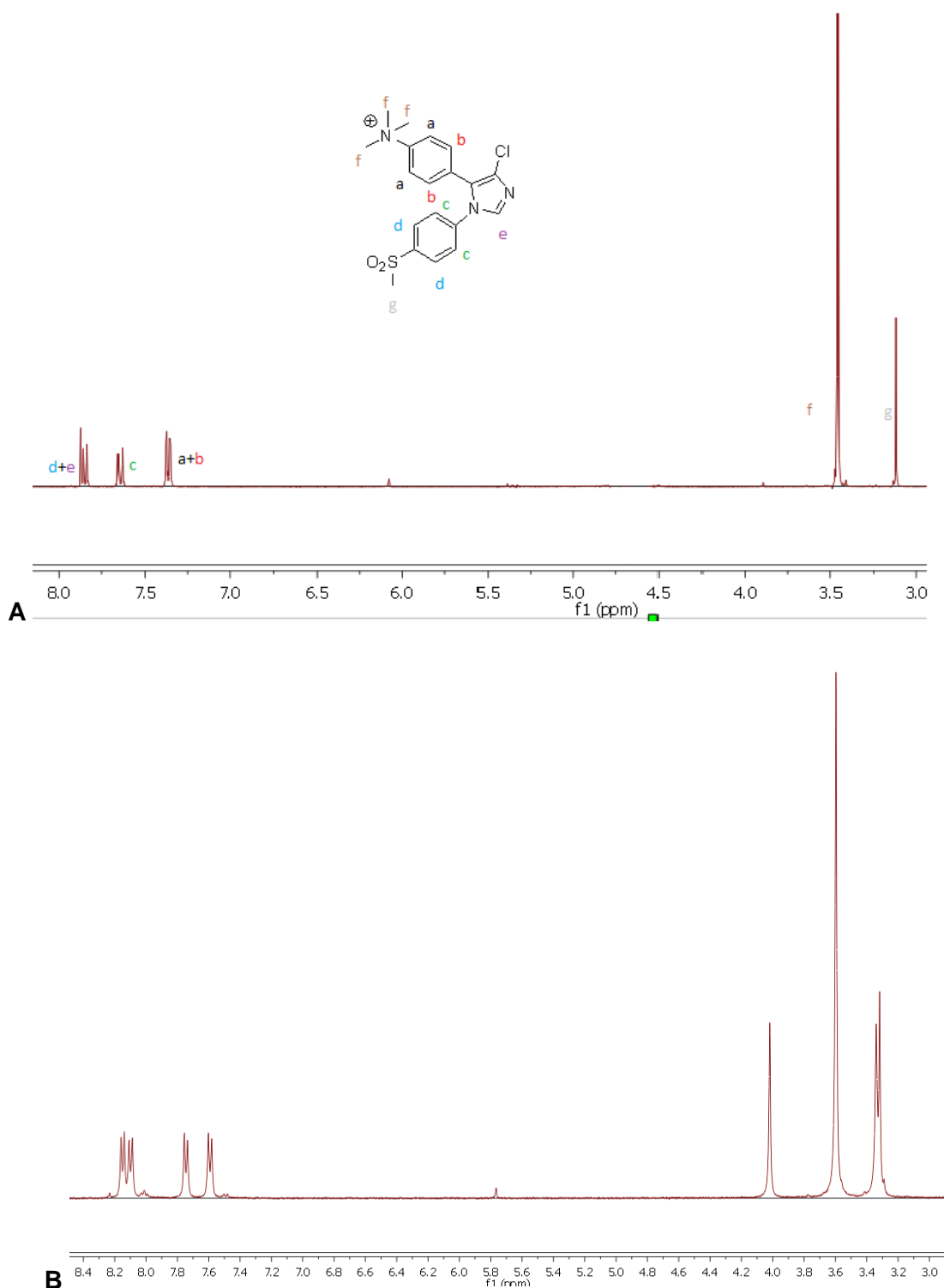
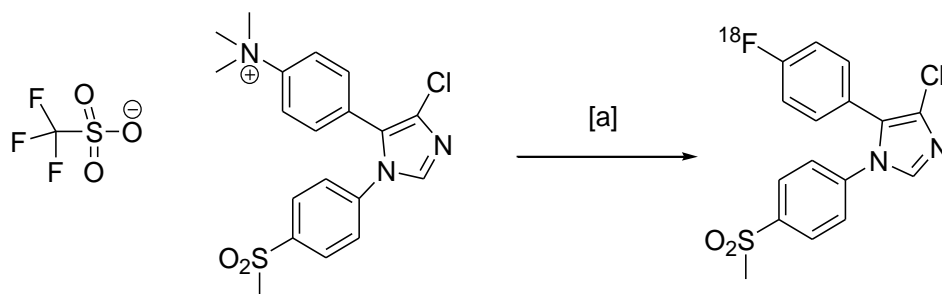


Figure 26: ^1H NMR spectra of product (A) and byproduct (B) from the synthesis of [55]. Notice how the byproduct has an extra methyl group at 4 ppm and lacks the C2 imidazole proton.

Whenever the byproduct was synthesised, purification was necessary, as this compound also had a trimethylammonium group; purification was achieved via semipreparative HPLC.

The radiolabelling of **[55]** was performed following the conditions that afforded the best yield when starting from **[52]** (Scheme 29).



Scheme 29: radiolabelling of **[55]**. [a]: DMF, K_2CO_3 , K222, 160 °C, MW

The reaction was monitored after 5, 10 and 15 minutes. The radioTLC performed after 5 minutes suggested complete radiochemical conversion, as shown in Figure 27.

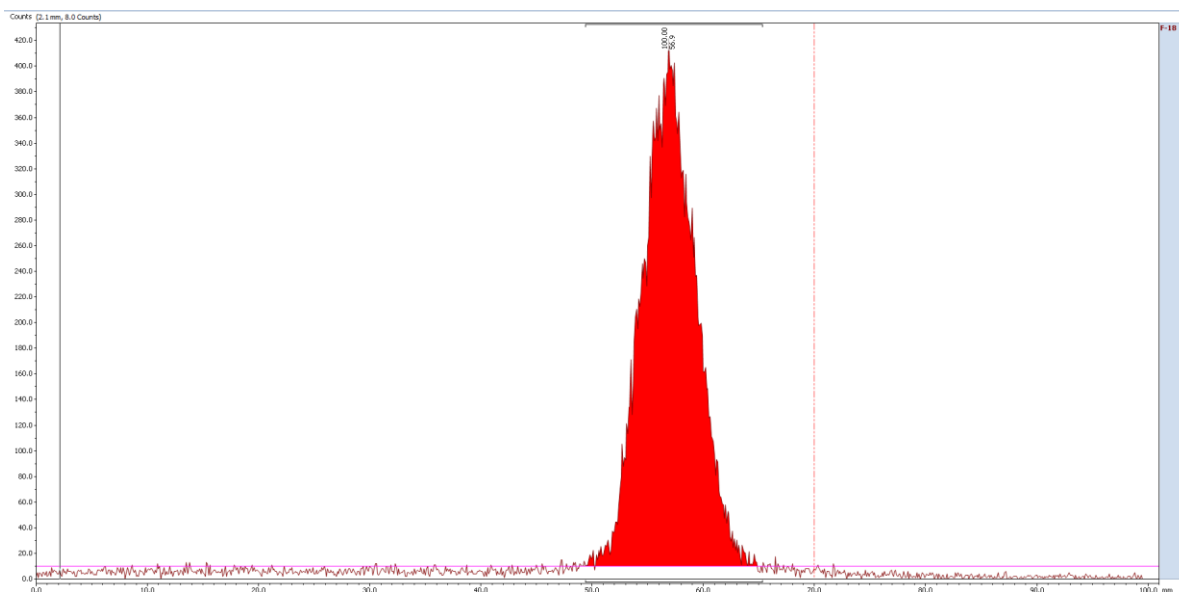


Figure 27: radioTLC of radiolabelling of **[55]** after 5 minutes

After 5 more minutes, the yield was notably reduced, suggesting that these harsh conditions are not suitable for **[55]** (Figure 28). A similar result was obtained after 5 more minutes, proving that shorter reaction times are more favourable in this case, as opposed to the nitroprecursor. The disappearance of the radiolabelled compound when longer reactions are performed could be a result of a reaction with the precursor, but this matter needs further investigation.

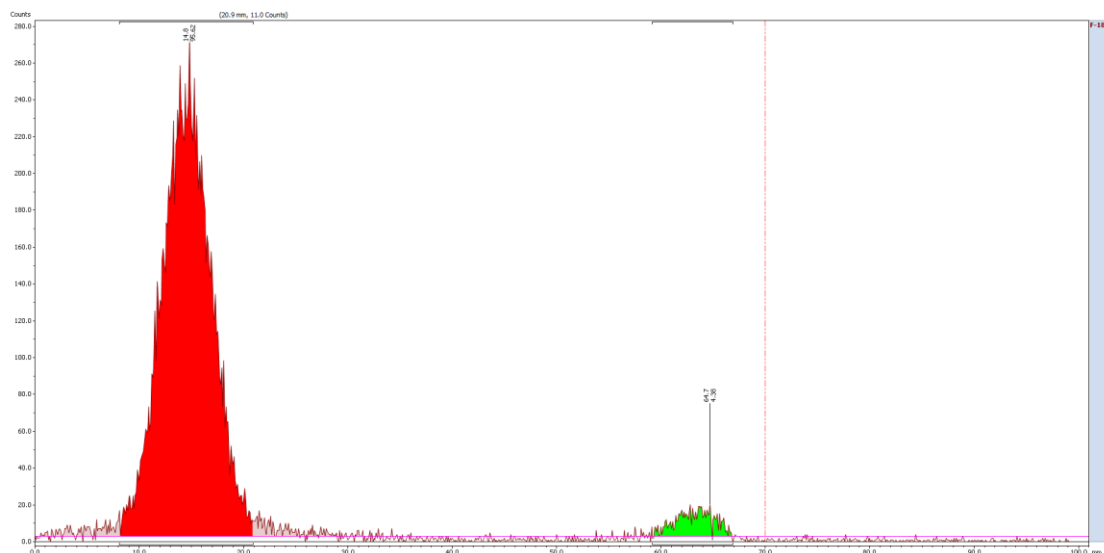


Figure 28: radioTLC of radiolabelling of [55] after 10 minutes

7.3 Further work

In conclusion, the trimethylammonium group of [55] has been shown to be a better leaving group than the nitro of [52] for radiofluorination to [^{18}F] [19], both in terms of radiochemical conversion yield and reaction time. Furthermore, the chemical differences between the final product and the starting salt would allow for an easier HPLC separation. However, its synthetic route is less accessible than [52] and needs optimisation of the last step, including the identification of the methylated impurity to understand the mechanism of the side reaction and plan the final methylation accordingly.

Diaryliodonium salts would have been precursors of interest as well, and their use had been considered, but lack of time was a major factor in the decision of not pursuing this possibility. It would also have been interesting to explore the synthesis and radiofluorination of spirocyclic iodonium ylides, as well as metal-catalysed fluorine radiochemical conversion.

The radiolabelling of [55] itself would have been optimised by testing more conditions, including shorter reaction times and milder conditions, as well as calculating the specific activity. With the radiosynthesis optimised, the project would have moved on to further assessment for the validation of [^{18}F] [19] as a PET probe. Biodistribution studies with COX-2 negative and positive tumour xenografts such as, respectively, HCT116 and HNSCC1483, would have been conducted in order to assess the COX-2 uptake of the tracer; further *in vivo* studies would have been carried by pre-injecting cold celecoxib in

a HNSCC1483 bearing mouse before [^{18}F] [19] injection to determine the specificity of the binding.

7.4 Conclusions

COX-2 is an attractive biomarker in the oncological setting, as literature shows that its expression is an early event in tumourigenesis and plays a role in tumour progression; furthermore, COX-2 expression correlates with the depth of invasion and advanced tumour stage, as positive expression of this isozyme is more common among advanced stage tumours than in early stage tumours.

Uddin's group has arguably published the most advanced research in the field of COX-2 molecular imaging, encompassing potential fluorescent, SPECT and PET probes; the most notable example of the latter is an [^{18}F]fluoromethyl analogue of celecoxib, which is slightly less potent than celecoxib *in vitro*, though its affinity should be sufficient for *in vivo* use. Furthermore, its structural similarity to celecoxib suggests that it should be safe for clinical use. However, *in vivo* defluorination and potentially slow blood clearance due to the binding of the sulfonamide moiety to carbonic anhydrase in erythrocytes, might indicate that the search for a COX-2 PET probe is still ongoing.

This research project suggested a feasible alternative, showing a high affinity and selectivity COX-2 inhibitor library with a 1,5-diphenyl imidazole core structure and a methylsulfone pharmacophore, which does not bind to carbonic anydrases, and a fluorine-18 radiolabelling point on an aromatic position, thus preventing *in vivo* defluorination.

On the other hand, the 5,5-diphenyl hydantoin core displayed no COX affinity; this lack of biological activity is probably due to an imperfect spatial orientation of the two phenyl rings, which are on germinal positions instead of the optimal vicinal positions. The optimistic results shown in literature regarding the same core structure, might be due to a compensation of this shortcoming with the extra binding point provided by the hydrogen bonds formed between hydrophilic amino acids of the active site and the unsubstituted NH. When this anchoring point is removed by alkylation, COX affinity is lost.

A comparison between Uddin's probe and the potential probe suggested by this project can be drawn, though considering that different *in vitro* assays give different results when testing COX-2 inhibitors. These two compounds are both high affinity inhibitors; Uddin's compound has an IC_{50} of 0.16 μM in a purified enzyme assay (0.08 μM in a whole cell assay), while the imidazole has an IC_{50} of 0.014 μM in a whole blood assay. Most compounds of the imidazoles library are comparable to several established COX-2

inhibitors in terms of affinity, including celecoxib, rofecoxib, valdecoxib and apricoxib, and have higher affinity than etoricoxib for COX-2.

Such high affinity is crucial for a COX-2 inhibitor, since there might be reason to doubt that COX-2 levels in malignancies is high enough to be amenable to detection with a radionuclide. However, quantitative data of COX-2 levels could not be found in literature.

The first probe showed optimistic results, therefore the imidazole has a potential of displaying similar results, with the addition of increased metabolic stability and reduced plasma protein binding.

However, the radiochemistry of this compound needs to be optimised, both in terms of yield and purification, before any attempt to further develop this potential PET tracer.

Furthermore, it is pivotal to focus on facilitating the translation from small-scale radiolabelling to clinical PET imaging through the use of automatable protocols and efficient purification methods. [181]

Notably, there has been an increasing interest towards COX-1 as an ovarian cancer biomarker. COX-1 overexpression has been found in various stages of human epithelial ovarian cancers, where it controls the biosynthesis of PGs and promotes angiogenic growth factor production. Furthermore, in an *in vivo* model obtained with ovarian surface epithelial cells allografted in female nude mice, SC-560, a highly selective COX-1 inhibitor, significantly reduces tumour growth, while celecoxib has no effect, indicating that COX-1 has a primary role for the production of PGs in murine epithelial ovarian cancers. [221]

A preliminary investigation performed by Uddin's group in collaboration with Scilimati and co-workers led to a novel fluorine-18 labelled compound which shows promising results, including high *in vitro* and *in vivo* COX-1 selectivity and *in vivo* stability. [221]

[19] could potentially be the starting core structure for a new class of COX-1 inhibitors, with the appropriate modifications, such as substitution of the methylsulfone moiety with a sulfide group, which has been shown to reverse COX isozyme selectivity.

COX-1/2 PET probes are still in their early stages of development, and they require further assessment prior to testing them in a clinical setting. Yet, they could potentially be implemented in the care of patients with a wide variety of cancers. Therefore, further research in this field is crucial for the improvement of the quality of oncology patients' treatment.

8. EXPERIMENTAL

8.1 GENERAL NOTES

Bulk solvent was removed by rotary evaporation on a Buchi R-210 equipped with a vacuum pump V-700; trace solvent was removed on a Schlenk line equipped with an oil pump.

Materials

Solvents were used as received, except when dry solvents were required. Solvents were dried over molecular sieves (10-20 mesh, 3 Å pore diameter), which were oven dried at 130 °C for 24 hours.

Chemicals were purchased from Sigma-Aldrich, Fisher Scientific, Apollo Scientific and used without any further purification.

NMR spectroscopy

¹H NMR, ¹³C NMR and ¹⁹F NMR were obtained using a Jeol JNM-LA400 spectrometer at respectively 400 MHz, 100 MHz and 376.17 MHz in the solvents indicated, referenced against standard internal TMS or CFCI₃. Chemical shifts (δ) are quoted in parts per million (ppm). Splitting patterns are designated as s (singlet), d (doublet), t (triplet), q (quartet), quin (quintet), dd (doublet of doublets), dt (doublet of triplets), m (multiplet) and br (broad).

MS

High resolution MS was performed either by Karl Heaton from the University of York using a Bruker microTOF mass spectrometer with electrospray ionisation (ESI) or by Dr Kevin Welham at the University of Hull.

Melting points

Melting points were measured using a Stuart SMP10 melting point apparatus and Jaytec melting point capillaries, 100 mm in length and 1.3-1.4 mm in diameter.

Silica based methods

Column chromatography purification was performed using Sigma Aldrich silica gel technical grade, pore size 60 Å, 70-230 mesh.

Thin layer chromatography was performed on pre-coated TLC plates silica gel 60, 0.2 mm layer, with fluorescent indicator UV₂₅₄.

Preparative thin layer chromatography was performed on pre-coated TLC plates 20x20 cm, 0.25 mm layer, with fluorescent indicator UV₂₅₄.

High performance liquid chromatography

High performance liquid chromatography (HPLC) was carried out using a Phenomenex Gemini 5u C18 110A 150x4.60 mm 5 micron at 1 ml/min, equipped with a UV detector (series G1315B). Data was recorded using Lablogix Laura (version 4.1.13.91).

Standard HPLC methods

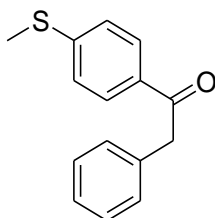
Gradient conditions:

- 80% buffer (imidazoles: 10 mM ammonium acetate pH=4.5 corrected by acetic acid; hydantoins: 2mM ammonium acetate pH=3.4 corrected by formic acid) and 20% acetonitrile from start to 14 minutes
- 10% buffer and 90% acetonitrile from 14 minutes to 19 minutes
- 50% of each solvent from 19 minutes to 30 minutes.

8.2 CHEMISTRY

8.2.1 5,5-diphenyl hydantoins

Synthesis of 1-[4-(methylsulfonyl)phenyl]-2-phenylethanone ([13]) [195]



Phenacetyl chloride (24 mmol, 4 ml, 1.25 eq) was added to a suspension of dry aluminium chloride (31.6 mmol, 4.2 g, 1.3 eq) in dry DCM (50 ml) under nitrogen atmosphere at 0 °C. This temperature was maintained for 30 minutes, then thioanisole (24 mmol, 3 ml, 1 eq) was added dropwise over 15 minutes and the mixture was stirred at 0 °C. After 2 hours, the reaction mixture was allowed to stir at room temperature overnight. The mixture was poured over 50 ml of crushed ice and extracted with DCM (20 ml × 3), dried over MgSO₄, filtered and bulk solvent removed *in vacuo*. The crude compound was recrystallised from boiling EtOH.

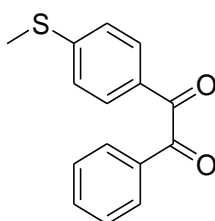
6.9 g of yellow solid. Yield: 94%

¹H NMR (400 MHz, CDCl₃) δ: 2.51 (3H, s, CH₃), 4.24 (2H, s, CH₂), 7.24-7.30 (7H, m, Ph), 7.92 (2H, d, J=8.3 Hz, Ph)

¹³C {¹H} NMR (100 MHz, CDCl₃) δ: 14.69, 45.35, 124.96, 126.84, 128.66, 129.04, 129.35, 132.79, 134.66, 146.01, 196.64

LC-MS (ESI): m/z 243.1 (M+1) (100)

Synthesis of 1-[4-(methylsulfonyl)phenyl]-2-phenylethan-1,2-dione ([14]) [195]



Selenium dioxide (142 mmol, 15.77 g, 5 eq) was added portionwise to a warm solution of [13] (28.47 mmol, 6.89 g, 1 eq) in glacial acetic acid (100 ml) over 5 minutes and the reaction mixture was refluxed for 3 hours. The reaction mixture was filtered to remove selenium and the filtrate was poured onto crushed ice and extracted with chloroform (20

ml x 3). The organic layer was dried over MgSO₄, filtered and bulk solvent removed *in vacuo*.

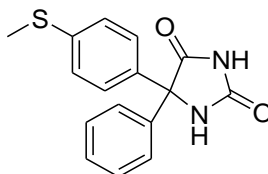
7.18 g of dark yellow solid. Yield: 98%

¹H NMR (400 MHz, CDCl₃) δ: 2.52 (3H, s, CH₃), 7.29 (2H, d, J= 8.3 Hz, Ph), 7.51 (2H, t, J=7.1 Hz, Ph), 7.64 (1H, t, J=7.1 Hz, Ph), 7.87 (2H, d, J=8.6 Hz, Ph), 7.96 (2H, d, J=7.1 Hz, Ph)

¹³C {¹H} NMR (100 MHz, CDCl₃) δ: 14.52, 124.99, 127.24, 128.59, 129.09, 129.8, 133.00, 134.79, 149.90, 193.49, 194.52

LC-MS (ESI): m/z 257.1 (M+1) (100)

Synthesis of 5-[4-[methylsulfanyl]phenyl]-5-phenylimidazoline-2,4-dione ([15]) [195]



A solution of **[14]** (28.06 mmol, 7.185 g, 1 eq) and urea (33.67 mmol, 2.02 g, 1.2 eq) in 30% aqueous NaOH (60 ml) and EtOH (240 ml) was refluxed for 3 hours. The reaction mixture was then cooled, bulk solvent was removed *in vacuo* and chilled water (50 ml) was added. The mixture was acidified with conc HCl to pH= 1, cooled in an ice bath and the precipitated product was isolated by filtration, washing with chilled water.

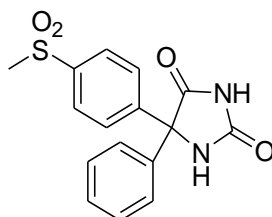
4.1 g of dark brown solid. Yield: 50%

¹H NMR (400 MHz, CDCl₃) δ: 2.47 (3H, s, CH₃), 7.20-7.34 (9H, m, Ph), 8.73 (1H, s, NH)

¹³C {¹H} NMR (100 MHz, CDCl₃) δ: 15.35, 71.42, 123.60, 126.33, 126.74, 127.21, 128.23, 134.94, 138.39, 139.85, 156.70, 173.59

LC-MS (ESI): m/z 299.1 (M+1) (100)

Synthesis of 5-[4-(methylsulfonyl)phenyl]-5-phenylimidazolidine-2,4-dione ([16]) [195]



[15] (13.76 mmol, 4.1 g, 1 eq) was dissolved in THF (50 ml) and Oxone® (68.8 mmol, 21.12 g, 5 eq) in THF/water (100 ml, 1:1) was added. The mixture was stirred at room temperature for 4 hours. After evaporation of THF, the residue was extracted with EtOAc (3x20 ml) and dried over MgSO₄, filtered and concentrated *in vacuo*. The crude compound was recrystallised in EtOAc at ambient temperature.

2.09 g of off-white solid. Yield: 46%

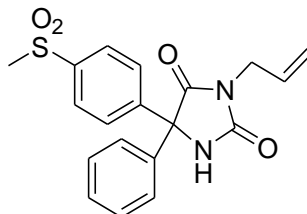
¹H NMR (400 MHz, CDCl₃) δ: 3.02 (3H, s, CH₃), 7.19-7.32 (5H, m, Ph), 7.58 (2H, d, *J*= 8.3 Hz, Ph), 7.85 (2H, d, *J*= 8.3 Hz, Ph), 8.87 (1H, s, NH)

¹³C {¹H} NMR (100 MHz, CDCl₃) δ: 44.1, 71.1, 126.1, 128.3, 128.7, 129.4, 129.6, 136.2, 139.8, 144.9, 157.0, 174.6;

General procedure for the synthesis of [1]-[12]

K₂CO₃ (1.1 eq) was suspended in DMF (2 ml) and **[16]** (1 eq) was added, followed by the halide or the mesylate (1 eq). The mixture was stirred at room temperature for three hours. The reaction mixture was added to three volumes of water and extracted once with EtOAc (10 ml). The organic layer was washed with 5% NaOH and water, dried over Na₂SO₄, filtered and concentrated *in vacuo*. The crude compound was purified *via* silica column chromatography (EtOAc: Hexane 3:2).

5-[4-(methylsulfonyl)phenyl]-5-phenyl-3-(prop-2-en-1-yl)imidazolidine-2,4-dione **([1])**
[195]



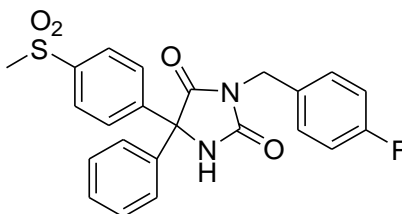
95 mg of pale yellow oil. Yield= 59%. R_t: 9:27 (95.4%)

¹H NMR (400 MHz, CDCl₃) δ: 3.03 (3H, s, CH₃), 4.16 (2H, d, *J*= 5.7 Hz, CH₂CH=CH₂), 5.21 (2H, d, *J*= 4.1 Hz, CH₂CH=CH₂), 5.81 (1H, tt, ¹*J*= 5.7 Hz, ²*J*= 4.1 Hz, CH₂CH=CH₂), 7.01 (1H, s, NH), 7.26-7.28 (2H, m, *Ph*), 7.36-7.38 (3H, m, *Ph*), 7.63 (2H, d, *J*= 8.3 Hz, *Ph*), 7.91 (2H, d, *J*= 8.3 Hz, *Ph*)

¹³C {¹H} NMR (100 MHz, CDCl₃) δ: 41.17, 44.40, 69.89, 118.49, 126.57, 127.84, 128.01, 129.12, 129.25, 130.52, 138.45, 140.72, 144.82, 156.05, 171.98

High Res GS-MS *m/z*: 393 (M⁺+Na, 7), 371 (M⁺+1, 100)

3-(4-Fluorobenzyl)-5-[4-(methylsulfonyl)phenyl]-5-phenyl-imidazolidine-2,4-dione **([2])**



87 mg of yellow oil. Yield: 47%. R_t: 11:25 (98.6%)

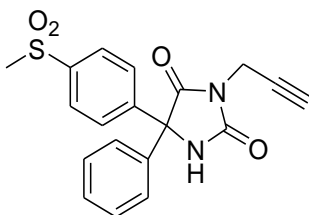
¹H NMR (400 MHz, CDCl₃) δ: 3.06 (3H, s, CH₃), 4.68 (2H, s, CH₂), 6.87 (1H, s, NH), 7.01 (2H, t, *J*= 8.5 Hz, *Ph*), 7.19-7.23 (2H, m, *Ph*), 7.36-7.38 (5H, m, *Ph*), 7.60 (2H, d, *J*= 8.3 Hz, *Ph*), 7.92 (2H, d, *J*= 8.3 Hz, *Ph*)

¹³C {¹H} NMR (100 MHz, CDCl₃) δ: 42.12, 44.37, 69.88, 115.69 (d, *J*= 22 Hz), 126.52, 127.82, 127.98, 129.15, 129.23, 130.38, 130.46, 138.31, 140.70, 144.62, 155.92, 162.49 (d, *J*= 246 Hz), 171.22

¹⁹F {¹H} NMR (376.17 MHz, CDCl₃) δ: -113.78

High Res GS-MS *m/z*: 461 (M⁺+Na, 7), 439 (M⁺+1, 100)

5-[4-(Methylsulfonyl)phenyl]-5-phenyl-3-(prop-2ynyl)imidazolidine-2,4-dione (**[3]**)



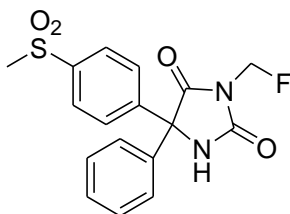
130 mg of pale yellow oil. Yield: 42%. R_t : 9:22 (95.2%)

^1H NMR (400 MHz, CDCl_3) δ : 2.26 (1H, t, $J = 2.4$ Hz, $\text{CH}_2\text{C}\equiv\text{CH}$), 3.05 (3H, s, CH_3), 4.34 (2H, d, $J = 2.4$ Hz, $\text{CH}_2\text{C}\equiv\text{CH}$), 6.13 (1H, s, NH), 7.25-7.28 (2H, m, Ph), 7.38-7.41 (3H, m, Ph), 7.63 (2H, d, $J = 8.3$ Hz, Ph), 7.94 (2H, d, $J = 8.3$ Hz, Ph)

^{13}C $\{^1\text{H}\}$ NMR (100 MHz, CDCl_3) δ : 28.29, 44.38, 70.00, 72.05, 76.35, 126.67, 127.77, 128.09, 129.12, 129.20, 138.28, 140.67, 144.64, 154.84, 162.56

High Res GS-MS m/z : 391 (M^+Na , 18), 369 (M^++1 , 100)

3-Fluoromethyl-5-[4-(methylsulfonyl)phenyl]-5-phenyl-imidazolidine-2,4-dione (**[4]**)



35 mg of white solid. Yield: 23%. Melting point: 204-206 °C. R_t : 9:48 (100%)

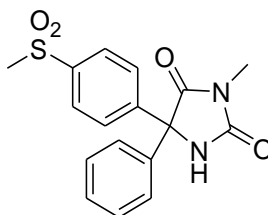
^1H NMR (400 MHz, CDCl_3) δ : 3.04 (3H, s, CH_3), 5.62 (2H, d, $J = 51$ Hz, CH_2F), 7.35-7.37 (2H, m, Ph), 7.71 (2H, d, $J = 8.3$ Hz, Ph), 7.93 (2H, d, $J = 8.3$ Hz, Ph), 7.94-7.99 (3H, m, Ph)

^{13}C $\{^1\text{H}\}$ NMR (100 MHz, CDCl_3) δ : 38.45, 76.84, 97.40 (d, $J = 40$ Hz), 128.68, 129.72, 130.10, 130.98, 131.02, 140.15, 142.60, 146.52, 155.60, 164.51

^{19}F $\{^1\text{H}\}$ NMR (376.17 MHz, CDCl_3) δ : -176.03

High Res GS-MS m/z : 385 (M^+Na , 7), 363 (M^++1 , 56), 343 (100)

3-Methyl-5-[4-(methylsulfonyl)phenyl]-5-phenyl-imidazolidine-2,4-dione ([5]) [195]



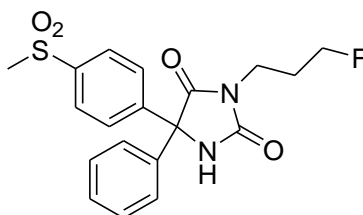
80 mg of white solid. Yield: 56%. Melting point: 216-218 °C. R_t : 8:26 (95.2%)

^1H NMR (400 MHz, CDCl_3) δ : 2.99 (3H, s, NCH_3), 3.05 (3H, s, SO_2CH_3), 6.22 (1H, s, NH), 7.20-7.22 (2H, m, *Ph*), 7.32-7.34 (3H, m, *Ph*), 7.59 (2H, d, $J = 8.3$ Hz, *Ph*), 7.88 (2H, d, $J = 8.3$ Hz, *Ph*)

^{13}C $\{^1\text{H}\}$ NMR (100 MHz, CDCl_3) δ : 25.50, 44.43, 76.68, 126.63, 127.84, 128.09, 129.21, 129.28, 131, 142.50, 147, 154.60, 161.50

High Res GS-MS m/z : 367 ($\text{M}^+\text{+Na}$, 16), 345 ($\text{M}^+\text{+1}$, 100)

3-(3-Fluoro-propyl)-5-(4-methanesulfonyl-phenyl)-5-phenyl-imidazolidine-2,4-dione ([6])



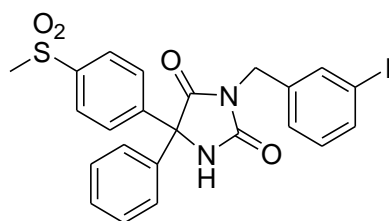
16 mg of pale yellow oil. Yield: 10%. R_t : 9:42 (95.1%)

^1H NMR (400 MHz, CDCl_3) δ : 2.06 (2H, dq, $J_1 = 21.4$ Hz, $J_2 = 5.9$ Hz, $\text{FCH}_2\text{CH}_2\text{CH}_2$), 3.04 (3H, s, SO_2CH_3), 3.76 (2H, t, $J = 5.9$ Hz, $\text{FCH}_2\text{CH}_2\text{CH}_2$), 4.46 (2H, dt, $J_1 = 45.7$ Hz, $J_2 = 5.9$ Hz, $\text{FCH}_2\text{CH}_2\text{CH}_2$), 6.55 (1H, s, NH), 7.24-7.27 (2H, m, *Ph*), 7.37-7.39 (3H, m, *Ph*), 7.63 (2H, d, $J = 8.3$ Hz, *Ph*), 7.92 (2H, d, $J = 8.3$ Hz, *Ph*)

^{13}C $\{^1\text{H}\}$ NMR (100 MHz, CDCl_3) δ : 28.77 (d, $J = 19.8$ Hz), 38.90 (d, $J = 4.6$ Hz), 44.38, 73.30, 81.55 (d, $J = 165$ Hz), 126.59, 127.81, 128.04, 129.11, 129.23, 138, 141, 144.5, 156, 172

^{19}F $\{^1\text{H}\}$ NMR (376.17 MHz, CDCl_3) δ : 149.13

High Res GS-MS m/z : 413 ($\text{M}^+\text{+Na}$, 100), 391 ($\text{M}^+\text{+1}$, 28)

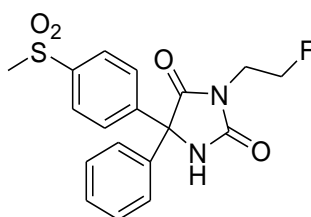
3-(3-Iodobenzyl)-5-[4-(methylsulfonyl)phenyl]-5-phenyl-imidazolidine-2,4-dione (**[7]**)

180 mg of yellow oil. Yield: 82%. R_f : 12:58 (95%)

^1H NMR (400 MHz, CDCl_3) δ : 3.05 (3H, s, CH_3), 4.66 (2H, s, CH_2), 6.61 (1H, s, NH), 7.05 (1H, t, $J=7.76$ Hz, Ph), 7.21-7.25 (2H, m, Ph), 7.28-7.39 (4H, m, Ph), 7.59-7.67 (4H, m, Ph), 7.93 (2H, d, $J=8.36$ Hz, Ph)

^{13}C $\{^1\text{H}\}$ NMR (100 MHz, CDCl_3) δ : 41.96, 44.43, 76.68, 94.50, 126.59, 127.60, 127.92, 128.03, 129.23, 129.34, 130.51, 136.99, 137.28, 137.60, 138.20, 140.80, 144.40, 155.80, 172.20

High Res GS-MS m/z : 610 (78), 569 ($\text{M}^+\text{+Na}$, 100)

3-(2-Fluoro-ethyl)-5-(4-methanesulfonyl-phenyl)-5-phenyl-imidazolidine-2,4-dione (**[8]**)

18 mg of pale yellow oil. Yield: 7%. R_f : 7:56 (95.6%).

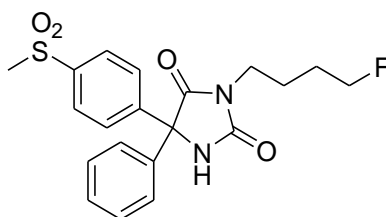
^1H NMR (400 MHz, CDCl_3) δ : 3.05 (3H, s, CH_3), 3.90 (2H, dt, $J_1=24$ Hz, $J_2=5.12$ Hz, $\text{CH}_2\text{CH}_2\text{F}$), 4.62 (2H, dt, $J_1=46.92$ Hz, $J_2=5.12$ Hz, $\text{CH}_2\text{CH}_2\text{F}$), 6.57 (1H, s, NH), 7.26-7.27 (2H, m, Ph), 7.37-7.38 (3H, m, Ph), 7.63 (2H, d, $J=8.52$ Hz, Ph), 7.92 (2H, d, $J=8.52$ Hz, Ph)

^{13}C $\{^1\text{H}\}$ NMR (100 MHz, CDCl_3) δ : 35.80 (d, $J=20$ Hz), 40.84, 66.45, 76.14 (d, $J=171$ Hz), 123.09, 124.32, 124.54, 125.68, 125.74, 134.60, 137.10, 141, 152.20, 168.90

^{19}F $\{^1\text{H}\}$ NMR (376.17 MHz, CDCl_3) δ : 176.6

High Res GS-MS m/z : 399 ($\text{M}^+\text{+Na}$, 9), 377 ($\text{M}^+\text{+1}$, 2), 209 (100)

3-(4-Fluorobutyl)-5-[4-(methylsulfonyl)phenyl]-5-phenyl-imidazolidine-2,4-dione (**[9]**)



50 mg of yellow oil. Yield: 41%. R_t : 10:09 (95%)

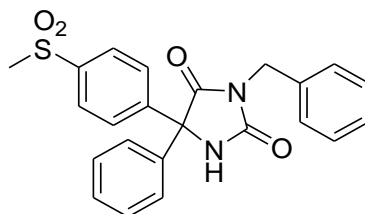
^1H NMR (400 MHz, CDCl_3) δ : 1.59-1.75 (4H, m, $\text{NCH}_2\text{CH}_2\text{CH}_2\text{CH}_2\text{F}$), 3.02 (3H, s, CH_3), 3.61 (2H, t, $J = 6.92$ Hz, $\text{NCH}_2\text{CH}_2\text{CH}_2\text{CH}_2\text{F}$), 4.42 (2H, dt, $^1J = 47.08$ Hz, $^2J = 5.72$ Hz, $\text{NCH}_2\text{CH}_2\text{CH}_2\text{CH}_2\text{F}$), 6.25 (1H, s, NH), 7.25-7.28 (2H, m, Ph), 7.36-7.40 (3H, m, Ph), 7.62 (2H, d, $J = 8.76$ Hz, Ph), 7.92 (2H, d, $J = 8.76$ Hz, Ph)

^{13}C $\{^1\text{H}\}$ NMR (100 MHz, CDCl_3) δ : 24.09 (d, $J = 4.58$ Hz), 27.52 (d, $J = 19.87$ Hz), 38.76, 44.39, 69.79, 83.16 (d, $J = 165.01$ Hz), 126.54, 127.85, 127.99, 129.14, 129.27, 138.45, 140.71, 144.77, 156.25, 171.20

^{19}F $\{^1\text{H}\}$ NMR (376.17 MHz, CDCl_3) δ : 183.60

High Res GS-MS m/z : 427 ($\text{M}^+ + \text{Na}$, 100)

3-Benzyl-5-(4-methanesulfonyl-phenyl)-5-phenyl-imidazolidine-2,4-dione (**[10]**)



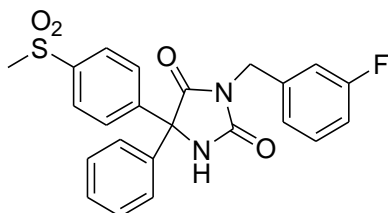
21 mg of white solid. Yield: 27%. Melting point: 208-210 °C. R_t : 11:13 (97.2%)

^1H NMR (400 MHz, CDCl_3) δ : 3.06 (3H, s, CH_3), 4.38 (2H, s, CH_2), 6.39 (1H, s, NH), 7.27-7.40 (8H, m, Ph), 7.59-7.66 (3H, m, Ph), 7.91-7.97 (3H, m, Ph)

^{13}C $\{^1\text{H}\}$ NMR (100 MHz, CDCl_3) δ : 45.47, 76.70, 116.02, 118.44, 122.85, 122.93, 129.38, 129.56, 130.09, 133.33, 139.68, 156.24, 171.50

High Res GS-MS m/z : 443 ($\text{M}^+ + \text{Na}$, 100)

3-(3-Fluoro-benzyl)-5-(4-methanesulfonyl-phenyl)-5-phenyl-imidazolidine-2,4-dione
(111)



18 mg of white solid. Yield: 14%. Melting point: 106-108 °C. R_t : 11:24 (99.2%)

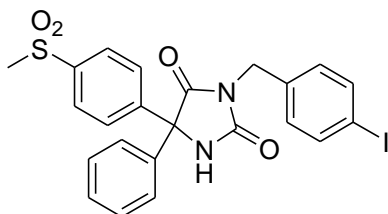
^1H NMR (400 MHz, CDCl_3) δ : 3.07 (3H, s, CH_3), 4.73 (2H, s, CH_2), 6.52 (1H, s, NH), 7.02 (1H, td, *Ph*), 7.09 (dd, 1H, *Ph*), 7.18 (d, 1H, *Ph*), 7.21-7.32 (6H, m, *Ph*), 7.39-7.41 (3H, m, *Ph*), 7.61 (2H, d, $J = 8.56$ Hz), 7.95 (2H, d, $J = 8.56$ Hz)

^{13}C $\{^1\text{H}\}$ NMR (100 MHz, CDCl_3) δ : 42.31, 44.39, 73.50, 115.70 (d, $J = 20$ Hz), 123.99, 126.55, 127.88, 128.01, 129.23, 129.30, 130.37, 138.50 (d, $J = 250$ Hz), 156.24, 171.50

^{19}F $\{^1\text{H}\}$ NMR (376.17 MHz, CDCl_3) δ : -112.06

High Res GS-MS m/z : 461 ($\text{M}^+ + \text{Na}$, 100)

3-(4-Iodo-benzyl)-5-(4-methanesulfonyl-phenyl)-5-phenyl-imidazolidine-2,4-dione **(112)**



31 mg of pale yellow oil. Yield= 20%. R_t : 12:40 (95.7%)

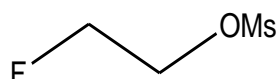
^1H NMR (400 MHz, CDCl_3) δ : 3.06 (3H, s, CH_3), 4.66 (2H, s, CH_2), 6.67 (1H, s, NH), 7.11 (2H, d, $J = 8.16$ Hz, *Ph*), 7.09 (dd, 1H, *Ph*), 7.18-7.22 (2H, m, *Ph*), 7.36-7.38 (3H, m, *Ph*), 7.59 (2H, d, $J = 8.36$ Hz *Ph*), 7.64 (2H, d, $J = 8.36$ Hz), 7.91 (2H, d, $J = 8.56$ Hz)

^{13}C $\{^1\text{H}\}$ NMR (100 MHz, CDCl_3) δ : 42.32, 44.39, 69.93, 93.80, 126.52, 127.85, 127.99, 129.19, 129.27, 130.39, 135.07, 137.91, 155.77, 172.07

High Res GS-MS m/z : 569 ($\text{M}^+ + \text{Na}$, 100)

General procedure for the synthesis of [18] and [17]

The alcohol (1 eq) was dissolved in DCM and TEA (1.1 eq) was added. MsCl (1.1 eq) in DCM was added dropwise to the cold solution of alcohol. The reaction mixture was stirred at 0-5°C for two hours. The reaction mixture was then washed with water, a saturated solution of NaHCO₃, water and brine; the organic layer was dried over MgSO₄, filtered and concentrated *in vacuo* to yield pure product.

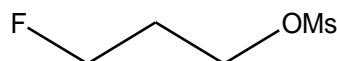
2-Fluoroethylmesylate ([18])

1.02 g of colourless liquid. Yield: 72%

¹H NMR (400 MHz, CDCl₃) δ: 3.05 (3H, s, Ms), 4.44 (2H, dt, *J*₁= 27.92 Hz, *J*₂= 4.08 Hz, FCH₂CH₂), 4.65 (2H, dt, *J*₁= 47.12 Hz, *J*₂= 4.08 Hz, FCH₂CH₂)

¹³C {¹H} NMR (100 MHz, CDCl₃) δ: 37.64, 68.23 (*J*= 19.86 Hz), 80.09 (*J*= 85.65 Hz)

¹⁹F {¹H} NMR (376.17 MHz, CDCl₃) δ: 149.11

2-Fluoropropylmesylate ([17])

1.26 g of colourless liquid. Yield: 80%

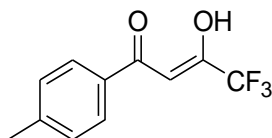
¹H NMR (400 MHz, CDCl₃) δ: 2.08 (2H, dq, *J*₁= 23.53 Hz, *J*₂= 5.68 Hz, FCH₂CH₂CH₂), 2.97 (3H, s, Ms), 4.3 (2H, t, *J*= 5.68 Hz, FCH₂CH₂CH₂), 4.51 (2H, dt, *J*₁= 39.21 Hz, *J*₂= 5.68 Hz, FCH₂CH₂CH₂)

¹³C {¹H} NMR (100 MHz, CDCl₃) δ: 26.85 (*J*= 20.60 Hz), 33.94, 62.37 (*J*= 4.60 Hz), 76.17 (*J*= 165 Hz)

¹⁹F {¹H} NMR (376.17 MHz, CDCl₃) δ: 178.85

8.2.2 Celecoxib

4,4,4-Trifluoro-3-hydroxy-1-p-tolyl-but-2-en-1-one [182]



4'-methylacetophenone (360 μ l, 2.7 mmol, 1 eq) was dissolved in dry THF (15 ml) under N_2 atmosphere and NaH (60% in mineral oil, 963 mg, 24 mmol, 1.2 eq) was added at 0°C. After stirring at this temperature for 30 minutes, ethyl trifluoroacetate (390 μ l, 3.24 mmol, 1.2 eq) was added and the reaction mixture was allowed to stir at ambient temperature for 5 hours. Afterwards, the reaction mixture was poured into ice water, acidified with HCl 2 M and extracted with EtOAc (20 ml \times 3). The combined organic layers were dried over $MgSO_4$, filtered and bulk solvent was removed *in vacuo* to yield the crude 1,3-dione, which was used in the next reaction with no further purification.

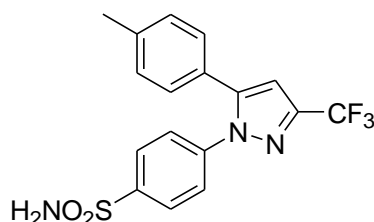
590 mg of yellow oil (crude).

1H NMR (400 MHz, $CDCl_3$) δ : 0.86 (1H, br s, OH), 2.04 (3H, s, CH_3), 7.64 (2H, d, $J= 8.4$ Hz, Ph), 7.87 (2H, d, $J= 8.4$ Hz, Ph)

^{13}C $\{^1H\}$ NMR (100 MHz, $CDCl_3$) δ : 29.69, 93.29 ($J= 2.2$ Hz), 102.06, 117.10 ($J= 280$ Hz), 128.78, 132.23, 138.39, 165.09 ($J= 35$ Hz), 185.04

^{19}F $\{^1H\}$ NMR (376.17 MHz, $CDCl_3$) δ : -76.41

4-(5-p-Tolyl-3-trifluoromethyl-pyrazol-1-yl)-benzenesulfonamide (Celecoxib) [182]



(4-sulfamoylphenyl)hydrazine hydrochloride (630 mg, 2.83 mmol, 1.1 eq) was added to a stirred solution of the crude AP1 (590 mg, 2.57 mmol, 1 eq) in EtOH (14 ml). The mixture was heated to reflux and stirred for 20 hours. The mixture was allowed to cool down, then bulk solvent was removed *in vacuo*. The residue was dissolved in EtOAc and washed with water and brine (10 ml). The organic layer was dried over $MgSO_4$, filtered and bulk solvent removed *in vacuo* to yield the crude final compound, which was purified via column chromatography (hexane:EtOAc 4:1) and recrystallised from EtOAc/hexane.

294 mg of white solid. Yield (over two steps): 30%. R_f : 13:00 (98.1%).

^1H NMR (400 MHz, CDCl_3) δ : 2.37 (3H, s, CH_3), 4.20 (2H, s, SO_2NH_2), 6.90 (1H, s, Py), 7.15-7.20 (4H, m, Ph), 7.48 (2H, d, $J = 8.8$ Hz, Ph), 7.92 (2H, d, $J = 8.8$ Hz, Ph)

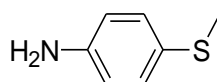
^{13}C $\{^1\text{H}\}$ NMR (100 MHz, CDCl_3) δ : 21.27, 106.89, 117.40 (q, $J = 200$ Hz), 127.04, 127.22, 128.31, 128.33, 130.09, 130.73, 141.02, 143.29, 145.12, 147.12

^{19}F $\{^1\text{H}\}$ NMR (376.17 MHz, CDCl_3) δ : -63.79

High Res GS-MS m/z : 382 ($\text{M}^+ + 1$, 100)

8.2.3 1,5-diphenyl imidazoles

Synthesis of 4-methylsulfonylaniline ([29]) [205]



A mixture of Na_2WO_4 dihydrate (0.0075 mg, 0.023 mmol), 1 drop of acetic acid and 1.9 ml of H_2O was heated to 65 °C. 4-methyl thioaniline (1.9 ml, 15.29 mmol) was added, followed by dropwise addition of H_2O_2 over 10 minutes (3.45 ml) and the mixture was stirred at 65°C for 1.5 hours. After cooling to ambient temperature, 80 ml of HCl 1 M and 50 ml of CHCl_3 were added. The layers were separated and the aqueous phase was washed with CHCl_3 (50 ml \times 3). The aqueous phase was basified to pH= 10 with 25% NaOH and washed with brine (50 ml), then dried over MgSO_4 . Bulk solvent was removed *in vacuo* to yield pure compound.

1.51 g (8.83 mmol) of yellow solid. Yield: 58%

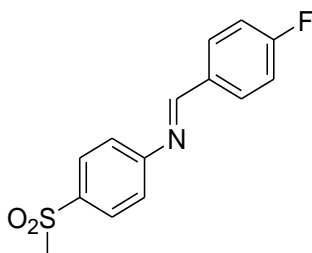
^1H NMR (400 MHz, CDCl_3) δ : 2.98 (3H, s, SO_2CH_3), 4.20 (2H, s, NH_2), 6.69 (2H, d, $J = 8.5$ Hz, Ph), 7.66 (2H, d, $J = 8.5$ Hz, Ph).

^{13}C $\{^1\text{H}\}$ NMR (100 MHz, CDCl_3) δ : 44.95, 114.06, 128.78, 129.44, 151.29

General procedure for the synthesis of [30]-[39], [50]

A mixture of [29] (1 eq) and 4-fluorobenzaldehyde (1 eq) in toluene (15 ml) was refluxed for two days in a round bottom flask which was charged with dry molecular sieves (3 Å pore diameter). Bulk solvent was removed *in vacuo* and the crude compound was used directly in the next reaction.

(4-Fluoro-benzylidene)-(4-methanesulfonyl-phenyl)-amine ([30]) [205]



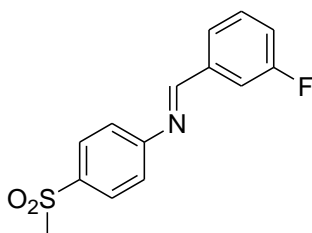
1.34 g (4.84 mmol) of white solid (crude).

^1H NMR (400 MHz, CDCl_3) δ : 3.11 (3H, s, SO_2CH_3), 7.19 (2H, t, $J = 8.3$ Hz, *Ph*), 7.28 (2H, t, $J = 8.3$ Hz, *Ph*), 7.91-7.97 (4H, m, *Ph*), 8.38 (1H, s, $\text{N}=\text{CH}$)

^{13}C $\{^1\text{H}\}$ NMR (100 MHz, CDCl_3) δ : 44.70, 116.18 (d, $J = 22.2$ Hz), 121.45, 128.78, 131.30 (d, $J = 9.2$ Hz), 131.80 (d, $J = 3$ Hz), 137.24, 156.81, 161.05, 165.17 (d, $J = 254$ Hz)

^{19}F $\{^1\text{H}\}$ NMR (376.17 MHz, CDCl_3) δ : -106.18

(3-Fluoro-benzylidene)-(4-methanesulfonyl-phenyl)-amine ([31]) [205]

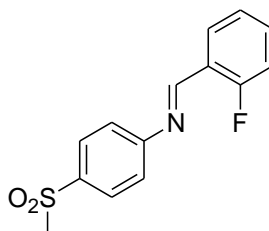


1.25 g (4.5 mmol) of light brown solid (crude).

^1H NMR (400 MHz, CDCl_3) δ : 3.11 (3H, s, SO_2CH_3), 7.19 (2H, t, $J = 8.3$ Hz, *Ph*), 7.28 (2H, t, $J = 8.3$ Hz, *Ph*), 7.91-7.97 (4H, m, *Ph*), 8.38 (1H, s, $\text{N}=\text{CH}$)

^{13}C $\{^1\text{H}\}$ NMR (100 MHz, CDCl_3) δ : 44.68, 114.96 (d, $J = 22.1$ Hz), 119.21 (d, $J = 21.4$ Hz), 121.44, 125.48 (d, $J = 3.1$ Hz), 128.81, 130.51 (d, $J = 8.4$ Hz), 137.51, 137.65 (d, $J = 8.9$ Hz), 156.21, 161.18, 162.8 (d, $J = 308$ Hz)

^{19}F $\{^1\text{H}\}$ NMR (376.17 MHz, CDCl_3) δ : -111.85

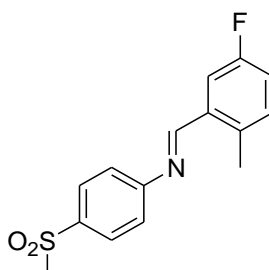
(2-Fluoro-benzylidene)-(4-methanesulfonyl-phenyl)-amine ([32]) [205]

1.26 g (4.54 mmol) of light brown solid (crude).

^1H NMR (400 MHz, CDCl_3) δ : 3.06 (3H, s, SO_2CH_3), 7.14-7.29 (4H, m, *Ph*), 7.51 (1H, s, *Ph*), 7.95 (2H, d, $J = 7.7$ Hz, *Ph*), 8.15 (1H, m, *Ph*), 8.72 (1H, s, $\text{N}=\text{CH}$)

^{13}C $\{^1\text{H}\}$ NMR (100 MHz, CDCl_3) δ : 44.70, 116.07 (d, $J = 21.4$ Hz), 116.08 (d, $J = 22.2$ Hz), 121.57, 124.66 (d, $J = 3.9$ Hz), 128.04, 128.79, 133.98 (d, $J = 8.4$ Hz), 137.50, 155.96 (d, $J = 5$ Hz), 156.92, 163.10 (d, $J = 260$ Hz)

^{19}F $\{^1\text{H}\}$ NMR (376.17 MHz, CDCl_3) δ : -120.354

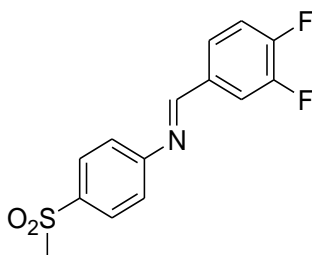
(5-Fluoro-2methyl-benzylidene)-(4-methanesulfonyl-phenyl)-amine ([33])

596 mg (2.15 mmol) of light brown solid (crude).

^1H NMR (400 MHz, CDCl_3) δ : 2.57 (3H, s, CH_3), 3.10 (3H, s, SO_2CH_3), 7.13 (1H, m, *Ph*), 7.22-7.31 (3H, m, *Ph*), 7.81 (1H, d, $J = 8.3$ Hz, *Ph*), 7.98 (2H, d, $J = 7.7$ Hz, *Ph*), 8.66 (1H, s, $\text{N}=\text{CH}$)

^{13}C $\{^1\text{H}\}$ NMR (100 MHz, CDCl_3) δ : 14.05, 44.71, 114.03 (d, $J = 26.5$ Hz), 114.08, 118.91 (d, $J = 22$ Hz), 121.47, 128.80 (d, $J = 2.3$ Hz), 129.67, 132.65 (d, $J = 10$ Hz), 133.02 (d, $J = 8$ Hz), 158.4 (d, $J = 280$ Hz), 159.9, 162.60

^{19}F $\{^1\text{H}\}$ NMR (376.17 MHz, CDCl_3) δ : -112.85

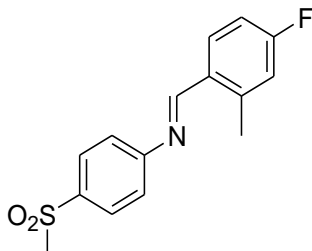
(3,4-Difluoro-benzylidene)-(4-methanesulfonyl-phenyl)-amine ([34])

1.48 g (5 mmol) of light yellow solid (crude).

^1H NMR (400 MHz, CDCl_3) δ : 3.08 (3H, s, SO_2CH_3), 7.14-7.37 (4H, m, *Ph*), 7.83 (1H, t, $J = 8.4$ Hz, *Ph*), 7.97 (2H, d, $J = 8.4$ Hz, *Ph*), 8.34 (1H, s, $\text{N}=\text{CH}$)

^{13}C $\{^1\text{H}\}$ NMR (100 MHz, CDCl_3) δ : 44.64, 116.9-118.2 (2C), 121.4, 125.2, 126.3 (2C, $J = 6.8$ Hz, $J = 3$ Hz), 128.2, 128.8, 129.0, 150.8 (dd, $J = 249$ Hz, $J = 12.9$ Hz), 152.8 (dd, $J = 254.4$ Hz, $J = 13$ Hz), 156.2, 159.9

^{19}F $\{^1\text{H}\}$ NMR (376.17 MHz, CDCl_3) δ : -130.7, -135.8

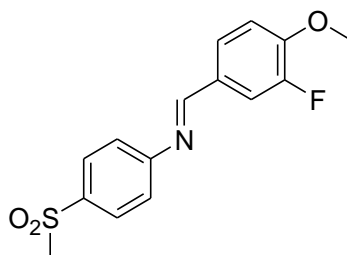
(4-Fluoro-2-methyl-benzylidene)-(4-methanesulfonyl-phenyl)-amine ([35])

660 mg (2.27 mmol) of white solid (crude).

^1H NMR (400 MHz, CDCl_3) δ : 2.35 (3H, s, CH_3), 3.08 (3H, s, SO_2CH_3), 6.97 (2H, m, *Ph*), 7.17-7.28 (2H, m, *Ph*), 7.96 (2H, d, $J = 8.8$ Hz, *Ph*), 8.08 (1H, m, *Ph*), 8.66 (1H, s, $\text{N}=\text{CH}$)

^{13}C $\{^1\text{H}\}$ NMR (100 MHz, CDCl_3) δ : 19.48, 44.72, 113.84 (d, $J = 21.4$ Hz), 117.85 (d, $J = 21.4$ Hz), 121.47, 128.79, 129.75 (d, $J = 3.5$ Hz), 130.86 (d, $J = 9.2$ Hz), 137.12, 142.07 (d, $J = 9.1$ Hz), 157.39, 159.90, 164.72 (d, $J = 251.4$ Hz)

^{19}F $\{^1\text{H}\}$ NMR (376.17 MHz, CDCl_3) δ : -116.47

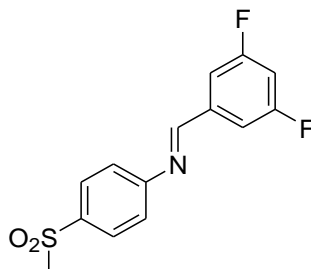
(4-Methoxy-3-fluoro-benzylidene)-(4-methanesulfonyl-phenyl)-amine ([36])

435 mg (1.41 mmol) of yellow solid (crude).

^1H NMR (400 MHz, CDCl_3) δ : 3.06 (3H, s, SO_2CH_3), 3.95 (3H, s, OCH_3), 7.01-7.03 (1H, m, *Ph*), 7.24-7.27 (1H, m, *Ph*), 7.54-7.74 (3H, m, *Ph*), 7.94 (2H, d, $J = 8.5$ Hz, *Ph*), 8.29 (1H, s, $\text{N}=\text{CH}$)

^{13}C $\{^1\text{H}\}$ NMR (100 MHz, CDCl_3) δ : 44.7, 56.2 (d, $J = 7.6$ Hz), 112.73, 115.24, 115.43, 121.49, 126.98, 128.77, 137.07, 151.1 (d, $J = 20$ Hz), 152.4 (d, $J = 250$ Hz), 156.81, 160.76

^{19}F $\{^1\text{H}\}$ NMR (376.17 MHz, CDCl_3) δ : -133.7

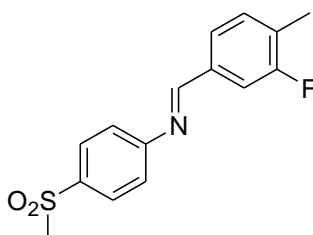
(3,5-Difluoro-benzylidene)-(4-methanesulfonyl-phenyl)-amine ([37])

397 mg (1.34 mmol) of white solid (crude).

^1H NMR (400 MHz, CDCl_3) δ : 3.07 (3H, s, SO_2CH_3), 6.95 (1H, tt, $^1J = 8.4$ Hz, $^2J = 2$ Hz, *Ph*), 7.28 (2H, dt, $^1J = 8.8$ Hz, $^2J = 2$ Hz, *Ph*), 7.43 (2H, d, $J = 8.6$ Hz, *Ph*), 7.96 (2H, d, $J = 8.6$ Hz, *Ph*), 8.33 (1H, s, $\text{N}=\text{CH}$)

^{13}C $\{^1\text{H}\}$ NMR (100 MHz, CDCl_3) δ : 44.66, 107.41 (t, $J = 25.2$ Hz), 111.74 (dd, $J = 25.9$ Hz, $J = 7.6$ Hz), 114.08, 121.42, 128.86, 129.48, 138.60 (t, $J = 8$ Hz), 155.90, 163.15 (dd, $J = 250$ Hz, $J = 20$ Hz)

^{19}F $\{^1\text{H}\}$ NMR (376.17 MHz, CDCl_3) δ : -108.2, -107.1

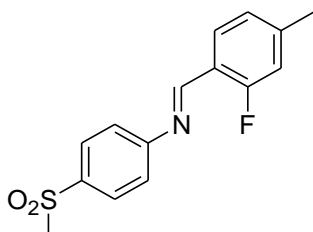
(3-Fluoro-4-methyl-benzylidene)-(4-methanesulfonyl-phenyl)-amine ([38])

612 mg (2.10 mmol) of pale yellow solid (crude)

^1H NMR (400 MHz, CDCl_3) δ : 2.34 (3H, s, CH_3), 3.06 (3H, s, SO_2CH_3), 7.24-7.37 (2H, m, *Ph*), 7.51-7.63 (3H, m, *Ph*), 7.94 (2H, d, $J = 8.5$ Hz, *Ph*), 8.33 (1H, s, $\text{N}=\text{CH}$)

^{13}C $\{^1\text{H}\}$ NMR (100 MHz, CDCl_3) δ : 14.9 (d, $J = 3.8$ Hz), 44.7, 114.5 (d, $J = 22.9$ Hz), 121.4, 127.25 (d, $J = 3.1$ Hz), 128.77, 129.8 (d, $J = 17.5$ Hz), 131.9 (d, $J = 6.4$ Hz), 135.2 (d, $J = 7.7$ Hz), 137.28, 156.7, 161.3, 161.54 (d, $J = 245.2$ Hz)

^{19}F $\{^1\text{H}\}$ NMR (376.17 MHz, CDCl_3) δ : -116.11

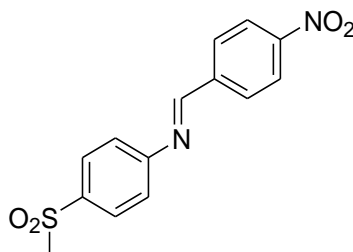
(2-Fluoro-4-methyl-benzylidene)-(4-methanesulfonyl-phenyl)-amine ([39])

180 mg (0.62 mmol) of yellow solid (crude).

^1H NMR (400 MHz, CDCl_3) δ : 2.34 (3H, s, CH_3), 3.06 (3H, s, SO_2CH_3), 6.69 (1H, dd, $^1J = 6.7$ Hz, $^2J = 2.04$ Hz, *Ph*), 7.05 (1H, d, $J = 8.0$ Hz, *Ph*), 7.25 (2H, d, $J = 8.3$ Hz, *Ph*), 7.66 (1H, m, *Ph*), 7.94 (2H, d, $J = 8.3$ Hz, *Ph*)

^{13}C $\{^1\text{H}\}$ NMR (100 MHz, CDCl_3) δ : 21.6, 44.7, 116.3 (d, $J = 20.6$ Hz), 116.5 (d, $J = 20.6$ Hz), 120.5 (d, $J = 9.0$ Hz), 121.6, 124.6, 127.6 (d, $J = 2.3$ Hz), 129.4, 145.5 (d, $J = 8.4$ Hz), 155.9, 157.1, 163.1 (d, $J = 252.9$ Hz)

^{19}F $\{^1\text{H}\}$ NMR (376.17 MHz, CDCl_3) δ : -121.25

(4-Nitro-benzylidene)-(4-methanesulfonyl-phenyl)-amine ([50])

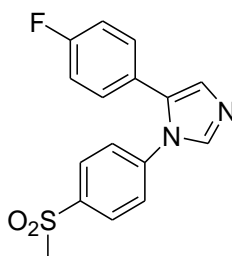
7.42 g (24.41 mmol) of impure yellow amorphous solid.

^1H NMR (400 MHz, CDCl_3) δ : 3.03 (3H, s, SO_2CH_3), 7.94 (2H, d, $J=8.4$ Hz, Ph), 8.01 (2H, d, $J=8.8$ Hz, Ph), 8.30 (2H, d, $J=8.4$ Hz, Ph), 8.33 (2H, d, $J=8.8$ Hz, Ph), 8.46 (1H, s, $\text{N}=\text{CH}$)

^{13}C $\{^1\text{H}\}$ NMR (100 MHz, CDCl_3) δ : 44.66, 121.46, 124.32, 129.87, 130.47, 138.20, 139.80, 149.70, 155.80, 159.98

General procedure for the synthesis of [40]-[49], [51]

A mixture of the proper aldimine (1 eq), tosyl methyl isocyanide (1.5 eq) and K_2CO_3 (2 eq) in MeOH/DME (2:1, 45 ml) was refluxed for 2 hours. The solvent mixture was removed and the residue was redissolved in DCM (15 ml) and washed with brine (10 ml). The organic phase was dried over MgSO_4 and bulk solvent was removed *in vacuo*. The compound was purified via column chromatography using EtOAc as eluent.

5-(4-Fluoro-phenyl)-1-(4-methanesulfonyl-phenyl)-1H-imidazole ([40]) [205]

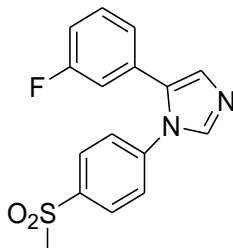
916 mg (2.9 mmol) of yellow solid. Yield (over two steps): 33%

^1H NMR (400 MHz, CDCl_3) δ : 3.11 (3H, s, SO_2CH_3), 6.99-7.02 (2H, m, Ph), 7.07-7.09 (2H, m, Ph), 7.24 (1H, d, $J=0.8$ Hz, Im), 7.34 (2H, d, $J=8.56$ Hz, Ph), 7.74 (1H, d, $J=0.8$ Hz, Im), 7.97 (2H, d, $J=8.56$ Hz)

^{13}C $\{^1\text{H}\}$ NMR (100 MHz, CDCl_3) δ : 44.41, 115.97 (d, J = 22.2 Hz), 124.75 (d, J = 3.8 Hz), 125.83, 129.06, 129.84, 130.19 (d, J = 8.4 Hz), 131.94, 138.44, 139.98, 140.86, 162.47 (d, J = 247.5 Hz)

^{19}F $\{^1\text{H}\}$ NMR (376.17 MHz, CDCl_3) δ : -112.59

5-(3-Fluoro-phenyl)-1-(4-methanesulfonyl-phenyl)-1*H*-imidazole ([41]) [205]



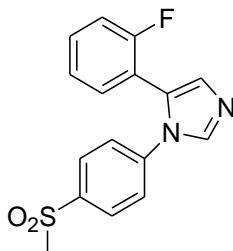
480 mg (1.52 mmol) of white solid. Yield (over two steps): 34%

^1H NMR (400 MHz, CDCl_3) δ : 3.11 (3H, s, SO_2CH_3), 6.87-6.89 (2H, m, *Ph*), 6.98-7.25 (1H, m, *Ph*), 7.26-7.31 (1H, m, *Ph*), 7.32 (1H, d, J = 1.2 Hz, *Im*), 7.39 (2H, d, J = 8.56 Hz, *Ph*), 7.76 (1H, d, J = 1.2 Hz, *Im*), 8.01 (2H, d, J = 8.56 Hz)

^{13}C $\{^1\text{H}\}$ NMR (100 MHz, CDCl_3) δ : 44.47, 115.10 (d, J = 21.4 Hz), 115.17 (d, J = 22.2 Hz), 123.99 (d, J = 3.1 Hz), 125.87, 129.16, 130.47 (d, J = 8 Hz), 130.51, 130.71 (d, J = 8 Hz), 131.80, 138.92, 140.16, 140.80, 162.65 (d, J = 250 Hz)

^{19}F $\{^1\text{H}\}$ NMR (376.17 MHz, CDCl_3) δ : -111.49

5-(2-Fluoro-phenyl)-1-(4-methanesulfonyl-phenyl)-1*H*-imidazole ([42]) [205]



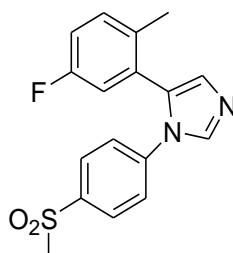
437 mg (1.38 mmol) of white solid. Yield (over two steps): 47%

^1H NMR (400 MHz, CDCl_3) δ : 3.08 (3H, s, SO_2CH_3), 6.99 (1H, t, J = 6.5 Hz, *Ph*), 7.16 (1H, t, J = 6.5 Hz, *Ph*), 7.24-7.26 (3H, m, *Ph+Im*), 7.32-7.35 (2H, m, *Ph*), 7.81 (1H, d, J = 1.2 Hz, *Im*), 7.95 (2H, d, J = 6.7 Hz)

^{13}C $\{^1\text{H}\}$ NMR (100 MHz, CDCl_3) δ : 44.46, 116.20 (d, $J = 21.4$ Hz), 116.96 (d, $J = 16$ Hz), 124.61 (d, $J = 4.5$ Hz), 124.93, 127.08, 129.00, 130.69 (d, $J = 7$ Hz), 131.14 (d, $J = 3.6$ Hz), 131.49, 138.43, 139.75, 141.33, 159.15 (d, $J = 250$ Hz)

^{19}F $\{^1\text{H}\}$ NMR (376.17 MHz, CDCl_3) δ : -112.48

5-(5-Fluoro-2-methyl-phenyl)-1-(4-methanesulfonyl-phenyl)-1*H*-imidazole ([43])



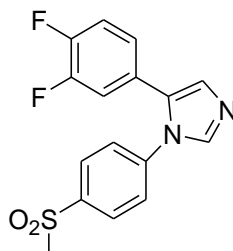
223 mg (0.67 mmol) of yellow solid. Yield (over two steps): 29%

^1H NMR (400 MHz, CDCl_3) δ : 1.95 (3H, s, CH_3), 3.07 (3H, s, SO_2CH_3), 6.91 (1H, dd, $J = 8.8$ Hz, $J = 2.8$ Hz, *Ph*), 6.99 (1H, td, $J = 8.8$ Hz, $J = 2.8$ Hz, *Ph*), 7.15 (1H, dd, $J = 8.8$ Hz, $J = 6$ Hz, *Ph*), 7.21 (1H, d, $J = 1.2$ Hz, *Im*), 7.28 (2H, d, $J = 8.8$ Hz, *Ph*), 7.84 (1H, d, $J = 1.2$ Hz, *Im*), 7.94 (2H, d, $J = 8.8$ Hz, *Ph*)

^{13}C $\{^1\text{H}\}$ NMR (100 MHz, CDCl_3) δ : 19.34, 44.44, 116.08 (d, $J = 20.6$ Hz), 117.68 (d, $J = 21.4$ Hz), 124.56, 129.09, 129.50 (d, $J = 6$ Hz), 130.87, 132.06 (d, $J = 7.7$ Hz), 133.14 (d, $J = 3.8$ Hz), 137.66, 139.64, 140.89, 160.71 (d, $J = 243.7$ Hz)

^{19}F $\{^1\text{H}\}$ NMR (376.17 MHz, CDCl_3) δ : -116.62

5-(3,4-Difluoro-phenyl)-1-(4-methanesulfonyl-phenyl)-1*H*-imidazole ([44])



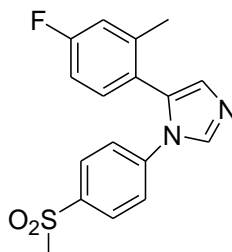
389 mg (1.16 mmol) of yellow oil. Yield (over two steps): 50%

^1H NMR (400 MHz, CDCl_3) δ : 3.11 (3H, s, SO_2CH_3), 6.79-6.83 (1H, m, *Ph*), 6.92-6.97 (1H, m, *Ph*), 7.05-7.12 (1H, m, *Ph*), 7.25 (1H, d, $J = 0.4$ Hz, *Im*), 7.35 (2H, d, $J = 8.4$ Hz, *Ph*), 7.73 (1H, d, $J = 0.4$ Hz, *Im*), 7.99 (2H, d, $J = 8.4$ Hz, *Ph*)

^{13}C $\{^1\text{H}\}$ NMR (100 MHz, CDCl_3) δ : 44.68, 107.43 (t, $J=25.2$ Hz), 111.74 (dd, $J=7.6$ Hz, $J=19.1$ Hz), 114.08, 121.43, 128.87, 129.49, 137.88, 155.88, 159.91 (t, $J=3.1$ Hz), 163.20 (dd, $J=250$ Hz, $J=10$ Hz)

^{19}F $\{^1\text{H}\}$ NMR (376.17 MHz, CDCl_3) δ : -137.13, -135.73

5-(4-Fluoro-2-methyl-phenyl)-1-(4-methanesulfonyl-phenyl)-1H-imidazole ([45])



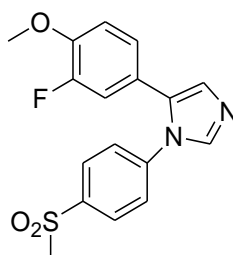
320 mg (0.97 mmol) of yellow solid. Yield (over two steps): 59%

^1H NMR (400 MHz, CDCl_3) δ : 1.96 (3H, s, CH_3), 3.00 (3H, s, SO_2CH_3), 6.08-6.94 (2H, m, *Ph*), 7.09 (1H, s, *Ph*), 7.13 (1H, d, $J=0.8$ Hz, *Im*), 7.19 (2H, d, $J=8.8$ Hz, *Ph*), 7.76 (1H, d, $J=0.8$ Hz, *Im*), 7.84 (2H, d, $J=8.8$ Hz, *Ph*)

^{13}C $\{^1\text{H}\}$ NMR (100 MHz, CDCl_3) δ : 21.03, 44.41, 113.22 (d, $J=21.4$ Hz), 117.39 (d, $J=21.4$ Hz), 124.39 (d, $J=4$ Hz), 124.63, 129.01, 130.76, 132.83 (d, $J=8.4$ Hz), 137.46, 139.55, 140.22 (d, $J=8.4$ Hz), 140.98, 162.93 (d, $J=243.7$ Hz)

^{19}F $\{^1\text{H}\}$ NMR (376.17 MHz, CDCl_3) δ : -115.45

5-(3-Fluoro-4-methoxy-phenyl)-1-(4-methanesulfonyl-phenyl)-1H-imidazole ([46])



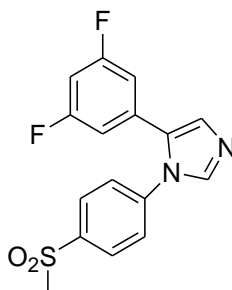
130 mg (0.37 mmol) of yellow oil. Yield (over two steps): 16%

^1H NMR (400 MHz, CDCl_3) δ : 3.11(3H, s, SO_2CH_3), 3.89 (3H, s, OCH_3), 6.80-6.91 (3H, m, *Ph*), 7.23 (1H, d, $J=1.2$ Hz, *Im*), 7.37 (2H, d, $J=8.4$ Hz, *Ph*), 7.73 (1H, d, $J=1.2$ Hz, *Im*), 8.00 (2H, d, $J=8.4$ Hz, *Ph*)

^{13}C $\{^1\text{H}\}$ NMR (100 MHz, CDCl_3) δ : 44.46, 56.19, 113.50 (d, $J= 2.3$ Hz), 116.21 (d, $J= 19.1$ Hz), 121.44 (d, $J= 6.9$ Hz), 124.55 (d, $J= 4.5$ Hz), 125.84, 129.09, 129.73, 131.70, 138.36, 139.98, 140.09, 146.63 (d, $J= 13$ Hz), 245.9 (d, $J= 152.07$ Hz)

^{19}F $\{^1\text{H}\}$ NMR (376.17 MHz, CDCl_3) δ : -133.73

5-(3,5-Difluoro-phenyl)-1-(4-methanesulfonyl-phenyl)-1*H*-imidazole ([47])



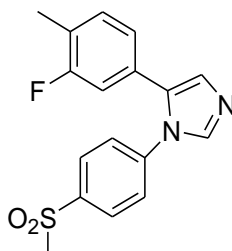
293 mg (0.88 mmol) of white solid. Yield (over two steps): 38%

^1H NMR (400 MHz, CDCl_3) δ : 3.01 (3H, s, SO_2CH_3), 6.61-6.63 (2H, m, *Ph*), 6.74 (1H, td, $J= 8.4$ Hz, $J= 2.4$ Hz, *Ph*), 7.32 (1H, d, $J=0.8$ Hz, *Im*), 7.37 (2H, d, $J= 8.4$ Hz, *Ph*), 7.74 (1H, d, $J=0.8$ Hz, *Im*), 8.02 (2H, d, $J= 8.4$ Hz, *Ph*),

^{13}C $\{^1\text{H}\}$ NMR (100 MHz, CDCl_3) δ : 44.48, 103.62 (t, $J= 25.2$ Hz), 111.06 (dd, $J= 19.2$ Hz, $J= 7.7$ Hz), 125.87, 129.33, 131.08, 131.67 (t, $J= 10$ Hz), 139.41, 140.46, 162.99 (dd, $J= 250$ Hz, $J= 14$ Hz)

^{19}F $\{^1\text{H}\}$ NMR (376.17 MHz, CDCl_3) δ : -107.88

5-(3-Fluoro-4-methyl-phenyl)-1-(4-methanesulfonyl-phenyl)-1*H*-imidazole ([48])



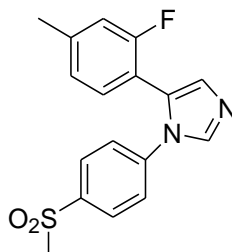
482 mg (1.45 mmol) of amorphous pale yellow solid. Yield (over two steps): 62%

^1H NMR (400 MHz, CDCl_3) δ : 2.26 (3H, s, CH_3), 3.10 (3H, s, SO_2CH_3), 6.74-6.81 (2H, m, *Ph*), 7.10 (1H, t, $J= 8$ Hz, *Ph*), 7.26 (1H, d, $J=1.2$ Hz, *Im*), 7.37 (2H, d, $J= 8.8$ Hz, *Ph*), 7.73 (1H, d, $J=1.2$ Hz, *Im*), 7.99 (2H, d, $J= 8.8$ Hz, *Ph*)

^{13}C $\{^1\text{H}\}$ NMR (100 MHz, CDCl_3) δ : 14.33, 44.39, 114.83 (d, $J = 22.9$ Hz), 123.77 (d, $J = 3.1$ Hz), 125.01 (d, $J = 16.8$ Hz), 125.83, 127.87 (d, $J = 9.2$ Hz), 129.85, 129.99, 131.88 (d, $J = 5.4$ Hz), 135.14, 137.88, 139.98, 140.87, 161.07 (d, $J = 244.5$ Hz)

^{19}F $\{^1\text{H}\}$ NMR (376.17 MHz, CDCl_3) δ : -115.88

5-(2-Fluoro-4-methyl-phenyl)-1-(4-methanesulfonyl-phenyl)-1*H*-imidazole ([49])



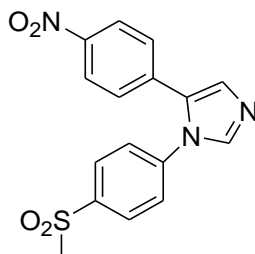
76 mg (0.23 mmol) of pale yellow solid. Yield (over two steps): 32%

^1H NMR (400 MHz, CDCl_3) δ : 2.34 (3H, s, CH_3), 3.07 (3H, s, SO_2CH_3), 6.79 (1H, d, $J = 9.6$ Hz, *Ph*), 6.94 (1H, d, $J = 8.4$ Hz, *Ph*), 7.11 (1H, t, $J = 8.4$ Hz, *Ph*), 7.27 (1H, d, $J = 1.2$ Hz, *Im*), 7.32 (2H, d, $J = 8.4$ Hz, *Ph*), 7.77 (1H, d, $J = 1.2$ Hz, *Im*), 7.93 (2H, d, $J = 8.4$ Hz, *Ph*)

^{13}C $\{^1\text{H}\}$ NMR (100 MHz, CDCl_3) δ : 30.92, 44.48, 116.70 (d, $J = 21$ Hz), 119.10 (d, $J = 25$ Hz), 123.12, 124.80, 124.94, 125.33 (d, $J = 4$ Hz), 128.95, 130.80 (d, $J = 5$ Hz), 131.21 (d, $J = 2.6$ Hz), 137.01, 138.18, 139.67, 160.8 (d, $J = 240$ Hz)

^{19}F $\{^1\text{H}\}$ NMR (376.17 MHz, CDCl_3) δ : -113.55

5-(4-Nitro-phenyl)-1-(4-methanesulfonyl-phenyl)-1*H*-imidazole ([51])



5.48 g (15.97 mmol) of yellow amorphous solid. Overall yield (over 2 steps): 40%

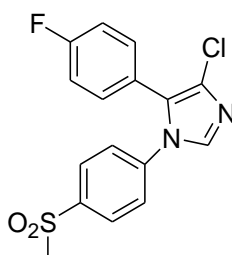
^1H NMR (400 MHz, CDCl_3) δ : 3.33 (3H, s, SO_2CH_3), 7.30 (2H, d, $J = 8.8$ Hz, *Ph*), 7.41 (2H, d, $J = 8.4$ Hz, *Ph*), 7.47 (1H, d, $J = 1.2$ Hz, *Im*), 7.83 (1H, d, $J = 1.2$ Hz, *Im*), 8.06 (2H, d, $J = 8.8$ Hz, *Ph*), 8.19 (2H, d, $J = 8.4$ Hz, *Ph*)

^{13}C $\{^1\text{H}\}$ NMR (100 MHz, CDCl_3) δ : 44.43, 124.22, 125.99, 128.34, 129.46, 130.90, 132.02, 134.99, 140.17, 140.45, 140.76, 147.50

General procedure for the synthesis of [19]-[28], [52]

A mixture of the appropriate imidazole (1 eq) and NCS (1.05 eq) in CHCl_3 (3 ml) was refluxed for 18 hours. The mixture was washed with HCl 1 M (2 ml), NaOH 1 M (2 ml), and brine (2 ml). The organic phase was dried over MgSO_4 , filtered and bulk solvent was removed *in vacuo*. The crude compound was purified *via* column chromatography using EtOAc as eluent.

4-Chloro-5-(4-Fluoro-phenyl)-1-(4-methanesulfonyl-phenyl)-1*H*-imidazole ([19]) [205]



590 mg (1.68 mmol) of yellow solid. Yield: 58%. Melting point: 163-165 °C. R_f : 10:24 (97.4%)

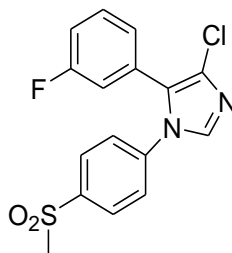
^1H NMR (400 MHz, CDCl_3) δ : 3.08 (3H, s, SO_2CH_3), 7.05-7.07 (2H, m, *Ph*), 7.16-7.17 (2H, m, *Ph*), 7.30 (2H, d, $J = 8.5$ Hz, *Ph*), 7.66 (1H, s, *Im*), 7.98 (2H, d, $J = 8.5$ Hz)

^{13}C $\{^1\text{H}\}$ NMR (100 MHz, CDCl_3) δ : 44.39, 116.09 (d, $J = 21.4$ Hz), 122.84 (d, $J = 4$ Hz), 123.12, 125.64, 126.02, 129.21, 130.15, 131.58 (d, $J = 8.4$ Hz), 135.53, 140.42, 162.65 (d, $J = 250$ Hz)

^{19}F $\{^1\text{H}\}$ NMR (376.17 MHz, CDCl_3) δ : -111.16

High Res GS-MS m/z : 351 ($\text{M}^+ + 1$, 100)

4-Chloro-5-(3-Fluoro-phenyl)-1-(4-methanesulfonyl-phenyl)-1H-imidazole ([20])
[205]



165 mg (0.47 mmol) of yellow solid. Yield: 31%. Melting point: 170-172 °C. R_t: 10:28 (99.4%)

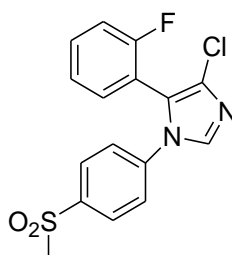
¹H NMR (400 MHz, CDCl₃) δ: 3.12 (3H, s, SO₂CH₃), 6.86 (1H, dt, *J* = 8 Hz, *J* = 1.2 Hz, *Ph*), 6.89 (1H, dt, *J* = 9.6 Hz, *J* = 1.2 Hz, *Ph*), 6.99 (1H, tdd, *J* = 8 Hz, *J* = 1.2 Hz, *Ph*), 7.22-7.28 (3H, m, *Ph*), 7.61 (1H, s, *Im*), 7.99 (2H, d, *J* = 8.4 Hz, *Ph*)

¹³C {¹H} NMR (100 MHz, CDCl₃) δ: 44.42, 115.81 (d, *J* = 21.4 Hz), 116.58 (d, *J* = 22.9 Hz), 125.38 (d, *J* = 4 Hz), 125.63, 128.79 (d, *J* = 8 Hz), 129.26, 130.44 (d, *J* = 9.1 Hz), 130.64, 130.73, 135.94, 140.34, 140.53, 162.55 (d, *J* = 250 Hz)

¹⁹F {¹H} NMR (376.17 MHz, CDCl₃) δ: -111.18

High Res GS-MS *m/z*: 351 (M⁺+1, 100)

4-Chloro-5-(2-Fluoro-phenyl)-1-(4-methanesulfonyl-phenyl)-1H-imidazole ([21])
[205]



138 mg (0.39 mmol) of yellow solid. Yield: 28%. Melting point: 142-144 °C. R_t: 9:58 (97.2%)

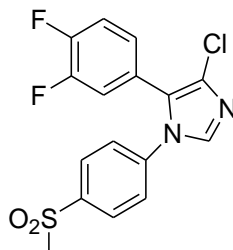
¹H NMR (400 MHz, CDCl₃) δ: 3.07 (3H, s, SO₂CH₃), 7.00 (1H, t, *J* = 8.3 Hz, *Ph*), 7.24-7.29 (3H, m, *Ph*), 7.31-7.42 (2H, m, *Ph*), 7.71 (1H, s, *Im*), 7.94 (2H, d, *J* = 8.8 Hz, *Ph*)

¹³C {¹H} NMR (100 MHz, CDCl₃) δ: 44.42, 115.13 (d, *J* = 15.5 Hz), 116.23 (d, *J* = 21.3 Hz), 121.78, 124.73 (d, *J* = 6 Hz), 129.10, 131.47, 131.63 (d, *J* = 9 Hz), 132.09 (d, *J* = 3 Hz), 133.71, 135.77, 140.27, 140.78, 159.35 (d, *J* = 250 Hz)

¹⁹F {¹H} NMR (376.17 MHz, CDCl₃) δ: -111.36

High Res GS-MS m/z : 351 ($M^+ + 1$, 100)

4-Chloro-5-(3,4-difluoro-phenyl)-1-(4-methanesulfonyl-phenyl)-1H-imidazole ([22])



51 mg (0.14 mmol) of off-white solid. Yield: 12%. Melting point: 173-175 °C. R_f : 10:53 (98.1%)

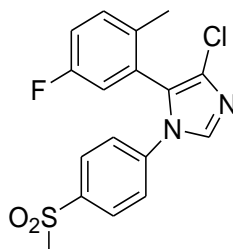
¹H NMR (400 MHz, CDCl₃) δ : 3.08 (3H, s, SO₂CH₃), 6.86-6.88 (1H, m, *Ph*), 7.04-7.09 (1H, m, *Ph*), 7.12-7.17 (1H, m, *Ph*), 7.31 (2H, d, $J = 8.4$ Hz, *Ph*), 7.64 (1H, s, *Im*), 7.99 (2H, d, $J = 8.4$ Hz, *Ph*)

¹³C {¹H} NMR (100 MHz, CDCl₃) δ : 44.42, 118.01 (dd, $J = 16.8$ Hz, $J = 6$ Hz), 118.80 (dd, $J = 18.3$ Hz, $J = 8$ Hz), 121.04, 121.90, 125.68, 126.17 (dd, $J = 7$ Hz, $J = 4$ Hz), 129.37, 133.54 (dd, $J = 8$ Hz, $J = 4$ Hz), 135.95, 140.16, 140.77, 150.27 (dd, $J = 255$ Hz, $J = 20$ Hz), 250.35 (dd, $J = 250$ Hz, $J = 20$ Hz)

¹⁹F {¹H} NMR (376.17 MHz, CDCl₃) δ : -135.65, -135.37

High Res GS-MS m/z : 369 ($M^+ + 1$, 100)

4-Chloro-5-(5-fluoro-2-methyl-phenyl)-1-(4-methanesulfonyl-phenyl)-1H-imidazole ([23])



54 mg (0.15 mmol) of yellow oil. Yield= 22%. R_f : 10:53 (99.5%)

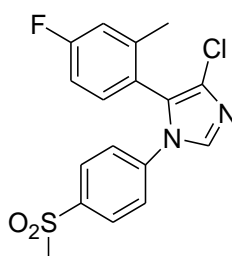
¹H NMR (400 MHz, CDCl₃) δ : 1.95 (3H, s, CH₃), 2.99 (3H, s, SO₂CH₃), 6.82 (1H, dd, $J = 8.8$ Hz, $J = 2.8$ Hz, *Ph*), 6.98 (1H, td, $J = 8.8$ Hz, $J = 2.8$ Hz, *Ph*), 7.14 (1H, dd, $J = 8.8$ Hz, $J = 5.6$ Hz, *Ph*), 7.19 (2H, d, $J = 8.4$ Hz, *Ph*), 7.68 (1H, s, *Im*), 7.87 (2H, d, $J = 8.4$ Hz, *Ph*)

^{13}C $\{^1\text{H}\}$ NMR (100 MHz, CDCl_3) δ : 19.02, 44.39, 116.97 (d, $J = 20.6$ Hz), 118.01 (d, $J = 21.4$ Hz), 123.05, 124.50, 127.96 (d, $J = 9$ Hz), 129.23, 131.02, 132.15, 132.24, 134.07 (d, $J = 3$ Hz), 135.31, 140.30 (d, $J = 10$ Hz), 160.65 (d, $J = 250$ Hz)

^{19}F $\{^1\text{H}\}$ NMR (376.17 MHz, CDCl_3) δ : -116.64

High Res GS-MS m/z : 365 ($\text{M}^+ + 1$, 100)

4-Chloro-5-(4-fluoro-2-methyl-phenyl)-1-(4-methanesulfonyl-phenyl)-1H-imidazole ([24])



126 mg (0.34 mmol) of yellow oil. Yield: 35%. R_f : 10:54 (96.6%).

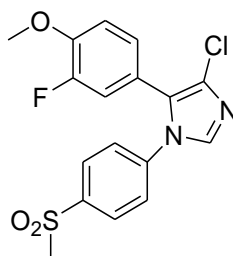
^1H NMR (400 MHz, CDCl_3) δ : 2.05 (3H, s, CH_3), 3.05 (3H, s, SO_2CH_3), 6.89-6.97 (2H, m, *Ph*), 7.12 (1H, dd, $J = 8.4$ Hz, $J = 5.6$ Hz, *Ph*), 7.23 (2H, d, $J = 8.8$ Hz, *Ph*), 7.74 (1H, s, *Im*), 7.92 (2H, d, $J = 8.8$ Hz, *Ph*)

^{13}C $\{^1\text{H}\}$ NMR (100 MHz, CDCl_3) δ : 14.16, 44.36, 113.56 (d, $J = 22.1$ Hz), 117.55 (d, $J = 21.4$ Hz), 122.46 (d, $J = 3$ Hz), 124.6, 125.59, 129.14, 130.98, 133.24 (d, $J = 8.4$ Hz), 135.16, 140.11, 140.43, 141.13 (d, $J = 8.4$ Hz), 163.29 (d, $J = 248.3$ Hz)

^{19}F $\{^1\text{H}\}$ NMR (376.17 MHz, CDCl_3) δ : -110.89

High Res GS-MS m/z : 365 ($\text{M}^+ + 1$, 100)

4-Chloro-5-(3-fluoro-4-methoxy-phenyl)-1-(4-methanesulfonyl-phenyl)-1H-imidazole ([25])



73 mg (0.19 mmol) of yellow oil. Yield= 51%. R_f : 10:01 (98.8%)

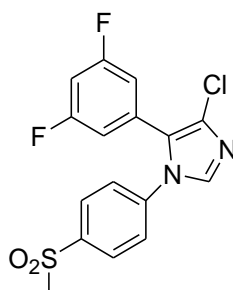
^1H NMR (400 MHz, CDCl_3) δ : 3.12 (3H, s, SO_2CH_3), 3.91 (3H, s, OCH_3), 6.87-6.98 (3H, m, *Ph*), 7.33 (2H, d, $J = 8.4$ Hz, *Ph*), 7.65 (1H, s, *Im*), 7.99 (2H, d, $J = 8.4$ Hz, *Ph*)

^{13}C $\{^1\text{H}\}$ NMR (100 MHz, CDCl_3) δ : 44.42, 56.14, 113.37, 113.39, 117.36 (d, $J = 20$ Hz), 119.28 (d, $J = 7.4$ Hz), 125.62, 125.74, 126.04 (d, $J = 3.1$ Hz), 129.21, 130.05, 135.43, 140.40 (d, $J = 4.6$ Hz), 148.03 (d, $J = 12$ Hz), 151.95 (d, $J = 250$ Hz)

^{19}F $\{^1\text{H}\}$ NMR (376.17 MHz, CDCl_3) δ : -133.48

High Res GS-MS m/z : 381 ($\text{M}^+ + 1$, 100)

**4-Chloro-5-(3,5-difluoro-phenyl)-1-(4-methanesulfonyl-phenyl)-1*H*-imidazole
([26])**



51 mg (0.14 mmol) of white solid. Yield= 16%. Melting point: 186-188 °C. R_f : 10:52 (99.3%)

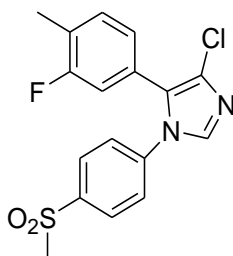
^1H NMR (400 MHz, CDCl_3) δ : 3.09 (3H, s, SO_2CH_3), 6.72 (2H, dt, $J = 8$ Hz, $J = 1.6$ Hz, *Ph*), 6.79 (1H, tt, $J = 8$ Hz, $J = 1.6$ Hz, *Ph*), 7.32 (2H, d, $J = 8.4$ Hz, *Ph*) 7.65 (1H, s, *Im*), 8.01 (2H, d, $J = 8.4$ Hz, *Ph*)

^{13}C $\{^1\text{H}\}$ NMR (100 MHz, CDCl_3) δ : 44.45, 104.51 (t, $J = 25$ Hz), 112.55 (dd, $J = 18.9$ Hz, $J = 3.9$ Hz), 118.35, 119.70, 125.64, 129.45, 136.40, 140.04, 140.90, 145.10 (t, $J = 7$ Hz), 158.70 (dd, $J = 225$ Hz, $J = 10$ Hz)

^{19}F $\{^1\text{H}\}$ NMR (376.17 MHz, CDCl_3) δ : -107.58

High Res GS-MS m/z : 369 ($\text{M}^+ + 1$, 100)

4-Chloro-5-(3-fluoro-4-methyl-phenyl)-1-(4-methanesulfonyl-phenyl)-1H-imidazole ([27])



182 mg (0.5 mmol) of white solid. Yield= 34%. Melting point: 184-186 °C. R_t: 11:16 (99.8%)

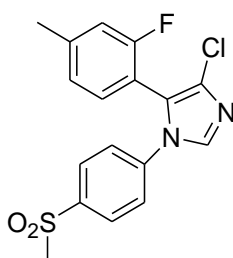
¹H NMR (400 MHz, CDCl₃) δ: 2.26 (3H, s, CH₃), 3.07 (3H, s, SO₂CH₃), 6.79 (1H, dd, *J*= 8 Hz, *J*= 1.6 Hz, *Ph*), 6.88 (1H, dd, *J*= 8 Hz, *J*= 1.6 Hz, *Ph*), 7.13 (1H, t, *J*= 8 Hz, *Ph*), 7.30 (2H, d, *J*= 8.4 Hz, *Ph*), 7.63 (1H, s, *Im*), 7.96 (2H, d, *J*= 8.4 Hz, *Ph*)

¹³C {¹H} NMR (100 MHz, CDCl₃) δ: 14.47, 44.43, 116.17 (d, *J*= 23.7 Hz), 125.13 (d, *J*= 3.9 Hz), 125.62, 125.87 (d, *J*= 22.9 Hz), 125.90, 125.92, 129.20, 130.29, 135.64, 131.87 (d, *J*= 6.2 Hz), 139.09, 140.43 (d, *J*= 5 Hz), 161.01 (d, *J*= 244.4 Hz)

¹⁹F {¹H} NMR (376.17 MHz, CDCl₃) δ: -115.48

High Res GS-MS *m/z*: 365 (M⁺+1, 100)

4-Chloro-5-(2-fluoro-4-methyl-phenyl)-1-(4-methanesulfonyl-phenyl)-1H-imidazole ([28])



31 mg (0.085 mmol) of yellow oil. Yield= 37%. R_t: 10:59 (99.5%)

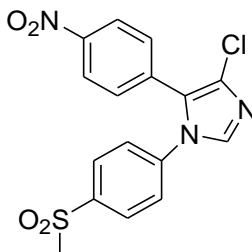
¹H NMR (400 MHz, CDCl₃) δ: 2.35 (3H, s, CH₃), 3.01 (3H, s, SO₂CH₃), 6.75 (1H, d, *J*= 8 Hz, *Ph*), 6.97 (1H, d, *J*= 8 Hz, *Ph*), 7.22 (1H, s, *Ph*), 7.25 (2H, d, *J*= 8.4 Hz, *Ph*), 7.65 (1H, s, *Im*), 7.88 (2H, d, *J*= 8.4 Hz, *Ph*)

¹³C {¹H} NMR (100 MHz, CDCl₃) δ: 21.35, 44.42, 111.95 (d, *J*= 15 Hz), 116.75 (d, *J*= 21.4 Hz), 117.95 (d, *J*= 9 Hz), 124.77, 125.52 (d, *J*= 3 Hz), 129.06, 130.64, 131.40, 135.54, 140.17, 140.80, 142.68 (d, *J*= 8 Hz), 159.25 (d, *J*= 250 Hz)

¹⁹F {¹H} NMR (376.17 MHz, CDCl₃) δ: -112.51

High Res GS-MS m/z : 365 (M^{+1} , 100)

4-Chloro-5-(4-Nitro-phenyl)-1-(4-methanesulfonyl-phenyl)-1H-imidazole ([52])



1.63 g (4.32 mmol) of yellow solid. Yield: 27%

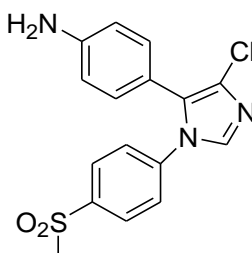
¹H NMR (400 MHz, CDCl₃) δ : 3.08 (3H, s, SO₂CH₃), 7.32 (2H, d, J = 8.4 Hz, *Ph*), 7.37 (2H, d, J = 8.8 Hz, *Ph*), 7.71 (1H, s, *Im*), 8.00 (2H, d, J = 8.4 Hz, *Ph*), 8.19 (2H, d, J = 8.8 Hz, *Ph*)

¹³C {¹H} NMR (100 MHz, CDCl₃) δ : 44.38, 124.02, 125.74, 127.88, 128.83, 129.55, 130.08, 131.99, 133.27, 13.05, 139.99, 141.09, 147.30

High Res GS-MS m/z : 378 (M^{+1} , 100)

Synthesis of 4-[5-Chloro-3-(4-methanesulfonyl-phenyl)-3H-imidazol-4-yl]-phenylamine ([53])

Iron powder (2.42 g, 43.32 mmol, 10 eq) and concd HCl (1.96 ml) were added to a solution of the [52] (1.63 g, 4.32 mmol, 1 eq) in EtOH (100 ml) and H₂O (25 ml) and the reaction mixture was heated to reflux for 90 minutes. Any iron powder left was removed by gravity filtration and the volume was reduced *in vacuo*. EtOAc (50 ml) was added and the organic layer was dried with MgSO₄. The organic layer was filtered and bulk solvent was removed *in vacuo* to yield pure compound.



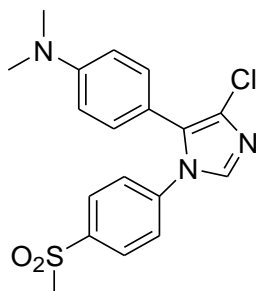
811 mg (2.34 mmol) of yellow amorphous solid. Yield: 54%

^1H NMR (400 MHz, CDCl_3) δ : 2.15 (2H, s, NH_2), 3.06 (3H, s, SO_2CH_3), 6.60 (2H, d, $J=8.1$ Hz, *Ph*), 6.94 (2H, d, $J=8.1$ Hz, *Ph*), 7.30 (2H, d, $J=8.3$ Hz, *Ph*), 7.61 (1H, s, *Im*), 7.93 (2H, d, $J=8.3$ Hz, *Ph*)

^{13}C $\{^1\text{H}\}$ NMR (100 MHz, CDCl_3) δ : 44.44, 114.97, 116.26, 125.61, 127.30, 128.99, 130.92, 134.80, 139.93, 140.92, 145.62, 146.85

Synthesis of {4-[5-Chloro-3-(4-methanesulfonyl-phenyl)-3H-imidazol-4-yl]-phenyl}-dimethyl-amine ([54])

[53] (811 mg, 2.34 mmol, 1 eq) was dissolved in EtOH (25 ml) and K_2CO_3 (1.61 g, 11.7 mmol, 5 eq) and a large excess of MeI (1.54 ml, 23.4 mmol, 10 eq) were added. The reaction mixture was refluxed for 24 hours. EtOH was removed *in vacuo*, the solid was dissolved in DCM (50 ml) and washed with water (10 ml). The volume of DCM was reduced *in vacuo* to ca. 10 ml and the suspended solid was filtered to yield pure compound.



115 mg (0.31 mmol) of yellow solid. Yield: 13%

^1H NMR (400 MHz, CDCl_3) δ : 2.99 (6H, s, $\text{N}(\text{CH}_3)_2$), 3.09 (3H, s, SO_2CH_3), 6.65 (2H, d, $J=8.8$ Hz, *Ph*), 7.04 (2H, d, $J=8.8$ Hz, *Ph*), 7.35 (2H, d, $J=8.4$ Hz, *Ph*), 7.62 (1H, s, *Im*), 7.96 (2H, d, $J=8.4$ Hz, *Ph*)

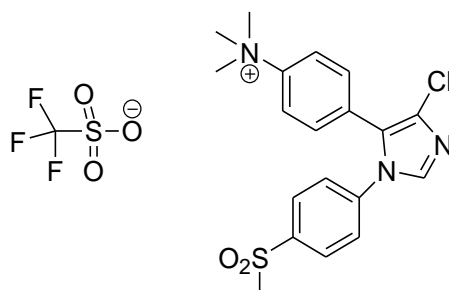
^1H NMR (400 MHz, D_2O) δ : 3.28 (6H, s, $\text{N}(\text{CH}_3)_2$), 3.54 (3H, s, SO_2CH_3), 7.44 (2H, d, $J=8.8$ Hz, *Ph*), 7.53 (2H, d, $J=8.8$ Hz, *Ph*), 7.94-7.98 (4H, m, *Ph*), 8.18 (1H, s, *Im*)

^{13}C $\{^1\text{H}\}$ NMR (100 MHz, D_2O) δ : 41.42, 55.29, 118.46, 121.26, 123.50, 124.74, 127.02, 127.11, 129.83, 135.78, 137.23, 138.42, 144.51

Synthesis of Trifluoro-methanesulfonate{4-[5-chloro-3-(4-methanesulfonyl-phenyl)-3H-imidazol-4-yl]-phenyl}-trimethyl-ammonium ([55])

[54] (50 mg, 0.14 mmol, 1 eq) was added to a dry flask and dissolved in dry DCM (8 ml) under nitrogen atmosphere. Methyl triflate (16 μl , 0.14 mmol, 1 eq) was added and the

solution was stirred overnight at RT. The red solid suspended was filtered. Diethyl ether (5 ml) was added to the filtrate to precipitate a white solid, which was filtered to yield pure trimethyl ammonium triflate.



16 mg (0.03 mmol) of white solid. Yield= 23%

^1H NMR (400 MHz, D_2O) δ : 3.09 (3H, s, SO_2CH_3), 3.42 (6H, s, $\text{N}(\text{CH}_3)_3$), 7.31-7.34 (4H, m, *Ph*), 7.60 (2H, d, $J = 8.8$ Hz, *Ph*), 7.81 (2H, d, $J = 8.8$ Hz, *Ph*), 7.83 (1H, s, *Im*)

^1H NMR (400 MHz, D_2O) δ : 43.04, 56.94, 121.22, 123.47, 125.51, 127.24, 128.51, 129.35, 132.25, 136.42, 137.52, 141.33, 143.75, 144.10 ($J = 200$ Hz)

^{19}F $\{^1\text{H}\}$ NMR (376.17 MHz, D_2O) δ : -78.83

High Res GS-MS m/z : 390 (cation M^+ , 100)

8.3 BIOLOGY

8.3.1 Purified enzymes assays

Colourimetric COX assay kits were purchased from Cayman Chemical and used according to manufacturer's instructions. Imidazoles were tested by Dr Cawthorne.

8.3.2 Whole cell assays

RAW 264.7 (purchased from American Type Culture Collection), passage 5-12, were grown in a 6 well plates in Dulbecco's modified Eagles medium (DMEM) + 10% FBS until they reached 40% confluence; the medium was removed and cells were washed with serum free DMEM, which was then added to the wells. LPS (200 ng/ml) and IFN- γ (10 u/ml) were then added to induce COX-2 expression, and cells were incubated for 7 hours at 37 °C. DMSO or inhibitors dissolved in DMSO were then added at several

concentrations, and cells were incubated for 30 minutes. Arachidonic acid was then added (10 μ M/l) and cells were incubated for 20 minutes.

For the assessment of extracellular PG levels, supernatants were collected and used according to the manufacturer's instructions (Cayman Chemical, R&D Systems).

For the assessment of intracellular PGE₂ levels, supernatants were removed, cells were washed with DMEM, and lysed with the cell lysis agents provided by the manufacturer. PGE₂ levels were then analysed via ELISA according to the manufacturer's instructions (GE Healthcare).

8.4 RADIOCHEMISTRY

8.4.1 [¹⁸F]fluoride production

[¹⁸F]fluoride was produced by Goncalo dos santos Clemente, in the PET Research Facility at The University of Hull, via the ¹⁸O(p,n)¹⁸F reaction and delivered as [¹⁸F]fluoride in [¹⁸O]water with a typical activity of 1 GBq. A smaller quota of 140 MBq was collected in a separate 2 ml clear glass vial for each reaction; this quota was dried under compressed air at 100-110 °C adding small volumes of dry ACN (250 μ l \times 3) over 20 minutes.

8.4.2 Radiolabelling

A vial or a MW vessel were charged with Kryptofix 2.2.2 (2 mg), precursor (2 or 6 mg) and a base (K₂CO₃ or KHCO₃, 2 mg). Dry [¹⁸F]fluoride was dissolved in dry solvent (DMF, DMSO, NMF, ACN, 50, 250 or 500 μ l) and transferred in the vial/MW vessel; the mixture was heated at different temperatures (in the 100-180 °C range) for a time ranging from 5 minutes to 40 minutes. The reaction was monitored via radioTLC (silica plates, eluent ACN:buffer 1:1).

The MW reactor used was a CEM discover SP. The reactions were performed with a ramp time of 1 minute and at full power.

9. APPENDIX

9.1 ^1H NMR spectra of novel compounds

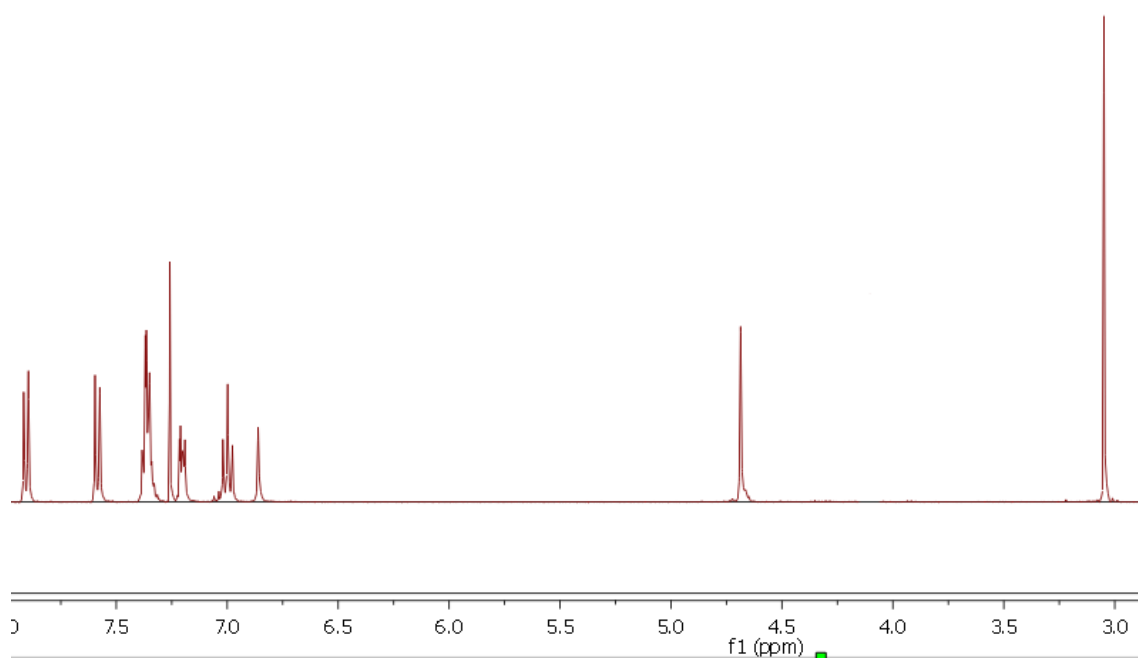


Figure 29: ^1H NMR spectrum of [2].

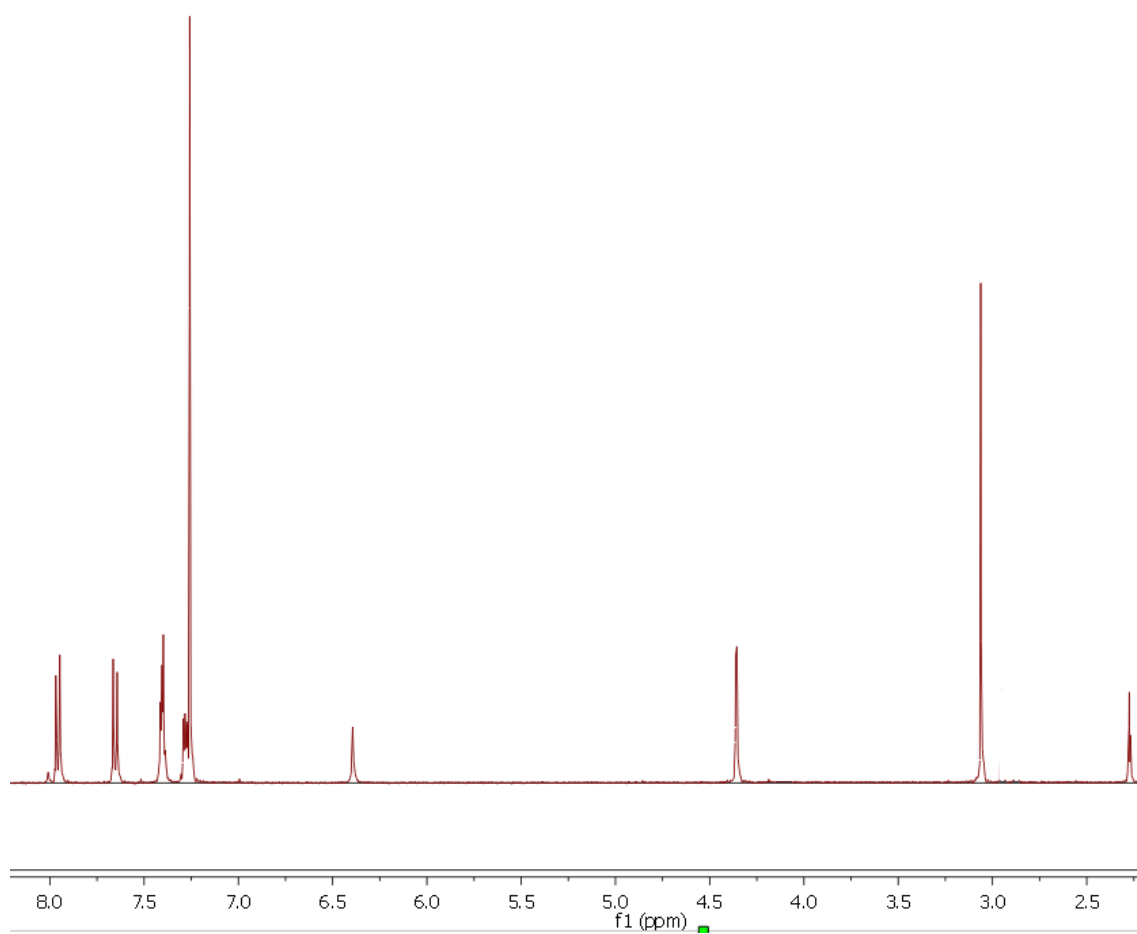


Figure 30: ^1H NMR spectrum of [3].

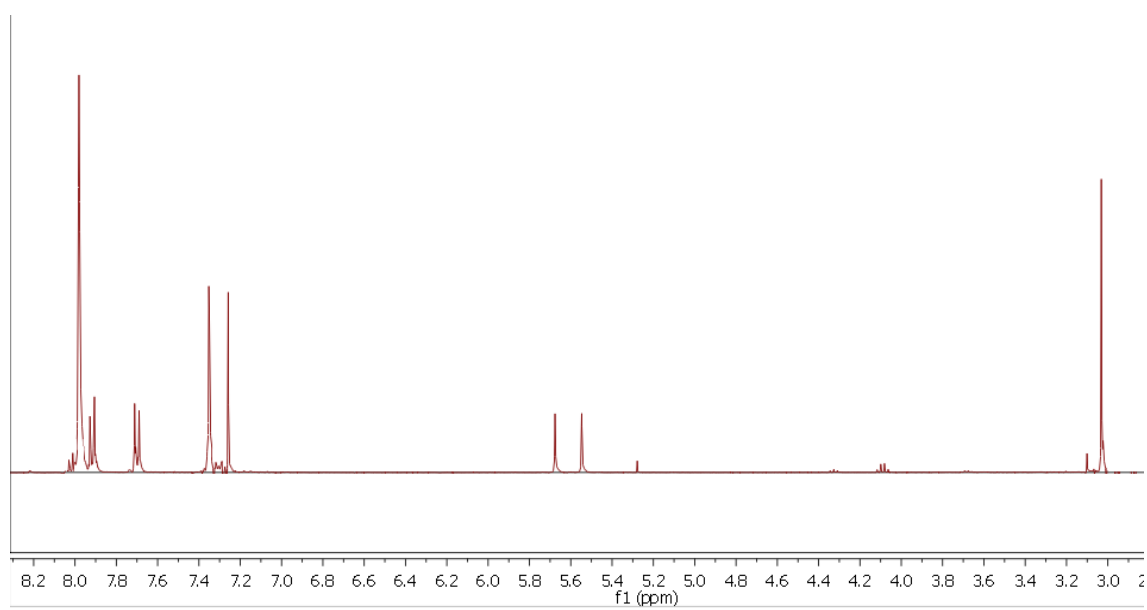


Figure 31: ^1H NMR spectrum of [4].

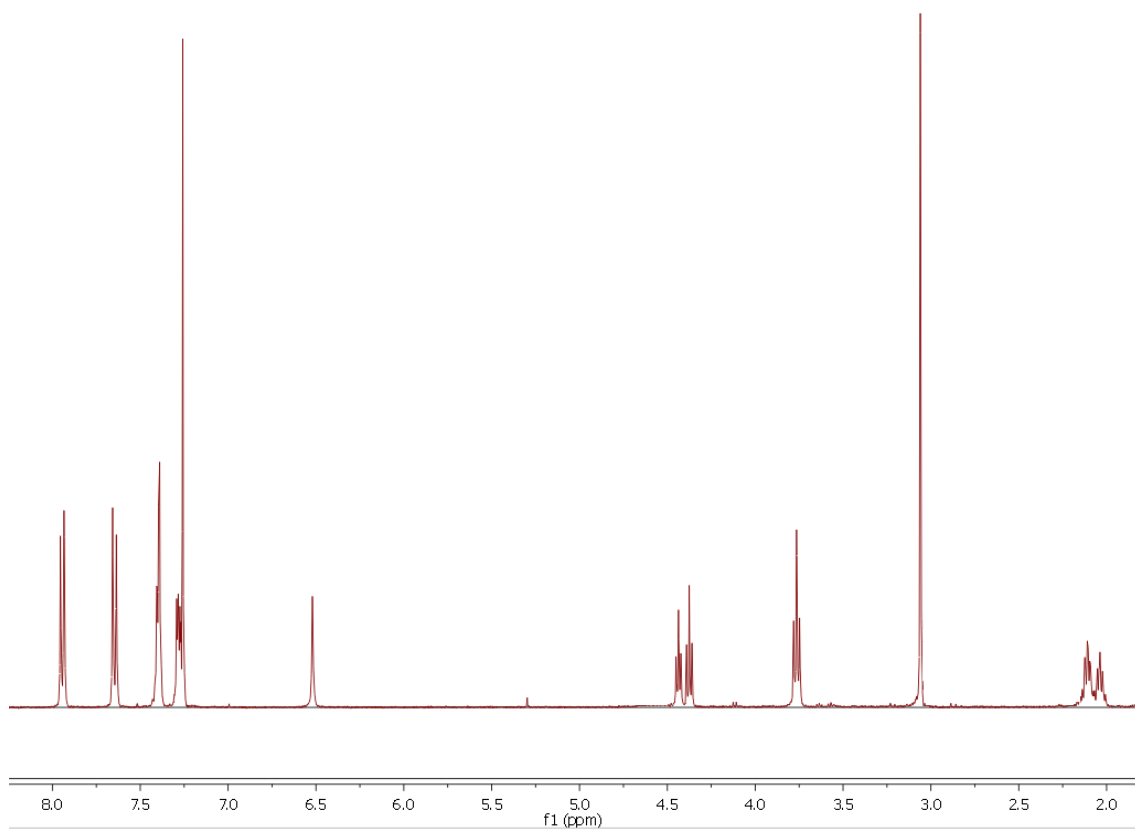


Figure 32: ^1H NMR spectrum of [6].

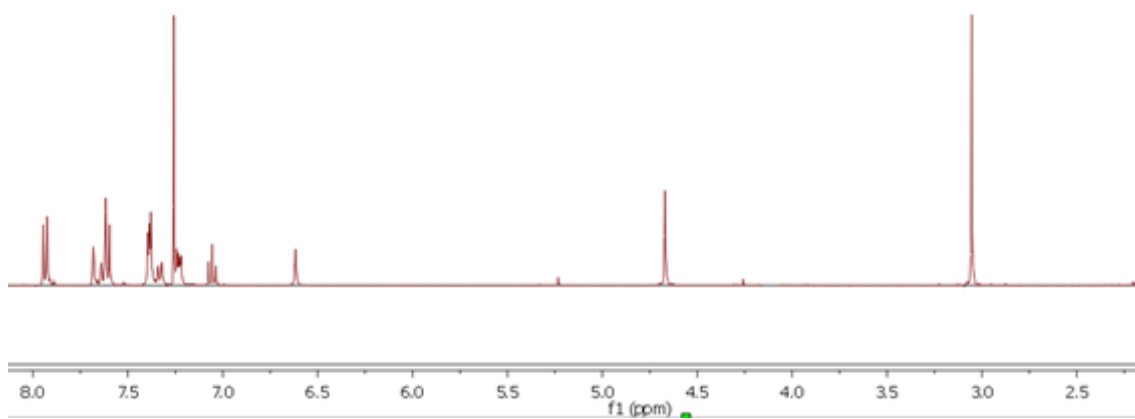


Figure 33: ^1H NMR spectrum of [7].

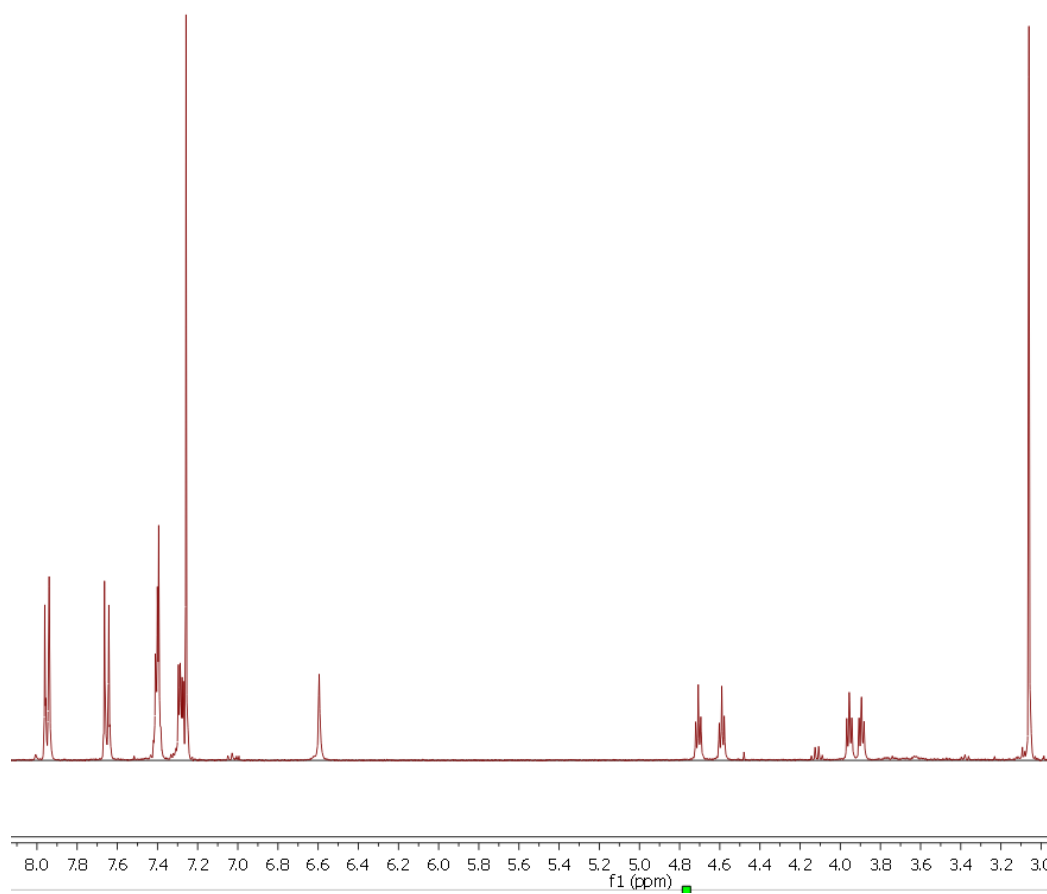


Figure 34: ^1H NMR spectrum of [8].

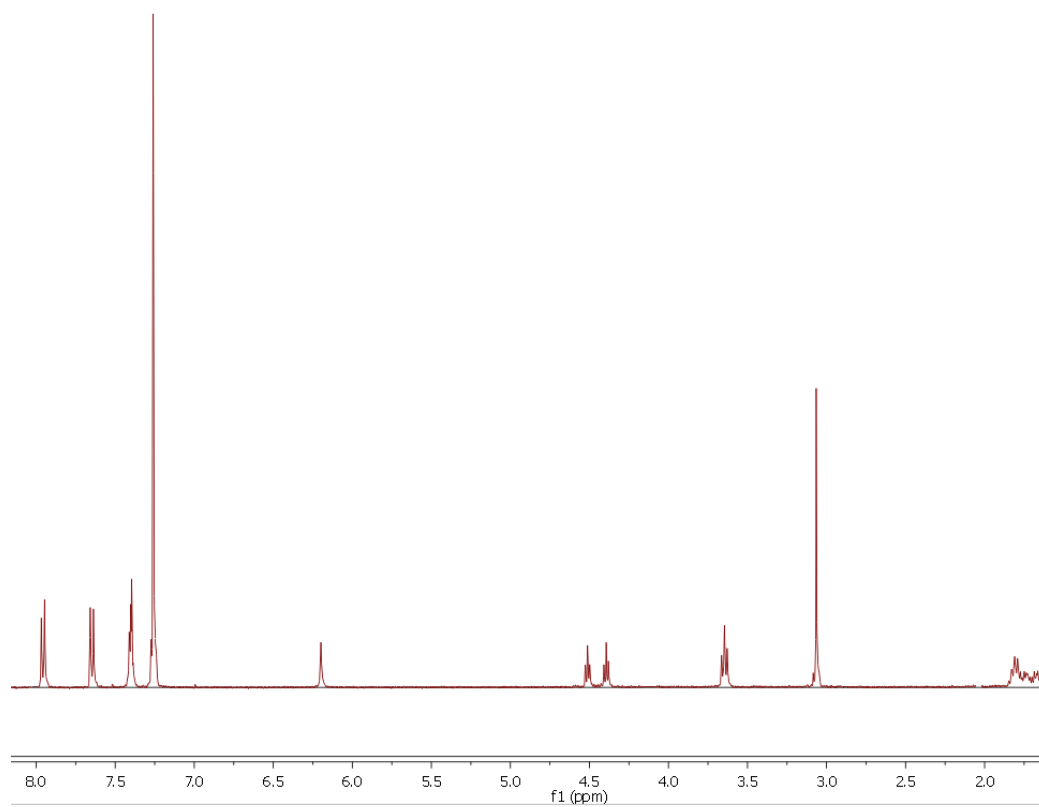


Figure 35: ^1H NMR spectrum of [9].

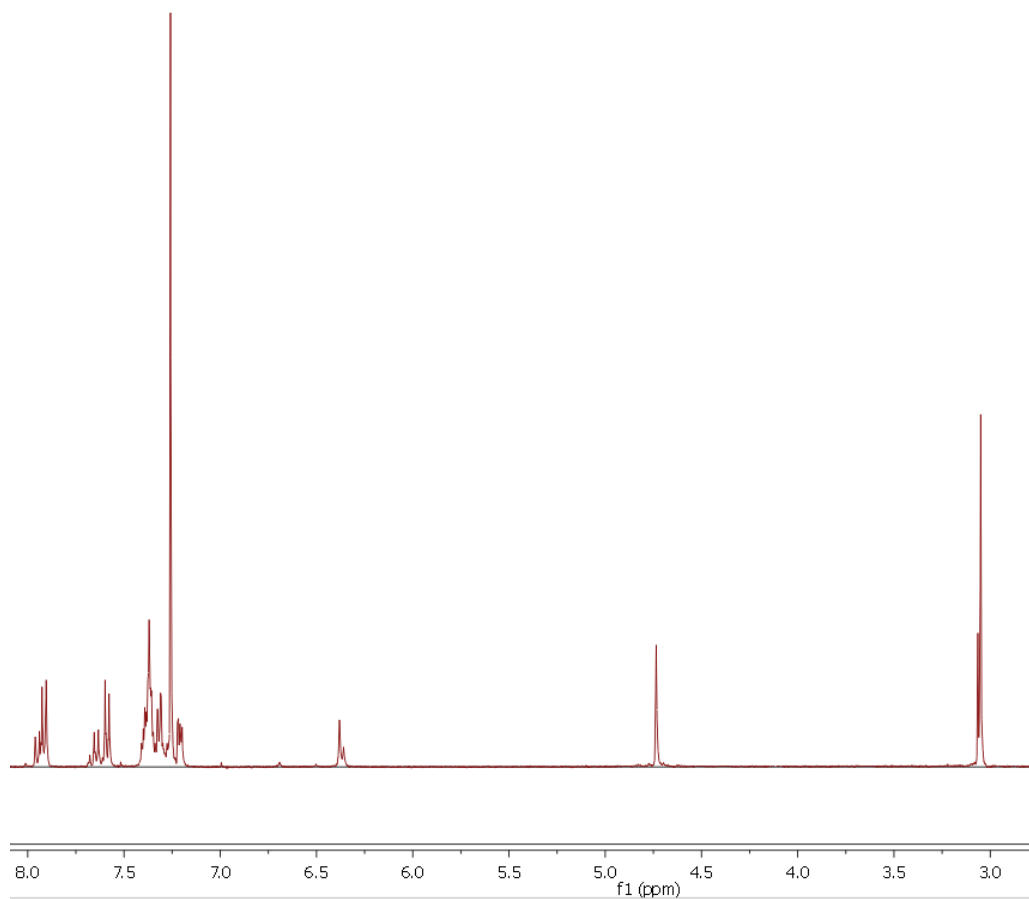


Figure 36: ^1H NMR spectrum of [10].

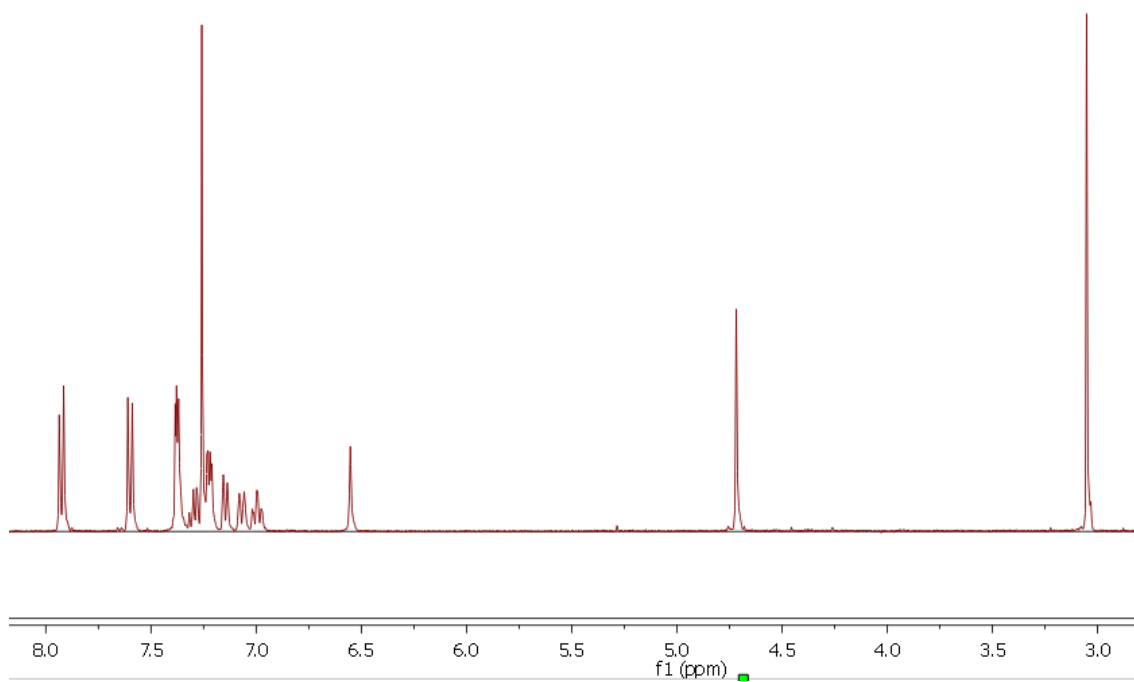


Figure 37: ^1H NMR spectrum of [11].

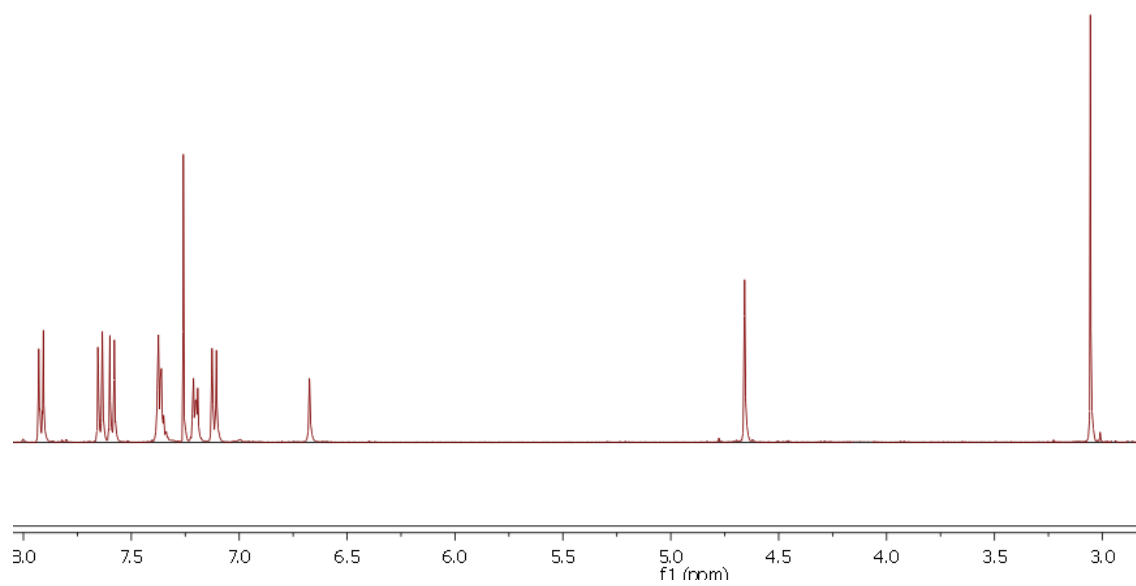


Figure 38: ^1H NMR spectrum of [12].

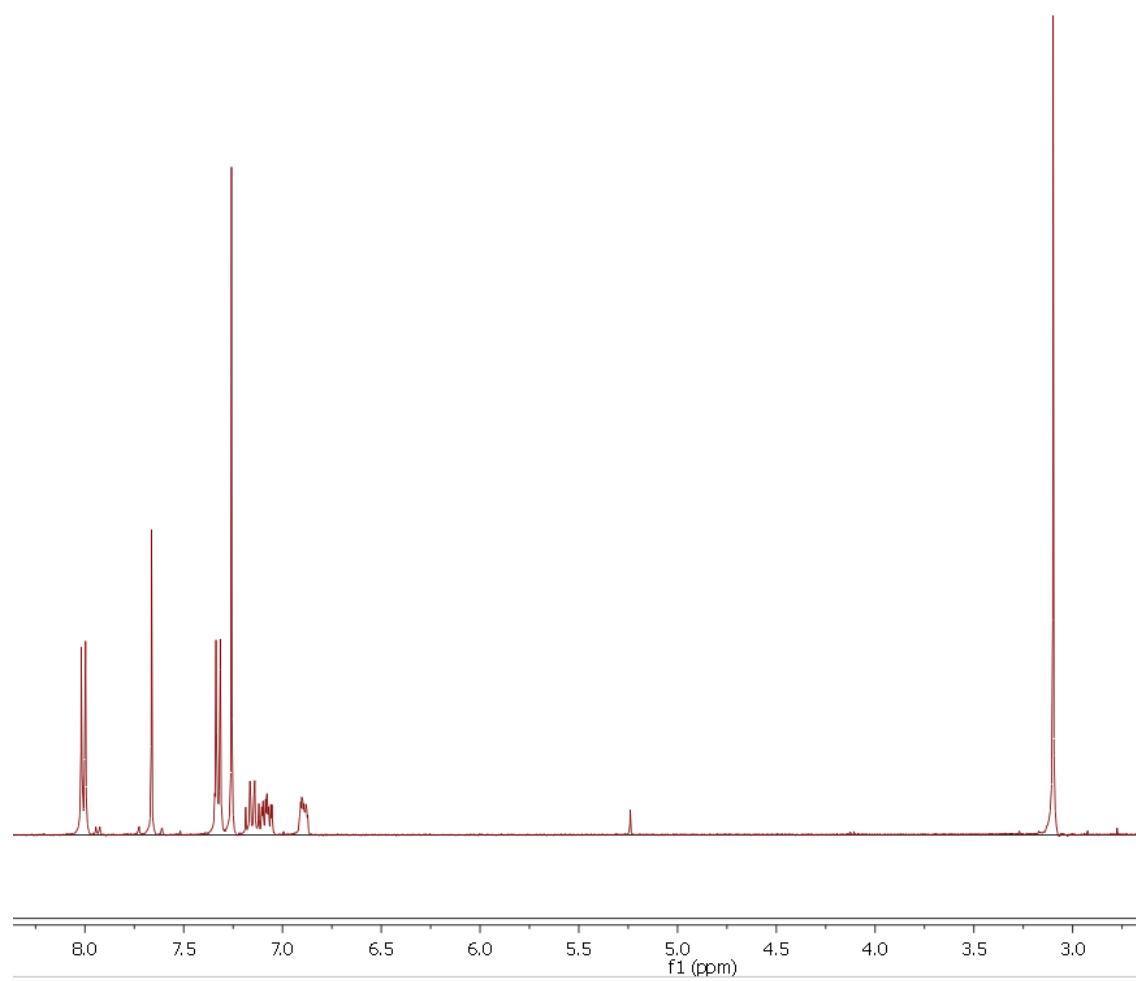


Figure 39: ^1H NMR spectrum of [22].

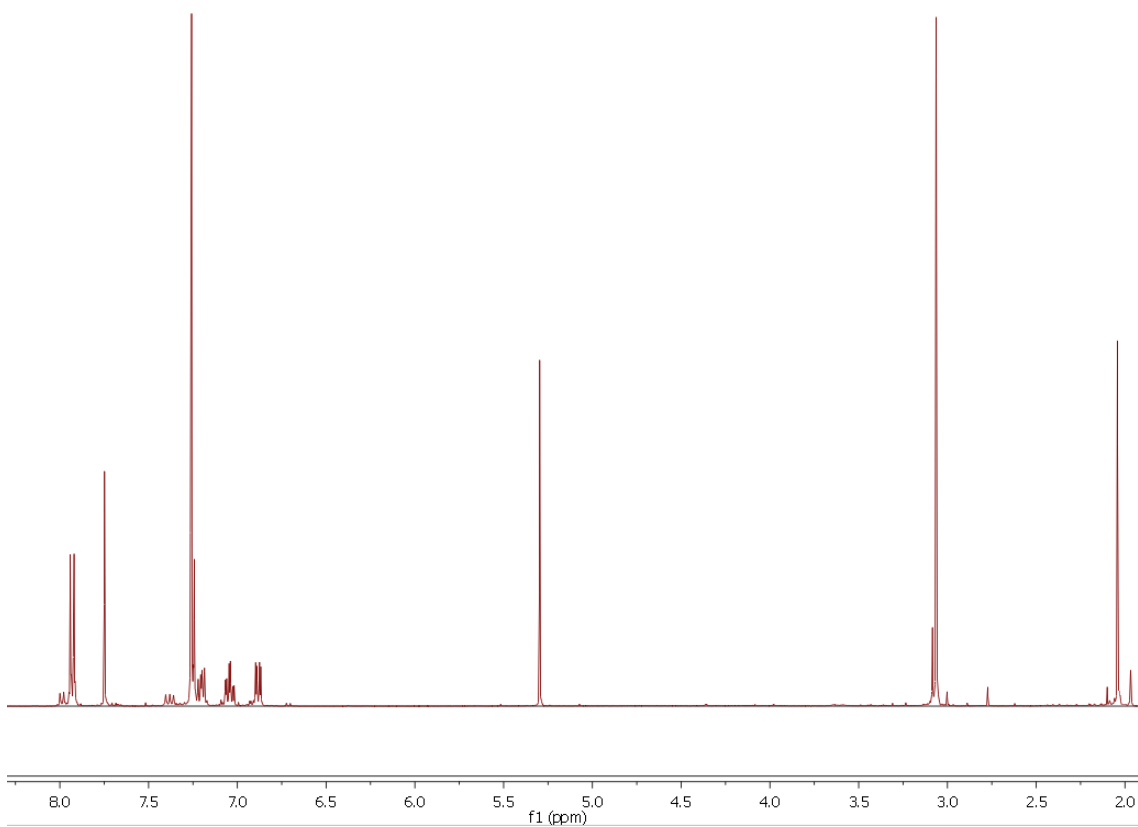


Figure 40: ^1H NMR spectrum of [23].

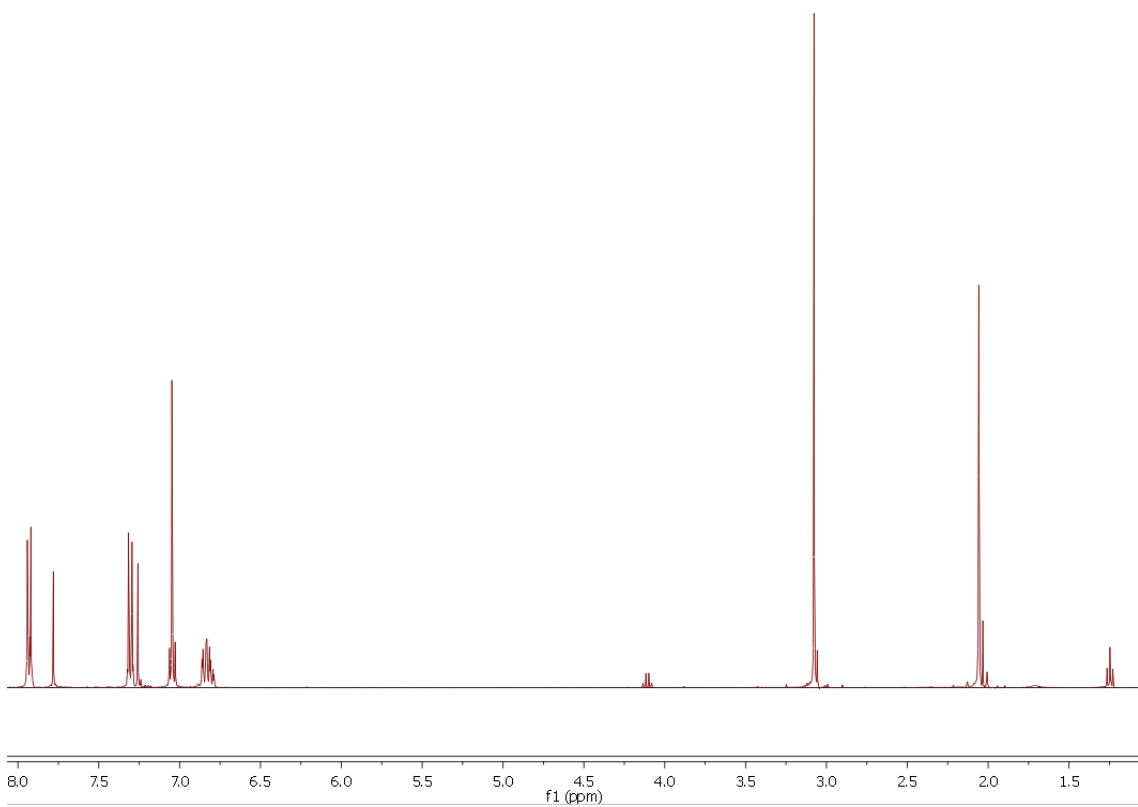


Figure 41: ^1H NMR spectrum of [24].

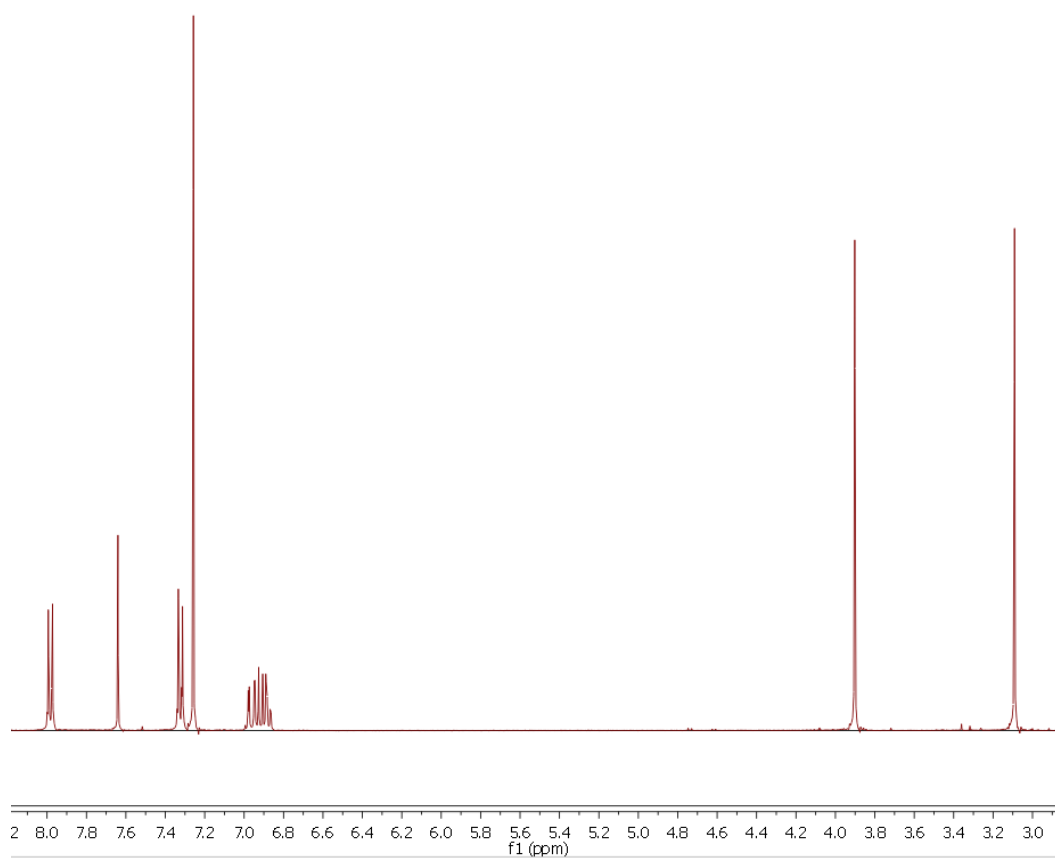


Figure 42: ^1H NMR spectrum of [25].

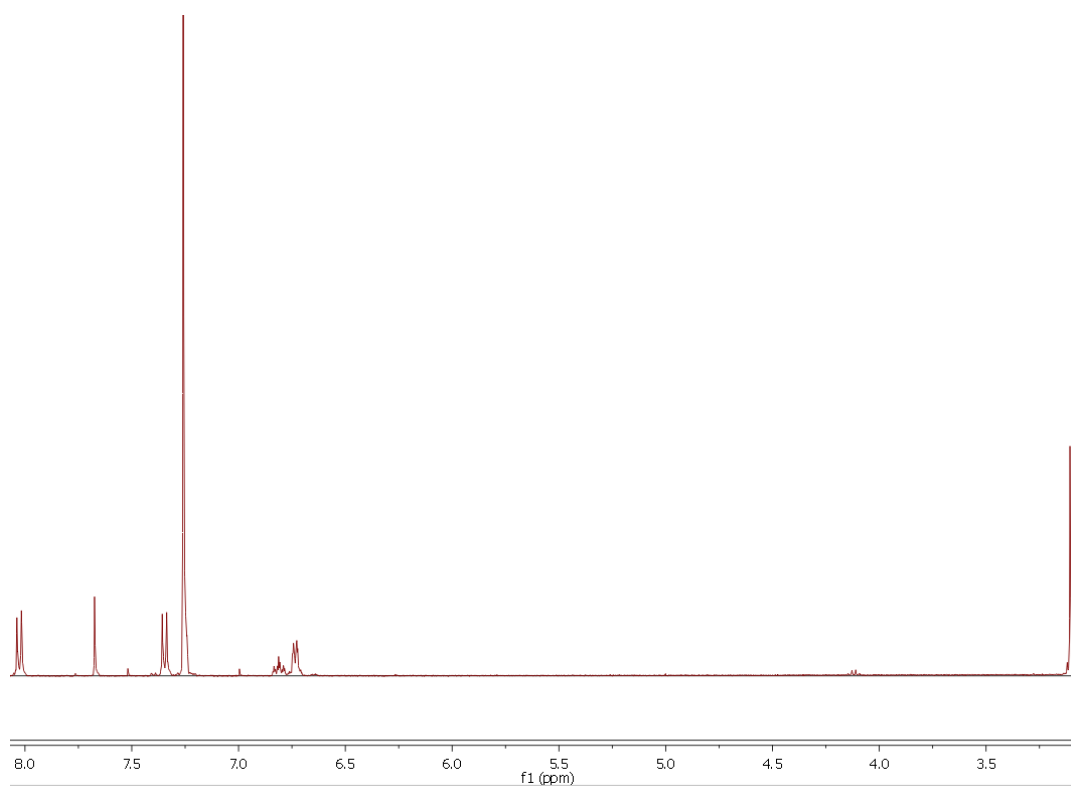


Figure 43: ^1H NMR spectrum of [26].

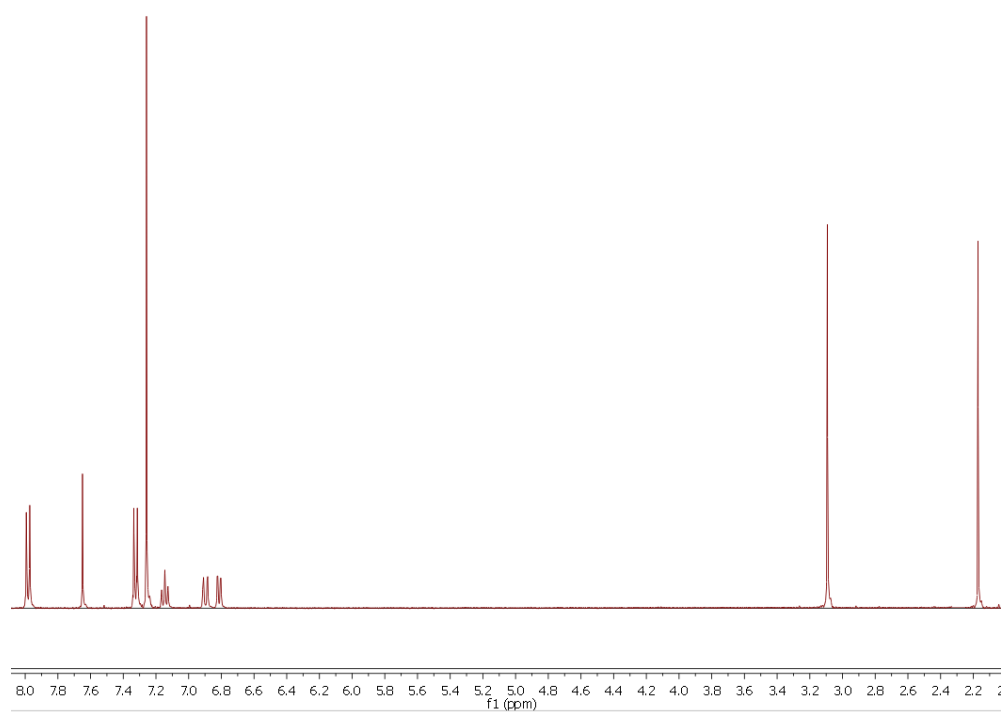


Figure 44: ^1H NMR spectrum of [27].

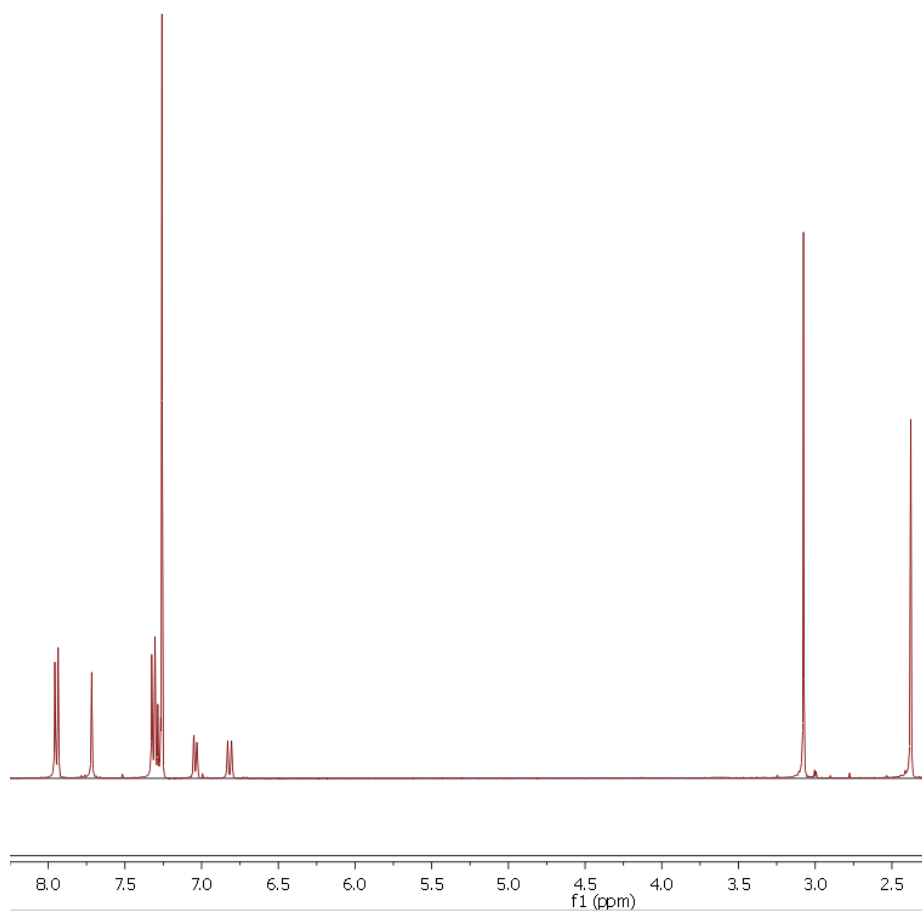


Figure 45: ^1H NMR spectrum of [28].

9.2 Some HPLC data of the final compounds

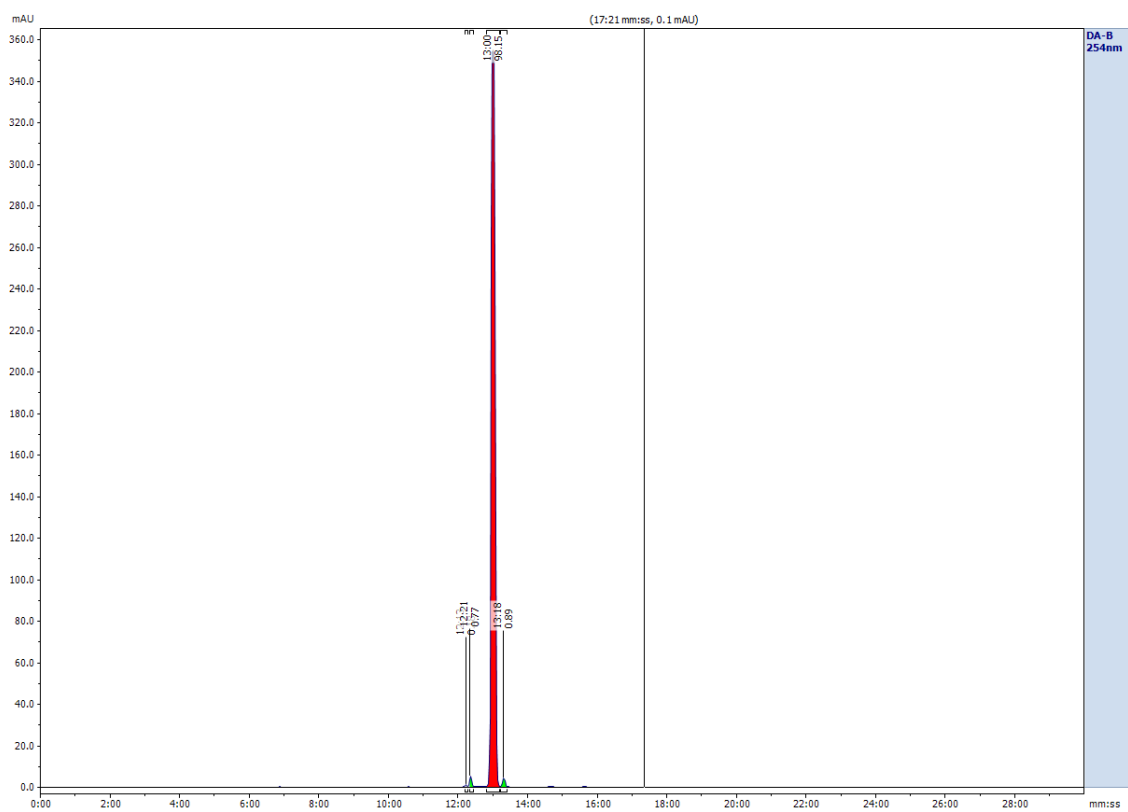


Figure 46: HPLC chromatogram of celecoxib

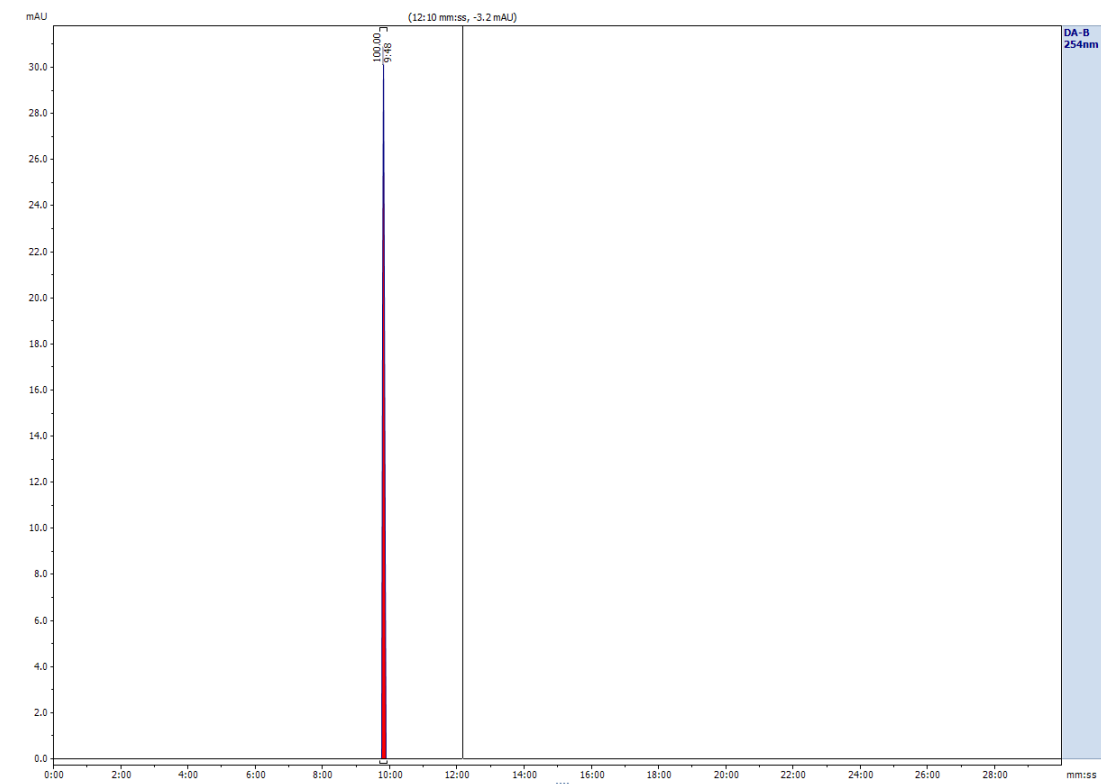


Figure 47: HPLC chromatogram of [5]

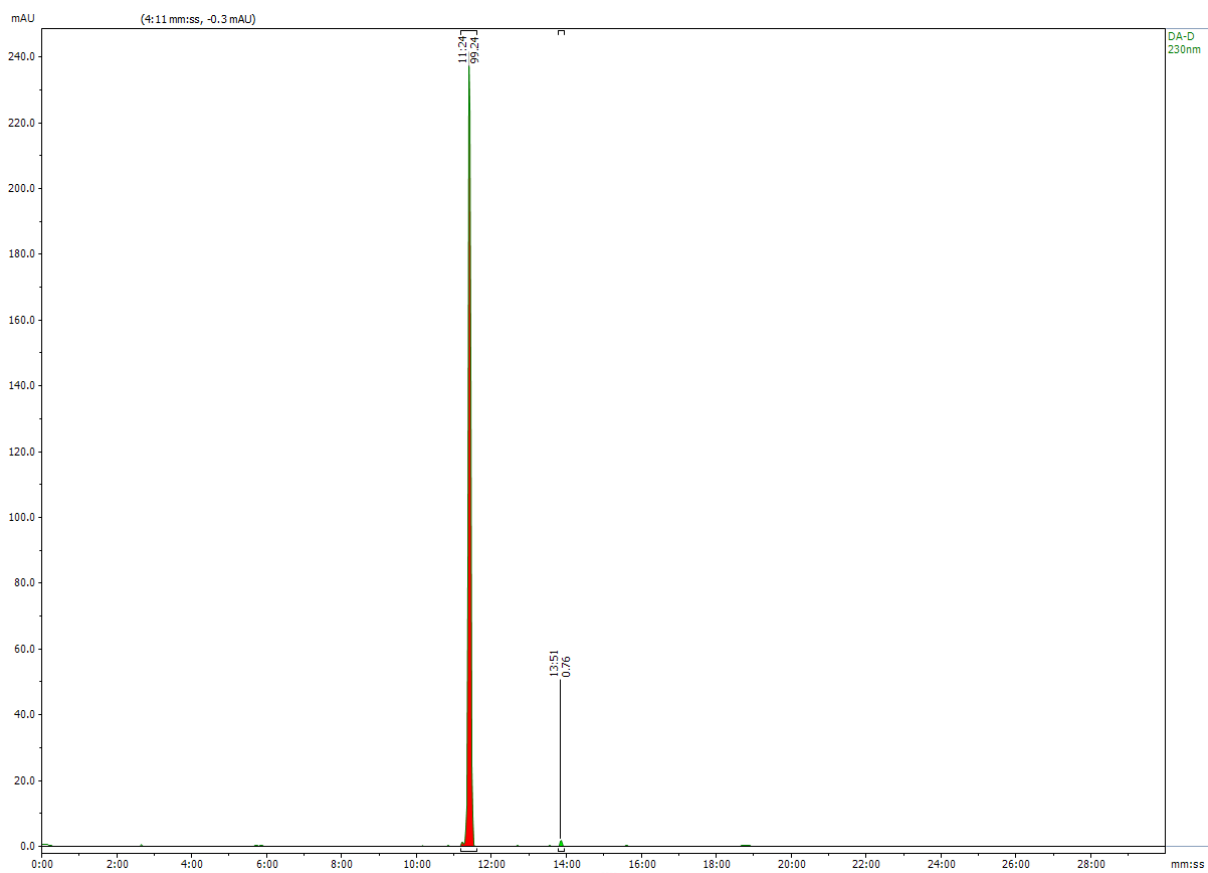


Figure 48: HPLC chromatogram of [11]

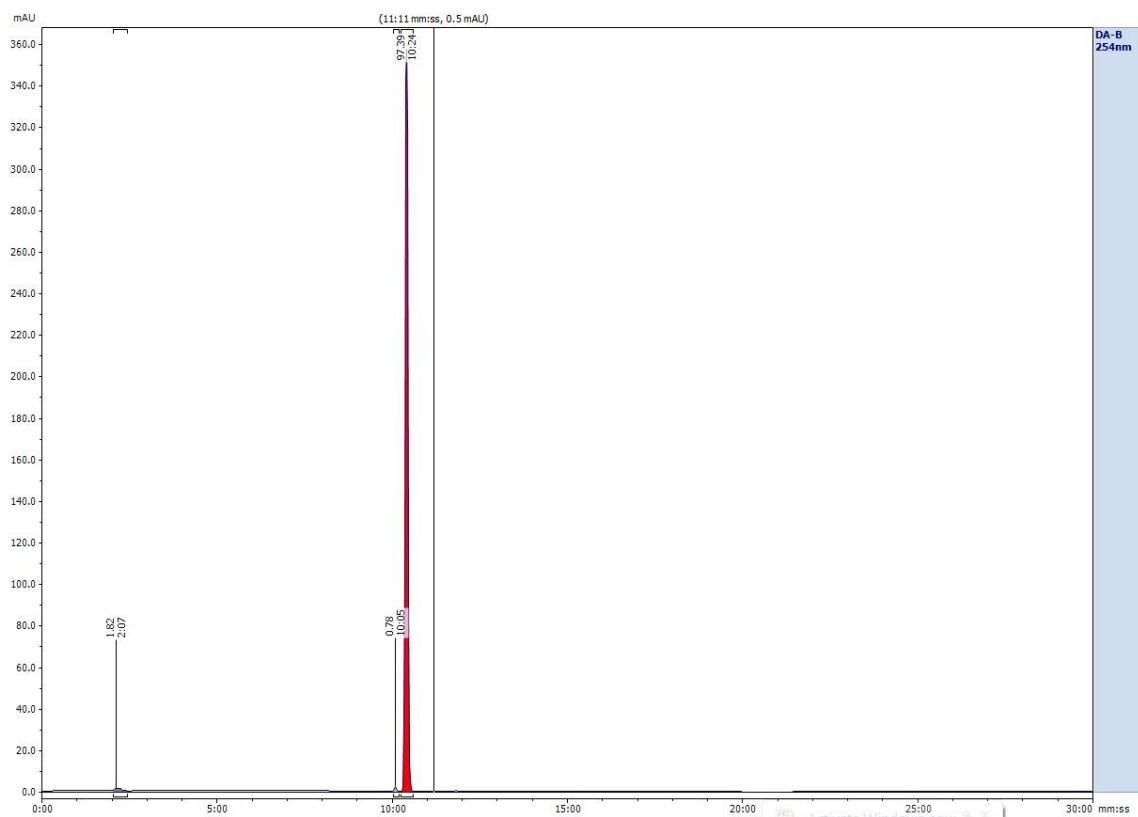


Figure 49: HPLC chromatogram of [19]

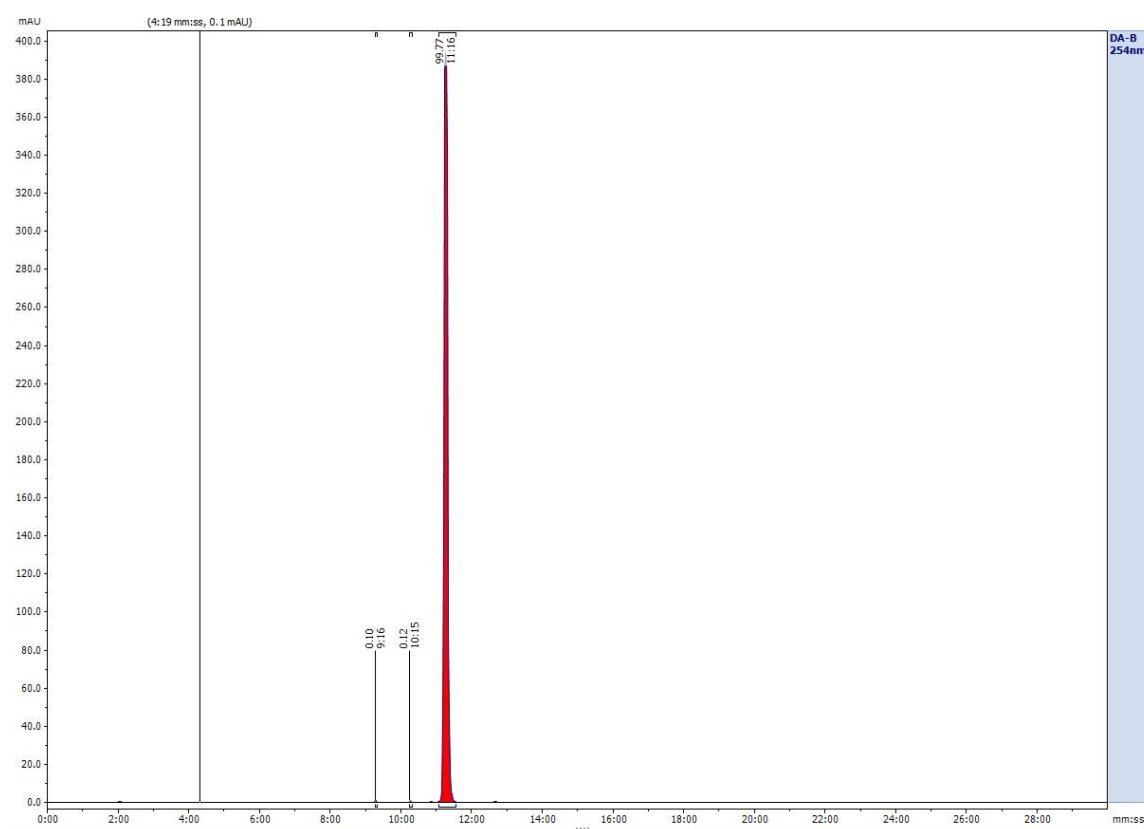


Figure 50: HPLC chromatogram of [27]

9.3 Colourimetric assay data

Figures below show the IC_{50} curves obtained when screening the imidazoles for COX-2 inhibition with the colourimetric assay kits.

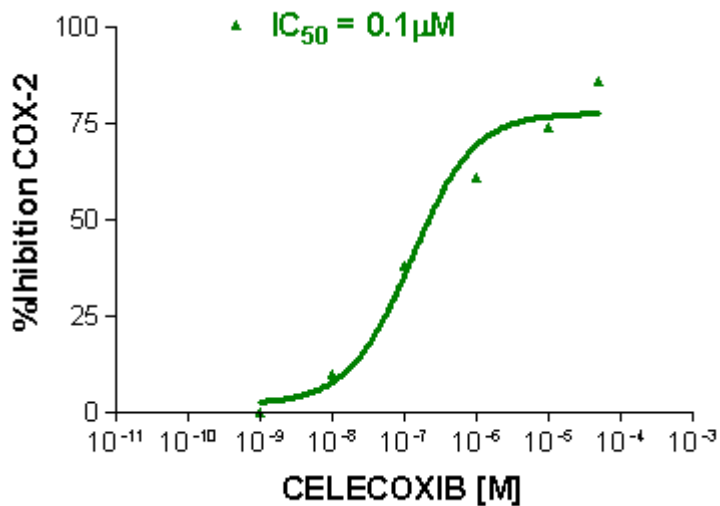


Figure 51: IC_{50} curve of celecoxib, used as a reference compound.

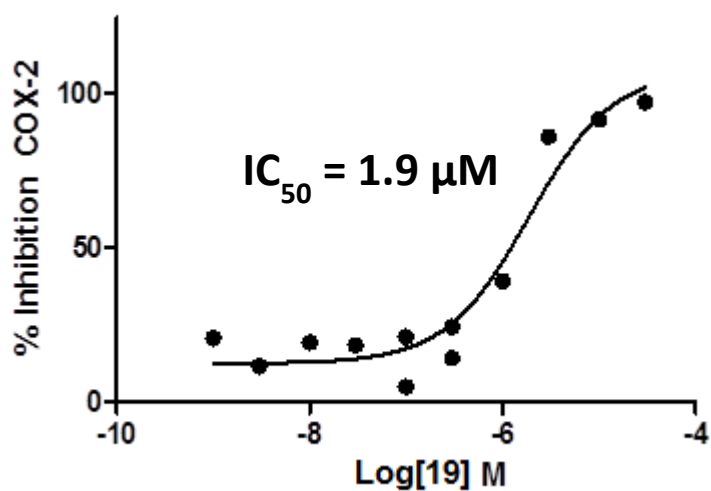


Figure 52: IC_{50} curve of [19].

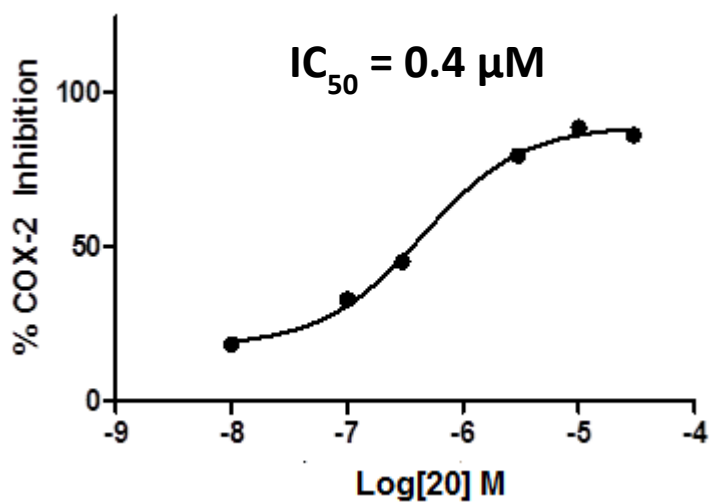


Figure 53: IC_{50} curve of [20].

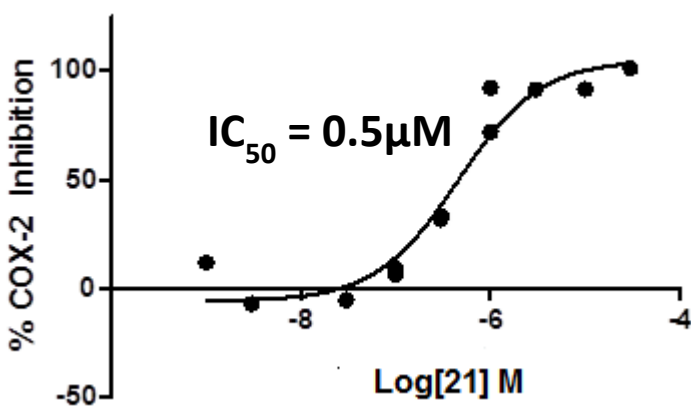


Figure 54: IC_{50} curve of [21].

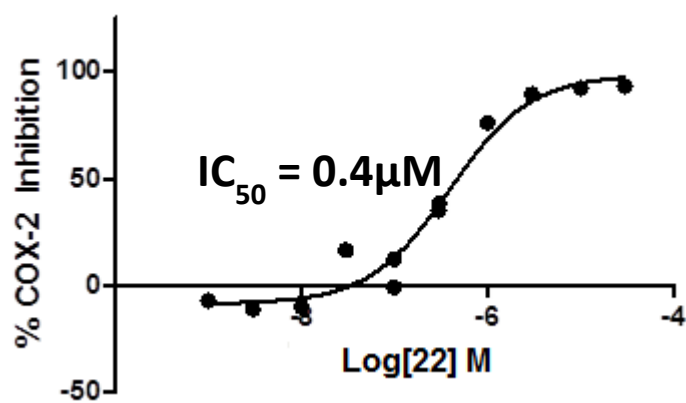


Figure 55: IC_{50} curve of [22].

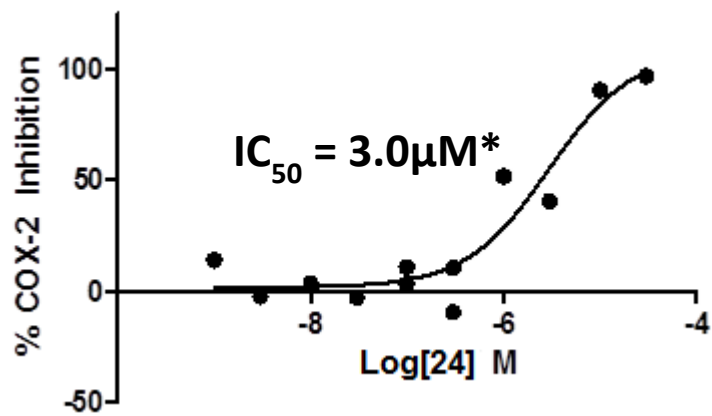


Figure 56: IC_{50} curve of [24].

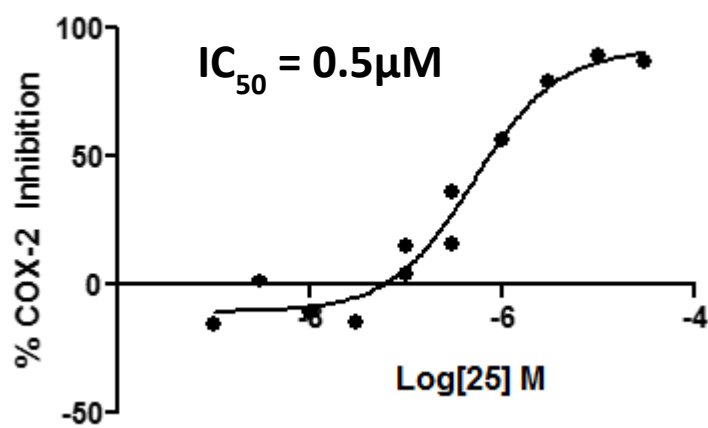


Figure 57: IC_{50} curve of [25].

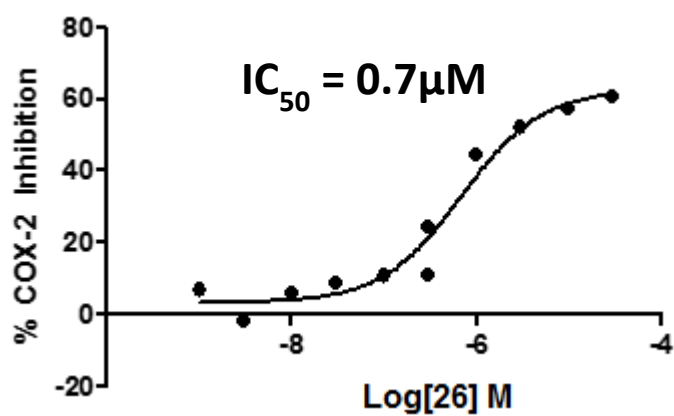


Figure 58: IC_{50} curve of [26].

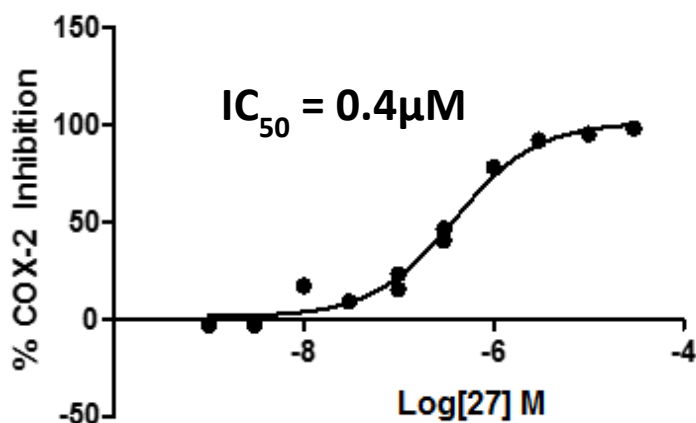


Figure 59: IC₅₀ curve of [27].

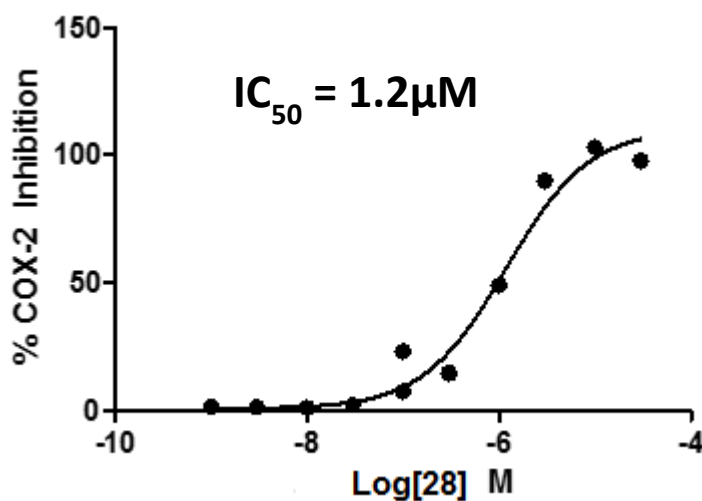


Figure 60: IC₅₀ curve of [28].

9.4 ELISA data

The data below show the conflicting results obtained when RAW 264.7 cells were treated to induce the expression of COX-2 with LPS and IFN- γ and PG levels were assayed via ELISA.

The several attempts were run following the manufacturer's instructions (Cayman Chemical, GE Healthcare, R&D Systems). [222]

9.4.1 Cayman Chemical ELISA assay

The assay was performed with **[19]** and celecoxib as a reference compound. IC₅₀ curves for both inhibitors could not be fitted, as the percent inhibition resulted in negative values. Figure 43 shows the binding saturation curve of **[19]**.

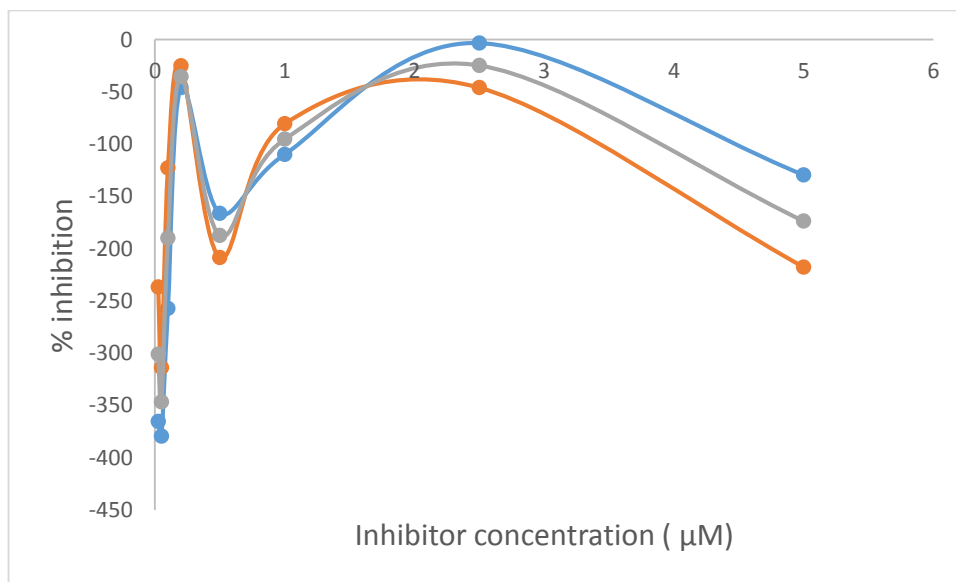


Figure 61: binding saturation curve of **[19]**, as assessed via Cayman Chemical ELISA kit. The grey plot is the average between the duplicates, shown in orange and blue.

9.4.2 GE Healthcare ELISA assay

The assay was performed by analysing intracellular levels of PGE₂, when cells were induced to express COX-2 and then treated with celecoxib, **[19]**, **[20]** and **[21]** at concentrations concentrations between 25 nM and 5 µM. Absorbance values were mostly in the 0.5-0.6 range, which resulted in almost homogeneous inhibition.

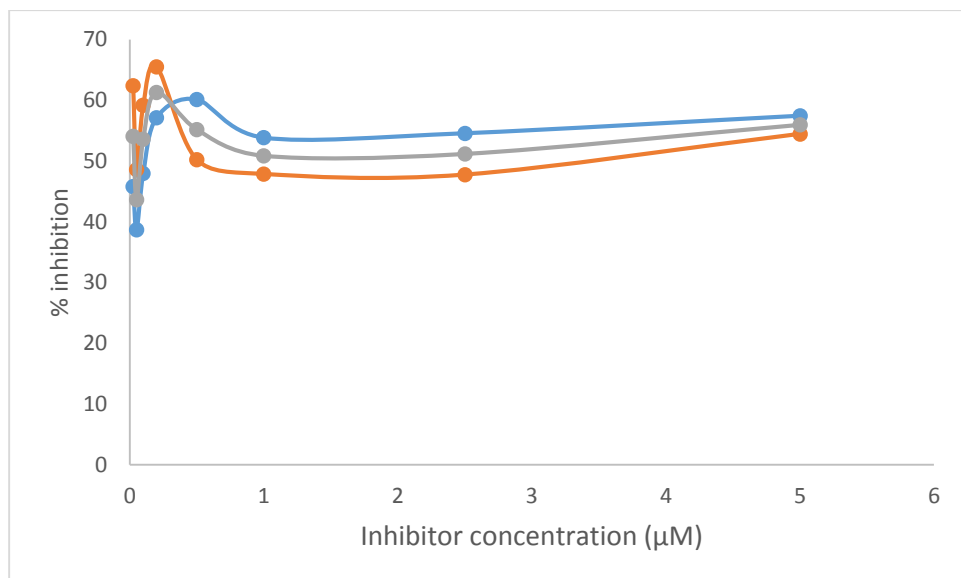


Figure 62: binding saturation curve of [19], as assessed via GE Healthcare ELISA kit. The grey plot is the average between the duplicates, shown in orange and blue.

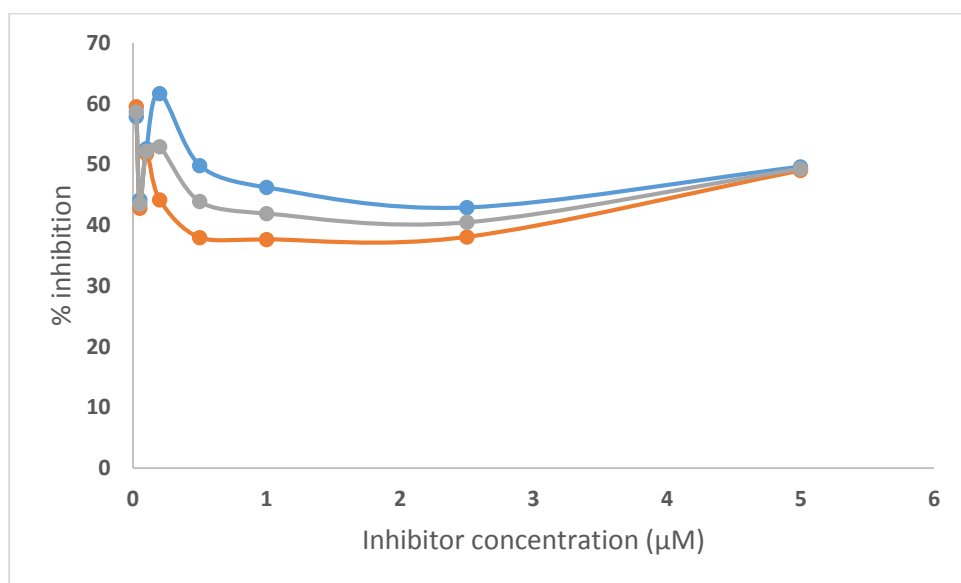


Figure 63: binding saturation curve of [20], as assessed via GE Healthcare ELISA kit. The grey plot is the average between the duplicates, shown in orange and blue.

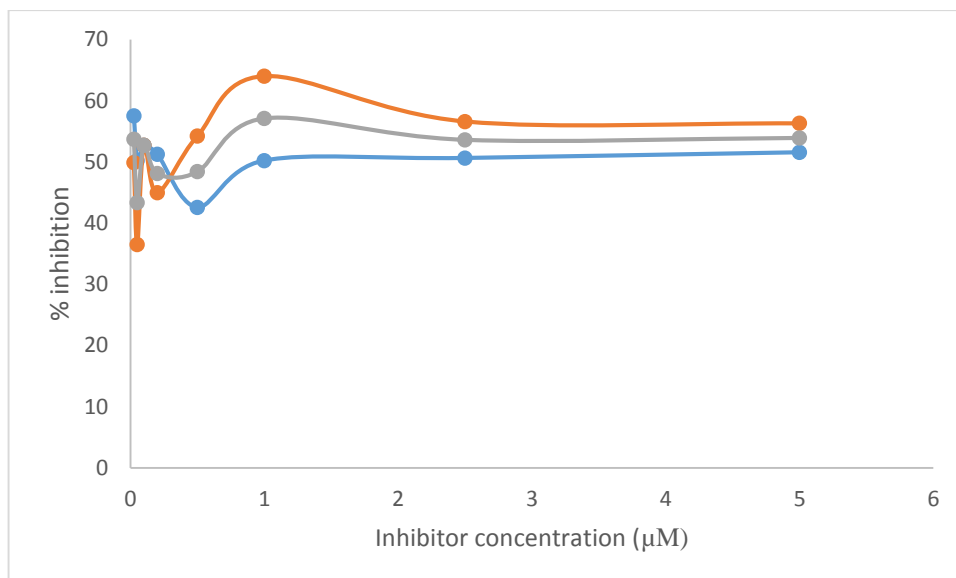


Figure 64: binding saturation curve of **[21]**, as assessed via GE Healthcare ELISA kit. The grey plot is the average between the duplicates, shown in orange and blue.

9.4.3 R&D Systems ELISA assay

The R&D kit system was tested using only few conditions, in order to optimise the protocol before assaying the imidazoles. The conditions tested were with either high concentrations of celecoxib or no celecoxib at all with LPS and IFN- γ induced cells, and cells that were not treated to induce COX-2.

Table 18 shows the incongruences observed when running the assay several times, in the same conditions. As the absorbance read at the end of the assay is inversely proportional to the concentration of PGE₂ in the sample, only assay 1 showed somewhat favourable results, which were not replicated in the following assays.

Table 18: comparison of absorbance at 450 nm in all the R&D Systems ELISA assays performed. The data below were recorded 10 minutes after adding the stop solution.

Well	Absorbance at 450 nm			
	Assay 1	Assay 2	Assay 3	Assay 4
NSB	0.077	0.069	0.178	0.092
Well	1.4	1.207	1.157	1.42
No induction	1.54	0.18	1.047	1.159
No induction	1.273	0.123	0.98	0.672
LPS + IFN-γ	1.131	0.807	3.109	0.985
LPS + IFN-γ	0.541	0.615	2.185	1.198
celecoxib + LPS + IFN-γ	0.911	0.908	2.904	1.059
celecoxib + LPS + IFN-γ	0.921	0.957	1.419	0.394

10. BIBLIOGRAPHY

1. Zidar N, Odar K., Glavac D, Jerse M, Zupanc T, Stajer D, *J Cell Mol Med*, 2009. **13**: p. 3753-3763.
2. Chandrasekharan NV, Dai H., Roos KL, Evanson NK, Tomsik J, Elton TS, Simmons DL, *Proc Natl Acad Sci U S A*, 2002. **99**: p. 13926-13931.
3. McAdam BF, Mardini IA, Habib A, Burke A, Lawson JA, Kapoor S, FitzGerald GA, *J Clin Invest*, 2000. **105**: p. 1473–1482.
4. Lipsky PE, Brooks L, Crofford LJ, DuBois R, Graham D, Simon LS, van de Putte LB, Abramson SB, *Arch Intern Med*, 2000. **160**: p. 913-920.
5. Otto JC, Smith WL, *J Lipid Mediat Cell Signal*, 1995. **12**: p. 139-156.
6. Rouzer CA, Marnett LJ, *J Lipid Res*, 2009. **50**: p. S29–S34.
7. Smith WL, DeWitt DL, Garavito RM, *Annu Rev Biochem*, 2000. **69**: p. 145-182.
8. Luong C, Miller A., Barnett J, Chow J, Ramesha C, Browner MF, *Nat Struct Mol Biol*, 1996. **3**: p. 927-933.
9. Picot D, Loll P, Garavito RM, *Nature*, 1994. **367**: p. 243-249.
10. Kurumbail RG, Stevens AM, Gierse JK, McDonald JJ, Stegeman RA, Pak JY, Gildehaus D, Miyashiro JM, Penning TD, Seibert K, Isakson PC, Stallings WC, *Nature*, 1996. **384**: p. 644-648.
11. Mancini JA, O'Neill GP, Bayly C, Vickers PJ, *FEBS Lett*, 1994. **342**: p. 33-37.
12. Rang PH, Dale MM, Ritter JM, *Rang & Dale's Pharmacology*. 2008: Elsevier. p. 213-223
13. Kawai S, Kojima F, Kusunoki N, *Allergol Int*, 2005. **54**: p. 209-215.
14. Wang D, DuBois R, *Nat Rev Cancer*, 2010. **10**: p. 181-193.
15. Park JM, Kanaoka Y, Eguchi N, Aritake K, Grujic S, Materi AM, Buslon VS, Tippin BL, Kwong AM, Salido E, French SW, Urade Y, Lin HJ, *Cancer Res*, 2007. **67**: p. 881-889.
16. Mutoh M, Watanabe K, Kitamura T, Shoji Y, Takahashi M, Kawamori T, Tani K, Kobayashi M, Maruyama T, Kobayashi K, Ohuchida S, Sugimoto Y, Narumiya S, Sugimura T, Wakabayashi K, *Cancer Res*, 2002. **62**: p. 28-32.
17. Larré S, Tran N, Fan C, Hamadeh H, Champigneulle J, Azzouzi R, Cussenot O, Mangin P, Olivier JL, *Prostaglandins Other Lipid Mediat*, 2008. **87**: p. 14-19.
18. Zhou J, Suzuki T, Kovacic A, Saito R, Miki Y, Ishida T, Moriya T, Simpson ER, Sasano H, Clyne CD, *Cancer Res*, 2005. **65**: p. 657-663.
19. Matsuyama M, Hayama T, Funao K, Sano H, Takemoto Y, Nakatani T, Yoshimura R, *Oncol Rep*, 2007. **18**: p. 99-104.
20. Magnusson C, Ehrnstrom R, Olsen J, Sjolander A, *Cancer Res*, 2007. **67**: p. 9190-9198.
21. Kudo T, Narisawa T, Abo S, Gann, 1980. **71**: p. 260-264.
22. Labayle D, Fischer D, Vielh P, Drouhin F, Pariente A, Bories C, Duhamel O, Troussset M, Attali P, *Gastroenterology*, 1991. **101**: p. 635-639.
23. Giardiello FM, Hamilton SR, Krush AJ, Piantadosi S, Hyland LM, Celano P, Booker SV, Robinson CR, Offerhaus GJ, *N Engl J Med*, 1993. **328**: p. 1313-1316.

24. Dannenberg AJ, Altorki NK, Boyle JO, Dang C, Howe LR, Weksler BB, Subbaramaiah K, *Lancet Oncol*, 2001. **2**: p. 544-551.
25. Gupta RA, Dubois RN, *Nature Rev Cancer*, 2001. **1**: p. 11-21.
26. Yamagata R, Shimoyama T, Fukuda S, Yoshimura T, Tanaka M, Munakata A, *Eur J Gastroenterol Hepatol*, 2001. **14**: p. 359-363.
27. Ristimaki A, Sivula A, Lundin J, Lundin M, Salminen T, Haglund C, Joensuu H, Isola J, *Cancer Res*, 2002. **62**: p. 632-635.
28. Lim SC, Cho H, Lee TB, Choi CH, Min YD, Kim SS, Kim KJ, *Yonsei Med J*, 2010. **51**: p. 692-699.
29. Al-Maghrabi J, Buhmeida A, Emam E, Syrjänen K, Sibiany A, Al-Qahtani M, Al-Ahwal M, *World J Gastroenterol*, 2012. **18**: p. 1793-1799.
30. Jemal A, Siegel R, Xu J, Ward E, *Ca Cancer J Clin*, 2010. **60**: p. 277-300.
31. Waddel W, Loughry R, *J Surg Oncol*, 1983. **24**: p. 83-87.
32. Oka M, Inaba A, Uchiyama T, Hazama S, Shimoda K, Suzuki M, Suzuki T, *Am J Surg*, 1994. **167**: p. 264-267.
33. Eberhart CE, Coffey RG, Radhika A, Giardiello FM, Ferrenbach S, DuBois RN, *Gastroenterology*, 1004. **107**: p. 1183-1188.
34. DuBois RN, Radhika A, Reddy BS, Entingh AJ, *Gastroenterology*, 1996. **110**: p. 1259-1262.
35. Pereira MA, Barnes LH, Rassman VL, Kelloff GV, Steele VE, *Carcinogenesis*, 1994. **15**: p. 1049-1054.
36. Oshima M, Dinchuk JE, Kargman SL, Oshima H, Hancock B, Kwong E, Trzaskos JM, Evans JF, Taketo MM, *Cell*, 1996. **87**: p. 803-809.
37. Grösch S, Tegeder I, Niederberger E, Bräutigam L, Geisslinger G, *FASEB J*, 2001. **15**: p. 2742-2744.
38. Elder DJ, Halton DE, Hague A, Paraskeva C, *Clin Cancer Res*, 1997. **3**: p. 1679-1683.
39. Marnett LJ, DuBois RN, *Annu Rev Pharmacol Toxicol*, 2002. **42**: p. 55-80.
40. Spechler SJ, Goyal RK, *N Engl J Med*, 1986. **315**: p. 362-271.
41. Wilson KT, Fu SD, Ramanujam KS, Meltzer SJ, *Cancer Res*, 1998. **58**: p. 2929-2934.
42. Zimmermann KC, Sarbia M, Weber AA, Borchard F, Gabbert HE, Shror K, *Cancer Res*, 1999. **59**: p. 198-204.
43. Shirvani VN, Ouatu-Lascar R, Kaur BS, Omary MB, Triadafilopoulos G, *Gastroenterology*, 2000. **118**: p. 487-496.
44. Morris CD, Armstrong GR, Bigley G, Green H, Attwood SEA, *Am J Gastroenterol*, 2001. **96**: p. 990-996.
45. Buskens CJ, van Rees BP, Sivula A, Reitsma JB, Haglund C, Bosma PJ, Offerhaus GJ, van Lanschot JJ, Ristimaki A, *Gastroenterology*, 2002. **122**: p. 1800-1807.
46. Corley DA, Kerlikowske K, Verma R, Buffler P, *Gastroenterology*, 2003. **124**: p. 47-56.
47. Lauren P, *Acta Path Microbiol Scand*, 1965. **64**: p. 31-49.

48. Thun MJ, Namboodiri MM, Calle EE, Flanders WD, Heath CW Jr, *Cancer Res*, 1993. **53**: p. 1322-1327.
49. Langman MJS, Cheng KK, Gilman EA, Lancashire RJ, *BMJ*, 2000. **320**: p. 1642-1646.
50. Schreinemachers DM, Everson RB, *Epidemiology*, 1994. **5**.
51. Zaridze D, Borisova E, Maximovitch D, Chkhikvadze V, *Int J Cancer*, 1999. **82**: p. 473-476.
52. Saukkonen K, Nieminen O, van Rees B, Vilkki S, Harkonen M, Juhola M, Mecklin JP, Sipponen P, Ristimaki A, *Clin Cancer Res*, 2001. **7**: p. 1923-1931.
53. Murata H, Kawano S, Tsuji S, Tsuji M, Sawaoka H, Kimura Y, Shiozaki H, Hori M, *Am J Gastroenterol*, 1999. **94**: p. 451-455.
54. Lee TL, Leung WK, Lau JY, Tong JH, Ng EK, Chan FK, Chung SC, Sung JJ, To KF, *Cancer Lett*, 2001. **168**: p. 133-140.
55. Yamamoto H, Itoh F, Fukushima H, Hinoda Y, Imai K, *Int J Cancer*, 1999. **84**: p. 400-403.
56. Uefuji K, Ichikura T, Mochizuki H, *Clin Cancer Res*, 2000. **6**: p. 135-138.
57. Khuder SA, Mutgi AB, *Br J Cancer*, 2001. **84**: p. 1188-1192.
58. Liu CH, Chang SH, Narko K, Trifan OC, Wu MT, Smith E, Haudenschild C, Lane TF, Hla T, *J Biol Chem*, 2001. **267**: p. 18563-18569.
59. Subbaramaiah K, Norton L, Gerald W, Dannenberg AJ, *J Biol Chem*, 2002. **62**: p. 632-635.
60. Brueggemeier RW, Quinn AL, Parrett ML, Joarder FS, Harris RE, Robertson FM, *Cancer Lett*, 1999. **140**: p. 27-35.
61. Brodie AM, Lu Q, Long BJ, Fulton A, Chen T, Macpherson N, DeJong PC, Blankenstein MA, Nortier JW, Slee PH et al, *J Steroid Biochem Mol Biol* 79, 2001. **79**: p. 41-47.
62. Kang JH, Song KH, Jeong KC, Kim S, Choi C, Lee CH, Oh SH, *BMC Cancer*, 2011. **11**: p. 334.
63. Hara A, Okayasu I, *Acta Neuropathol*, 2004. **108**: p. 43-48.
64. Deininger MH, Weller M, Streffer J, Mittelbronn M, Meyermann R, *Acta Neuropathol*, 1999. **98**: p. 240-244.
65. Joki T, Heese O, Nikas DC, Bello L, Zhang J, Kraeft SK, Seyfried NT, Abe T, Chen LB, Carroll RS, Black PM, *Cancer Res*, 2000. **60**: p. 4926-4931.
66. Shono T, Tofilon PJ, Bruner JM, Owolabi O, Lang FF, *Cancer Res*, 2001. **61**: p. 4375-4381.
67. Pairet M, van Ryn J, *COX-2 inhibitors*. 2004: Birkhäuser. p: 232-233.
68. Mascaux C, Martin B, Paesmans M, Berghmans T, Dusart M, Haller A, Lothaire P, Meert A-P, Lafitte J-J, Sculier J-P, *Br J Cancer*, 2006. **95**: p. 139-145.
69. Edelman MJ, Hodgson L., Wang X, Kratzke RA, Vokes EE, *J Clin Oncol*, 2012. **30**: p. 2019-2020.
70. Mutter R, Lu B, Carbone DP, Csiki I, Moretti L, Johnson DH, Morrow JD, Sandler AB, Shyr Y, Ye F, Choy H, *Clin Cancer Res*, 2009. **15**: p. 2158-2165.
71. Akutsu Y, Hanari N, Yusup G, Komatsu-Akimoto A, Ikeda N, Mori M, Yoneyama Y, Endo S, Miyazawa Y, Matsubara H, *Ann Surg Oncol*, 2011. **18**: p. 2946-2951.

72. Akutsu Y, Matsubara H, Shuto K, Uesato M, Mori M, Hoshino I, Shiratori T, Miyazawa Y, Ito H, Uno T, *World J Surg*, 2009. **33**: p. 1002-1009.
73. Kaneko M, Kaneko S, Suzuki K, *Cancer Sci*, 2009. **100**: p. 2193-2201.
74. Zhao S, Cai J, Bian H, Gui L, Zhao F, *Cancer Invest*, 2009. **27**: p. 636-640.
75. Palayoor ST, Bump E, Calderwood SK, Bartol S, Coleman CN, *Clin Cancer Res*, 1998. **1998**: p. 763-771.
76. Shin YK, Park JS, Kim HS, Jun HJ, Kim GE, Suh CO, Yun YS, Pyo H, *Cancer Res*, 2005. **65**: p. 9501-9509.
77. Jun HJ, Kim YM, Park SY, Park JS, Lee EJ, Choi SA, Pyo H, *Int Radiat Oncol Biol Phys*, 2009. **75**: p. 225-234.
78. Raju U, Ariga H, Dittmann K, Nakata E, Ang KK, Milas L, *Int J Radiat Oncol Biol Phys*, 2005. **63**: p. 520-528.
79. Kim BM, Won J, Maeng KA, Han YS, Yun YS, Hong SH, *Int J Oncol*, 2009. **34**: p. 1467-1473.
80. Subbaramaiah K, Hart JC, Norton L, Dannenberg AJ, *J Biol Chem*, 2000. **275**: p. 14838-14845.
81. Altorki NK, Port J, Zhang F, Golijanin D, Thaler HT, Duffield-Lillico AJ, Subbaramaiah K, Dannenberg AJ, *Clin Cancer Res*, 2005. **11**: p. 4191-4197.
82. Lilenbaum R, Socinski M, Altorki NK, Hart LL, Keresztes RS, Hariharan S, Morrison ME, Fayyad R, Bonomi P, *J Clin Oncol*, 2006. **24**: p. 4825-4832.
83. Gradilone A, Pulcinelli FM, Lotti LV, Martino S, Mattiello T, Frati L, Aglianò AM, Gazzaniga P, *J Clin Oncol*, 2007. **25**: p. 4318-4320.
84. Saikawa Y, Sugiura T, Toriumi F, Kubota T, Suganuma K, Isshiki S, Otani Y, Kumai K, Kitajima M, *Anticancer Res*, 2004. **24**: p. 2723-2728.
85. Raspollini MR, Amunni G, Villanucci A, Boddi V, Taddei GL, *Int J Gynecol Cancer*, 2005. **15**: p. 255-260.
86. Kalalinia F, Elahian F, Behravan J, *J Cancer Res Clin Oncol*, 2011. **137**: p. 321-330.
87. Edelman MJ, Watson D, Wang X, Morrison C, Kratzke RA, Jewell S, Hodgson L, Mauer AM, Gajra A, Masters GA, Bedor M, Vokes EE, Green MJ, *J Clin Oncol*, 2008. **26**: p. 848-855.
88. European Commission Health Research Directorate, *Biomarkers for patient stratification*. 2010. p. 5-6.
89. Ostrov DA, Contag CH, *Cancer Prev Res*, 2011. **4**: p. 1523-1526.
90. Rainsford KD, *Aspirin and related drugs*. 2004. p. 2-3
91. Otterness IG, *The Discovery of Drugs to Treat Arthritis: A Historical View*. The Search for Anti-Inflammatory Drugs, ed. J.A. Vincent J. Merluzzi. 1995. p. 1-26
92. Dannenberg AJ, Dubois RN, *COX-2: A New Target for Cancer Prevention and Treatment*. 2003. p. 30-32
93. Gans KR, Galbraith W, Roman RJ, Haber SB, Kerr JS, Schmidt WK, Smith C, Hewes WE, Ackerman NR, *J Pharmacol Exp Ther*, 1990. **254**: p. 180-187.
94. Leblanc Y, Gauthier JY, Ethier D, Guay J, Mancini J, Riendeau D, Tagari P, Vlckers P, Wong E, Prasit P, *Bioorg Med Chem Lett*, 1995. **5**: p. 2123-2128.
95. Kalgutkar AS, Crews BC, Marnett LJ, *Biochemistry*, 1996. **35**: p. 9076-9082.

96. Hashimoto H, Imamura K, Haruta J, Wakitani K, J Med Chem, 2002. **45**: p.1511-1517.
97. Hashimoto H, Maeda K, Ozawa K, Haruta J, Wakitani K, Bioorg Med Chem Lett, 2002. **12**: p. 65-68.
98. Weber A, Casini A, Heine A, Kuhn D, Supuran CT, J Med Chem, 2004. **47**: p. 550-557.
99. Kuge Y, Obokata N, Kimura H, Katada Y, Temma T, Sugimoto Y, Aita K, Seki K, Tamaki N, Saji H, Nucl Med Biol, 2009. **36**: p. 869-876.
100. Walker MC, Kurumbail RG, Kiefer JR, Moreland KT, Koboldt CM, Isakson PC, Seibert K, Gierse JK, Biochem J, 2001. **357**: p. 709-718.
101. Gierse JK, Koboldt CM, Walker MC, Seibert K, Isakson PC, Biochem J, 1999. **339**: p. 607-614.
102. Copeland RA, Williams JM, Glannaras J, Nurnberg S, Covington M, Pinto D, Pick S, Trzaskos JM, Proc Natl Acad Sci U S A, 1996. **91**: p. 11202-11206.
103. Lanzo CA, Sutin J, Rowlinson S, Talley K, Marnett LJ, Biochemistry, 2000. **39**: p. 6228-6234.
104. Timofeevski SL, Prusakiewicz JJ, Rouzer CA, Marnett LJ, Biochemistry, 2002. **41**: p. 6228-6234.
105. Kiefer JR, Pawlitz JL, Moreland KT, Stegeman RA, Hood WF, Gierse JK, Stevens AM, Goodwin DC, Rowlinson SW, Marnett LJ et al, Nature, 2000. **405**: p. 97-101.
106. Price MLP, Jorgensen WL, J Am Chem Soc, 2000. **122**: p. 9455-9466.
107. Selinsky BS, Gupta K., Sharkey CT, Loll PJ, Biochemistry, 2001. **40**: p. 5172-5180.
108. Fumita M, Innis RB, *Neuropsychopharmacology: The Fifth Generation of Progress*. 2002. p. 413
109. Tao, Y., *Characterization of cyclooxygenase-2 inhibitors from ginger dietary supplements*, in *Department of Medicinal Chemistry and Pharmacognosy*. 1995, University of Illinois. p. 20-22
110. Petrovic N, Murray M, Methods Mol Biol, 2010. **594**: p. 129-140.
111. Uddin MJ, Crews BC, Ghebreselasie K, Huda I, Kingsley PJ, Ansari MS, Tantawy MN, Reese J, Marnett LJ, Cancer Prev Res, 2011. **4**: p. 1536-1545.
112. Knights KM, Mangoni AA, Miners JO, Expert Rev Clin Pharmacol, 2010. **3**: p. 769-776.
113. James ML, Gambhir SS, Physiol Rev, 2013. **92**: p. 897-965.
114. de Jong M, Essers J, van Weerden WM, Nat Rev Cancer, 2014. **14**: p. 481-493.
115. Alander JT, Kaartinen I, Laakso A, Patila T, Spillmann T, Tuchin VV, Venermo M, Valisuo P, Int J Biomed Imaging, 2012. **2012**: p. 1-26.
116. Nguyen QT, Tsien RY, Nat Rev Cancer, 2013. **13**: p. 653-662.
117. Keereweer S, K.J., van Driel PB, Xie B, Kaijzel EL, Snoeks TJ, Que I, Hutteman M, van der Vorst JR, Mieog JS, Vahrmeijer AL, van de Velde CJ, Baatenburg de Jong RJ, Löwik CW., Mol Imaging Biol, 2011. **13**: p. 199-207.
118. Khalil MM, Tremoleda JR, Bayomy TB, Gsell W, Int J Mol Imaging, 2011. **2011**: p. 1-15.
119. James ML, Gambhir SS, Physiol Rev, 2012. **92**: p. 897-965.

120. Andriès J, Lemoine L, Mouchel-Blaisot A, Tang S, Verdurand M, Le Bars D, Zimmer L, Billard T, *Bioorg Med Chem Lett*, 2010. **3730-3733**.
121. Workman P, Aboagye EO, Chung YL, Griffiths JR, Hart R, Leach MO, Maxwell RJ, McSheehy PM, Price PM, Zweit J, *J Natl Cancer Inst*, 2006. **98**: p. 580-598.
122. Cherry SR, Dahlbom M, *PET: Physics, Instrumentation, and Scanners*. 2006: Springer. p. 4-6
123. Eckelman WC, Mankoff DA, *Nucl Med Biol*, 2015. **42**: p. 421-425.
124. Huang Y, Zheng MQ, Gerdes JM, *Curr Top Med Chem*, 2010. **10**: p. 1499-1526.
125. Serdons K, Verbruggen A, Bormans GM, *Methods*, 2009. **48**: p. 104-111.
126. Chen K, Chen XY, *Curr Top Med Chem*, 2010. **10**: p. 1227-1236.
127. Conn MP, *Essential Bioimaging Methods*. 2009: Elsevier. p 111
128. Davis KL, Charney D, Coyle JT, Nemeroff C, *Neuropsychopharmacology: the fifth generation of progress*. 2002: Lippincott Williams & Wilkins. p. 412
129. Schulthess GKV, *Molecular Anatomic Imaging*. 2007: Lippincott Williams & Wilkins.
130. Pike VW, *Trends Pharmacol Sci*, 2009. **30**: p. 431-440.
131. Patuzzi J, *Making cancer visible: the role of imaging in oncology*, European Society of Radiology, 2012. p.33-40
132. Wahl RL, Jasene H, Kasamon Y, Lodge MA, *J Nucl Med*, 2009. **Suppl 1**: p. 122S-150S.
133. Gerlinger M, Rowan AJ, Horswell S, Larkin J, Endesfelder D, Gronroos E, Martinez P, Matthews N, Stewart A, Tarpey P, Varela I, Phillimore B, Begum S, McDonald NQ, Butler A, Jones D, Raine K, Latimer C, Santos CR, Nohadani M, Eklund AC, Spencer-Dene B, Clark G, Pickering L, Stamp G, Gore M, Szallasi Z, Downward J, Futreal PA, Swanton C, *N Engl J Med*, 2012. **366**: p. 883-892.
134. Lambin P, Rios-Velazquez E, Leijenaar R, Carvalho S, van Stiphout RG, Granton P, Zegers CM, Gillies R, Boellard R, Dekker A, Aerts HJ, *Eur J Cancer*, 2012. **48**: p. 441-446.
135. Gambhir SS, Czernin J, Schwimmer J, Silverman DH, Coleman RE, Phelps ME, *J Nucl Med*, 2001. **42**: p. 1S-93S.
136. Gallamini A, Zwarthoed C, Borra A, *Cancers*, 2014. **6**: p. 1821-1889.
137. Jelercic S, Rajer M, *Radiol Oncol*, 2015. **49**: p. 1-9.
138. Weber WA, Ott K, Becker K, Dittler HJ, Helmberger H, Avril NE, Meiesetschlager G, Busch R, Siewert JR, Schwaiger M, *J Clin Oncol*, 2001. **19**: p. 3058-3065.
139. Leyton J, Latigo JR, Perumal M, Dhaliwal H, He Q, Aboagye EO, *Cancer Res*, 2005. **65**: p. 4202-4210.
140. Nguyen QD, Smith G, Glaser M, Perumal M, Arstad E, Aboagye EO, *Proc Natl Acad Sci U S A*, 2009. **106**: p. 16375-16380.
141. Murphy MP, Smith R, *Adv Drug Deliv Rev*, 2000. **41**: p. 235-250.
142. Madar I, Huang Y, Ravert H, Dalrymple SL, Davidson NE, Isaacs JT, Dannals RF, Frost JJ, *J Nucl Med*, 2009. **50**: p. 774-780.
143. Oosting SF, Brouwers AH, van Es SC, Nagengast WB, Oude Munnink TH, Lub-de Hooge MN, Hollema H, de Jong JR, de Jong IJ, de Haas S, Scherer SJ, Sluiter WJ, Dierckx RA, Bongaerts AH, Gietema JA, de Vries EG., *J Nucl Med*, 2015. **56**: p. 63-69.

144. Zhu A, Lee D, Shim H, *Semin Oncol*, 2011. **38**: p. 55–69.
145. Pacelli A, Greenman J, Cawthorne C, Smith G, *J Labelled Compd Rad*, 2013.
146. Prabhakaran J, Majo VJ, Simpson NR, Van Heertum RL, Mann JJ, Kumar JSD, *J Labelled Compd Rad*, 2005. **58**: p. 887-895.
147. Takashima-Hirano M, Takashima T, Katayama Y, Wada Y, Sugiyama Y, Watanabe Y, Doi H, Suzuki M, *Bioorg Med Chem*, 2011. **19**: p. 2997-3004.
148. Gao M, Wang M, Miller KD, Zheng QH, *Eur J Med Chem*, 2011. **46**: p. 4760-4767.
149. de Vries EF, Doorduyn J, Dierckx RA, van Waarde A, *Nucl Med Biol*, 2008. **35**: p. 35-42.
150. Tanaka M, Fujisaki Y, Kawamura K, Ishiwata K, Qinggeletu, Yamamoto F, Mukai T, Maeda M, *Biol Pharm Bull*, 2006. **29**: p. 2087-2094.
151. Prabhakaran J, Underwood MD, Parsey RV, Arango V, Majo VJ, Simpson NR, Van Heertum R, Mann JJ, Kumar JS, *Bioorg Med Chem*, 2007. **15**: p. 1802-1807.
152. Toyokuni T, Kumar JS, Walsh JC, Shapiro A, Talley JJ, Phelps ME, Herschman HR, Barrio JR, Satyamurthy N, *Bioorg Med Chem Lett*, 2005. **15**: p. 4699-4702.
153. Riese J, Hoff T, Nordhoff A, DeWitt DL, Resch K, Kaefer V, *J Leukoc Biol*, 1994. **55**: p. 476-482.
154. McCarthy TJ, Sheriff AU, Graneto MJ, Talley JJ, Welch MJ, *J Nucl Med*, 2002. **43**: p. 117-124.
155. de Vries EF, van Waarde A, Buursma AR, Vaalburg W, *J Nucl Med*, 2003. **44**: p. 1700-1706.
156. Kniess T, Laube M, Bergmann R, Sehn F, Graf F, Steinbach J, Wuest F, Pietzsch J, *Bioorg Med Chem*, 2012. **20**: p. 3410-3421.
157. Wuest F, Tang L, Kniess T, Pietzsch J, Suresh M, *Bioorg Med Chem*, 2009. **17**: p. 1146-1151.
158. Al-Hourani BJ, Sharma S, Suresh M, Wuest F, *Bioorg Med Chem Lett*, 2012. **22**: p. 2235-2238.
159. Kuge Y, Katada Y, Shimonaka S, Temma T, Kimura H, Kiyono Y, Yokota C, Minematsu K, Seki K, Tamaki N, Ohkura K, Saji H, *Nucl Med Biol*, 2006. **33**: p. 21-27.
160. Uddin MJ, Crews BC, Ghebreselasie K, Tantawy MN, Marnett LJ, *ACS Med Chem Lett*, 2011. **2**: p. 160-164.
161. Uddin MJ, Crews BC, Blobaum AL, Kingslay PJ, Ghebraselase K, Saleh SS, Clanton JA, Baldwin RM, Marnett LJ, *J Labelled Compd Rad*, 2009. **52**: p. 387-393.
162. Vallabhajosula S, *Semin Nucl Med*, 2007. **37**: p. 400-419.
163. Coenen HH, Ernst Schering Res Found Workshop, 2007. **62**: p. 15-50.
164. Wester JH, *Pharmaceutical radiochemistry: 1*. 2010: Scintomics. p. 5-8
165. Lu S, Pike VW, *J Fluor Chem*, 2010. **131**: p. 1032–1038.
166. Constantinou M, Aigbirhio FI, Smith RG, Ramsden CA, Pike VW, *J Am Chem Soc*, 2001. **123**: p. 1780-1781.
167. Vasdev N, Pointner BE, Chirakal R, Schrobilgen GJ, *J Am Chem Soc*, 2002. **124**: p. 12863-12868.

168. Ross TL, Ermert J, Hocke C, Coenen HH, *J Am Chem Soc*, 2007. **129**: p. 8018-8025.
169. Brooks AF, Topczewski JJ, Ichiishi N, Sanford MS, Scott PJ., *Chem Sci*, 2014. **5**: p. 4545-4553.
170. Rotstein BH, Stephenson NA, Vasdev N, Liang SH, *Nat Commun*, 2014. **5**: p. 1-7.
171. Lee E, Kamlet AS, Powers DC, Neumann CN, Boursalian GB, Furuya T, Choi DC, Hooker JM, Ritter T, *Science*, 2011. **334**: p. 639-642.
172. Lee E, Hooker JM, Ritter T, *J Am Chem Soc*, 2012. **134**: p. 17456-17458.
173. Ichiishi N, Canty AJ, Yates BF, Sanford MS, *Organometallics*, 2014. **33**: p. 5525-5534.
174. Ichiishi N, Brooks AF, Topczewski JJ, Rodnick ME, Sanford MS, Scott PJ, *Org Lett*, 2014. **16**: p. 3224-3227.
175. Hollingworth C, Hazari A, Hopkinson MN, Tredwell M, Benedetto E, Huiban M, Gee AD, Brown JM, Gouverneur V, *Angew Chem Int Ed Engl*, 2011. **50**: p. 2613-2617.
176. Benedetto E, Tredwell M., Hollingworth C, Khotavivattana T, Brown JM, Gouverneur V, *Chem Sci*, 2013. **4**: p. 89-96.
177. Graham TJ, Lambert RF, Ploessl K, Kung HF, Doyle AG, *J Am Chem Soc*, 2014. **136**: p. 5291-5294.
178. Kettenbach K, Schieferstein H, Ross TL, *Biomed Res Int*, 2014. **2014**: p. 1-16.
179. Bouvet V, Wuest M, Wuest F, *Org Biomol Chem*, 2011. **9**: p. 7393-7399.
180. Li Z, Cai H, Hassink M, Blackman ML, Brown RC, Conti PS, Fox JM, *Chem Commun*, 2010. **46**: p. 8043-8045.
181. Neumann CN, Ritter T, *Angew Chem Int Ed Engl*, 2015. **54**: p. 3216-3221.
182. Penning TD, Talley JJ, Bertenshaw SR, Carter JS, Collins PW, Docter S, Graneto MJ, Lee LF, Malecha JW, Miyashiro JM, Rogers RS, Rogier DJ, Yu SS, AndersonGD, Burton EG, Cogburn JN, Gregory SA, Koboldt CM, Perkins WE, Seibert K, Veenhuizen AW, Zhang YY, Isakson PC, *J Med Chem*, 1997. **40**: p. 1347-1365.
183. Miller JL, *Am J Health Syst Pharm*, 1999. **56**: p. 1294.
184. Cheer SM, Goa KL, *Drugs*, 2001. **61**: p. 1133-1141.
185. Talley JJ, Brown D, Carter JS, Graneto MJ, Koboldt CM, Masferrer JL, Perkins WE, Rogers RS, Shaffer AF, Zhang YY, Zweifel BS, Seibert K, *J Med Chem*, 2000. **43**: p. 775-777.
186. Riendeau D, Percival MD, Brideau C, Charleson S, Dubé D, Ethier D, Falguyret JP, Friesen RW, Gordon R, Greig G, Guay J, Mancini J, Ouellet M, Wong E, Xu L, Boyce S, Visco D, Girard Y, Prasit P, Zamboni R, Rodger IW, Gresser M, Ford-Hutchinson AW, Young RN, Chan CC, *J Pharmacol Exp Ther*, 2001. **296**: p. 558-566.
187. Kirane A, Toombs JE, Ostapoff K, Carbon JG, Zaknoen S, Braunfeld J, Schwarz RE, Burrows FJ, Brekken RA, *Clin Cancer Res*, 2012. **18**: p. 5031-5042.
188. Yamamoto H, Kondo M, Nakamori S, Nagano H, Wakasa K, Sugita Y, Chang-De J, Kobayashi S, Damdinsuren B, Dono K, Umeshita K, Sekimoto M, Sakon M, Matsuura N, Monden M., *Gastroenterology*, 2003. **125**: p. 556-571.

189. Kvaternick V, Pollmeier M, Fischer J, Hanson PD, *J Vet Pharmacol Ther*, 2007. **30**: p. 208-217.
190. Gierse JK, Hauser SD, Creeley DP, Koboldt C, Rangwala SH, Isakson PC, Seibert K, *Biochem J*, 1995. **305**: p. 479-484.
191. Rao P, Knaus EE, *J Pharm Pharm Sci*, 2008. **11**: p. 81s-110s.
192. Ushiyama S, Yamada T, Murakami Y, Kumakura S, Inoue S, Suzuki K, Nakao A, Kawara A, Kimura T, *Eur J Pharmacol*, 2008. **578**: p. 76-86.
193. Doherty AM, *Annual Reports in Medicinal Chemistry*. 2004: Elsevier. p.133
194. Wakitani K, Yamada T, Masaki M, Matsushita M, *Jpn J Pharmacol*, 1998. **78**: p. 365-371.
195. Zarghi A, Javid FS, Ghodsi R, Dadrass OG, Daraei B, Hedayati M, *Sci Pharm*, 2011. **79**: p. 449-460.
196. Gamble AB, Garner J, Gordon CP, O'Conner SMJ, Keller PA, *Synth Commun*, 2007. **37**: p. 2777-2786.
197. Chandrappa S, Vinaya K, Ramakrishnappa T, Rangappa KS, *Synlett*, 2010. **20**: p. 3019-3022.
198. Rahaim RJ, Maleczka RE, *Org Lett*, 2005. **7**: p. 5087-5090.
199. Shah CP, Dwivedi C, Singh KK, Kumar M, Bajaj PN, *Mater Res Bull*, 2010. **45**: p. 1213-1217.
200. Pankaskie MC, Small L, *J Chem Educ*, 1986. **63**: p. 650.
201. Butler AR, Leitch E, *J Chem Soc, Perkin Trans*, 1977. **2**: p. 1972-1976.
202. Travis BR, Sivakumar M, Hollist GO, Borhan B, *Org Lett*, 2003. **5**: p. 1031-1034.
203. Dannhardt G, Kiefer W, *Eur J Med Chem*, 2001. **36**: p. 109-126.
204. Park HS, Choi H, Shin HS, Lee SK, Park MS, *Bull Korean Chem Soc*, 2007. **28**: p. 751-757.
205. Almansa C, Alfon J, de Arriba AF, Cavalcanti FL, Escamilla I, Gómez LA, Miralles A, Soliva R, Bartrolí J, Carceller E, Merlos M, García-Rafanell J., *J Med Chem*, 2003. **46**: p. 3463-3475.
206. Tipe DN, Zoghbi SS, Liow JS, Green MV, Seidel J, Ichise M, Innis RB, Pike VW, *J Nucl Med*, 2006. **47**: p. 345-353.
207. Yoder KK, Mock BH, Zheng QH, McCarthy BP, Riley AA, Hutchins GD, *J Neurosci Methods*, 2011. **196**: p. 70-75.
208. Milicevic-Sephton S, Dennler P, Leutwiler DS, Mu L, Wanger-Baumann CA, Schibli R, Krämer SD, Ametamey SM, *Am J Nucl Med Mol Imaging*, 2012. **2**: p. 14-28.
209. Van Leusen D, Oldenziel O, Van Leusen A, *J Org Chem*, 1977. **42**: p. 3114-3118.
210. Che H, Tuyen TN, Kim HP, Park H, *Bioorg Med Chem Lett*, 2010. **20**: p. 4035-4037.
211. Barta T, Stealey MA, Collins PW, Weier RM, *Bioorg Med Chem Lett*, 1998. **8**: p. 3443-3448.
212. Perrone MG, Scilimati A, Simone L, Vitale P, *Curr Med Chem*, 2010. **17**: p. 3769-3805.

213. Khanna IK, Weier RM, Yu Y, Xu XD, Koszyk FJ, Collins PW, Koboldt CM, Veenhuizen AW, Perkins WE, Casler JJ, Masferrer JL, Zhang YY, Gregory SA, Seibert K, Isakson PC., *J Med Chem*, 1997. **40**: p. 1634-1647.
214. Barrios-Rodiles M, Chadee K, *J Immunol*, 1998. **161**: p. 2441-2448.
215. Cayman Chemical, COX (ovine/human) inhibitor Screening Assay kit booklet.
216. Hood WF, Gierse JK, Isakson PC, Kiefer JR, Kurumbail RG, Seibert K, Monahan JB, *Mol Pharmacol*, 2003. **63**: p. 870-877.
217. Cai L, Lu S, Pike VW, *Eur J Org Chem*, 2008. **2008**: p. 2853–2873.
218. Emran AM, *New Trends in Radiopharmaceutical Synthesis, Quality Assurance, and Regulatory Control*. 1991: Plenum Press. p. 437
219. Wieland DM, Tobes M., Mangner TJ, *Analytical and Chromatographic Techniques in Radiopharmaceutical Chemistry*. 2011: Springer. p. 52
220. Nolting DD, Nickels ML, Guo N, Pham W, *Am J Nucl Med Mol Imaging*, 2012. **2**: p. 273-306.
221. Perrone MG, Malerba P, Uddin MJ, Vitale P, Panella A, Crews BC, Daniel CK, Ghebreselasie K, Nickels M, Tantawy MN, Manning HC, Marnett LJ, Scilimati A, *Eur J Med Chem*, 2014. **80**: p. 562-568.
222. R&D Systems, Prostaglandin E₂ Parameter Assay Kit booklet.